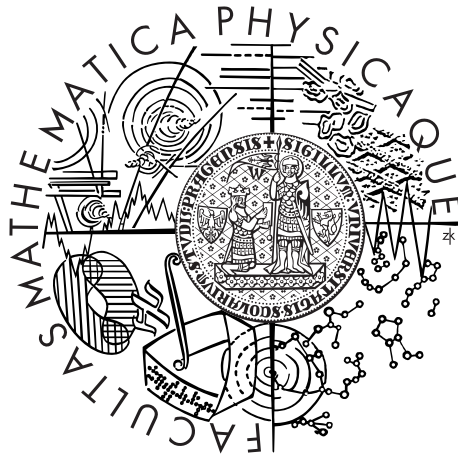


Charles University in Prague
Faculty of Mathematics and Physics

DOCTORAL THESIS



Martin Slezák

Monitoring of the energy scale in the **KATRIN** neutrino experiment

Nuclear Physics Institute
Czech Academy of Sciences

Supervisor of the doctoral thesis: Mgr. Drahošlav Vénos, CSc.

Study programme: Physics

Specialization: Subnuclear physics

Prague 2015

Prohlašuji, že jsem tuto disertační práci vypracoval samostatně a výhradně s použitím citovaných pramenů, literatury a dalších odborných zdrojů.

Beru na vědomí, že se na moji práci vztahují práva a povinnosti vyplývající ze zákona č. 121/2000 Sb., autorského zákona v platném znění, zejména skutečnost, že Univerzita Karlova v Praze má právo na uzavření licenční smlouvy o užití této práce jako školního díla podle §60 odst. 1 autorského zákona.

V Praze, dne 30. listopadu 2015

Martin Slezák

Název práce: Monitorování energetické stupnice v neutrinovém experimentu KATRIN

Autor: Martin Slezák

Ústav: Ústav jaderné fyziky, Akademie věd České republiky, v.v.i.

Vedoucí disertační práce: Mgr. Drahoslav Vénos, CSc., Oddělení jaderné spektroskopie

Abstrakt: Otázka absolutní škály hmotností neutrin je předmětem mimořádného zájmu v částicové fyzice, astrofyzice a kosmologii. Experiment KATRIN (KARlsruhe TRItium Neutrino experiment) má za cíl měření efektivní hmotnosti elektronového antineutrina z tvaru β -spektra tritia s nebývalou citlivostí $0,2 \text{ eV}/c^2$. Jeden z hlavních systematických efektů se týká experimentální energetické škály, která musí být stabilní na úrovni pouhých několika miliontin. Pro její kalibraci a monitorování budou rozsáhle využívány monoenergetické elektrony, které jsou emitovány při vnitřní konverzi γ -přechodu metastabilního izotopu $^{83\text{m}}\text{Kr}$. Předmětem této disertace je problematika zkreslení energetické škály KATRIN a jejího monitorování. Je studován zdroj elektronů založený na $^{83\text{m}}\text{Kr}$ zabudovaném v pevné látce jakožto i zdroj založený na plynném $^{83\text{m}}\text{Kr}$. Na základě experimentálních výsledků je navrhnout postup nepřetržitého monitorování stability.

Klíčová slova: KATRIN, hmotnost neutrin, beta rozpad, jaderná spektroskopie, krypton

Title: Monitoring of the energy scale in the KATRIN neutrino experiment

Author: Martin Slezák

Department: Nuclear Physics Institute, Czech Academy of Sciences

Supervisor: Mgr. Drahoslav Vénos, CSc., Department of Nuclear Spectroscopy

Abstract: The question of the absolute mass scale of neutrinos is of particular interest for particle physics, astrophysics, and cosmology. The KATRIN experiment (KARlsruhe TRItium Neutrino experiment) aims to address the effective electron antineutrino mass from the shape of the tritium β -spectrum with an unprecedented sensitivity of $0.2 \text{ eV}/c^2$. One of the major systematic effects concerns the experimental energy scale, which has to be stable at the level of only a few parts in a million. For its calibration and monitoring the monoenergetic electrons emitted in the internal conversion of γ -transition of the metastable isotope $^{83\text{m}}\text{Kr}$ will be extensively applied. The aim of this thesis is to address the problem of KATRIN energy scale distortions and its monitoring in detail. The source of electrons based on $^{83\text{m}}\text{Kr}$ embedded in a solid as well as the source based on gaseous $^{83\text{m}}\text{Kr}$ are studied. Based on the experimental results an approach for the continuous stability monitoring is proposed.

Keywords: KATRIN, neutrino mass, beta decay, nuclear spectroscopy, krypton

Acknowledgements

I am sincerely grateful to everyone who supported me in the work for this thesis. In particular, I would like to thank

- Drahoslav Vénos and Klaus Schlösser for their professional leadership, support, encouragement, many discussions of the measurement results, for showing me the art of practical work in experimental nuclear physics, and K.S. for lending me a handy bike,
- Marius Arenz and the whole mass separator team for dealing with the production of the solid $^{83\text{m}}\text{Kr}$ source samples, for showing me the Bonn Isotopen Separator, M.A. for his opinions and discussions of the other infinitely many topics, for asking nasty questions that made me think about the deepest nature of things, and for his understanding and trust,
- Moritz Erhard for his great improvements on the neutrino conference poster, for the model of the monitor spectrometer in Kassiopeia, for tireless switching of the sources at the monitor spectrometer, for the discussions, cooperation in the lab, and feedback about the fit program for the monitor spectrometer, and for throwing a conifer cone into the office of M.A. and myself,
- Andreas Kopmann for the kind stays at his house during my visits to KIT,
- Otokar Dragoun for the stimulating physics discussions, support, and trust, Antonín Špalek for the discussions of the Monte Carlo simulations, Ondřej Lebeda for dealing with the chemistry regarding the ^{83}Rb , and Jana Sentkerestiová for support with the gamma-spectroscopy measurements of the zeolite source,
- Christian Weinheimer for providing the high-precision high-voltage divider K35, Stephan Bauer, Marcel Kraus, Oliver Rest, and the whole high-voltage group for support and discussions about the divider and regular calibrations of the voltmeters,
- Norbert Hillebrand for the regular maintenance and care of the monitor spectrometer cryogenic liquids,
- Norman Haußmann for getting the opportunity to program in LabVIEW with him and for the cooperation in development of the monitor spectrometer software,
- Nancy Wandkowsky for applying for the stipendium for a visiting researcher at the Karlsruhe House of Young Scientists,
- and Marco Kleesiek, Suren Chilingaryan, Till Bergmann, and Armen Beglarian for the great software support and problem solutions.

I gratefully acknowledge the organizations or foundations which supported my numerous visits to foreign workplaces and conferences, in particular the Grant Agency of the Czech Republic (contract no. P203/12/1896), the Czech Ministry of Education, Youth

and Sports (CENAP LC07050, SVV-2011-263309, SVV-2012-265309, SVV-2013-267309, SVV-2014-260097), the Deutsche Forschungsgemeinschaft (WE 1843/6-1), the European Nuclear Science and Applications Research at ISOLDE (262010), the Karlsruhe House of Young Scientists, the Wilhelm und Else Heraeus-Stiftung, and the Neutrino 2014 conference organizing committee.

I am grateful to the Institute of Experimental and Applied Physics at the Czech Technical University in Prague for lending the complete Timepix detector and to the Advacam (formerly Widepix) company for lending the next-generation FitPIX interface. I would like to thank Jan Jakůbek for teaching me the operation, calibration, and data acquisition of the Timepix detector.

Above all, I am indebted to my family for their unconditional support, encouragement, and assistance, in particular to my wonderful Lucia for helping me stay alive.

Contents

Introduction	1
Thesis outline	2
1 Neutrino physics	5
1.1 Description in the Standard Model and beyond	5
1.2 Neutrino flavor oscillations	10
1.3 Determination of the neutrino mass	16
2 The KATRIN experiment	21
2.1 Tritium as β -emitter	21
2.2 MAC-E filter electron spectroscopy	22
2.3 Overview of the experimental setup	25
2.4 Experimental uncertainties	28
3 Energy scale in KATRIN	31
3.1 Effects of energy scale distortions in β -decay neutrino mass measurements .	31
3.2 Conversion electrons of $^{83\text{m}}\text{Kr}$	41
3.3 Applications of $^{83\text{m}}\text{Kr}$ for energy scale calibration and monitoring	43
4 Conversion electron line shape of the solid $^{83\text{m}}\text{Kr}$ source	51
4.1 The monitor spectrometer	51
4.2 The least-squares method	61
4.3 Observed line shape	64
4.4 Doniach-Šunjić conversion line shape	67
4.5 Reference method	86
5 The solid $^{83\text{m}}\text{Kr}$ source	91
5.1 Implantation of ^{83}Rb	93
5.2 Basic SKrS characteristics	96
5.3 Electron spectroscopy measurements at the monitor spectrometer	117
5.4 Correlation between peak concentration and line position drift	142
5.5 Valence electrons of the SKrS	144
5.6 More accurate transmission function of the monitor spectrometer	147
5.7 Conclusion	149

6	The gaseous $^{83\text{m}}\text{Kr}$ source	153
6.1	The $^{83}\text{Rb}/^{83\text{m}}\text{Kr}$ zeolite source	153
6.2	Retention of $^{83\text{m}}\text{Kr}$ in the zeolite source	154
6.3	Emanation of absorbed air from zeolite in ultra-high vacuum	159
6.4	Conclusion	159
7	Monitoring of the KATRIN high-voltage stability	161
7.1	Optimization of the retarding energy and time distribution	161
7.2	The method of high-voltage stability monitoring	167
7.3	Conclusion	176
8	Conclusion	179
8.1	Outlook	181
A	Dead time of the silicon drift detector	183
A.1	Analogue and digital electronics	183
A.2	Measurement of the SDD dead time	186
A.3	Conclusion	189
	References	191
	List of Figures	203
	List of Tables	207
	List of publications	209

Introduction

The elementary particle which we today call the neutrino was proposed by W. Pauli in 1930 in his famous letter to a group of physicists present at a meeting in Tübingen. At that time it was an attempt to remedy the baffling experimental observations regarding the radioactive nuclear β -decay. The emitted electron energy spectrum was observed continuous in contrast to the discrete spectrum seen in the α - and γ -decay. Also the angular momentum seemed not to be conserved when only the parent and daughter nuclei and the electron were taken into account. Adding a spin- $\frac{1}{2}$ particle which is emitted in the decay together with the electron explained the spectrum continuity and the missing angular momentum. Moreover, the particle's electrical neutrality and non-participation in the nuclear force also explained the difficulty to detect it. It was not until about 20 years later before the neutrino was discovered in an experiment by C. Cowan and F. Reines.

Since then our understanding of the neutrino properties and interactions has evolved substantially and is now part of what is known as the Standard Model of particle physics. The weak interaction, which is responsible for the β -decay, is one of the three fundamental forces described by the Standard Model and there are three neutrino flavors (electron, muon, tauon) known to participate in the interaction. It is well experimentally established that the neutrinos undergo the so-called neutrino oscillations meaning that the flavor of the neutrino can change with some probability as a function of its energy and distance travelled. The oscillations are the solution to the long-standing solar neutrino problem when a less than expected number of electron neutrinos coming from the Sun is observed.

The neutrino oscillations require that the flavor eigenstates are a quantum-mechanical superposition of the mass eigenstates and that the mass eigenvalues are not equal. Therefore, observation of the oscillations implies non-zero neutrino masses. But since neutrino oscillations are a variation of an interference experiment, only differences of the masses squared can be obtained from the oscillation experiment results. The neutrino masses or, in other words, the absolute neutrino mass scale have to be obtained by different means.

However, to date only experimental limits have been given. The limits point to neutrino masses smaller by several orders of magnitude than for the other fermions, but the actual observation of the neutrino mass scale, a fundamental parameter of particle physics, is still missing. Furthermore, despite its great successes the Standard Model gives neither any prediction about the pattern of the individual fermion masses nor at least an explanation why the neutrino masses are so different. An observation of an actual non-zero neutrino mass may point to specific new physics beyond the Standard Model.

The implications go beyond particle physics. In cosmology, the Big Bang theory predicts presence of cosmic neutrino background in analogy to cosmic microwave background. The relative mass of these neutrinos with respect to other matter in the early Universe had an impact on structure formation in the Universe. Therefore, the neutrino mass scale

represents a valuable input and cross-check for cosmological models.

The direct observation of a non-zero neutrino mass is thus highly motivated. The Karlsruhe TRitium Neutrino (KATRIN) experiment, being set up in Karlsruhe, Germany, aims to address the question of the absolute mass scale of neutrinos with unprecedented sensitivity. The experimental technique follows the proposal of E. Fermi who already in 1934 showed that the neutrino mass information can be extracted from the endpoint region of the β -electron energy spectrum. This approach has the advantage that it is based only on kinematic laws and thus it is model independent in contrast to other means such as cosmology observations or neutrinoless double β -decay. KATRIN combines high-luminosity and high-resolution electron spectroscopy technique, which is based on a special type of electrostatic spectrometer with inhomogeneous magnetic field known as the MAC-E filter (magnetic adiabatic collimation with electrostatic filter), with the advantages of using tritium as the β -emitter having the low endpoint energy of 18.6 keV.

In order to reach the KATRIN design sensitivity several systematic effects have to be under control. One of the major effects comprises distortions of the experimental energy scale. This is due to the fact that unrecognized fluctuations of the observed electron energy may lead to systematic shifts of the measured neutrino mass. The requirement is challenging: at 18.6 keV the standard deviation of unrecognized energy scale distortions must not exceed 60 meV over the length of a KATRIN run planned for two months. In other words, the energy scale has to be stable at the level of 3 ppm (parts per million) for two months.

Besides high-precision and high-stability electronic equipment developed specifically for KATRIN the energy scale calibration and monitoring will rely also on a nuclear standard, an emitter of monoenergetic electrons. The metastable excited state of ^{83}Kr , denoted as $^{83\text{m}}\text{Kr}$, seems to be the most promising electron source. $^{83\text{m}}\text{Kr}$ emits internal conversion electrons in a highly converted nuclear transition with the energy of 17.8 keV which is only about 800 eV lower than the tritium endpoint energy. Moreover, it has a rather short half-life of only about two hours which excludes any possibility of long-term contamination of the experimental apparatus. The $^{83\text{m}}\text{Kr}$ can be conveniently generated in sufficient amount from the decay of ^{83}Rb with the half-life of about three months.

To assess the energy scale systematic effects the $^{83\text{m}}\text{Kr}$ will be applied in three different forms. The gaseous form will be utilized at the KATRIN source together with the gaseous tritium and mainly the source systematics will be investigated. The condensed film will be applied beyond the source downstream of the KATRIN main beamline for precise calibration of the electrostatic spectrometer between individual runs. The $^{83\text{m}}\text{Kr}$ embedded in a solid substrate through the implantation of its mother isotope ^{83}Rb will be used for continuous monitoring of the spectrometer high-voltage system using a beamline parallel to the tritium one at the so-called monitor spectrometer.

Thesis outline

The aim of this thesis is to address in detail the KATRIN energy scale distortions and monitoring of its stability using the nuclear standard $^{83\text{m}}\text{Kr}$. In Chapter 1 the physics of

neutrinos with the emphasis on the neutrino mass is summarized. Besides, the approaches for determination of the absolute neutrino mass scale are reviewed. Chapter 2 discusses the distinguishing features of KATRIN, the tritium as the β -electron emitter and the MAC-E filter spectroscopy technique. The KATRIN experimental setup and uncertainties are then briefly described. The energy scale distortions and their influence on the observed neutrino mass are addressed in Chapter 3. Furthermore, the chapter discusses the properties of the $^{83\text{m}}\text{Kr}$ and the emitted conversion electrons as well as the applications of $^{83\text{m}}\text{Kr}$ for the KATRIN energy scale calibration and monitoring. Chapter 4 addresses description of the conversion electron line shape of the solid $^{83\text{m}}\text{Kr}$ source which is required for the source to be applicable in KATRIN. The monitor spectrometer setup and measurement is also described. The solid and gaseous $^{83\text{m}}\text{Kr}$ sources and their development for KATRIN are discussed in Chapter 5 and Chapter 6, respectively. The Chapter 7 addresses the strategy of the actual high-voltage stability monitoring using the solid $^{83\text{m}}\text{Kr}$ source and the monitor spectrometer. Finally, the thesis is concluded in the Chapter 8.

1 Neutrino physics

The neutrino is an elementary particle with half-integer spin (a fermion), no electric charge, no color charge, and non-zero mass. Thus, it is known to participate only in the weak and gravitational interactions. There are three known weak interaction flavor neutrinos and correspondingly three known massive neutrino states. The non-zero mass was established by observation of the neutrino flavor oscillations which are, however, sensitive merely to differences of the neutrino masses squared. Direct measurements of the absolute neutrino mass scale point to values several orders of magnitude smaller than for the other elementary fermions, but the experiments have so far yielded only upper limits. A direct observation of the neutrino mass may show the way to new physics and is thus one of the primary goals of present experimental effort. Moreover, the neutrinos are predicted to be the second-most abundant particles in the Universe after the photons thus having an influence on the evolution of the Universe to the present state. The neutrino mass scale may thus lead to better understanding of the Universe as a whole.

In this chapter, the present understanding of neutrino physics is briefly reviewed with the emphasis on the neutrino mass. The description of the neutrino within the current particle physics framework, the Standard Model, is given. The phenomenon of neutrino flavor oscillations is discussed and experimental evidence is summarized. Lastly, the possibilities for neutrino mass determination are overviewed.

1.1 Description in the Standard Model and beyond

The modern description of neutrinos and their interactions is governed by the Standard Model (SM) of particle physics with its mathematical framework based on quantum field theory (QFT) [Man84, Giu07]. The neutrino as other fermions is generally described by a four-component wavefunction $\psi(x)$ obeying the free-particle Dirac equation. The equation is written in covariant form using the Einstein summation convention and the natural units $\hbar = c = 1$ as

$$(i\gamma^\mu \partial_\mu - m)\psi(x) = 0, \quad (1.1)$$

where x denotes position, $\partial_\mu \equiv \frac{\partial}{\partial x^\mu}$, m is the particle's mass and γ^μ are the four Dirac gamma matrices satisfying the anticommutation relations

$$\{\gamma^\mu, \gamma^\nu\} \equiv \gamma^\mu \gamma^\nu + \gamma^\nu \gamma^\mu = 2g^{\mu\nu}, \quad (1.2)$$

where $g^{\mu\nu}$ is the flat space-time metric $g^{\mu\nu} = \text{diag}(1, -1, -1, -1)$. This is an equation of motion for ψ which in the context of field theory follows from the corresponding Dirac Lagrangian density (or simply the Lagrangian)

$$\mathcal{L}_{\text{Dirac}} = i\bar{\psi}\gamma^\mu \partial_\mu \psi - m\bar{\psi}\psi, \quad (1.3)$$

where $\bar{\psi}$ denotes the adjoint field, $\bar{\psi} \equiv \psi^\dagger \gamma^0$, via the Euler-Lagrange equations. In second quantization the Dirac field $\psi(x)$ becomes a quantum mechanical operator on the many-particle Fock space through the particle creation and annihilation operators.

Interactions between the fields follow from the requirement that the Lagrangian, which is free from fermionic mass terms of the form

$$\mathcal{L}_{\text{Dirac}}^{\text{mass}} = -m\bar{\psi}\psi \quad (1.4)$$

is invariant under certain local gauge transformations. The weak interaction, in which the neutrinos participate, is a part of the unified electroweak model based on the $SU(2)_L \times U(1)_Y$ local gauge symmetry [Gla61, Wei67, Sal68]. The subscripts L and Y denote left-handed chirality and weak hypercharge, respectively. The chirality is defined using the fifth gamma matrix γ_5 , which anticommutes with the four Dirac gamma matrices γ^μ . The left- and right-handed components ψ_L and ψ_R are then the chiral projections

$$\psi_L \equiv \frac{1 - \gamma_5}{2}\psi, \quad \gamma_5\psi_L = -\psi_L, \quad (1.5a)$$

$$\psi_R \equiv \frac{1 + \gamma_5}{2}\psi, \quad \gamma_5\psi_R = +\psi_R. \quad (1.5b)$$

The group $SU(2)_L$ is also called the weak isospin and its elements act only on the left-handed chiral components ψ_L of the fermion fields. The leptons are arranged in $SU(2)_L$ left-handed doublets (neutrino and the charged fermion) and right-handed singlets. Denoting the charged lepton wavefunction as l_α and the neutrino one as ν_α for the flavor α , this can be written as

$$\begin{pmatrix} \nu_{\alpha L} \\ l_{\alpha L} \end{pmatrix}, l_{\alpha R}, (\nu_{\alpha R}). \quad (1.6)$$

The right-handed neutrino, written in parentheses, is usually not considered in the SM, see further.

The mass terms of the weak interaction gauge bosons¹ and the fermions cannot be added by hand directly into the Lagrangian because the left- and right-handed components of the fields transform differently under the gauge transformations and thus gauge invariance would be violated. Instead, the Higgs mechanism [Hig64a, Hig64b, Eng64, Gur64] provides the masses in a gauge invariant way. The term spontaneous symmetry breaking, which is widely used in this context, refers to the system suddenly occupying a particular ground state (vacuum) thus breaking the symmetry². In the minimal model the weak isospin Higgs doublet Φ after the spontaneous symmetry breaking is

$$\Phi(x) = \begin{pmatrix} \varphi^+(x) \\ \varphi^0(x) \end{pmatrix} = \frac{1}{\sqrt{2}} \begin{pmatrix} 0 \\ v + H(x) \end{pmatrix}, \quad (1.7)$$

where v is the vacuum expectation value of the Higgs potential of about 246 GeV and $H(x)$ describes the physical scalar Higgs boson with zero spin. The charged lepton masses

¹ A massive spin-1 particle is described by the four-vector $A^\mu(x)$ which follows the Proca equation. The corresponding mass term in the Lagrangian is $\frac{1}{2}m^2 A_\mu A^\mu$.

² It has been suggested to state more appropriately that the symmetry becomes hidden [Hoř02, Giu07].

are generated via Yukawa coupling of the left-handed doublets and right-handed singlets to the Higgs doublet. In terms of the Lagrangian this is

$$\mathcal{L}_{\text{Yukawa}}^l = -y_\alpha (\bar{\nu}_{\alpha L}, \bar{l}_{\alpha L}) \Phi l_{\alpha R} + \text{h.c.}, \quad (1.8)$$

where y_α is a dimensionless coupling constant for the lepton flavor α and h.c. denotes hermitian conjugation of the written term(s). Writing the expression out gives the Dirac mass term

$$\mathcal{L}_{\text{Dirac}}^{\text{mass}} = -y_\alpha \frac{v}{\sqrt{2}} \bar{l}_{\alpha L} l_{\alpha R} + \text{h.c.} = -y_\alpha \frac{v}{\sqrt{2}} \bar{l}_\alpha l_\alpha \quad (1.9)$$

and thus the particle gets the mass of $y_\alpha v/\sqrt{2}$, cf. Eq. (1.4). In the SM usually the neutrinos are assumed massless. Thus, in the SM the right-handed neutrino $\nu_{\alpha R}$ in Eq. (1.6) is not required.

1.1.1 Neutrino mass term

It is known from the results of the neutrino oscillation experiments, to be discussed in Section 1.2, that the neutrinos do have a non-zero mass. The neutrino mass term considerations are, however, more complicated due to neutrino being neutral. It is yet unclear whether neutrino is distinct from its antiparticle, in which case it would be called a Dirac particle, or not, in which case it would be a Majorana particle.

In the first case, it is possible to generate the neutrino mass via the same Higgs mechanism as for the charged leptons. We utilize the $SU(2)_L$ doublet

$$\tilde{\Phi} = i\tau_2 \Phi^*, \quad (1.10)$$

where τ_2 is the second Pauli matrix, in the Yukawa coupling as

$$\mathcal{L}_{\text{Yukawa}}^\nu = -z_\alpha (\bar{\nu}_{\alpha L}, \bar{l}_{\alpha L}) \tilde{\Phi} \nu_{\alpha R} + \text{h.c.}, \quad (1.11)$$

where z_α is the corresponding coupling constant. The only condition is that the right-handed neutrino field $\nu_{\alpha R}$ is introduced. Since it must be an $SU(2)_L$ singlet and have a hypercharge of zero such neutrino field would not participate in any of the SM interactions and would be sterile. However, the neutrinos have masses much smaller than the charged leptons but there is no explanation for that in such an approach.

In the second case, the so-called Majorana mass term is constructed utilizing charge and parity conjugated field $\nu_{\alpha L}^c$ [Kin04]. Suppressing the flavor index α for simplicity, this can be written as

$$\mathcal{L}_{\text{Majorana}}^{\text{mass}} = -\frac{1}{2} m_L \bar{\nu}_L \nu_L^c + \text{h.c.} \quad (1.12)$$

This mass term has similar form as the Dirac mass term, Eq. (1.4), written using the chiral field components as $\mathcal{L}_{\text{Dirac}} = -m(\bar{\nu}_L \nu_R + \bar{\nu}_R \nu_L)$, but now the left- and right-handed components are no longer independent [Giu07],

$$\nu_R = \nu_L^c. \quad (1.13)$$

Thus, the Majorana neutrino field $\nu = \nu_L + \nu_R = \nu_L + \nu_L^c$ satisfies

$$\nu = \nu^c, \quad (1.14)$$

which implies that the particle and antiparticle are equal. Only neutrinos can be Majorana particles due to charge conservation. This mass term does not require the existence of an independent right-handed field component, but it would also need to have a different origin than the Higgs mechanism described above such as a new Higgs triplet³ [Kin04]. This mechanism is known as the see-saw type 2.

The most general mass term compatible with the SM Higgs mechanism can be composed of the Dirac and right-handed Majorana mass terms written compactly as

$$\mathcal{L}_{\text{Dir \& Maj}}^{\text{mass}} = -\frac{1}{2}(\bar{\nu}_L^c, \bar{\nu}_R) \begin{pmatrix} 0 & m_D \\ m_D & m_R \end{pmatrix} \begin{pmatrix} \nu_L \\ \nu_R^c \end{pmatrix} + \text{h.c.} \quad (1.15)$$

with m_D and m_R being the corresponding Dirac and right-handed Majorana mass constants. In such a case, the chiral fields ν_L and ν_R^c do not have definite masses. If m_D is generated by the Higgs mechanism and m_R is very large, the mass eigenvalues m_1 and m_2 can be expressed as

$$m_1 \simeq \frac{m_D^2}{m_R}, \quad (1.16a)$$

$$m_2 \simeq m_R. \quad (1.16b)$$

The Dirac mass term m_D has to be at the same order as other fermion masses and the very large m_R could point to new physics beyond the SM possibly at the so-called grand unification scale. It follows that $m_1 \ll m_2$, the active (participating in the weak interaction) neutrino ν_L is composed primarily of m_1 and thus a small neutrino mass is obtained. This mechanism is known as the see-saw type 1.

The two mechanisms prefer different neutrino mass hierarchies [Kin04], to be discussed in Section 1.3, and thus knowledge of the absolute neutrino mass scale is essential for pointing to physics beyond the SM.

1.1.2 Three-generation mixing

It is experimentally well established⁴ that there are three light active neutrinos (with mass smaller than half of the Z boson mass of about 91 GeV) corresponding to the three charged leptons: electron, muon and tauon. Therefore, in the SM there are three ‘‘generations’’ of $SU(2)_L$ doublets, one for each pair charged lepton - neutrino, see Eq. (1.6).

Considering the Dirac nature of neutrinos for simplicity, the most general Yukawa interaction for the lepton masses is now written as

$$\mathcal{L}_{\text{Yukawa}} = - \sum_{\alpha, \beta=e, \mu, \tau} \left(Y_{\alpha\beta} (\bar{\nu}_{\alpha L}, \bar{l}_{\alpha L}) \Phi l_{\beta R} + Z_{\alpha\beta} (\bar{\nu}_{\alpha L}, \bar{l}_{\alpha L}) \tilde{\Phi} \nu_{\beta R} \right) + \text{h.c.}$$

³ The reason is that ν_L is in a weak isospin doublet and thus the term $\bar{\nu}_L \nu_L^c$ violates the weak isospin.

⁴ From the invisible decay width of the Z boson measured at the Large Electron-Positron collider [LEP06].

$$= -\frac{v+H}{\sqrt{2}} \sum_{\alpha,\beta=e,\mu,\tau} (Y_{\alpha\beta} \bar{l}_{\alpha L} l_{\beta R} + Z_{\alpha\beta} \bar{\nu}_{\alpha L} \nu_{\beta R}) + \text{h.c.}, \quad (1.17)$$

where $Y_{\alpha\beta}$ and $Z_{\alpha\beta}$ are the elements of Yukawa coupling matrices for the charged leptons and the neutrinos, respectively. The complex matrices Y and Z are generally non-diagonal and therefore the fermion fields do not have defined masses. In order to obtain fields with definite masses (physical fields), the matrices have to be diagonalized using a biunitary transformation.

The implication of the physical fields getting their mass through the Yukawa coupling is the mixing phenomenon in charged current weak interactions. In other words, the neutrino mass eigenstates, which follow from the diagonalization of the coupling matrix in the Yukawa interaction, do not correspond to the states participating in the weak interaction⁵. The corresponding Lagrangian can be written as

$$\mathcal{L}_{CC} = -\frac{g}{\sqrt{2}} \sum_{\substack{\alpha=e,\mu,\tau \\ i=1,2,3}} \bar{\nu}_{iL} \gamma^\mu U_{\alpha i}^* l_{\alpha L} W_\mu^+ + \text{h.c.}, \quad (1.18)$$

where $W_\mu^+(x)$ is the field describing the W boson and ν_i is a neutrino mass eigenstate. The unitary matrix U is the so-called Pontecorvo-Maki-Nakagawa-Sakata (PMNS) neutrino mixing matrix⁶ [Pon57, Pon58, Mak62, Pon68, Gri69]. A similar matrix appears in the Lagrangian in case of Majorana nature of neutrinos.

It can be shown that in the Dirac case there are four independent parameters in the PMNS matrix. A convenient parametrization is through three mixing angles $\theta_{12}, \theta_{13}, \theta_{23}$ and one complex phase δ . In the Majorana case, two additional physical complex phases α_1 and α_2 appear. This can be written as

$$\begin{aligned} U &= \begin{pmatrix} U_{e1} & U_{e2} & U_{e3} \\ U_{\mu 1} & U_{\mu 2} & U_{\mu 3} \\ U_{\tau 1} & U_{\tau 2} & U_{\tau 3} \end{pmatrix} \\ &= \begin{pmatrix} 1 & 0 & 0 \\ 0 & c_{23} & s_{23} \\ 0 & -s_{23} & c_{23} \end{pmatrix} \begin{pmatrix} c_{13} & 0 & s_{13} e^{-i\delta} \\ 0 & 1 & 0 \\ -s_{13} e^{i\delta} & 0 & c_{13} \end{pmatrix} \begin{pmatrix} c_{12} & s_{12} & 0 \\ -s_{12} & c_{12} & 0 \\ 0 & 0 & 1 \end{pmatrix} \begin{pmatrix} 1 & 0 & 0 \\ 0 & e^{i\alpha_1/2} & 0 \\ 0 & 0 & e^{i\alpha_2/2} \end{pmatrix} \\ &= \begin{pmatrix} c_{12}c_{13} & s_{12}c_{13} & s_{13} e^{-i\delta} \\ -s_{12}c_{23} - c_{12}s_{23}s_{13} e^{i\delta} & c_{12}c_{23} - s_{12}s_{23}s_{13} e^{i\delta} & s_{23}c_{13} \\ s_{12}s_{23} - c_{12}c_{23}s_{13} e^{i\delta} & -c_{12}s_{23} - s_{12}c_{23}s_{13} e^{i\delta} & c_{23}c_{13} \end{pmatrix} \begin{pmatrix} 1 & 0 & 0 \\ 0 & e^{i\alpha_1/2} & 0 \\ 0 & 0 & e^{i\alpha_2/2} \end{pmatrix}, \end{aligned} \quad (1.19)$$

where $s_{ij} \equiv \sin \theta_{ij}$ and $c_{ij} \equiv \cos \theta_{ij}$. The neutrino mixing is a necessary though not sufficient requirement for the neutrino oscillations.

⁵ The charged leptons are defined by their mass, which distinguishes the different flavors. Therefore, the charged leptons are by definition particles with definite mass. The neutrinos, on the other hand, are defined by the flavor of the corresponding charged lepton participating in the charged-current weak interaction. Thus, flavor neutrinos do not have definite masses resulting in neutrino mixing [Giu07].

⁶ For historical reasons the PMNS matrix connects charged leptons with weak isospin $I_3 = -\frac{1}{2}$ on the left to neutrinos with $I_3 = \frac{1}{2}$ on the right, which is the opposite to the Cabibbo–Kobayashi–Maskawa matrix in the quark sector [Giu07].

1.2 Neutrino flavor oscillations

The neutrino mixing leads to the situation when a neutrino produced in a charged current weak interaction (production) with a flavour α later participates in another charged current weak interaction (detection) with some probability having a different flavor β . Moreover, if the neutrino masses are mutually different, the probability oscillates as a function of the neutrino energy and the distance propagated which justifies the term neutrino oscillations. Thus, observation of the oscillations implies non-zero neutrino mass.

The usual treatment of the oscillation probability for neutrinos travelling in vacuum is based on plane-wave approximation of the neutrino mass eigenstates. However, this approach requires several unrealistic assumptions despite it gives the correct answer. A more accurate approach is based on describing the neutrinos as wave packets. The fully consistent approach is based on QFT (from which the wave packets follow rather than being postulated) when the production and detection processes are considered as a whole and the neutrino is treated as an intermediate particle described by a propagator [Akh09].

If the flavor state $|\nu_\alpha\rangle$ is expressed as a superposition of the mass states $|\nu_i\rangle$ as

$$|\nu_\alpha\rangle = \sum_i U_{\alpha i}^* |\nu_i\rangle, \quad (1.20)$$

the transition probability of $\nu_\alpha \rightarrow \nu_\beta$ is [Giu07]

$$P_{\nu_\alpha \rightarrow \nu_\beta}(L, E) = \sum_{i,j} U_{\alpha i}^* U_{\beta i} U_{\alpha j} U_{\beta j}^* \exp\left(-i \frac{\Delta m_{ij}^2 L}{2E}\right), \quad (1.21)$$

where $\Delta m_{ij}^2 \equiv m_i^2 - m_j^2$ is the difference of masses squared, L is the distance from the source to the detector (baseline) and E is the neutrino energy. The formula shows that if the oscillation is observed, at least one of the mass eigenvalues has to be non-zero. It also shows that from the oscillation experiment results only the differences in masses squared, but not the absolute masses, can be obtained.

The oscillation is the consequence of interference of the different massive states. A necessary requirement for the interference is that the states are produced and detected in a coherent way and that the coherence is not lost during neutrino propagation. If e.g. both energy and momentum are measured accurately enough the mass eigenstate is determined via the relativistic energy-momentum relation, coherence is lost and the oscillations do not appear. Let us recast the expression in Eq. (1.21) to

$$P_{\nu_\alpha \rightarrow \nu_\beta}(L, E) = \sum_i |U_{\alpha i}|^2 |U_{\beta i}|^2 + 2 \operatorname{Re} \sum_{i>j} U_{\alpha i}^* U_{\beta i} U_{\alpha j} U_{\beta j}^* \exp\left(-2\pi i \frac{L}{L_{ij}^{\text{osc}}}\right), \quad (1.22)$$

where the oscillation lengths are

$$L_{ij}^{\text{osc}} \equiv \frac{4\pi E}{\Delta m_{ij}^2}. \quad (1.23)$$

If coherence is lost, the oscillation probability reduces to the constant term in Eq. (1.22),

$$P_{\nu_\alpha \rightarrow \nu_\beta}^{\text{const}} = \sum_i |U_{\alpha i}|^2 |U_{\beta i}|^2. \quad (1.24)$$

The same constant probability can appear if the oscillations are incoherently averaged over the detector resolution or over the uncertainty in the baseline L .

1.2.1 Two-flavor case

The oscillation formula in Eq. (1.22) leads to complicated expressions in case of more than two neutrino flavors. Moreover, many experimental results can be described using only an effective two-neutrino mixing. In the case of two neutrino flavors (and two neutrino mass eigenstates) the oscillation formula has the simple form

$$P_{\nu_\alpha \rightarrow \nu_\beta}(L, E) = \frac{1}{2} \sin^2 2\theta \left[1 - \cos \left(\frac{\Delta m^2 L}{2E} \right) \right] = \sin^2 2\theta \sin^2 \left(\frac{\Delta m^2 L}{4E} \right), \quad (1.25)$$

where θ is the mixing angle, the only parameter in the 2×2 mixing matrix, and Δm^2 is the single difference of masses squared. In practical units the probability is

$$P_{\nu_\alpha \rightarrow \nu_\beta}(L, E) = \sin^2 2\theta \sin^2 \left(1.27 \frac{\Delta m^2 [\text{eV}^2] L [\text{km}]}{E [\text{GeV}]} \right). \quad (1.26)$$

In practice, the values of L and E are smeared out by spatial uncertainty of the source and the detector and by finite resolution of the detector, respectively. In such a case, an averaged oscillation probability is observed,

$$\langle P_{\nu_\alpha \rightarrow \nu_\beta}(L, E) \rangle = \frac{1}{2} \sin^2 2\theta \left[1 - \int \cos \left(\frac{\Delta m^2 L}{2E} \right) \phi \left(\frac{L}{E} \right) d \frac{L}{E} \right], \quad (1.27)$$

where $\phi(L/E)$ is the probability distribution of L/E . This is illustrated in Fig. 1.1 where the dotted line shows the oscillation probability governed by Eq. (1.25) and the solid line shows the probability governed by Eq. (1.27) as a function of $\Delta m^2 \langle L/E \rangle$ with $\sin^2 2\theta = 1$. The distribution $\phi(L/E)$ was assumed to be a Gaussian distribution with the standard deviation $\sigma_{L/E} = 0.2 \langle L/E \rangle$. For large $\langle L/E \rangle$ the oscillations are completely averaged out leading only to observation of the constant term $\frac{1}{2} \sin^2 2\theta$.

The Eq. (1.25) shows the probability for the new flavor β to appear in an original pure beam of flavor α . Such a situation is usually referred to as an appearance experiment. In a disappearance experiment the interesting parameter is the survival probability that the flavor α remains α . From the unitarity of U it follows that the probability is

$$P_{\nu_\alpha \rightarrow \nu_\alpha}(L, E) = 1 - P_{\nu_\alpha \rightarrow \nu_\beta}(L, E) = 1 - \sin^2 2\theta \sin^2 \left(\frac{\Delta m^2 L}{4E} \right). \quad (1.28)$$

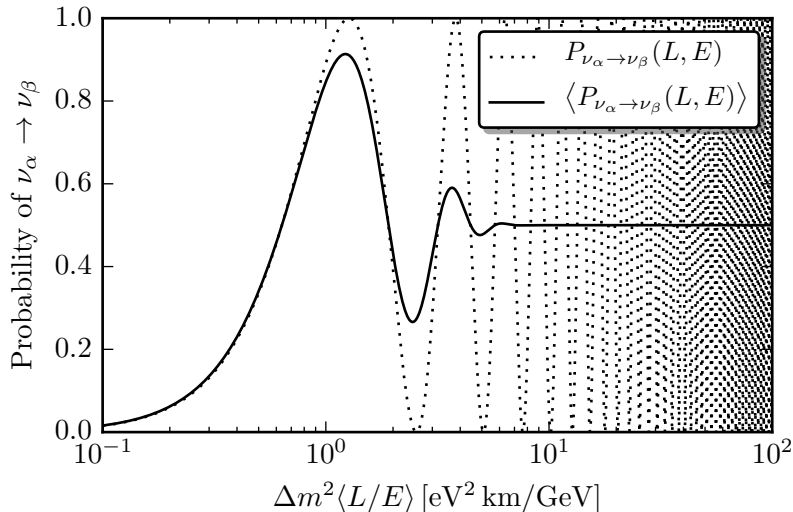


Figure 1.1: The oscillation probability for $\nu_\alpha \rightarrow \nu_\beta$ as a function of $\Delta m^2 \langle L/E \rangle$ assuming $\sin^2 2\theta = 1$. Dotted line: the transition probability in Eq. (1.25) with $L/E = \langle L/E \rangle$. Solid line: the probability averaged over a Gaussian distribution of L/E with $\sigma_{L/E} = 0.2 \langle L/E \rangle$, Eq. (1.27).

1.2.2 Matter effects

The oscillation probability can be significantly different when the neutrinos travel through matter due to their interactions with the particles in the matter [Wol78, Mik85, Mik86]. This is essential for understanding the neutrinos coming from the Sun. The electron (anti)neutrinos experience both charged and neutral current interactions (the former involving electrons) whereas muon and tauon neutrinos experience only the neutral current interactions. This leads to an extra interaction potential for the electron (anti)neutrinos of the form

$$V_e = \pm\sqrt{2} G_F N_e, \quad (1.29)$$

where G_F is the Fermi constant⁷ and N_e is the matter electron density. The plus sign holds for neutrinos and the minus sign for the antineutrinos.

The extra potential leads to neutrino mixing in matter with the effective mixing angle θ_M satisfying (for the two-flavor case)

$$\sin^2 2\theta_M = \frac{\sin^2 2\theta}{\sin^2 2\theta + (\cos 2\theta - x)^2}, \quad (1.30)$$

where

$$x \equiv \pm \frac{2\sqrt{2} G_F N_e E}{\Delta m^2} \quad (1.31)$$

and the effective mass splitting Δm_M^2 satisfying

$$\Delta m_M^2 = \Delta m^2 \sqrt{\sin^2 2\theta + (\cos 2\theta - x)^2}. \quad (1.32)$$

⁷ $G_F = \frac{1}{2\sqrt{2}} \frac{g^2}{m_W^2}$, where m_W is the mass of the W boson.

When the situation is such that $x = \cos 2\theta$ the mixing becomes maximal independent of the vacuum mixing angle θ . This situation is called the Mikheyev–Smirnov–Wolfenstein (MSW) resonance and can lead to a complete transition of one flavor to another provided that the resonance region is wide enough.

1.2.3 Experimental evidence

The experimental evidence for neutrino oscillations and non-zero mass square differences was pioneered by observation of the solar and atmospheric neutrinos and later confirmed by observation of reactor and accelerator neutrinos.

Solar neutrinos

The Sun is a strong source of electron neutrinos coming from the fusion reactions which take place in the Sun’s core. Overall the reactions can be summarized as



where Q is the energy release. Since first observations of these neutrinos by the Homestake experiment (chlorine radiochemical detector) [Dav68, Cle98] also other experiments reported deficit in the neutrino rate with respect to the prediction of the standard solar model [Bah63, Bah01]. This concerned experiments such as SAGE [SAG94] and GALLEX [GAL92] (gallium radiochemical detectors), Kamiokande [KAM89] and Super-Kamiokande [SK06] (light water Cherenkov detectors). The deficit became known as the solar neutrino problem.

The resolution came with the SNO experiment [SNO01] which comprised a heavy water Cherenkov detector. Besides the charged-current reaction



sensitive only to electron neutrinos, and the elastic scattering



sensitive only weakly to other flavors, it was also possible to measure the neutral-current reaction



which was sensitive to all active neutrino flavors equally. The observed rate for the neutral-current reaction was in perfect agreement with the standard solar model prediction whereas the rate for the other two reactions confirmed the deficit seen by the previous experiments. The result implied that the electron neutrinos must have changed their flavor.

The oscillation explanation for the solar neutrino problem was further supported by KamLAND [KL03], which was a liquid-scintillator disappearance experiment involving

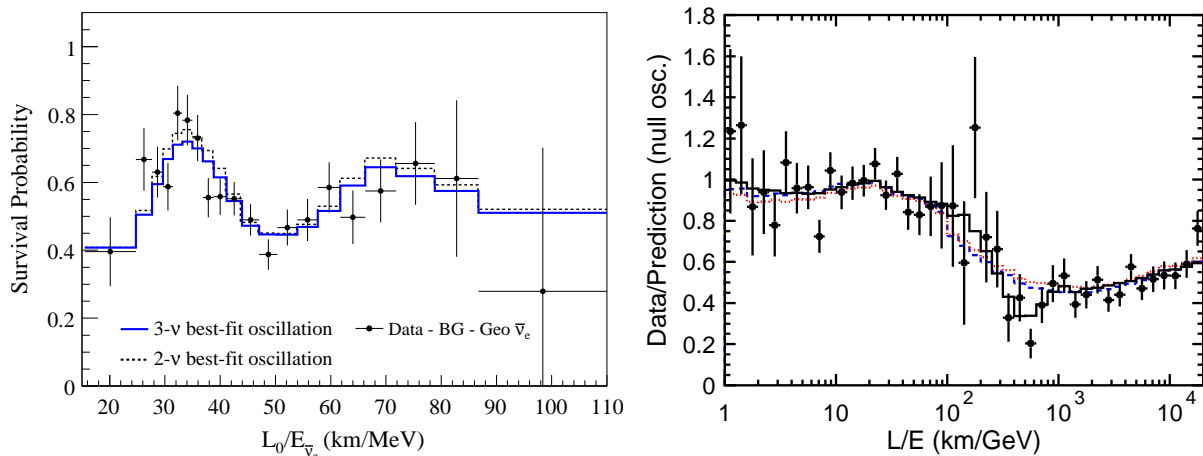


Figure 1.2: Ratio of the observed neutrino spectrum to the expectation for no-oscillation in dependence of L/E . Left: Reactor electron antineutrino results from the KamLAND experiment. $L_0 = 180$ km is the flux-weighted average baseline. Right: Atmospheric muon neutrino and antineutrino results from the Super-Kamiokande experiment. The solid line shows the best-fit expectation for two-flavor oscillations. The dashed and dotted lines show the best-fit expectation for the alternative hypotheses of neutrino decay and neutrino decoherence, respectively. Note the dip characteristic for the neutrino oscillations at $L/E \sim 500$ km/GeV. The figures are taken from [KL11] and [SK04].

electron antineutrinos⁸ produced at nuclear reactors by β -decays of neutron-rich fission products. KamLAND has $L \sim 180$ km and $E \sim 1$ MeV and so a sensitivity for Δm^2 down to $\sim 10^{-5}$ eV². During a later stage the results [KL11] showed the expected periodic nature of the oscillation probability as a function of L/E , see Fig. 1.2. The corresponding oscillation parameters are $\Delta m_{\text{sol}}^2 \approx 7.6 \times 10^{-5}$ eV² and $\sin^2 2\theta_{\text{sol}} \approx 0.8$ [PDG14] leading the so-called large mixing angle MSW solution to the solar neutrino problem. Consistent solar neutrino results have been reported also by the low-background liquid scintillator experiment Borexino [BOR08].

Atmospheric neutrinos

The interactions of primary cosmic rays with nuclei in the Earth's atmosphere generate secondary cosmic rays, which are composed of hadrons, in particular pions. The pion decays mainly into a muon and the corresponding neutrino. Furthermore, the muon itself decays into an electron and the corresponding two neutrinos, i.e.

$$\pi^\pm \rightarrow \mu^\pm + \nu_\mu(\bar{\nu}_\mu), \quad \mu^\pm \rightarrow e^\pm + \nu_e(\bar{\nu}_e) + \bar{\nu}_\mu(\nu_\mu). \quad (1.37)$$

These neutrinos are called atmospheric neutrinos. From the decays the expected ratio of muon to electron neutrinos is about two⁹. A number of experiments such as Kamiokande

⁸ In the SM it holds that $P_{\nu_\alpha \rightarrow \nu_\alpha} = P_{\bar{\nu}_\alpha \rightarrow \bar{\nu}_\alpha}$.

⁹ At higher energies the kaon decays also contribute to the neutrino flux. Moreover, at higher energies more muons reach the ground without decaying.

[KAM88] and IMB [IMB91] reported a significant deviation from the expected ratio which became known as the atmospheric neutrino anomaly.

The resolution was provided by the Super-Kamiokande experiment [SK98] which was able to measure the zenith-angle distribution of the charged leptons emerging from the neutrino-nucleon collisions

$$\nu_\alpha(\bar{\nu}_\alpha) + N \rightarrow l_\alpha^\mp + X. \quad (1.38)$$

The lepton momentum direction strongly correlates with the neutrino one provided that the lepton momentum is high enough. A strong deviation from the expectation was observed for muon-like events, which are characterized by absence of an electromagnetic shower, in the zenith-angle distribution for up-going neutrinos but no deviation was found for electron-like events. Therefore, some of the up-going muon neutrinos must have changed flavor during their much longer way to the detector from the other side of the Earth in contrast to the down-going neutrinos. Moreover, the expected oscillation pattern as a function of L/E was later found [SK04], see Fig. 1.2. The results suggest $|\Delta m_{\text{atm}}^2| \approx 2.4 \times 10^{-3} \text{ eV}^2$ and $\sin^2 2\theta_{\text{atm}} \approx 1$ [PDG14].

These results are supported by accelerator experiments such as K2K [K2K05], MINOS [MIN06] and T2K [T2K12]. In these experiments the neutrinos are produced from decays of pions, muons and kaons which are created by bombarding a target with a proton beam. The experiments have typically $E \sim 1 \text{ GeV}$, L of several hundred km and the sensitivity for Δm^2 down to $\sim 10^{-3} \text{ eV}^2$. Moreover, the appearance of ν_τ in the ν_μ beam, which is suggested by the ν_μ disappearance data, has been demonstrated by the OPERA experiment at the statistical significance of more than 3σ [OPE14].

Neutrino mass ordering

Measurements of the solar and atmospheric neutrinos have provided conclusive evidence for neutrino oscillations with two different mass squared differences Δm_{sol}^2 and Δm_{atm}^2 . These can be realized in the minimal mixing scheme which comprises the three known neutrino flavors. In such a case, there are only two independent mass squared differences because

$$\Delta m_{32}^2 + \Delta m_{21}^2 - \Delta m_{31}^2 = 0. \quad (1.39)$$

Therefore, the observation $\Delta m_{\text{sol}}^2 \ll \Delta m_{\text{atm}}^2$ can be described by one of the two possible schemes usually referred to as the normal and inverted ordering. If we set the numbering of the massive states such that $m_2 > m_1$ then for the normal ordering $m_1 < m_2 < m_3$ and for the inverted ordering $m_3 < m_1 < m_2$. Then with identifying $\Delta m_{21}^2 = \Delta m_{\text{sol}}^2$ we can associate the Δm_{atm}^2 with the larger $|\Delta m_{31}^2|$ or $|\Delta m_{32}^2|$. The effects of Δm_{31}^2 or Δm_{32}^2 in the solar neutrino oscillations and of Δm_{21}^2 in the atmospheric neutrino oscillations are relatively small [PDG14].

Moreover, it is known from the results of reactor antineutrino disappearance experiments such as Daya Bay [DB12], RENO [REN12] and Double Chooz [DCH13] at a baseline of $L \sim 1 \text{ km}$ that the mixing matrix element $|U_{e3}| = \sin \theta_{13} \approx 0.15$ is relatively small. This enables to identify $\theta_{12} = \theta_{\text{sol}}$ and $\theta_{23} = \theta_{\text{atm}}$ [PDG14]. The Dirac phase δ is currently not

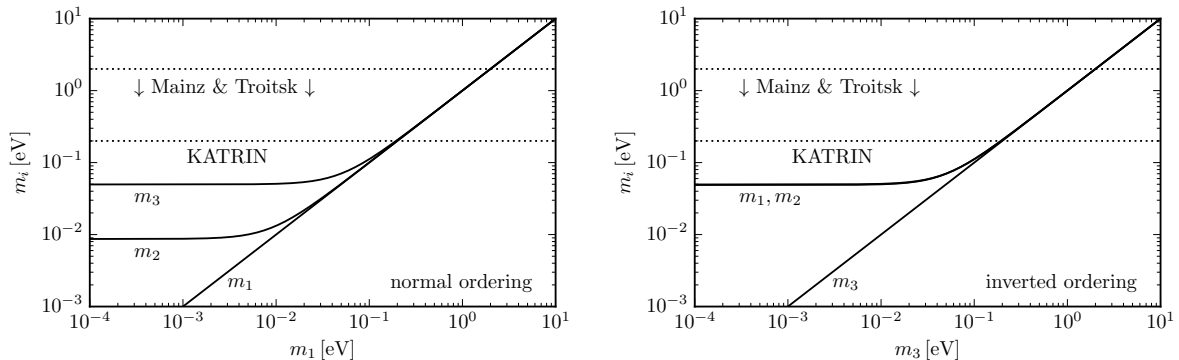


Figure 1.3: Neutrino masses as functions of the lightest neutrino mass in the two possible scenarios of normal ordering (left) and inverted ordering (right). For $m_i \gtrsim 100$ meV the neutrino masses are quasi-degenerate in both orderings. The current limit from the Mainz and Troitsk tritium β -decay experiments are shown together with the limit which will be obtained from the upcoming KATRIN experiment if no signal is observed.

known with enough statistical significance. No information is available for the Majorana phases α_1 and α_2 .

1.3 Determination of the neutrino mass

As noted before only the mass squared differences are reachable by the neutrino oscillation experiments. Depending on the value of the lightest neutrino mass the neutrino mass spectrum can have one of the three patterns, see Fig. 1.3:

- normal hierarchy, $m_1 \ll m_2 < m_3$ with the heaviest $m_3 \cong |\Delta m_{31}^2|^{\frac{1}{2}} \cong 50$ meV,
- inverted hierarchy, $m_3 \ll m_1 < m_2$ with $m_1 \cong m_2 \cong |\Delta m_{32}^2|^{\frac{1}{2}} \cong 50$ meV,
- quasi-degenerate, $m_1 \cong m_2 \cong m_3$, $m_i^2 \gg |\Delta m_{\text{atm}}^2|$ with $m_i \gtrsim 100$ meV.

Therefore, the oscillation results imply only a lower limit on the heaviest mass eigenvalue of about 50 meV. The absolute neutrino mass scale has to be addressed using other means. There are several complementary approaches pursued.

1.3.1 Cosmology

The Big Bang theory, which is the prevailing cosmological model of the evolution of the Universe, predicts presence of a cosmic neutrino background similar to cosmic microwave background which should have been created in the early times of the Universe. Today, the estimated number density of these relic neutrinos amounts to about 340 cm^{-3} making the neutrinos the second-most abundant particles after the photons. Due to such a large number density their contribution to the total energy density of the Universe can be substantial despite their small mass [Les06].

Let us denote the total energy density as Ω in relative units with respect to the so-called critical energy density, which is the density needed for the Universe to be spatially flat. Then according to the Λ CDM parametrization of the Big Bang model (cold dark matter with cosmological constant, also known as the concordance model) the density can be expressed as [Kom09]

$$\begin{aligned}\Omega &= \Omega_\Lambda + \Omega_c + \Omega_b + \Omega_\gamma + \Omega_\nu \\ &\approx 0.70 + 0.25 + 0.04 + \mathcal{O}(10^{-5}) + \Omega_\nu,\end{aligned}\tag{1.40}$$

where the indices correspond to dark energy, cold dark matter, baryonic matter, photons and neutrinos.

The neutrino contribution Ω_ν can also be inferred from the cosmological data. The neutrinos represent the so-called hot dark matter meaning that they were relativistic when decoupling from other matter shortly after the Big Bang. Due to that their influence on structure formation was to relax local fluctuations in the mass and energy density distribution by a diffusion-like transport. The information about the neutrino mass scale can be obtained from

$$\Omega_\nu h^2 = \frac{\sum_i m_i}{93 \text{ eV}}\tag{1.41}$$

for the neutrino mass in the range 0.5 meV to 1 MeV, where $h \simeq 0.68$ is the dimensionless Hubble parameter. Depending on the datasets included the recent data suggest the upper limit [PLA14]

$$\sum_i m_i < 0.23 \text{ eV to } 0.66 \text{ eV}.\tag{1.42}$$

However, there is a strong degeneracy of the neutrino mass with other parameters of the model. Moreover, the exact value of the limit is analysis and model dependent. It is therefore more profitable to use the neutrino mass as an input for the cosmological models.

1.3.2 Neutrinoless double β -decay

The neutrinoless double β -decay ($0\nu\beta\beta$), if observed, would confirm the Majorana nature of neutrinos [Sch82] besides giving information about the absolute neutrino mass scale and is thus heavily experimentally pursued. This process is characterized by the nuclear transition

$$N(A, Z) \rightarrow N(A, Z \pm 2) + 2e^\mp,\tag{1.43}$$

where A and Z are, respectively, the mass and atomic numbers of the parent nucleus. The experimental signature is a monoenergetic peak centered at the Q -value of the decay. The process is observable if energetically allowed, $m_{N(A,Z)} > m_{N(A,Z\pm 2)} + 2m_e$, and if the single β -decay is either energetically disallowed, $m_{N(A,Z)} < m_{N(A,Z\pm 1)}$, or highly forbidden. An irreducible background for this decay is the regular two-neutrino double β -decay ($2\nu\beta\beta$) when two (anti)neutrinos are emitted together with the electrons(positrons).

If the $0\nu\beta\beta$ process is mediated by a light Majorana neutrino¹⁰, its rate (inverse of half-life) is given by [Ell04]

$$\frac{1}{T_{1/2}^{0\nu}} = G_N^{0\nu} |\mathcal{M}_N^{0\nu}|^2 \frac{\langle m_{\beta\beta} \rangle^2}{m_e^2}, \quad (1.44)$$

where $G_N^{0\nu}$ is a phase space factor, $\mathcal{M}_N^{0\nu}$ is the nuclear matrix element and m_e is the electron mass. The value $\langle m_{\beta\beta} \rangle$ is the so-called effective Majorana mass given by the coherent sum

$$\langle m_{\beta\beta} \rangle = \left| \sum_i U_{ei}^2 m_i \right|. \quad (1.45)$$

Therefore, the effective Majorana mass can in principle be extracted from the measured half-life.

The largest problem in this approach is the nuclear matrix element $\mathcal{M}_N^{0\nu}$ which is needed to obtain the mass. Its calculation requires an accurate nuclear model and presently is subject to rather large uncertainties [Ell04]. The search for $0\nu\beta\beta$ thus requires to study as many different isotopes as possible. Moreover, the mass depends on the generally complex values U_{ei} squared which may lead to potential cancellation among the different contributions in the sum.

To date only lower limits of the half-life and thus upper limits of the effective Majorana mass have been given by the experiments [EXO14, KLZ13, NEM14]. Recently the results of the GERDA experiment [GER13] disfavored the claim by the part of the Heidelberg-Moscow collaboration [Kla04] which reported $0\nu\beta\beta$ observation in ${}^{76}\text{Ge}$ with the half-life¹¹ of about 1.2×10^{25} yr. The GERDA lower limit on the half-life amounts to $T_{1/2}^{0\nu} > 2.1 \times 10^{25}$ yr (90 % C.L.) which translates into the upper limit of the effective Majorana mass of about

$$\langle m_{\beta\beta} \rangle_{{}^{76}\text{Ge}} < 0.25 \text{ eV to } 0.52 \text{ eV} \quad (1.46)$$

depending on the nuclear matrix element used.

1.3.3 Single β -decay

The single β^- -decay is so far the most sensitive method to observe the absolute neutrino mass scale. The process is the nuclear transition

$$\text{N}(Z, A) \rightarrow \text{N}(A, Z + 1) + e^- + \bar{\nu}_e \quad (1.47)$$

resulting in a continuous electron spectrum. The information about the neutrino mass can be extracted from an interval close to the so-called endpoint energy E_0 which is the maximal energy the electron could carry if the neutrino was massless.

¹⁰ There are theoretical proposals for other mechanisms that could be responsible for the $0\nu\beta\beta$. However, whatever the underlying mechanism is, existence of $0\nu\beta\beta$ requires a Majorana neutrino mass term.

¹¹ The claim was later strengthened using pulse shape analysis to about 2.2×10^{25} yr [Kla06] which is not disfavored with enough statistical significance by GERDA alone. However, it seems to be disfavored by combined analysis with the experiments KamLAND-Zen and EXO-200 (${}^{136}\text{Xe}$) for most of the available nuclear matrix element calculations [Bhu13].

The differential rate for an allowed β -decay in dependence of the electron kinetic energy E is given by [Ott08]

$$\frac{d\Gamma}{dE} = \frac{G_F^2 \cos^2 \theta_C}{2\pi^3} |\mathcal{M}|^2 F(Z+1, E) p(E+m_e) \sum_f P_f \epsilon_f \sum_i |U_{ei}|^2 \sqrt{\epsilon_f^2 - m_i^2} \Theta(\epsilon_f - m_i) \quad (1.48)$$

with $\epsilon_f \equiv E_0 - V_f - E$, where θ_C is the Cabbibo angle, \mathcal{M} the energy-independent nuclear matrix element, $F(Z+1, E)$ is the Fermi function which accounts for the electromagnetic interaction of the emitted electron with the final-state atom, p is the electron momentum, P_f is the probability of exciting an atomic or molecular final state with the excitation energy V_f and $\Theta(\epsilon_f - m_i)$ is the Heaviside step function ensuring energy conservation. To show the influence of the neutrino mass it is useful to define the Kurie function (for simplicity let us assume a single final state with $V_f = 0$) as

$$\begin{aligned} K(E) &\equiv \left(\frac{d\Gamma/dE}{\frac{G_F^2 \cos^2 \theta_C}{2\pi^3} |M|^2 F(Z+1, E) p(E+m_e)} \right)^{\frac{1}{2}} \\ &= \left((E_0 - E) \sum_i |U_{ei}|^2 \sqrt{(E_0 - E)^2 - m_i^2} \Theta(E_0 - E - m_i) \right)^{\frac{1}{2}}. \end{aligned} \quad (1.49)$$

If all $m_i = 0$ the function reduces to a straight line, $K(E) = (E_0 - E) \Theta(E_0 - E)$, as it holds $\sum_i |U_{ei}|^2 = 1$. A non-zero m_i manifests as a characteristic kink in the spectrum. This is illustrated in Fig. 1.4 in the Kurie plot for $E_0 = 18\,575$ eV where the dotted line corresponds to all $m_i = 0$, the dashed line to a single $m_1 = 5$ eV and the solid line to m_1 and an additional $m_2 = 15$ eV with $|U_{e1}|^2 = |U_{e2}|^2 = 1/2$.

However, if the experimental resolution is not good enough to resolve the individual neutrino masses in the electron spectrum, the Kurie function can be reduced to

$$K(E) \simeq (E_0 - E) \sqrt{(E_0 - E)^2 - m_\beta^2} \Theta(E_0 - E - m_\beta), \quad (1.50)$$

where m_β^2 is given by the incoherent sum

$$m_\beta^2 \equiv \sum_i |U_{ei}|^2 m_i^2. \quad (1.51)$$

Thus, m_β is an effective electron neutrino mass in the single β -decay¹².

The advantage of the single β -decay approach is that the decay rate in Eq. (1.48), which is used to extract the neutrino mass from the electron spectrum, is derived only from kinematical laws and Fermi's golden rule. Thus, the approach is model independent and yields the same result regardless of whether neutrinos are Dirac or Majorana particles. Moreover, the form of the effective neutrino mass in Eq. (1.51) does not lead to potential cancellations because a mixing matrix element appears only inside modulus squared.

¹² Actually from the β^- -decay it is an effective electron antineutrino mass. However, the CPT invariance theorem, which holds for the SM, states that both masses are equal.

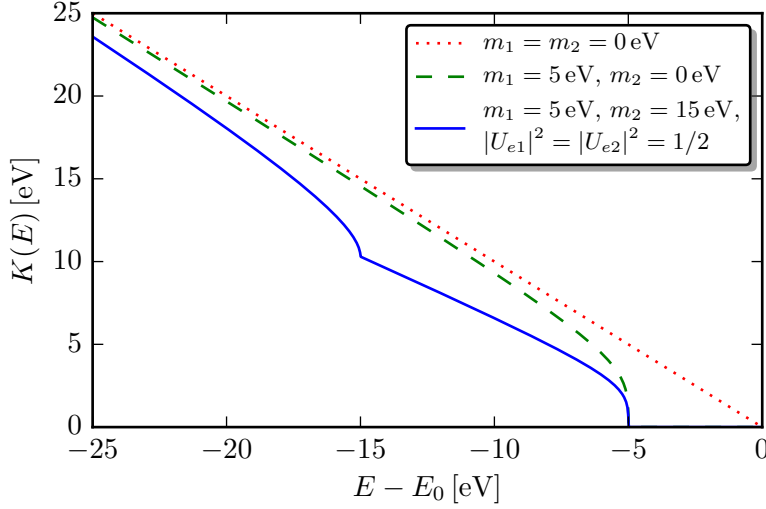


Figure 1.4: Kurie plot for $E_0 = 18575$ eV. Dotted line: Kurie function with all $m_i = 0$. Dashed line: Kurie function with a single $m_1 = 5$ eV. Solid line: Kurie function for $m_1 = 5$ eV and an additional $m_2 = 15$ eV with the mixing matrix element $|U_{e1}|^2 = |U_{e2}|^2 = 1/2$.

To date only upper limits of the m_β value have been given. The most stringent limits come from the tritium β -decay experiments of Mainz [Kra05] with

$$m_\beta^2 = (-0.6 \pm 2.2_{\text{stat}} \pm 2.1_{\text{syst}}) \text{eV}^2, \quad (1.52)$$

$$m_\beta < 2.3 \text{eV} \text{ (95 \% C.L.)} \quad (1.53)$$

and of Troitsk [Ase11] with

$$m_\beta^2 = (-0.7 \pm 1.9_{\text{stat}} \pm 1.7_{\text{syst}}) \text{eV}^2, \quad (1.54)$$

$$m_\beta < 2.05 \text{eV} \text{ (95 \% C.L.)}. \quad (1.55)$$

The combined current accepted limit is $m_\beta < 2.0$ eV (95 % C.L.) [PDG14].

It is the aim of the next-generation tritium β -decay experiment KATRIN, which will be described in Chapter 2, to push the sensitivity to the effective electron neutrino mass down to 0.2 eV. In Fig. 1.3 the current accepted limit is shown together with the limit obtainable by the KATRIN experiment if no neutrino mass signal is found. Thus KATRIN will explore the quasi-degenerate region of the neutrino mass hierarchy. In such a case, the limit or value of m_β^2 obtained from the experiment is about the same as any of the individual neutrino masses squared,

$$m_\beta^2 \simeq m_i^2 \sum_i |U_{ei}|^2 = m_i^2. \quad (1.56)$$

2 The KATRIN experiment

KATRIN (KARlsruhe TRItium Neutrino experiment) is a next-generation tritium β -decay experiment which aims to improve the effective electron antineutrino mass sensitivity by an order of magnitude compared to the previous experiments at Mainz and Troitsk. The design specifications are such that if no neutrino mass signal is observed, the upper limit will be $m_\beta < 0.2 \text{ eV}$ (90 % C.L.) after three years of data taking (five calendar years). If a signal is observed, the discovery potential will be $m_\beta = 0.35 \text{ eV}$ at the statistical significance of 5σ [KAT04]. Thus, the quasi-degenerate hierarchy of neutrino masses will be explored. The neutrino mass will be assessed in a model-independent way complementary to cosmological observations and neutrinoless double β -decay.

In this chapter, firstly the advantages of using tritium as the β -emitter are addressed. The KATRIN high-resolution and high-luminosity electron spectroscopy technique is explained. Further, the main components of KATRIN are briefly described. Finally, the experimental systematic and statistical uncertainties are discussed.

2.1 Tritium as β -emitter

Tritium was used in experiments which yielded the most stringent limit on the neutrino mass from β -decay and will be used also in the KATRIN experiment because it has several advantages over other β -radioactive isotopes.

As was shown in Section 1.3.3 the neutrino mass signature manifests itself in the β -spectrum close to the endpoint. However, it follows from the differential decay rate in Eq. (1.48) that the relative number of events Δn occurring in that region out of all events n is proportional to the inverse third power of the endpoint energy,

$$\frac{\Delta n}{n} \propto \frac{1}{E_0^3}. \quad (2.1)$$

Therefore, it is desirable that the endpoint is as low as possible in order to maximize $\Delta n/n$. The energy released in the β -decay of atomic tritium (the Q-value), obtained using Penning trap mass spectrometry technique, is¹ [Nag06]

$$Q = 18\,589.8(12) \text{ eV}. \quad (2.2)$$

Such a value gives the molecular tritium endpoint energy of [Ott08]

$$E_0 = 18\,571.8(12) \text{ eV} \quad (2.3)$$

¹ A more recent measurement reports the value of $Q = 18\,592.01(7) \text{ eV}$ [Mye15].

which is the second lowest from all β -emitters².

The decay rate is proportional to the nuclear matrix element squared. It is desirable that the matrix element is large so that the decay rate is high enough (or half-life is short enough). Tritium decay is a super-allowed transition between mirror nuclei which leads to a large overlap of initial and final nuclear wavefunctions and thus to a large nuclear matrix element. The half-life of tritium, which amounts to 12.3 yr, is thus relatively short. Moreover, no corrections arising from the nuclear matrix element have to be taken into account since for allowed and super-allowed transitions it is independent of β -electron energy.

Lastly, the decay rate is modified due to the atomic and molecular final states. The electronic structure of a tritium molecule is less complicated compared to heavier atoms which leads to a more accurate calculation of the final state spectrum. Moreover, the low atomic number of tritium leads to less inelastic scattering of the out-going electrons with the gaseous tritium source and the corrections due to the interactions can be calculated in a straightforward way.

2.2 MAC-E filter electron spectroscopy

In order to observe the tritium β -spectrum with high enough luminosity and at the same time high resolution, the magnetic adiabatic collimation with electrostatic filter technique [Lob85, Pic92a] was applied both at Mainz and Troitsk and will be also applied at KATRIN.

The basic principle is illustrated in Fig. 2.1. Two superconducting solenoids create an axially symmetric inhomogeneous magnetic field. The magnetic field B_{\min} , which is at the center of the spectrometer, is by several orders of magnitude smaller than the field B_{\max} at the bore of the solenoids. An electron is emitted at the source field B_S in the direction towards the center and performs a cyclotron motion superimposed to its parallel movement along a magnetic field line. The magnetic field gradient along the electron's trajectory leads to transformation of the electron perpendicular momentum component p_{\perp} into the parallel component p_{\parallel} , with respect to the magnetic field line, or conversely depending on the direction of the gradient. The magnetic field change is small over the parallel distance which the electron travels during one cyclotron revolution. The momentum component transformation is then adiabatic meaning that the electron orbital magnetic moment μ stays constant, i.e. in the non-relativistic limit

$$\mu = \frac{1}{2}qr v = \frac{p_{\perp}^2}{2mB} = \text{const.}, \quad (2.4)$$

where $q < 0$ is the electron charge, r is the cyclotron radius, v is the electron velocity, m is the electron mass and B is the magnetic field. Therefore, at the point of B_{\min} almost all the electron's momentum is in the component p_{\parallel} and the electron is heading almost

² The lowest endpoint of $E_0 = 2.67$ keV is observed for ¹⁸⁷Re. However, its decay is first unique forbidden and the isotope has a half-life of 4.3×10^{10} yr.

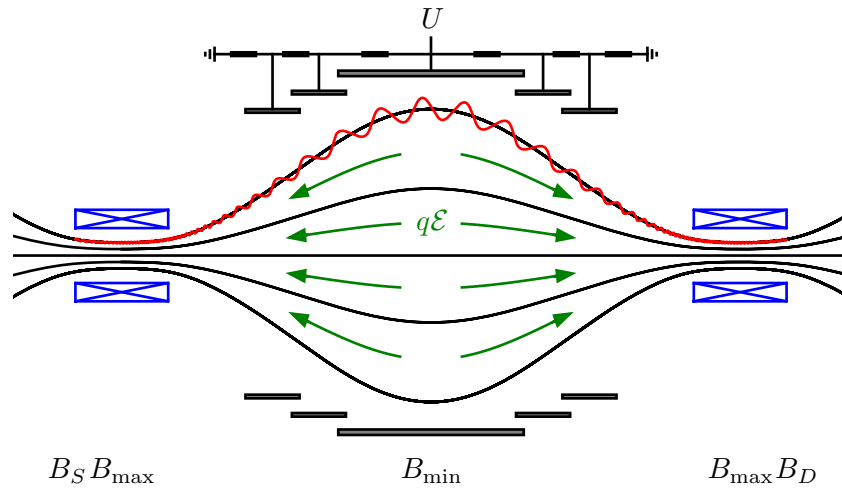


Figure 2.1: Principle of the MAC-E filter. Depicted are the two super-conducting solenoids and the field lines of the corresponding magnetic field. The set of cylindrical retarding electrodes is also shown together with the corresponding electrical field. An electron path around the topmost magnetic field line from the source side (left) to the detector side (right) is illustrated. The retarding potential U and the relevant magnetic field values are indicated. The value $q\mathcal{E}$ is the electrical force experienced by the electrons.

parallel to the spectrometer axis. The value $E_{\perp} \equiv p_{\perp}^2/2m$ is sometimes referred to as the “perpendicular energy component”. Similarly, $E_{\parallel} \equiv p_{\parallel}^2/2m$ is the “parallel energy component” and it holds for the total energy

$$E = E_{\perp} + E_{\parallel}. \quad (2.5)$$

At the minimum magnetic field an electrical field \mathcal{E} is applied by a set of cylindrical electrodes which are kept at a cascade of high potentials with the most negative value U . In this way the electrodes form an electrostatic barrier for the electron. Only if the electron’s energy is high enough it will pass the barrier, gets re-accelerated and focused onto the detector at the field B_D , otherwise it gets reflected and is generally lost. Hereby is the electron energy analysed and therefore the central plane is called the analysing plane. The whole electron spectrum is measured by varying the retarding voltage U in steps and recording the count rate for each step. This leads to the so-called integral spectrum because at each voltage step all electrons with energy higher than the retarding energy qU are counted.

The high luminosity feature follows from the fact that the spectrometer collects also those electrons which are emitted with a non-zero angle with respect to the spectrometer axis. If the electron source was placed in the field B_{\max} the spectrometer would accept all electrons emitted into the whole hemisphere, i.e. into the solid angle $\Omega = 2\pi$. In such a case the maximal acceptance angle would be $\theta_{\max} = \frac{\pi}{2}$. In practice, θ_{\max} is chosen smaller in order to avoid long electron trajectories within the finite-dimensional source. This is achieved by placing the source at a smaller field $B_S < B_{\max}$. Then the maximal

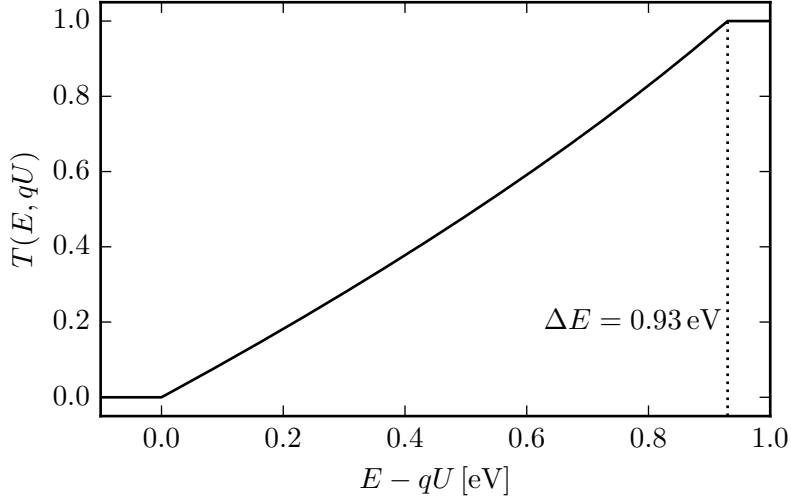


Figure 2.2: Transmission function $T(E, qU)$ of an ideal MAC-E filter with isotropic source and KATRIN magnetic field configuration. The depicted shape is a function of the electron energy E with the retarding energy fixed at $qU = E_0$, i.e. the tritium endpoint energy in Eq. (2.3). The energy resolution ΔE is indicated.

acceptance angle is given by

$$\theta_{\max} = \arcsin \sqrt{\frac{B_S}{B_{\max}}}. \quad (2.6)$$

Electrons emitted with a larger angle than θ_{\max} get reflected by the magnetic mirror effect and do not reach the analysing plane. At KATRIN the field configuration is $B_S = 3.6$ T and $B_{\max} = 6$ T [KAT04] which leads to $\theta_{\max} \simeq 51^\circ$ and $\Omega \simeq 2.31 \simeq 0.37 \cdot 2\pi$.

The resolution of the spectrometer follows basically from existence of the residual component E_\perp at the analysing plane, which cannot be measured but due to which the analysed component E_\parallel is reduced. Since the magnetic field drops by several orders of magnitude, so does the residual component leading to a high resolution. From Eq. (2.4) the energy resolving power $E/\Delta E$ is given by

$$\frac{E}{\Delta E} = \frac{B_{\max}}{B_{\min}}. \quad (2.7)$$

At KATRIN the field at the analysing plane is $B_{\min} = 0.3$ mT which leads to the resolving power $E/\Delta E = 2 \times 10^4$. At the tritium endpoint energy of 18.6 keV the energy resolution is thus $\Delta E \simeq 0.93$ eV.

The response function of an ideal MAC-E filter, known as the transmission function, for a source emitting electrons isotropically is given by

$$T(E, qU) = \begin{cases} 0, & \text{if } E < qU, \\ \frac{1 - \sqrt{1 - \frac{E - qU}{E} \frac{B_S}{B_{\min}}}}{1 - \sqrt{1 - \frac{B_S}{B_{\max}}}}, & \text{if } qU \leq E \leq qU \frac{B_{\max}}{B_{\max} - B_{\min}}, \\ 1, & \text{otherwise.} \end{cases} \quad (2.8)$$

The formula follows from the consideration that from the given solid acceptance angle (denominator) only electrons with enough forward energy and thus from a smaller solid angle (numerator) can pass the electrostatic barrier. At some point no (or all) electrons within the acceptance angle can pass the barrier. The function is depicted in Fig. 2.2 for the fixed retarding energy $qU = E_0$ from Eq. (2.3) as a function of the electron energy E . At high surplus energies at the analysing plane the adiabaticity condition, Eq. (2.4), does not hold anymore and a loss of transmission occurs, i.e. $T(E, qU) < 1$ for $E \gg qU$. If $I(E)$ is the electron energy spectrum, usually referred to as the differential spectrum, then the integral spectrum $S(qU)$ observed by the MAC-E filter as a function of the retarding energy qU reads

$$S(qU) = \int_{-\infty}^{+\infty} I(E) T(E, qU) dE. \quad (2.9)$$

In practice both the electric and magnetic fields in the analysing plane are radially dependent, i.e. $B_{\min} = B_{\min}(r)$ and $U = U(r)$ with r being the radial distance from the spectrometer axis. Therefore, the transmission function of a real MAC-E filter becomes a superposition of the ideal functions in Eq. (2.8) over the corresponding values of r if the source has a finite size. It leads to broadening and smearing of the shape in Fig. 2.2 and effectively to some deterioration of the energy resolution.

2.3 Overview of the experimental setup

The KATRIN experiment is being set up at the Karlsruhe Institute of Technology, Germany. An overview of the experimental setup is shown in Fig. 2.3. It comprises a 70 m-long β -electron beamline with the tritium β -electron source, the windowless gaseous tritium source, at one side and the analysing MAC-E filter, the main spectrometer, at the other side. The electrons are transported along magnetic field lines from the source through the transport section towards the spectrometer part and are counted at the detector. KATRIN features also a parallel beamline of the so-called monitor spectrometer, which is used for high-voltage stability monitoring. The major KATRIN components will be now briefly described [KAT04].

Windowless gaseous tritium source

The windowless gaseous tritium source (WGTS) is a complex cryostat used to contain and distribute the tritium gas and to magnetically guide the emitted β -electrons further in the beamline. It comprises a 10 m-long and 9 cm-wide cylindrical stainless steel tube operated at a temperature of 30 K by means of a two-phase liquid neon bath. The tritium with high purity of $> 95\%$ is injected at the tube center via a set of capillaries with the injection pressure of about 3×10^{-3} mbar. It diffuses inside the tube towards the ends where it is pumped out by a set of turbomolecular pumps (TMPs). No windows are present at the ends to prevent energy loss of electrons in the window material.

At the ends the tritium gas flow is reduced by a factor of 100. The tritium circulates in a closed cycle, the so-called inner loop, and after reprocessing it is injected again.

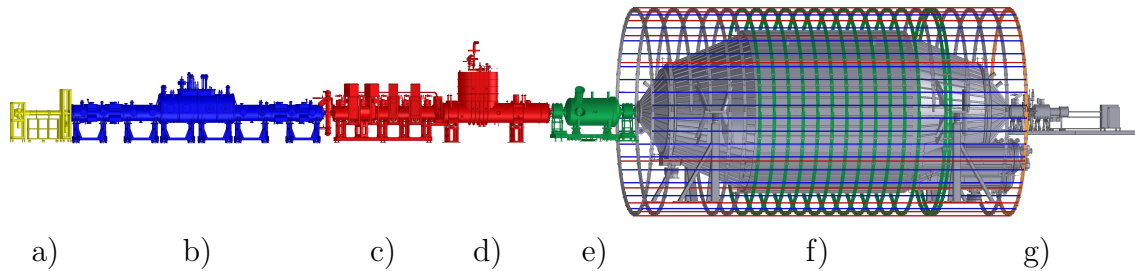


Figure 2.3: Overview of the KATRIN experiment. The main components are: a) rear section, b) windowless gaseous tritium source, c) differential pumping section, d) cryogenic pumping section, e) pre-spectrometer, f) main-spectrometer, g) detector. The monitor spectrometer is not shown.

The amount of tritium molecules contained in the WGTS is expressed using the so-called column density ρd which is the non-linear gas density integrated over the tube length. In the case of KATRIN its value is $\rho d = 5 \times 10^{17} \text{ cm}^{-2}$. Therefore, owing to the half-life of 12.3 yr, the rate of β -decays in the WGTS is about 10^{11} per second. The WGTS features seven superconducting magnets creating the magnetic field of $B_S = 3.6 \text{ T}$.

It is possible to circulate the gaseous $^{83\text{m}}\text{Kr}$ in the WGTS both without and with tritium. The metastable isotope has unique decay properties and is utilized for calibration and systematic studies. The krypton techniques are addressed in detail in Chapter 3.

Differential pumping section

The purpose of the differential pumping section (DPS) is to reduce the tritium flow from the WGTS towards the main spectrometer by an additional factor of 10^5 . Furthermore, five superconducting magnets (5.6 T) at the DPS provide guidance for the electrons. In the DPS the beam tube is split into five parts, which are tilted by 20° with respect to each other in order to avoid a direct line of sight for the tritium molecules. A set of four TMPs, placed at the pump ports between the beam tube parts, provide the necessary reduction.

Cryogenic pumping section

At the end of the DPS the tritium flow is still too high and would cause a considerable background in the main spectrometer. Therefore, the cryogenic pumping section (CPS) reduces the tritium flow by an additional factor of 10^7 . There are seven superconducting magnets (5.6 T) at the CPS for electron beam guidance. The tritium molecules will condense on the beam tube, which is several times bent and covered with argon frost at the temperature of about 4 K. As tritium accumulates in the CPS over the KATRIN run of two months, the beam tube has to be heated afterwards in order to regenerate it and to recover the adsorbed tritium.

Rear section

The rear section represents the termination of the tritium source at the very end of the beamline in the opposite direction to the spectrometer. It creates a defined electric potential of the tritium gas by providing a conducting surface, the rear wall. Furthermore, it provides continuous monitoring of the tritium source activity by detecting bremsstrahlung which is emitted from the impacting β -electrons. Lastly, an electron gun is provided for measuring the tritium column density and for systematic studies of the main spectrometer.

Pre-spectrometer

Most of the β -electrons do not carry information about the neutrino mass and would be rejected by the analysing MAC-E filter. However, the large rate of electrons could cause ionization of the residual gas molecules and as a consequence elevated background. To reduce the electron flux in the main spectrometer, another MAC-E filter, the pre-spectrometer, is applied in front of it and rejects β -electrons with energy of up to about 18.3 keV. The pre-spectrometer is a 3.4 m-long and 1.7 m-wide stainless steel vessel made with similar features as the main spectrometer with respect to high potential and vacuum (see further), but its energy resolution and high voltage stability are not critical.

Main spectrometer

The main spectrometer is the analysing MAC-E filter of KATRIN. It is a 24 m-long and 10 m-wide stainless steel vessel kept at ultra-high vacuum (UHV) at the level of 10^{-11} mbar. The large dimensions follow from the fact that a magnetic field flux of 191 T cm^2 , which has to be transported over the beamline, is conserved. At the WGTS with $B_S = 3.6 \text{ T}$ the diameter of the flux tube is 8.2 cm, i.e. slightly less than the WGTS beam tube diameter, but at the main spectrometer with $B_{\min} = 0.3 \text{ mT}$ the flux tube diameter is 9 m. Fine tuning of the magnetic field is done using a set of normal conducting coils.

The vessel itself is on high potential and the retarding field is determined by a set of two-layer wire electrodes which are installed at the inner surface of the vessel. The wires are kept at a slightly more negative potential than the vessel thus acting as an electrostatic shield against secondary electrons which are emitted after interactions of cosmic muons with the large surface of the vessel. The high voltage is reduced by two high-precision KATRIN voltage dividers K35 and K65 and read out by two high-precision voltmeters.

In order to reach the UHV conditions in a 1240 m^3 volume the main spectrometer is equipped, besides six TMPs, with the so-called non-evaporable getter (NEG) strips with the total length of 3 km. When activated by heating to a high temperature, the NEG acts as a sorption vacuum pump especially for hydrogen which is difficult to pump by other means. As the NEG emanates radon which is a major source of background in a MAC-E filter, there are the so-called copper baffles cooled with liquid nitrogen which adsorb the radon so that it does not decay in the flux tube inside the spectrometer. The vacuum vessel can be heated up to $350 \text{ }^\circ\text{C}$ to reduce outgassing from the 690 m^2 surface.

Detector

The energy-analysed electrons are focused and counted in the detector. It is based on a silicon PIN (positive-intrinsic-negative) diode segmented in radial and azimuthal directions into 148 equal-area pixels with the total diameter of 9 cm. The detector is placed in a magnetic field of $B_D = 3$ T which leads to the maximal incident angle for electrons of 45° . The segmentation compensates for radial inhomogeneities of the electric and magnetic fields within the main spectrometer. The so-called post-acceleration electrode increases the electron energy to a value which is more favorable with respect to the detector background. A surrounding veto system, based on a plastic scintillator, is utilized to tag cosmic muons.

Monitor spectrometer

The stability of the main spectrometer high voltage is subject to one of the major systematic uncertainties in KATRIN as will be discussed further. Therefore, besides the high-precision voltage dividers an additional complementary high-voltage monitoring system is applied. The main spectrometer high voltage is distributed to another MAC-E filter, the monitor spectrometer, which utilizes a solid $^{83\text{m}}\text{Kr}$ source as a nuclear standard. The solid $^{83\text{m}}\text{Kr}$ source technique is addressed in detail in Chapter 3.

2.4 Experimental uncertainties

The experimental uncertainties determine the ultimate sensitivity to the neutrino mass. The design goal of KATRIN is to reach similar contributions from the overall systematic and statistical uncertainties. Whereas the latter is determined primarily by strategy of the tritium spectrum measurement such as scanning technique and time-per-voltage distribution, the former involves several key experimental parameters which have to be under control during the measurement.

In KATRIN there are six known major systematic effects which contribute to the overall systematic uncertainty of the neutrino mass squared [KAT04]. The maximal allowed uncertainty of each contribution is

$$\sigma_{\text{syst}}^{(i)}(m_\beta^2) < 0.007 \text{ eV}^2. \quad (2.10)$$

Adding the maximal allowed individual contributions quadratically yields the expected systematic uncertainty

$$\sigma_{\text{syst}}(m_\beta^2) = 0.017 \text{ eV}^2. \quad (2.11)$$

The individual contributions can be described as follows.

1. Final state distribution of the $(^3\text{HeT})^+$ daughter molecule.

The final state distribution influences the shape of the electron β -spectrum as described by Eq. (1.48). The decay of one of the tritium atoms in T_2 leads to the

molecule (${}^3\text{HeT}^+$). In this molecule the first electronic excited states have an energy of about 27 eV which is relatively high and does not significantly influence the neutrino mass measurement. However, there are rotational-vibrational states of the (${}^3\text{HeT}^+$) ground state populated with the mean excitation energy of 1.7 eV and the full width at half maximum of about 0.7 eV. A small error in the width used for the neutrino mass analysis can lead to a substantial shift of the observed neutrino mass squared and thus the precise knowledge of the final state distribution is essential.

2. Electron inelastic scattering within the WGTS.

The electron may collide with a tritium molecule in the source and get inelastically scattered. Such an electron loses some of its energy and is transmitted through the MAC-E filter differently. However, the ideal transmission function in Eq. (2.8) does not account for that. Folding the electron energy loss distribution with the transmission function defines the response function of the experiment. Despite the fact that inelastic events contribute only a few percent to the total electron rate in the region of the β -spectrum with the highest sensitivity to the neutrino mass, the accurate knowledge of the response function is of crucial importance.

3. Fluctuations of the tritium column density in the WGTS.

The column density directly influences the electron inelastic scattering probability and thus the experimental response function and also determines the decay rate observed at the main spectrometer. The column density is determined by various factors such as the WGTS beam tube temperature, injection pressure or tritium purity. Thus, these parameters have to be stabilized and monitored in a stringent way. Additionally, repeated measurements of the column density itself with an electron gun in between successive neutrino mass measurements are foreseen.

4. Effects from space charging in the WGTS.

The β -decays and the large amount of β -electrons emitted in the decays produce ionization events in the tritium gas. Various ions and molecules such as T^+ , He^+ , (${}^3\text{HeT}^+$) and T_2^+ are formed. A variable space charge within the WGTS would result in β -spectra with different endpoint energies superimposed to each other. If not compensated by secondary electrons stemming from the ionization, additional low-energy electrons would have to be introduced from the rear plate e.g. by photoemission or dipole electrodes to drift out the ions would have to be utilized.

5. Transmission function of the main spectrometer.

As discussed in Section 2.2 the energy resolution of a real MAC-E filter is deteriorated by inhomogeneities of the electric and magnetic fields in the analysing plane. In KATRIN this is compensated for by having a segmented detector. Nevertheless, detailed knowledge of the transmission properties for each detector pixel has to be established by numerical simulations and verified experimentally in order to accurately derive the neutrino mass squared from the measured spectrum.

6. Fluctuations of the retarding high voltage.

The MAC-E filter principle relies on applying high voltage to the retarding electrodes. If the high voltage is subject to fluctuations, so is the retarding electrical field. Unrecognized voltage fluctuations will lead to a systematic shift of the observed neutrino mass squared. Thus, the high voltage has to be continuously monitored at high level of accuracy and precision.

Concerning the statistical uncertainty, the region of the β -spectrum around the endpoint is not equally sensitive to the neutrino mass squared over its entire length. With the MAC-E filter it is possible to set the retarding voltage in each step of the spectrum acquisition to an arbitrary value for an arbitrary time interval. Assuming a background rate of 10 mcps an optimized time-per-voltage pattern for KATRIN was determined while the scanning interval $[E_0 - 30 \text{ eV}, E_0 + 5 \text{ eV}]$ was chosen. After three years of data taking the statistical uncertainty will be

$$\sigma_{\text{stat}}(m_\beta^2) = 0.018 \text{ eV}^2. \quad (2.12)$$

Adding the systematic and statistical uncertainties in quadrature yields the total uncertainty of the neutrino mass squared

$$\sigma(m_\beta^2) = 0.025 \text{ eV}^2. \quad (2.13)$$

This value leads to the discovery potential of

$$m_\beta = 0.35 \text{ eV} \quad (5\sigma) \quad (2.14)$$

or, if no neutrino mass signal is found, to the limit

$$m_\beta < 0.2 \text{ eV} \quad (90\% \text{ C.L.}). \quad (2.15)$$

3 Energy scale in KATRIN

The β -electron energy spectrum measured by the experiment can be distorted by various systematic effects. The distortions may lead to systematic shifts of the observed parameters, the tritium endpoint energy E_0 or the neutrino mass squared m_β^2 , if they are not accounted for in the spectrum shape analysis. Such a situation is referred to as an energy scale distortion.

In this chapter, the issues of energy scale distortions are addressed in detail. Further, the role of the metastable isotope $^{83\text{m}}\text{Kr}$ as a nuclear standard for energy scale calibration and monitoring is introduced. Finally, the applications of $^{83\text{m}}\text{Kr}$ in KATRIN are discussed.

3.1 Effects of energy scale distortions in β -decay neutrino mass measurements

The influence of energy scale variations on m_β^2 were first pointed out in [Rob88] in connection to the tritium β -decay final states. In [Kaš04] the issue was studied further numerically by least-squares fitting a distorted integral β -spectrum by an undistorted one for some representative distortion patterns. In [Thü07] a result for the m_β^2 systematic shift is derived analytically using approximate shape of the differential β -spectrum near the endpoint and using a Gaussian distortion with the expectation value of zero. Further, in [Grö10] the effect of time-varying sinusoidal fluctuation is studied.

In the following a universal analytical approach is presented as a generalization of the approach of [Thü07] for an arbitrary distortion with non-zero expectation value and non-zero variance. Its influence on E_0 and m_β^2 is derived in case of the differential β -spectrum and also the integral β -spectrum idealized to the case of a step-like transmission function (corresponding to a MAC-E filter with infinitely good resolution). The latter case gives the same answer as for the differential β -spectrum. It is considered here since, to the author's knowledge, such a result has not been discussed or pointed out elsewhere.

3.1.1 Differential β -spectrum

The differential β -electron energy spectrum is described by Eq. (1.48). At present the individual neutrino masses m_i cannot be experimentally resolved and only the effective neutrino mass squared m_β^2 as expressed in Eq. (1.51) is measured. Neglecting the final state distribution, the spectrum in the region near the endpoint can be expressed in a simpler way as

$$\frac{d\Gamma}{dE} \approx a(E_0 - E)\sqrt{(E_0 - E)^2 - m_\beta^2}, \quad (3.1)$$

where a absorbed all constants and also values which can be considered constant in this region. Since m_β^2 is small, the spectrum can be approximated by the Taylor expansion around $m_\beta^2 = 0$ up to the first order in m_β^2 which we denote as $f(E)$,

$$\frac{d\Gamma}{dE} (m_\beta^2 \approx 0) \approx a(E_0 - E)^2 - \frac{a}{2}m_\beta^2 + \mathcal{O}(m_\beta^4) \equiv f(E) + \mathcal{O}(m_\beta^4). \quad (3.2)$$

Let us consider that the energy scale distortion is manifested by random fluctuations of the electron energy. The fluctuations are statistically described by the probability density function (PDF) $p(x)$, where x is the fluctuation value, for which it holds

$$\int_{-\infty}^{+\infty} p(x) dx = 1. \quad (3.3)$$

The probability of finding the fluctuation value in the interval $(x, x + dx)$ is $p(x) dx$. In such a case each point of the β -spectrum is smeared out by this function. The distorted spectrum $F(E)$ can be expressed by the convolution of the PDF and the undistorted spectrum,

$$\begin{aligned} F(E) &= \int_{-\infty}^{+\infty} f(E - y) p(y) dy \\ &= a \int_{-\infty}^{+\infty} p(y) \left[(E_0 - E)^2 + 2y(E_0 - E) + y^2 - \frac{m_\beta^2}{2} \right] dy. \end{aligned} \quad (3.4)$$

In the equation there are three terms each with a different power $n = 0, 1, 2$ of the integration variable y . Each is the corresponding n^{th} moment of the PDF $p(x)$. The zeroth moment is one since the function is normalized, see Eq. (3.3). The first moment is the expectation value μ of $p(x)$,

$$\mu = \int_{-\infty}^{+\infty} x p(x) dx. \quad (3.5)$$

The second moment is related to the variance σ^2 of $p(x)$,

$$\sigma^2 = \int_{-\infty}^{+\infty} (x - \mu)^2 p(x) dx = \int_{-\infty}^{+\infty} x^2 p(x) dx - \mu^2. \quad (3.6)$$

Thus we get

$$F(E) = a \left[(E_0 - E)^2 + 2\mu(E_0 - E) + \sigma^2 + \mu^2 - \frac{m_\beta^2}{2} \right]. \quad (3.7)$$

Consider now that the distortion is unrecognized and the spectrum $F(E)$ is analysed using the undistorted one in Eq. (3.2) which we denote as $\tilde{f}(E)$,

$$\tilde{f}(E) = a(\tilde{E}_0 - E)^2 - \frac{a}{2}\tilde{m}_\beta^2. \quad (3.8)$$

Then the observed parameters \tilde{E}_0 and \tilde{m}_β^2 are such that the equation $\tilde{f}(E) = F(E)$ is satisfied,

$$(\tilde{E}_0 - E)^2 - \frac{\tilde{m}_\beta^2}{2} = (E_0 - E)^2 + 2\mu(E_0 - E) + \sigma^2 + \mu^2 - \frac{m_\beta^2}{2}, \quad (3.9)$$

where the constant a was already dropped out. The equation holds if

$$\tilde{E}_0 = E_0 + \mu, \quad (3.10a)$$

$$\tilde{m}_\beta^2 = -2\sigma^2 + m_\beta^2, \quad (3.10b)$$

which can be seen from comparison of the coefficients at the individual powers of $(E_0 - E)$. Therefore, there is a systematic shift $\Delta E_0 \equiv \tilde{E}_0 - E_0$ and $\Delta m_\beta^2 \equiv \tilde{m}_\beta^2 - m_\beta^2$ of the observed endpoint and the observed neutrino mass squared, respectively, depending on the expectation value and the variance of the PDF $p(x)$,

$$\Delta E_0 = \mu, \quad (3.11a)$$

$$\Delta m_\beta^2 = -2\sigma^2. \quad (3.11b)$$

3.1.2 Integral β -spectrum

Consider an idealized MAC-E filter with infinitely good energy resolution. For such a spectrometer the transmission function, Eq. (2.8), shrinks to a step function $T(E, qU) = \Theta(E - qU)$, i.e.

$$\Theta(E - qU) = \begin{cases} 1, & \text{if } E > qU, \\ 0, & \text{otherwise.} \end{cases} \quad (3.12)$$

The spectrum $S(qU)$ observed by such a spectrometer is given by Eq. (2.9) and reads

$$\begin{aligned} S(qU) &= \int_{-\infty}^{+\infty} \frac{d\Gamma}{dE} \Theta(E - qU) dE = \int_{qU}^{+\infty} \frac{d\Gamma}{dE} dE \\ &\approx \int_{qU}^{E_0 - m_\beta} a(E_0 - E) \sqrt{(E_0 - E)^2 - m_\beta^2} dE = \frac{a}{3} [(E_0 - qU)^2 - m_\beta^2]^{\frac{3}{2}}, \end{aligned} \quad (3.13)$$

where Eq. (3.1) was used. Let us utilize the simpler notation $qU \equiv E$. Again we perform the Taylor expansion around $m_\beta^2 = 0$ up to the first order in m_β^2 and denote the result as $g(E)$,

$$S(E; m_\beta^2 \approx 0) \approx \frac{a}{3}(E_0 - E)^3 - a(E_0 - E)\frac{m_\beta^2}{2} + \mathcal{O}(m_\beta^4) \equiv g(E) + \mathcal{O}(m_\beta^4). \quad (3.14)$$

Proceeding similarly as in the case of differential β -spectrum, the distorted integral spectrum $G(E)$ is given by the convolution of the PDF $p(x)$ and the undistorted spectrum $g(E)$,

$$G(E) = \int_{-\infty}^{+\infty} g(E - y) p(y) dy$$

$$= a \int_{-\infty}^{+\infty} p(y) \left[\frac{1}{3}\epsilon^3 + y\epsilon^2 + y^2\epsilon + \frac{1}{3}y^3 - \frac{m_\beta^2}{2}(\epsilon + y) \right] dy, \quad (3.15)$$

where we have introduced $\epsilon \equiv E - E_0$ for simplicity. The integral involving y^3 is the third moment of $p(x)$ and is related to the skewness γ of $p(x)$ as

$$\gamma = \int_{-\infty}^{+\infty} \left(\frac{x - \mu}{\sigma} \right)^3 p(x) dx = \frac{1}{\sigma^3} \left(\int_{-\infty}^{+\infty} x^3 p(x) dx - 3\mu\sigma^2 - \mu^3 \right). \quad (3.16)$$

If the distribution is not skewed¹, which holds for a symmetrical distribution, then we get

$$G(E) = a \left[\frac{1}{3}\epsilon^3 + \mu\epsilon^2 + (\sigma^2 + \mu^2)\epsilon + \frac{1}{3}\mu^3 + \mu\sigma^2 - \frac{m_\beta^2}{2}(\epsilon + \mu) \right]. \quad (3.17)$$

Considering again that the distortion is unrecognized, we compare the observed spectrum, see Eq. (3.14),

$$\tilde{g}(E) = \frac{a}{3}(\tilde{E}_0 - E)^3 - a(\tilde{E}_0 - E)\frac{\tilde{m}_\beta^2}{2} \quad (3.18)$$

with the form $G(E)$ and the parameters \tilde{E}_0 and \tilde{m}_β^2 are such that $\tilde{g}(E) = G(E)$. The result is the same as in Eqs. (3.10a) and (3.10b).

3.1.3 Expected forms of energy scale distortions

Let us introduce several types of energy scale distortions which can be expected during the neutrino mass measurement. The task in each case is to find the corresponding PDF $p(x)$. In many cases the distribution $p(x)$ is not known beforehand (as e.g. the normal distribution), but it is known that the fluctuations are governed by a time dependence, i.e. $x = x(t)$ with $t \in [0, T]$. Given a randomly chosen time interval $(t, t + \Delta t)$ we are interested in the probability of finding the fluctuation in the interval $(x, x + \Delta x)$.

Consider a small region of the function $x(t)$ as shown in Fig. 3.1. The fluctuation interval $(x_1, x_1 + \Delta x)$ corresponds to the time interval $(t_1, t_1 + \Delta t_1)$ via the function $x(t)$. Similarly, the fluctuation interval $(x_2, x_2 + \Delta x)$ corresponds to the time interval $(t_2, t_2 + \Delta t_2)$. The choice of the time interval is random and since there is no particular preference, it is uniform on the whole interval $[0, T]$. Therefore, the interval $(t_1, t_1 + \Delta t_1)$ is chosen with the probability $\Delta t_1/T$ because this is the fraction the time intervals covers out of the whole interval. Similarly, the probability of choosing $(t_2, t_2 + \Delta t_2)$ is $\Delta t_2/T$. Since the slope of $x(t)$ at the second interval is larger, $\Delta t_2 < \Delta t_1$ for the same Δx .

As the fluctuation and time intervals correspond to each other uniquely, the probability of getting the fluctuation interval $(x_1, x_1 + \Delta x)$ is given by the probability of choosing the corresponding time interval which is $\Delta t_1/T$. Similarly, for getting the second fluctuation interval $(x_2, x_2 + \Delta x)$ we have the probability of $\Delta t_2/T$. The probability of obtaining

¹ In the case of a skewed distribution an additional constant term $\frac{a}{3}\gamma\sigma^3$ appears which is not eliminated. However, if a constant background term is introduced into Eq. (3.15) then the additional term can be interpreted as a systematic shift of the observed background.

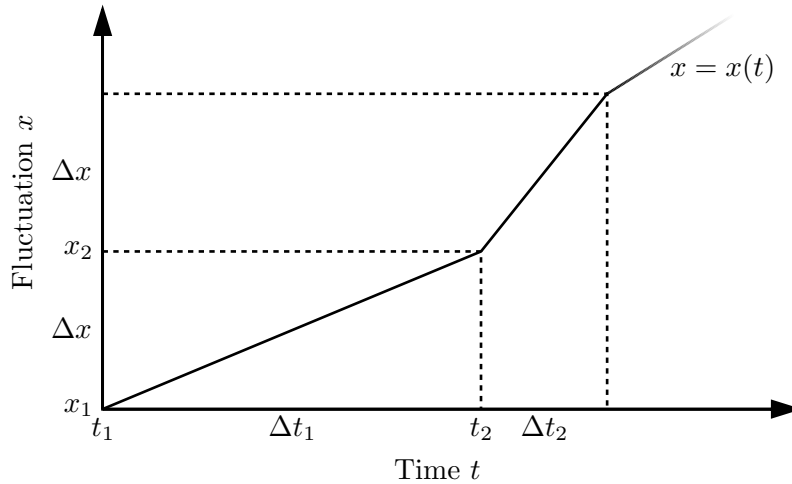


Figure 3.1: Illustration of the time dependence of an energy scale fluctuation and relevant quantities for obtaining the probability density function of the fluctuation. Due to unique correspondence via the function $x(t)$ the probability of obtaining the interval $(x_i, x_i + \Delta x)$ is given by the probability of obtaining $(t_i, t_i + \Delta t_i)$ in a random choice from the whole interval $[0, T]$. The probability is given by the relative size of the time interval $\Delta t_i/T$.

$(x_i, x_i + \Delta x)$ in general is given by $p(x_i) \Delta x$ from the definition of the PDF $p(x)$ and therefore we have $p(x_i) \Delta x = \Delta t_i/T$. Taking the differences as infinitesimal we obtain for the PDF $p(x)$ the relation

$$p(x) = \frac{1}{T} \frac{dt}{dx}. \quad (3.19)$$

Thus, given the function $x(t)$ we can calculate the corresponding PDF by differentiating its inverse function provided that it exists.

One notable case when the inverse function does not exist is when $x(t)$ is a constant in some time interval (t_1, t_2) with $t_2 - t_1 = \Delta t \leq T$. In this interval the fluctuation can take up only a single value v . In such a case the r.h.s. of Eq. (3.19) is not well defined. Fortunately, the probability density function still exists and can be expressed using the Dirac δ -function² as

$$p(x) = \frac{\Delta t}{T} \delta(x - v) + \dots, \quad (3.20)$$

where the dots refer to further terms in $p(x)$ which correspond to times outside the interval (t_1, t_2) .

² The more constant the function, the larger the slope of the inverse function and thus the derivative dt/dx . In a somewhat loose sense, in the limiting case $dt/dx \rightarrow \infty$ while $\int p(x) dx = 1$. The Dirac δ function has exactly this property.

Constant shift of the energy scale

The energy scale is shifted by the value v for the whole time, i.e. the fluctuations x take up only a single value. According to Eq. (3.20) the PDF $p(x)$ is given by

$$p(x) = \delta(x - v). \quad (3.21)$$

For such a PDF only the mean is non-zero and thus this distortion leads only to a shift of the endpoint,

$$\Delta E_0 = v, \quad (3.22a)$$

$$\Delta m_\beta^2 = 0. \quad (3.22b)$$

Sudden shift of the energy scale

The energy scale is stable for the fraction $(1 - f)$ of the whole measurement time and for the remaining fraction f it is shifted by the value v . In such a case the fluctuation can take up only one of two discrete values, zero and v , with the weights $(1 - f)$ and f , respectively. In terms of PDF this can be written using a sum of two δ -functions,

$$p(x) = (1 - f) \delta(x) + f \delta(x - v). \quad (3.23)$$

The endpoint and neutrino mass squared shifts are

$$\Delta E_0 = fv, \quad (3.24a)$$

$$\Delta m_\beta^2 = -2f(1 - f)v^2. \quad (3.24b)$$

The analytical approach enables to estimate the neutrino mass squared shift for any combination of the values f and v . Specifically, we may calculate at what fraction f_{\max} will the variance and thus the neutrino mass squared shift be maximal. Thus, we search for a stationary point f_{\max} such that

$$\frac{d\sigma^2}{df}(f_{\max}) = 0 \quad (3.25)$$

which leads to $f_{\max} = \frac{1}{2}$. This is indeed a maximum since $\frac{d^2\sigma^2}{df^2} = -2v^2 < 0$.

Wrong slope of the energy scale

Consider that at each point of the β -spectrum the value E is changed by an additive factor which is equal to the multiple of the value,

$$E \rightarrow E + kE, \quad (3.26)$$

where k is a small constant. The fluctuation x again takes up only a single value, which depends on the energy E . Thus, $p(x)$ is given by the δ function

$$p(x) = \delta(x - kE). \quad (3.27)$$

The endpoint and neutrino mass squared shifts are

$$\Delta E_0 = kE_0, \quad (3.28a)$$

$$\Delta m_\beta^2 = 0. \quad (3.28b)$$

For this distortion no shift of the neutrino mass squared appears. Note that having the spectrum as values $f(E)$ depending on $E + kE$ is the same as having the values $f(E - kE)$ depending on E . This exactly follows from the PDF in Eq. (3.27) because the distorted spectrum is

$$F(E) = \int_{-\infty}^{+\infty} f(E - y) \delta(y - kE) dy = f(E - kE). \quad (3.29)$$

The same holds for the integral spectrum $g(E)$ and the distorted $G(E)$. Note that the result in Eqs. (3.28a) and (3.28b) is the same as in Eqs. (3.22a) and (3.22b) if $v = kE_0$. In other words, to the first order the wrong slope of the energy scale has no further effect besides the endpoint shift similarly as the constant shift of the whole scale.

Gaussian distortion

Each point of the β -spectrum is observed as a continuous set of points which are normally distributed around the mean value μ with the variance σ^2 . In other words, the energy scale is smeared out by the Gaussian distribution

$$p(x) = \frac{1}{\sqrt{2\pi\sigma^2}} \exp\left(-\frac{(x - \mu)^2}{2\sigma^2}\right), \quad (3.30)$$

which propagates into the count rate. The values μ and σ^2 are used to define the distribution so these parameters can be directly utilized in Eqs. (3.11a) and (3.11b).

Time-varying sinusoidal distortion

The fluctuation x follows the sine function as

$$x(t) = A \sin(\omega t), \quad (3.31)$$

where A is the amplitude and ω the angular frequency. According to Eq. (3.19) the PDF is

$$p(x) = \frac{1}{\pi A} \frac{1}{\sqrt{1 - \left(\frac{x}{A}\right)^2}}, \quad x \in [-A, A], \quad (3.32)$$

where we have used $T = \pi/\omega$ as half of the sine wave period, i.e. $t \in [\frac{\pi}{2}, \frac{3\pi}{2}]$. In this interval all possible values of x are uniquely covered. The systematic shifts are

$$\Delta E_0 = 0, \quad (3.33a)$$

$$\Delta m_\beta^2 = -A^2. \quad (3.33b)$$

Linear drift of the energy scale

The fluctuation follows a linear function of time,

$$x(t) = dt, \quad (3.34)$$

where d is the drift constant. From Eq. (3.19) we get

$$p(x) = \frac{1}{dT}, \quad x \in [0, dT]. \quad (3.35)$$

Thus, the PDF is uniform in the corresponding interval. The systematic shifts yield

$$\Delta E_0 = \frac{1}{2}dT, \quad (3.36a)$$

$$\Delta m_\beta^2 = -\frac{1}{6}(dT)^2. \quad (3.36b)$$

Linear drift of the energy scale slope

The distorted spectrum will be a superposition of the undistorted spectra $f(E - kE)$ each with a different value of k , see Eq. (3.29). Let us denote the rate of change dk/dt as κ . Then for the linear case $k = \kappa t$ and the PDF is given by the superposition of PDFs from Eq. (3.27) as

$$p(x) = \frac{1}{T} \int_0^T \delta(x - \kappa tE) dt = -\frac{1}{\kappa TE} [\Theta(x - \kappa TE) - \Theta(x)] \quad (3.37)$$

which can be simplified to

$$p(x) = \frac{1}{|\kappa|TE}, \quad x \in \begin{cases} [0, \kappa TE], & \text{if } \kappa > 0, \\ [-|\kappa|TE, 0), & \text{if } \kappa < 0. \end{cases} \quad (3.38)$$

The endpoint and neutrino mass squared systematic shifts at the endpoint energy become

$$\Delta E_0 = \frac{1}{2}\kappa TE_0, \quad (3.39a)$$

$$\Delta m_\beta^2 = -\frac{1}{6}(\kappa TE_0)^2. \quad (3.39b)$$

The result in Eqs. (3.39a) and (3.39b) is the same as in Eqs. (3.36a) and (3.36b) if we set $\kappa E_0 = d$. Thus, as in the case of constantly different slope of the energy scale to the first order the linearly drifting slope behaves as a linear drift of the scale as a whole.

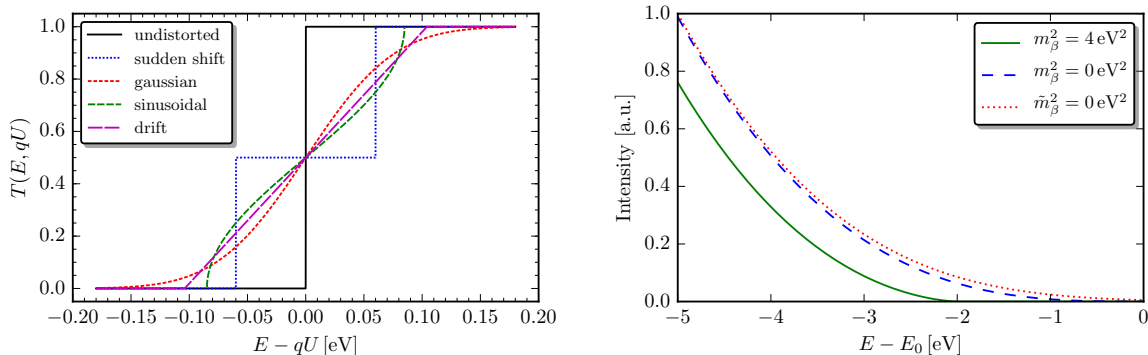


Figure 3.2: Illustration of the effects of energy scale distortions on the idealized MAC-E filter transmission function for the retarding energy of $qU = 18\,575\text{ eV}$ (left) and on the integral β -spectrum from Eq. (3.13) (right). In the left plot the distortion parameters are set such that the resulting neutrino mass squared shift $\Delta m_\beta^2 \approx -7 \times 10^{-3}\text{ eV}^2$. In the right plot the solid line is the undistorted integral β -spectrum from Eq. (3.13) with $m_\beta^2 = 4\text{ eV}^2$, the dashed line is the undistorted spectrum with $m_\beta^2 = 0\text{ eV}^2$, and the dotted line is distorted spectrum calculated as a numerical convolution of the solid line with the Gaussian function having the variance $\sigma^2 = 2\text{ eV}^2$.

3.1.4 Comparison with numerical results

The effects of distortions, which affect the observed neutrino mass squared, on the transmission function of an idealized MAC-E filter with infinitely good resolution are shown in Fig. 3.2 on the left for the fixed retarding energy of $qU = 18\,575\text{ eV}$. The step function $T(E, qU) = \Theta(E - qU)$ is also shown for comparison. The transmission functions influenced by distortions which also shift the observed endpoint energy were moved³ so that they are symmetrical with respect to $E - qU = 0\text{ eV}$. The effect of a Gaussian distortion on the integral spectrum, Eq. (3.13), is illustrated in Fig. 3.2 on the right. The Gaussian variance is $\sigma^2 = 2\text{ eV}^2$ and the neutrino mass squared is $m_\beta^2 = 4\text{ eV}^2$. Therefore, it holds $m_\beta^2 = 2\sigma^2$ and the distorted spectrum is practically identical to an undistorted one with $m_\beta^2 = 0\text{ eV}^2$. The situation illustrates how the true neutrino mass signature is hidden due to the distortion.

To further assess the theoretical results for the endpoint and neutrino mass squared shifts a distorted integral β -spectrum with $m_\beta = 0\text{ eV}$ and $E_0 = 18\,575\text{ eV}$ was calculated for each distortion type with the parameters expected for the KATRIN experiment and least-squares fitted by the undistorted integral β -spectrum. The transmission function was considered in the form of Eq. (2.8) and Fig. 2.2. No energy loss or final state effects were taken into account. The distorted spectrum was calculated with 0.5 eV steps in the interval $[E_0 - 30\text{ eV}, E_0 + 5\text{ eV}]$. The fitted parameters were amplitude (multiplicative factor of the spectrum), endpoint energy, neutrino mass squared and constant background. To allow

³ This corresponds to the situation that the energy scale is distorted already at the beginning of the measurement. Since the distortion in such a case is symmetrical around zero, the endpoint shift is also zero.

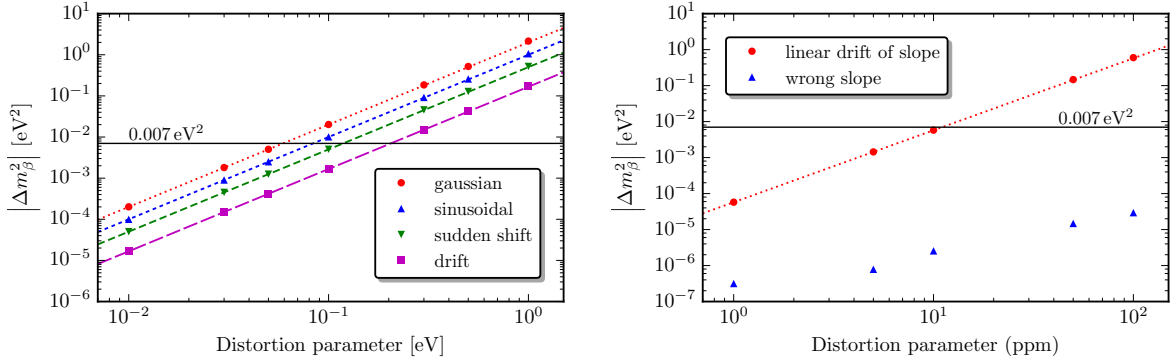


Figure 3.3: Comparison of neutrino mass squared shift obtained using the fits (points) and the corresponding approximate analytical prediction (dashed lines) in absolute value for various types of energy scale distortions. The distortion parameters are as follows. Left: the square root of the Gaussian variance σ^2 , the sinusoidal amplitude A , the sudden shift v with the fraction $f = \frac{1}{2}$ and the linear drift constant dT with the time $T = 1$ month. Right: the drifting slope constant κT with the time $T = 1$ month and the wrong slope constant k . The solid line indicates the KATRIN maximal allowed systematic uncertainty for a single contribution.

for negative m_β^2 the analytical continuation as in [Wei93] was utilized for Eq. (1.48) which is smooth and provides a parabolic χ^2 -distribution around $m_\beta^2 = 0$.

The distortions were made in the following way:

- Gaussian, sinusoidal and linear drift distortions: the transmission function for the distorted spectrum was numerically convoluted with the corresponding PDF,
- sudden shift: the spectrum value at E_i was calculated as $(1 - f)f(E_i) + f(E_i - v)$,
- wrong slope: the spectrum value at E_i was calculated as $f(E_i - kE_i)$,
- slope linear drift: the spectrum value at E_i was calculated as $\frac{1}{n} \sum_{i=0}^n f(E_i - E_i \frac{\kappa T}{n} i)$ with $n = 10^3$. In this way the continuous superposition of the undistorted spectra each with a different value of $k_i = \frac{\kappa T}{n} i$ was approximated.

The results of the neutrino mass squared shift obtained using the shifts are compared with the analytical expectations in Fig. 3.3 where also the KATRIN maximal allowed single systematic uncertainty of 0.007 eV^2 is indicated. The obtained shifts generally follow the analytical predictions. For the largest values of the distortion parameters the obtained values are larger in absolute value compared to the theoretical ones at the level of a few percent which is not visible in the figures. In the case of wrong slope distortion the prediction is $\Delta m_\beta^2 = 0 \text{ eV}^2$ but a small increase from the numerical results is observed. However, even for the large value of $k = 100 \text{ ppm} = 10^{-4}$, which leads to $\Delta E_0 = 1.86 \text{ eV}$, the observed neutrino mass squared shift is more than two orders of magnitude lower than the KATRIN limit and can be safely neglected.

The lastly discussed result is in contrast to [Kaš04] where an observation of a significant neutrino mass squared shift in dependence on the wrong slope value was reported. Such a result was also quoted in [KAT04]. It is worth noting that in the paper not only E is changed by the transformation similar as in Eq. (3.26) in the distorted spectrum but also E_0 is. However, the endpoint E_0 is a constant of nature and it does not change by e.g. imperfections of a voltmeter calibration. Thus, interpretation of such results is not entirely clear. The theoretical predictions and results for the constant shift, Gaussian and sudden shift ($f = \frac{1}{2}$) distortions presented here are in good agreement with [Kaš04].

Conclusion

The shift of the neutrino mass squared, Eq. (3.11b), which was recognized already in [Rob88], shows that *any* energy scale distortion with non-zero variance which is not accounted for *will* lead to a systematic shift of the observed neutrino mass squared to lower and possibly even negative values. Thus, control of the energy scale stability in a β -decay neutrino mass measurement is one of the most important parts of the experiment. The KATRIN maximal allowed systematic uncertainty from a single contribution, Eq. (2.10), translates via Eq. (3.11b) into the requirement for the standard deviation σ of the distortion of

$$\sigma < 60 \text{ meV}. \quad (3.40)$$

3.2 Conversion electrons of $^{83\text{m}}\text{Kr}$

The metastable isotope $^{83\text{m}}\text{Kr}$ with the half-life of 1.83(2) h [McC15] is a useful tool for energy calibration and systematic studies in the KATRIN experiment due to its unique decay characteristics. In decay to the ground state many conversion electrons are emitted with suitable energies and line widths. The most important are the 17.83 keV conversion electrons because their energy is only by about 760 eV lower than the tritium endpoint. Moreover, due to its short half-life, no long-term contamination of the experimental apparatus is possible. The electrons from $^{83\text{m}}\text{Kr}$ were successfully utilized in the previous tritium neutrino mass experiments [Rob83, Pic92a, Sto95, Lob02]. The $^{83\text{m}}\text{Kr}$ can be conveniently generated in a sufficient amount from the electron capture decay of ^{83}Rb with the half-life of 86.2(1) d [McC15].

The decay scheme of ^{83}Rb and $^{83\text{m}}\text{Kr}$ is shown in Fig. 3.4. ^{83}Rb decays by pure electron capture with the branching ratio of about 75 % into the isomeric state $^{83\text{m}}\text{Kr}$, which is the second excited state of ^{83}Kr with the spin-parity of $\frac{1}{2}^-$ and the excitation energy of 41.6 keV. The $^{83\text{m}}\text{Kr}$ decays further via a cascade of two electromagnetic transitions with the energies of 32.2 keV and 9.4 keV. These transitions give out a large number of conversion electrons. The total conversion coefficient as a ratio of the number of conversion electron to photon de-excitations amounts to 2035 for the 32 keV transition and to 17 for the 9.4 keV transition [McC15].

The energy E_i of a conversion electron emitted from an atomic orbital i is given by the difference of the gamma photon energy E_γ and the relevant electron binding energy

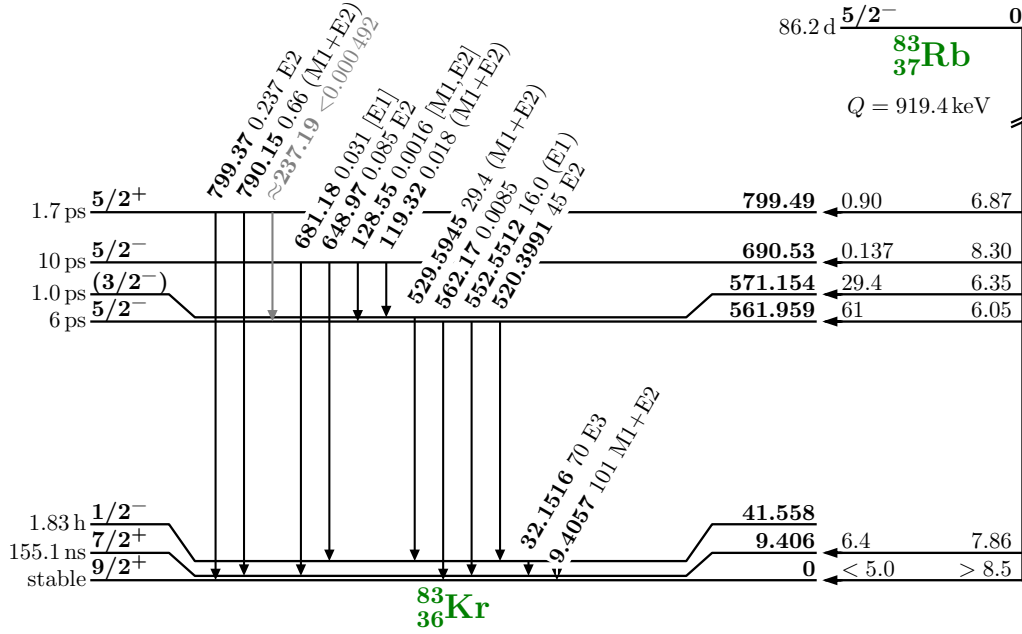


Figure 3.4: The decay scheme of ^{83}Rb and $^{83\text{m}}\text{Kr}$ as the second excited state of ^{83}Kr . For the nuclear levels the following is indicated: half-life, spin-parity, energy in keV, branching ratio in % and $\log ft$ values. The nuclear transitions between the levels are indicated with energy in keV, intensity per ^{83}Rb decay in % and multipolarity. The figure is based on ref. [McC15].

for the free atom B_i^{vac} , which refers to the vacuum level, plus small corrections that take into account recoil energies. This can be written as

$$E_i = E_\gamma + E_{\gamma,\text{rec}} - E_{e,\text{rec}} - B_i^{\text{vac}}, \quad (3.41)$$

where $E_{\gamma,\text{rec}}$ is the recoil energy after gamma emission and $E_{e,\text{rec}}$ is the recoil energy after electron emission. The term $E_\gamma + E_{\gamma,\text{rec}}$ is the energy of the nuclear transition. The K-shell (in spectroscopic notation $1s_{1/2}$ orbital) conversion electrons of the 32 keV transition, denoted as the K-32 electrons, have the binding energy of $B_K = 14.4$ keV and thus the energy of $E_K = 17.8$ keV which is desired in the tritium neutrino mass β -decay experiments. Other conversion electrons such as L₃-32 ($2p_{3/2}$) and L₁-9.4 ($2s_{1/2}$) have energies of 30.5 keV and 7.5 keV, respectively, which are more remote from the tritium endpoint but which are also measurable by the MAC-E filter. An overview of the full $^{83\text{m}}\text{Kr}$ conversion electron spectrum, which is discrete in contrast to the continuous β -spectrum, is shown in Fig. 3.5.

Due to finite lifetime of the vacancy, which is created after conversion electron emission, the electron energy distribution is not strictly sharp but has a certain spread which is comparable to the resolution of the MAC-E filter⁴. The energy distribution $I(E)$ is

⁴ Also the lifetime of the nuclear excited state contributes to the spread of the electron energy distribution. However, in the case of $^{83\text{m}}\text{Kr}$ this contribution is negligible.

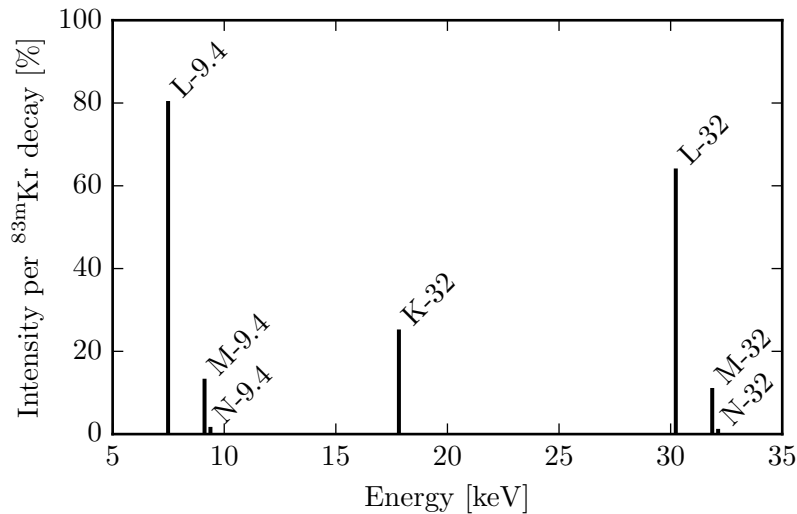


Figure 3.5: The conversion electron spectrum of $^{83\text{m}}\text{Kr}$ [McC15]. Shown are the summed intensities per $^{83\text{m}}\text{Kr}$ decay of conversion electrons which are of the same nuclear transition and from the same electron shell. The Auger electrons with the energies of 1.5 keV and 10.8 keV, which are also emitted in the decay, are not shown.

described by the Lorentzian function

$$I(E) = \frac{1}{\pi} \frac{\Gamma_i/2}{(E - E_i)^2 + \Gamma_i^2/4}, \quad (3.42)$$

where Γ_i is the full width at half maximum (FWHM) which is related to the mean lifetime of the vacancy τ_i through the “energy-time uncertainty relation” $\Gamma_i\tau_i = \hbar$. The values Γ_i range from a few tens of meV for the outer shell electrons (longer lifetime) to a few eV for the inner shell electrons (shorter lifetime) [Cam01]. The FWHM of the K-32 line is $\Gamma_K = 2.7$ eV. Fig. 3.6 shows the differential K-32 line shape $I(E)$ as described by Eq. (3.42) with⁵ $E_K = 17\,824.3$ eV. In the same figure the integral spectrum $S(qU)$, Eq. (2.9), of the conversion line is shown as observed by the MAC-E filter with the transmission function in Eq. (2.8) and the KATRIN magnetic field configuration.

3.3 Applications of $^{83\text{m}}\text{Kr}$ for energy scale calibration and monitoring

As described in detail in Section 2.2 the electrostatic barrier facing the electrons in the MAC-E filter is created by a set of retarding electrodes at high negative potential. Thus, fluctuations of the retarding field caused by instability of the high-voltage system are a potential source of energy scale distortions. Similarly, variations of the electrical potential

⁵ The binding energy for a free krypton atom is $B_K^{\text{vac}} = 14\,327.26(4)$ eV [Dra04] and the gamma photon energy is taken from Eq. (3.48a).

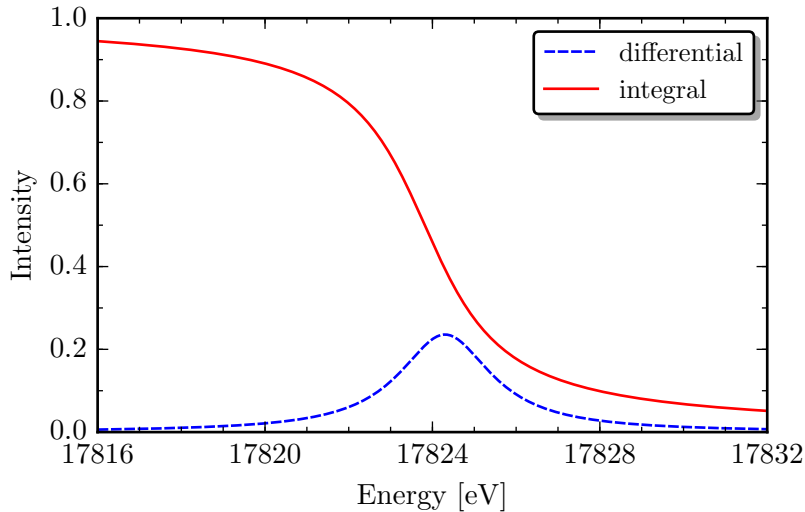


Figure 3.6: The K-32 conversion electron line. The differential shape is a function of the electron energy E and corresponds to Eq. (3.42) with $E_K = 17824.3$ eV and $\Gamma_K = 2.7$ eV. The integral shape, which corresponds to Eq. (2.9), is the conversion line as observed by an ideal MAC-E filter with the KATRIN magnetic field configuration as a function of the spectrometer retarding energy qU .

within the WGTS may also lead to energy scale distortions. However, the electrical field potential inside the MAC-E filter, neglecting any radial dependence and finite spectrometer resolution for simplicity, is not given only by the applied voltage but also by the work function of the electrode surface. Similarly, the WGTS field potential is modified due to the work function of the rear wall (a metal surface) because the electrical potential along a magnetic field line is shorted by WGTS high axial charge conductivity to the rear wall [KAT04].

The work function is the amount of work needed to remove an electron from the surface into vacuum close to the surface. Denoting the vacuum level as E^{vac} and the electron level in the surface as E^{Fer} (Fermi level), the work function φ is given as

$$\varphi = E^{\text{vac}} - E^{\text{Fer}}. \quad (3.43)$$

It is a property of the material and the condition of the surface and therefore its value is greatly influenced by adsorbed gases. The source and the retarding electrode, or simply the spectrometer, have generally different work functions φ_{src} and φ_{sp} , respectively, as illustrated in Fig. 3.7 on the left and correspondingly different Fermi levels $E_{\text{src}}^{\text{Fer}}$ and $E_{\text{sp}}^{\text{Fer}}$. Without the loss of generality we assume $\varphi_{\text{src}} > \varphi_{\text{sp}}$. If both are electrically insulated, the vacuum level E^{vac} is the same.

During the measurement the source and the spectrometer share a common ground. In such a case a conductive path is provided and thus electrons flow from the spectrometer into the source until the Fermi levels are aligned into E^{Fer} , see Fig. 3.7 in the middle. The consequence is that in a previously neutral source there is an excess of negative charge whereas in the retarding electrode there is an excess of positive charge. Thus, an electron

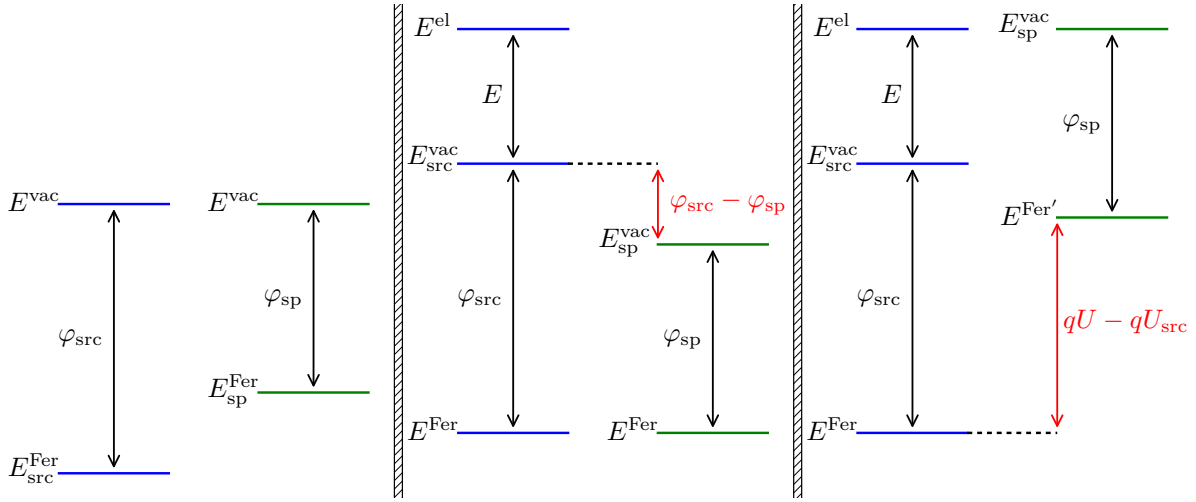


Figure 3.7: Energy diagrams for the source and spectrometer work function considerations. Left: both the source and the spectrometer are electrically insulated. Middle: the source and the spectrometer share a common ground and the Fermi levels get aligned. There is an electrical potential difference of $\frac{1}{q}(\varphi_{\text{src}} - \varphi_{\text{sp}})$ which leads to a higher apparent energy of the electron with respect to the spectrometer as compared to the source. Right: the spectrometer is biased with respect to the source by the retarding energy $qU - qU_{\text{src}}$ in order that the electron emitted with an energy E with respect to the source vacuum level just passes the electrostatic barrier of the MAC-E filter. Balancing the terms gives the electron energy observed by the spectrometer as described by Eq. (3.44).

emitted into the level E^{el} with the energy E with respect to the source vacuum level $E_{\text{src}}^{\text{vac}}$ appears to have an energy larger by $\varphi_{\text{src}} - \varphi_{\text{sp}}$ with respect to the spectrometer vacuum level $E_{\text{sp}}^{\text{vac}}$.

In order to analyse the electron energy the spectrometer is biased with respect to the source by the retarding energy $qU - qU_{\text{src}}$, where U_{src} is the source bias voltage, so that the spectrometer vacuum level $E_{\text{sp}}^{\text{vac}}$ is aligned to the electron level E^{el} (neglecting finite energy resolution), see Fig. 3.7 on the right. The spectrometer Fermi level $E^{\text{Fer}'}$ is now higher than the source Fermi level E^{Fer} by exactly the retarding energy. Balancing all terms in the figure we conclude that the electron energy observed by the spectrometer reads

$$q(U - U_{\text{src}}) = E - \varphi_{\text{sp}} + \varphi_{\text{src}}. \quad (3.44)$$

The equation shows that not only the electrical potentials but also the work functions are a potential source of energy scale distortions in KATRIN.

In order to assess the energy scale distortions, the $^{83\text{m}}\text{Kr}$ will be extensively applied in three different forms,

- gaseous krypton source (GKrS) at the WGTS for space charge measurement and energy calibration,
- quench-condensed krypton source (CKrS) at the CPS for energy calibration,

- solid krypton source (SKrS) at the monitor spectrometer for continuous high voltage stability monitoring.

In the following the three points are discussed in detail.

3.3.1 WGTS space charge distribution

Distortion of the WGTS potential U_{src} due to space charging effects is one of the major systematic effects in KATRIN, see Section 2.4. In accordance to the results of Section 3.1, the charging as a whole may lead to a systematic shift of the observed β -spectrum endpoint. Similarly, variations of the potential may lead to a shift of the observed neutrino mass squared towards more negative values. It is thus of the highest importance to investigate the WGTS potential distribution.

The GKrS is basically the only tool available for such a task because the two gases, T_2 and ^{83m}Kr , can share the common space in the WGTS. Given a conversion electron line with known centroid (line position) and line width, the experimental signature of WGTS charging as a whole is a shift of the measured conversion electron line position. Besides, variations of the WGTS charge will appear as broadening of the conversion line. Generally, if the WGTS charge potential energy x is described by some distribution $p(x)$ then the observed shape of the krypton conversion line $I^{\text{WGTS}}(E)$ is the convolution

$$I^{\text{WGTS}}(E) = \int_{-\infty}^{+\infty} I(E - y) p(y) dy. \quad (3.45)$$

In the above it was assumed that the krypton gas is distributed in the WGTS in the same way as the tritium gas, but in a more accurate treatment the possible difference in the distribution of the two gases due to their different mass has to be taken into account. Moreover, the observed line position is influenced by the work functions of the rear wall and the spectrometer. According to Eqs. (3.41) and (3.44) the observed energy is

$$E_i^{\text{GKrS}} \equiv q(U - U_{\text{src}}) = E_\gamma + E_{\gamma, \text{rec}} - E_{e, \text{rec}} - B_i^{\text{vac}} - \varphi_{\text{sp}}^{\text{MS}} + \varphi_{\text{src}}^{\text{WGTS}}, \quad (3.46)$$

where $\varphi_{\text{sp}}^{\text{MS}}$ and $\varphi_{\text{src}}^{\text{WGTS}}$ are the work functions of the main spectrometer and the WGTS, respectively.

The use of GKrS in the WGTS for space charge investigation was reported by the Troitsk neutrino mass group [Bel08]. The temperature of the WGTS tube had to be increased to 110K to avoid freeze-out of krypton onto the beam tube. Moreover, the measurement of the K-32 line was not possible due to small ^{83m}Kr activity and large tritium background so L₃-32 was measured instead. The krypton generator was a source of ^{83}Rb evaporated into a thin layer on a graphite substrate. The activity of the ^{83}Rb generator was about 1 MBq in the beginning of the measurements.

For KATRIN the implications are that the liquid neon coolant will have to be replaced by liquid argon or nitrogen to increase the WGTS beam tube temperature. A source with an activity of possibly up to 1 GBq will have to be used in order to be able to measure the K-32 line with tritium. Moreover, no contamination by the long-lived ^{83}Rb is allowed

which cannot be guaranteed by the evaporated source. A promising substrate seems to be zeolite, a highly porous aluminosilicate mineral, which acts as a cation exchanger thus possessing high ^{83}Rb retention capability [Vén05]. The source of $^{83\text{m}}\text{Kr}$ based on zeolite is further discussed in Chapter 6.

3.3.2 Energy calibration

The work function is a surface phenomenon and is thus heavily influenced by the surface properties and especially contamination. A gradual adsorption of residual gas molecules may result in a unrecognized slow drift of the work function over the measurement time. The work function influences the energy scale as an additive factor, i.e. as a whole. According to the results of Section 3.1 a drift of the whole energy scale may lead to a systematic shift of both the observed endpoint and the neutrino mass squared.

The systematic shift of the endpoint can be assessed if an energy calibration is performed by means of the $^{83\text{m}}\text{Kr}$ conversion electrons. After the tritium β -spectrum is measured, the observed endpoint energy E_0 can be compared with the value obtained by Penning trap mass spectrometry measurements. Until recently, the endpoint value, see Eq. (2.3), was not known with enough precision for this purpose. The more recent measurement [Mye15] reports the uncertainty of 70 meV and efforts are underway to push the uncertainty down to as low as 30 meV [Str14]. Apart from the K-32 electrons other more remote conversion lines can be used for refinement of the energy calibration in the endpoint region. Thus, the value of E_0 can be obtained with a smaller uncertainty. Besides, overall check of the spectrometer at a broader energy interval is possible.

The calibration of the energy scale will be performed between tritium runs by means of the CKrS which will be applied at the CPS. It can provide a clear electron signal even for the lower-energy conversion electrons of the 9.4 keV gamma transition because the WGTS can be uncoupled by a valve. The GKrS can provide the absolute calibration only by means of the K-32 and higher energy electrons after tritium is introduced into the WGTS because the huge tritium β -spectrum practically precludes the 9.4 keV conversion electron measurement. The CKrS, being developed at the University of Münster, is made by guiding the $^{83\text{m}}\text{Kr}$ from a ^{83}Rb source via a thin capillary onto a highly-oriented pyrolytic graphite (HOPG) substrate with the temperature of about 25 K where it is adsorbed. The substrate is placed in UHV chamber and additionally shielded by cold baffles to reduce adsorption of residual gas. The cleanliness of the substrate surface is monitored by means of laser ellipsometry. In [Ost08] the required stability of the K-32 conversion line energy was demonstrated for the period of about one week which is enough to accomplish the energy scale calibration. The electron kinetic energy observed by the spectrometer is given by, cf. Eqs. (3.41) and (3.44),

$$E_i^{\text{CKrS}} \equiv q(U - U_{\text{src}}) = E_\gamma + E_{\gamma,\text{rec}} - E_{e,\text{rec}} - (B_i^{\text{vac}} - \Delta B_i^{\text{CKrS}}) - \varphi_{\text{sp}}^{\text{MS}} + \varphi_{\text{src}}^{\text{CKrS}}, \quad (3.47)$$

where $\varphi_{\text{src}}^{\text{CKrS}}$ is the work function of the CKrS and ΔB_i^{CKrS} accounts for change in the binding energy for the krypton atom being adsorbed onto the substrate.

For the purpose of high-precision energy scale calibration, high precision of the conversion electron energies is desirable. The binding energies for the subshells of free krypton

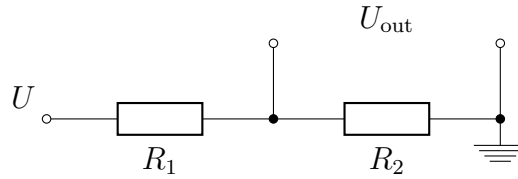


Figure 3.8: The principal scheme of a voltage divider. A current flows between the high-voltage node and the ground through the resistances R_1 and R_2 . Following from Ohm's law, the dividing ratio of the input high voltage U to the output voltage U_{out} is given by $M = (R_1 + R_2)/R_2$.

atom are known to sub-eV precision. The energies of the 32 keV and 9.4 keV gamma transitions were determined recently using gamma spectroscopy measurements of closely spaced lines as [Vén06, Sle12]

$$E_\gamma(32) = 32\,151.7(5) \text{ eV}, \quad (3.48a)$$

$$E_\gamma(9.4) = 9405.8(3) \text{ eV}. \quad (3.48b)$$

3.3.3 High voltage fluctuations

In order to obtain the integral spectrum in an accurate way, the retarding high voltage $U - U_{\text{src}}$ has to be measured precisely at each voltage step. At present the most precise measurement of voltages larger than 1 kV in absolute value can be done by using a high voltage divider, which reduces the voltage⁶ U to U_{out} at the order of around 10 V, and a state-of-the-art precise digital voltmeter, which is ideally suited for such a voltage. A principal scheme of a high voltage divider is depicted in Fig. 3.8. The input voltage U and the output voltage U_{out} are related through

$$U = \frac{R_1 + R_2}{R_2} U_{\text{out}} = M U_{\text{out}}, \quad (3.49)$$

where $M \equiv (R_1 + R_2)/R_2$ is the dividing ratio.

However, there is a stringent requirement from Eq. (3.40) on the stability of the high voltage measurement. At -18.6 keV the requirement for relative stability is about

$$\sigma < 3 \text{ ppm} \quad (3.50)$$

during the whole KATRIN run of two months. Such a stability is by no means obvious and despite suitable voltmeters exist, there is no commercially available high voltage divider with the dividing ratio stable at the desired level.

Therefore, two high-precision high voltage dividers, denoted as K35 and K65 according to the highest applicable voltage (in keV), were developed for KATRIN at the University of Münster in cooperation with the German Metrology Institute (PTB) in Braunschweig

⁶ The source voltage U_{src} is usually considered only up to 1 kV which can be measured precisely enough using a voltmeter only.

[Thü09, Bau13]. The dividers feature many high precision resistors selected according to their warm-up resistance change. The resistor chain, arranged in a helix structure and supported by plastic rods, is enclosed inside a stainless steel housing acting as a Faraday cup. The inside is filled with dry nitrogen gas and temperature stabilised within ± 0.1 K. Besides, K65 includes special “pre-aged” resistors thus further improving the long-term stability of the dividing ratio. The stability of the K65 dividing ratio at the level of < 0.1 ppm month $^{-1}$ was reported from a calibration measurement against the PTB high voltage reference divider MT100.

An additional method to monitor the retarding high voltage is to use the SKrS at a parallel MAC-E filter known as the monitor spectrometer (MoS) [Erh14]. In the SKrS the $^{83\text{m}}\text{Kr}$ is generated in place from ^{83}Rb which is ion implanted into a solid conducting substrate. The krypton retention in the substrate is high enough ($> 90\%$) so that the origin of electron emission is well defined. Owing to the long half-life of ^{83}Rb such a source does not require any maintenance and is thus suitable for continuous two-month monitoring of the high voltage stability. The MoS retarding electrode is kept at the same voltage U as the main spectrometer and the energy of K-32 electrons of $^{83\text{m}}\text{Kr}$ is continuously measured by stepping of the SKrS bias voltage. The electron integral spectrum is made by utilizing the voltage reading of the divider-voltmeter setup and the SKrS bias voltage. Provided that the electron energy is stable in time, any change of the observed conversion electron energy points to a possible instability of the high voltage system of KATRIN.

The MoS cannot address the issue of the main spectrometer work function $\varphi_{\text{sp}}^{\text{MS}}$. Also the conversion electron energy measurements are influenced by the MoS work function $\varphi_{\text{sp}}^{\text{MoS}}$ only, because in the case of the SKrS the source work function $\varphi_{\text{src}}^{\text{SKrS}}$ cancels out. The krypton atom, which emits the conversion electron, is situated in the substrate lattice representing the solid electron source. In this case, the binding energy which we denote as B_i^{Fermi} is related to the substrate Fermi level. The electron kinetic energy is given by Eq. (3.41) where, however, $B_i^{\text{vac}} = B_i^{\text{Fermi}} + \varphi_{\text{src}}^{\text{SKrS}}$. Thus we can write

$$E_i = E_\gamma + E_{\gamma, \text{rec}} - E_{e, \text{rec}} - (B_i^{\text{Fermi}} + \varphi_{\text{src}}^{\text{SKrS}}). \quad (3.51)$$

By inserting this into Eq. (3.44) for E we obtain

$$E_i^{\text{SKrS}} \equiv q(U - U_{\text{src}}) = E_\gamma + E_{\gamma, \text{rec}} - E_{e, \text{rec}} - B_i^{\text{Fermi}} - \varphi_{\text{sp}}^{\text{MoS}}. \quad (3.52)$$

Two complications with the SKrS arise as a consequence of inevitable solid-state effects. Firstly, the conversion line shape does not follow the simple form in Eq. (3.42) which makes interpretation of the observed spectrum difficult. Moreover, the electron binding energy which influences the emitted electron energy, see Eq. (3.41), is itself influenced by the environment of the $^{83\text{m}}\text{Kr}$ atom and thus the long-term stability of the electron energy is by no means obvious. The pilot studies of the SKrS were done in [Zbo11, Zbo13] and a promising result as for the energy stability was obtained but several questions regarding the source optimization were raised. The SKrS for KATRIN is addressed in Chapter 5.

An alternating current (AC) noise with high enough frequency (e.g. the typical 50 Hz) is not observable by the divider-voltmeter setup due to the integration time of the voltmeter, which is at the order of a few seconds. As will be discussed later, the MoS is not

usable to observe AC noise of the high voltage either unless its root mean square (RMS) is at the order of several tenths of eV. But Eq. (3.40) shows that the requirement on the RMS for the AC noise is more stringent. To reduce the AC noise an active post-regulation utilizing a high-pass filter and a triode shunt will be applied.

4 Conversion electron line shape of the solid $^{83\text{m}}\text{Kr}$ source

The solid $^{83\text{m}}\text{Kr}$ source (SKrS) as a nuclear standard emits internal conversion electrons whose energy is analysed by the MAC-E filter monitor spectrometer (MoS) in order to assess the KATRIN high voltage stability. The electron energy spectrum is obtained by recording the electron count rate in discrete voltage steps similarly as the β -spectrum is obtained at the main spectrometer. In order to extract the electron line position E_i the spectrum is least-squares fitted by an assumed line shape with several free parameters (model function), where the line position E_i is one of the parameters. Therefore, the line shape and the spectrometer transmission function are needed to obtain a reliable result. Besides, it is possible to obtain a relative shift of a spectrum with respect to another spectrum from their comparison. In such a case, neither the line shape nor the transmission function are needed. On the other hand, if due to solid-state effects the line shape of the two spectra is different, the comparison may give wrong results.

In this chapter, the monitor spectrometer and its properties are briefly reviewed [Erh14] and the MoS transmission function is discussed in detail. The least-squares method and the concept of obtaining the fitted parameter uncertainties are introduced. The actual observed electron line shape of the SKrS is described in relation to the expected Lorentzian shape. A new conversion line shape description is introduced [Sle13] and compared to the approach previously utilized in the work [Zbo11] where the first SKrS samples were investigated. Moreover, a method based on comparison of two spectra is described and its performance assessed. Conclusions regarding the recommended approach for SKrS electron spectra analysis at the MoS are drawn.

4.1 The monitor spectrometer

The monitor spectrometer (MoS) is the MAC-E filter of the former Mainz neutrino mass experiment which has been simplified, refurbished and reassembled in KIT for the KATRIN experiment [Erh14]. It is a stainless steel vessel with the length of about 3 m and the radius of 0.5 m equipped with a set of stainless steel retarding electrodes and a set of super- and normal-conducting coils to create and shape the guiding magnetic field. The MoS has a similar energy resolution as the KATRIN main spectrometer. The difference in size is due to the smaller magnetic flux that has to be transported from the electron source through the analysing plane to the detector.

The cross-section of the MoS along its symmetry axis and the electric and magnetic field configuration are shown in Fig. 4.1 using cylindrical coordinates. The field calcu-

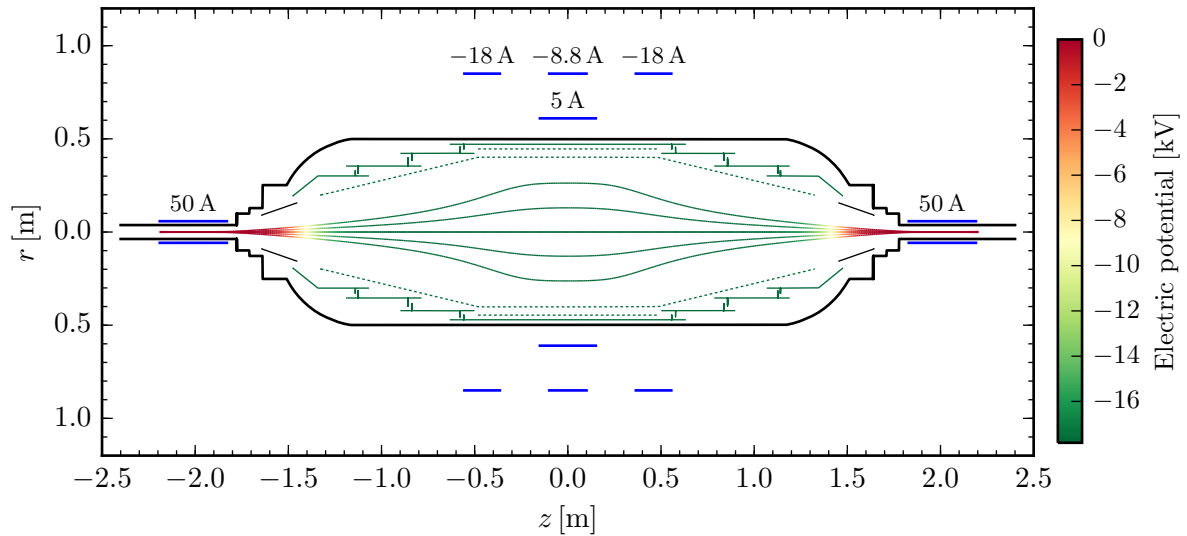


Figure 4.1: The cross-section of the monitor spectrometer and its electric and magnetic field configuration in cylindrical coordinates. Shown is the vessel hull and the ground electrodes, both on ground potential (black), the solid electrodes (solid lines) and the wire electrodes (dotted lines), both on retarding potential (see the color scale), and the two superconductors and a set of air coils (blue) with the value of the electric current indicated. The magnetic field lines, which end up at the axial distance $z = \pm 2.2$ m and at the radii $r = 0$ mm, 1.5 mm and 3 mm, are also shown. The color-coded electric potential along the field lines is visualized.

lations were performed using the KATRIN simulation package Kassiopeia [Gro15]. Two superconducting solenoids each with about 36 500 windings create an axially symmetric magnetic field. The field close to the analysing plane in the center of the spectrometer is shaped by a set of normal conducting coils (air coils), the low field correction system (LFCS), each with a few tens of windings [Thü07]. The maximal magnetic field is $B_{\text{max}} = 6.014$ T and the magnetic field on axis at the analysing plane amounts to about $B_{\text{min}} = 0.35$ mT. Thus, the relative energy resolving power, which follows from Eq. (2.7), reads

$$\frac{E}{\Delta E} = 17\,180. \quad (4.1)$$

This corresponds to $\Delta E = 1.04$ eV at the K-32 energy of $E = 17.83$ keV.

The electrode system comprises the cylindrical and conical solid electrodes and the wire electrodes, which are all on the high retarding potential, and the ground electrode which is on ground potential together with the vessel hull. A second outer wire electrode is present in the central part of the spectrometer. In the original setup a potential difference of a few hundred volts could be set between the inner and outer wire electrode and the solid electrode to suppress cosmic-induced background. At the MoS electron sources involving high count rates are measured so such a setting is no longer necessary. Thus, all the solid and wire electrodes are kept on the same potential.

The high voltage (HV) is supplied either from a local power supply (standalone mode) or, using a remotely controlled switch, from the main spectrometer HV system (parallel mode). The HV is scaled down by the high-precision KATRIN K35 and K65 dividers¹ and read out by two precise voltmeters². The electron source can be biased by a separate power supply with the potential of up to -1 kV and read out using a commercial divider and voltmeter³. The integral spectrum acquisition is done either by stepping the voltage at the retarding electrode or at the source. In the parallel mode only the latter approach is possible.

To preserve axial symmetry the Earth magnetic field of about 50 μ T, which is not considered in Fig. 4.1, is compensated by two coil sets, the Earth magnetic compensation system (EMCS). The EMCS produces both a horizontal and a vertical magnetic field perpendicular to the spectrometer axis. The winding follows a cosine-distributed electric current pattern with four windings for each set. A series of magnetic field measurements was carried out in order to find the optimal current settings of the EMCS. However, a different setting was found which gives a more favorable signal-to-background ratio in the conversion electron measurements. Such an empirical setting, which may potentially compensate imperfections of the superconducting magnets alignment [Erh14], was used for most of the measurements discussed in this work.

A CAD drawing of the MoS is shown in Fig. 4.2. The electron source is situated in the vacuum chamber on the left side in front of the super-conducting solenoid (grey housing with green dome). The detector is placed downstream on the right side behind the second solenoid in a similar way. Around the vessel in the center of the spectrometer a set of four axial copper air coils on aluminum formers is mounted (LFCS). The EMCS is realized with insulated, horizontal copper pipes (both in light green). The position of both the source and the detector can be adjusted in three dimensions using cross tables.

The spectrometer vessel is kept under ultra-high vacuum (UHV) which is maintained by a set of turbomolecular pumps (TMPs). The vessel, the source chamber and the detector chamber are each equipped with a TMP. The pump at the detector is utilized only in MoS service periods because its operation disturbs the detector electronics. Thus, during measurements the detector chamber is pumped out passively through a gate valve to the vessel. The three pumps are connected to an intermediate TMP which is backed by a scroll pump. The fore-vacuum is enlarged by a large buffer volume to reduce the running time of the scroll pump. The detector chamber can be heated up to only about 60 $^{\circ}$ C because it contains custom-made soldered electronics. The source chamber and the vessel can be baked out to 120 $^{\circ}$ C and 200 $^{\circ}$ C, respectively, in order to achieve the UHV conditions and to maintain good surface conditions of the retarding electrode, which greatly influence its work function. The imperfect detector vacuum condition is improved by a cool trap effect which occurs due to cooling of the detector and its electronics by a copper cold finger that is immersed in liquid nitrogen outside the vacuum.

¹ The dividing ratios for the K35 and K65 were measured to be 1972.4566(39) and 1818.1078(36), respectively, at the end of 2011 [Bau14].

² The power supply is the FuG HCN140M-35000 and the voltmeters are the Fluke 8508A.

³ Power supply: FuG MCP 14-1250, divider: Fluke 752A, voltmeter: Agilent 3458A.

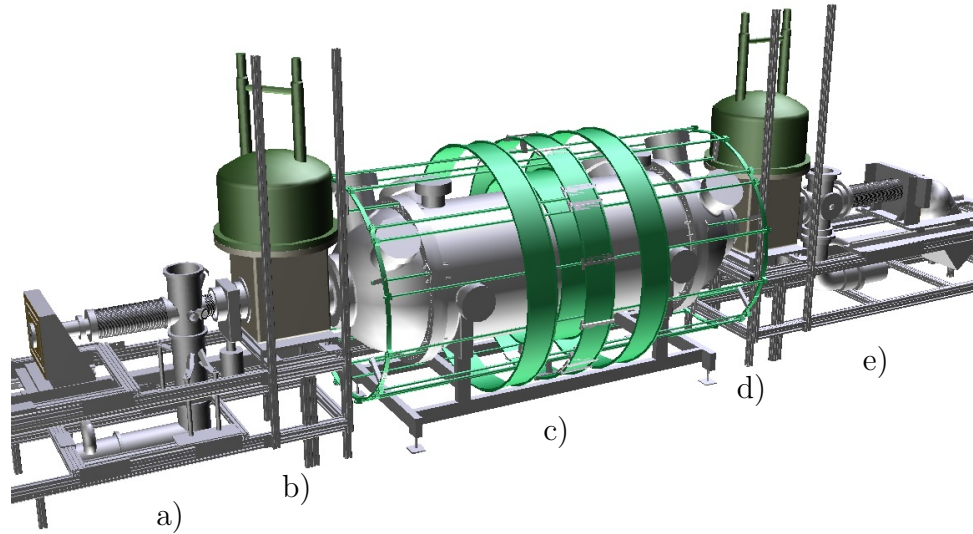


Figure 4.2: A CAD drawing of the monitor spectrometer. Shown are the a) source chamber, b) source-side superconducting magnet, c) vessel with LFCS and EMCS, d) detector-side superconducting magnet and e) detector chamber.

The electron detector, which is utilized for counting the electrons analysed for energy by the MAC-E filter, is a circular silicon PIN-diode with the sensitive area of 1.5 cm^2 and a depletion depth of 0.5 mm . There are four auxiliary square detectors (windowless PIN-photo diodes) around the central one which are utilized for centering of the electron beam. Both the detector and the first pre-amplifier stage are situated inside the vacuum chamber on a copper-beryllium rod which is attached to the copper cold finger. By this setup the detector temperature stabilizes at about $-45\text{ }^\circ\text{C}$.

The electron source, the solid $^{83\text{m}}\text{Kr}$ source, is a substrate (a thin foil) implanted with the generator ^{83}Rb . The maximal width of the substrate amounts to 12 mm . The source holder is a ceramic disk which is mounted on an insulated tip of a long tube welded into a base flange. The flange is mounted in the moveable cross table. On the source holder there are slots for up to four sources. In this way, the source intended for measurement can be shifted onto the spectrometer axis by moving the cross table without breaking vacuum. Each slot is individually connected with an insulated cable to a feedthrough which is either grounded or biased by the source power supply.

The manipulation of the cross table is carried out manually. In order to improve the precision and speed of changing the position the cross table is equipped with linear position sensors with sub-mm precision. The sensors are read out and the position values are displayed electronically. Each source is positioned close to its nominal coordinates which are usually established experimentally by searching for the highest electron rate when the spectrometer retarding voltage is set for electron transmission. In such a way, the reproducibility of the source position is better than 0.2 mm .

4.1.1 Integral spectrum acquisition

Retarding energy

The retarding energy, or equivalently the retarding potential, is obtained by measuring the high voltage applied to the retarding electrodes. The high voltage U of up to -35 kV is firstly scaled down by the high-precision voltage divider to a voltage of only up to -16 V. Then such a voltage is measured by a commercial high-precision voltmeter. By knowing the dividing ratio M the applied high voltage can be deduced from the voltmeter measurement U_{meas} . Following Eq. (3.49) the retarding energy can be written as

$$qU = MqU_{\text{meas}}. \quad (4.2)$$

In case the source is biased additionally the source voltage U_{src} is measured and the retarding energy becomes

$$qU = MqU_{\text{meas}} - M_{\text{src}}qU_{\text{src}}, \quad (4.3)$$

where M_{src} is the dividing ratio of the source voltage divider.

The voltmeter integration time for the required $7\frac{1}{2}$ -digit resolution amounts to about 2 s. In combination with the used (temporary) readout software and the KATRIN network communication, the voltmeter reading is available at every 3 s to 4 s [Kra12]. Since the measurement time per single retarding voltage setting is at least a couple of tens of seconds, several voltmeter readings are collected for the setting. Thus, the measured value U_{meas} is taken as the average of the voltmeter readings U_i within the single-voltage time interval. Similarly, its uncertainty $\sigma(U_{\text{meas}})$ is given by the estimated standard deviation of the values divided by square root of the number of values N , i.e.

$$U_{\text{meas}} = \frac{1}{N} \sum_{i=1}^N U_i, \quad (4.4a)$$

$$\sigma(U_{\text{meas}}) = \sqrt{\frac{1}{N(N-1)} \sum_{i=1}^N (U_i - U_{\text{meas}})^2}. \quad (4.4b)$$

The basic form in Eqs. (4.2) and (4.3) becomes more complex due to imperfections of the divider and voltmeter. Concerning the divider, its dividing ratio is generally not constant in time. To the first order the dividing ratio $M(t)$ as a function of time t can be expressed as

$$M(t) = M_0 \left(1 + \underbrace{\frac{1}{M_0} \frac{\partial M}{\partial t}}_{=m_t} (t - t_0) \right), \quad (4.5)$$

where M_0 is the dividing ratio at $t = t_0$ and m_t is the drift of the dividing ratio in relative units, i.e. usually ppm month⁻¹. Similarly, the dividing ratio is not constant over the range of applicable voltages. To the first order the dividing ratio $M(U)$ as a function of

the applied voltage U can be expressed as

$$M(U) = M_{\text{ref}} \left(1 + \underbrace{\frac{1}{M_{\text{ref}}} \frac{\partial M}{\partial U}}_{=m_U} (U - U_{\text{ref}}) \right), \quad (4.6)$$

where M_{ref} is the dividing ratio at the reference voltage U_{ref} and m_U is the voltage dependence of the dividing ratio in relative units, i.e. usually ppm kV^{-1} . Uniting the reference ratio M_{ref} and the initial ratio M_0 , we thus obtain in the first order of the corrections

$$M(t, U) = M_0 [1 + m_t(t - t_0) + m_U(U - U_{\text{ref}})]. \quad (4.7)$$

Typically, the constants are very small, $|m_t| < 1 \text{ ppm month}^{-1}$ and $|m_U| \ll 1 \text{ ppm kV}^{-1}$ [Thü09, Bau13].

Concerning the voltmeter, its reading is imperfect because the voltmeter has a certain offset U_{offset} , i.e. the voltage shown when the voltmeter contacts short-circuited, and a scale factor K which is different from one. The voltage U_{meas} which is at the input of the voltmeter, i.e. output of the voltage divider, reads [Thü07]

$$U_{\text{meas}} = K(U_{\text{read}} - U_{\text{offset}}), \quad (4.8)$$

where U_{read} is the voltmeter reading. Since the correction factors U_{offset} and, especially, K may depend on time, the voltmeter calibration is carried out on a regular basis by means of a reference -10 V power supply. Typically, in absolute values the offset U_{offset} is at the order of μV or less and the scale factor difference from one is at the order of a few 10^{-5} or less.

Using Eqs. (4.7) and (4.8) in Eq. (4.2) we obtain for the retarding energy

$$qU = qK(U_{\text{read}} - U_{\text{offset}})M_0 [1 + m_t(t - t_0) + m_U(M_0 U_{\text{read}} - U_{\text{ref}})], \quad (4.9)$$

where the divider input voltage U in Eq. (4.7) was approximated by $M_0 U_{\text{read}}$, which can be safely done due to the small size of m_U . The dividing ratio can be considered constant within a single conversion line measurement due to smallness of m_t and m_U . The correction term in the square bracket in Eq. (4.9) is then applied to the conversion line position obtained from the least-squares fit if needed.

It is worth pointing out how an originally unrecognized change of the dividing ratio would appear in terms of the observed electron energy during monitoring. Consider that the spectrometer retarding energy is set so that the electrons just pass the electrostatic barrier, i.e. the electron energy equals the retarding energy qU . At such a situation the actual dividing ratio M will produce the reading qU_{read} on the voltmeter, i.e.

$$qU = MqU_{\text{read}}. \quad (4.10)$$

Consider now that for some reason the dividing ratio M changes and the new value is M' . Then setting the spectrometer to transmission again for the same electron energy qU , the value M' produces the voltmeter reading qU'_{read} , i.e.

$$qU = M'qU'_{\text{read}}. \quad (4.11)$$

However, since the change of the dividing ratio is unrecognized, in calculation of the retarding energy we use the old value M together with the new reading to derive that the electron energy appears as

$$qU' = MqU'_{\text{read}} \quad (4.12)$$

which is different from qU . Assuming that the actual electron energy is constant, we conclude that the observed electron energy qU' is different due to a changed dividing ratio and from Eqs. (4.11) and (4.12) we calculate that the new dividing ratio has to be

$$M' = M \frac{qU}{qU'}. \quad (4.13)$$

This equation shows that a higher observed electron energy $qU' > qU$ has to be interpreted as a smaller dividing ratio $M' < M$ and vice versa.

Evidently, the ratio qU/qU' has to be the same regardless of the conversion line if the line position is constant. Therefore, the difference $\Delta qU = qU' - qU = qU(M/M' - 1)$ is directly proportional to the conversion line energy qU . On the other hand, if the spectrometer work function φ_{spec} changes the difference ΔqU will be common for all the lines according to Eq. (3.44). The equation shows that a higher observed electron energy has to be interpreted as a decreased work function and vice versa. Thus, the effect from change of the dividing ratio and the work function can in principle be distinguished by measuring the energy of at least two remote conversion electron lines, e.g. L₃-32 together with K-32.

Electron count rate

At each retarding energy in the integral spectrum a detector spectrum in 2048 analog-to-digital convertor (ADC) channels is obtained as shown in Fig. 4.3. The centroid of the conversion electron peak is seen at the channel of about 140 with the FWHM of about 28 channels, i.e. 3.5 keV. The noise begins at channel of around 50 which corresponds to the energy of 6.2 keV. Thus, the noise unfortunately disturbs a large part of the peak when the lowest energy L conversion lines at 7.4 keV to 7.7 keV are measured which effectively reduces the spectrometer luminosity (only part of the conversion line rate is obtained). The peak at around channel 1805 comes from a pulser which is utilized for dead time correction. The total electron counts N_e and pulser counts N_p are derived by summing up counts in channel within automatically selected intervals around the peaks which are marked in the Fig. 4.3. The peak maximum is found using the `TSpectrum::Search` method within the framework `ROOT` [Bru97], for details see e.g. [Mar67, Mor00, Sil96]. The interval is then determined by a $\pm 3\sigma$ interval, where σ is the width of a Gaussian function fitted in the predefined range (24 channels on each side) around the peak maximum (see also [Hau13]).

The dead time correction follows from the assumption that the fraction of events lost from the electron peak equals the fraction of events lost from the pulser peak. Since the pulser frequency f is known, the true electron counts N can be calculated as

$$N = \frac{ft}{N_p} N_e, \quad (4.14)$$

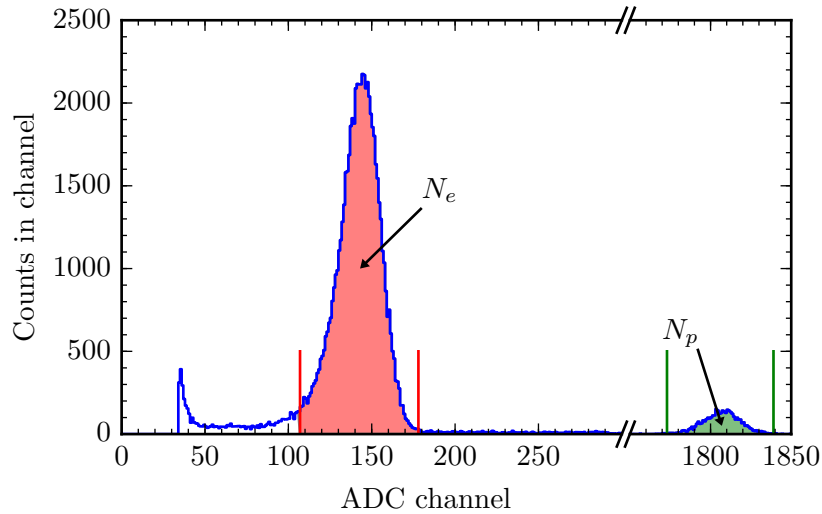


Figure 4.3: An example of the MoS detector spectrum at the retarding energy of 17 818 eV representing the transmitted no-energy-loss electrons during a measurement of the K-32 integral spectrum. The conversion line peak is seen at around channel 140 and the pulser peak at around channel 1805. The vertical lines delimit the intervals for summing the counts in channel to obtain the total observed electron counts N_e and pulser counts N_p .

where t is the measurement time spent at the particular retarding voltage. The uncertainty of N follows from the principle of propagation of the uncertainty of N_e and N_p . The electron counts follow the Poisson distribution with the variance

$$\sigma^2(N_e) = N_e \quad (4.15)$$

while the pulser counts follow the binomial distribution with the variance

$$\sigma^2(N_p) = N_p \left(1 - \frac{N_p}{ft}\right), \quad (4.16)$$

where the probability of a pulse event was estimated as $N_p/(ft)$, i.e. the expectation value N_p divided by the total number of events ft . Thus, for the variance $\sigma^2(N)$ we get the formula

$$\sigma^2(N) \approx N^2 \left[\frac{1}{N_e} + \frac{1}{N_p} \left(1 - \frac{N_p}{ft}\right) \right] \quad (4.17)$$

and the standard uncertainty can be estimated by taking the square root of Eq. (4.17). It is generally more convenient to work with count rates rather than counts. The count rate and its uncertainty are obtained by dividing the expressions for N and $\sigma(N)$ by the measurement time t . Usually, the count rate is high enough so that the possibility of $N_p > ft$ and thus negative $\sigma^2(N)$ is of little concern.

4.1.2 Transmission function

The transmission function (TF) $T_{\text{MoS}}(E, qU)$ of the MoS as a MAC-E filter is based on the analytical formula in Eq. (2.8). The formula holds for an isotropic point-like source

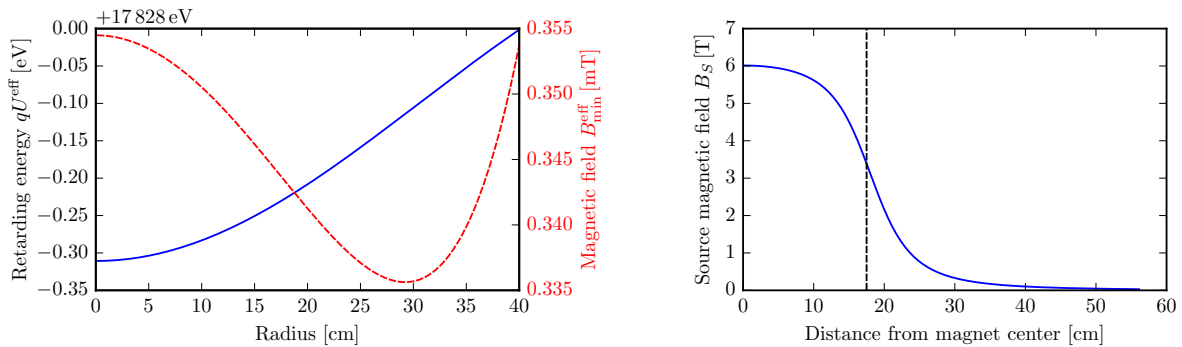


Figure 4.4: Left: Radial dependence of the MoS effective retarding energy qU^{eff} (solid) and the effective magnetic field $B_{\text{min}}^{\text{eff}}$ (dashed) at the analysing plane for the electrode retarding energy of $qU = 17828$ eV. On axis the retarding energy drops by about 0.3 eV (potential dip). The magnetic field inhomogeneity adds up to about 5%. Right: Magnetic field at the source B_S in dependence of the source position with respect to the superconducting magnet center. The dashed vertical line denotes the minimal possible distance due to space restrictions.

placed on the spectrometer symmetry axis. In practice, the source is not point-like, i.e. there are electrons which travel off axis. The retarding energy and the minimal magnetic field are not constant in the analysing plane but only axially symmetric. Therefore, an electron travelling on axis experiences different transmission than an electron travelling off axis. Since the detector is not segmented, the MoS TF is then a superposition of the basic TFs each with the relevant effective retarding energy qU^{eff} and effective minimal magnetic field $B_{\text{min}}^{\text{eff}}$.

The effective retarding energy and magnetic field at the analysing plane as a function of the radial distance from the symmetry axis are shown in Fig. 4.4 on the left. The calculation was done by Kassiopeia for the field configuration as in Fig. 4.1 and for the electrode retarding energy of $qU = 17828$ eV. The electrons at the annulus (ring) with the inner diameter r and the outer diameter $r + dr$ experience the fields $qU^{\text{eff}}(r)$ and $B_{\text{min}}^{\text{eff}}(r)$ and thus the effective TF which we denote as $T^{\text{eff}}(r; E, qU)$. Each effective TF contributes to the total TF with some weight $w(r)$ because there is generally a different number of electrons in each ring. Thus, the MoS transmission function is given by a weighted average of the effective transmission functions $T^{\text{eff}}(r; E, qU)$ with the weights $w(r)$,

$$T_{\text{MoS}}(E, qU) = \frac{\int_0^{R_A} r w(r) T^{\text{eff}}(r; E, qU) dr}{\int_0^{R_A} r w(r) dr}, \quad (4.18)$$

where R_A is the radius of the electron flux tube in the analysing plane. The factor r comes from the Jacobian of the transformation from cartesian to cylindrical coordinates.

The flux tube radius at the analysing plane $R_A(R_S)$ as a function of the radius at the

source R_S can be obtained numerically from the conservation of magnetic flux,

$$\pi R_S^2 B_S = 2\pi \int_0^{R_A(R_S)} r B_{\min}^{\text{eff}}(r) dr, \quad (4.19)$$

where we have neglected possible radial inhomogeneities of the magnetic field at the source. Neglecting the magnetic field radial inhomogeneities also at the analysing plane, we get to a good approximation

$$R_A \approx R_S \sqrt{\frac{B_S}{B_{\min}^{\text{eff}}(r=0)}}. \quad (4.20)$$

The source magnetic field B_S in dependence of the source axial position with respect to the superconducting magnet center is shown in Fig. 4.4 (calculation by Kassiopeia).

Fig. 4.5 shows examples of the MoS TF at the retarding energy of 17 828 eV for sources with different distributions of electrons in the flux tube cross section. The source magnetic field is assumed to $B_S = 1.75$ T, which corresponds to one of the usual MoS source positions of 21 cm from the magnet center. The considered distributions are:

- point-like with the basic TF assuming $qU^{\text{eff}}(0) = qU$ and $B_{\min}^{\text{eff}}(0) = B_{\min}$,
- circular and homogeneous with the weights given as $w(r) = 1$ and the flux tube radius at the source $R_S = 1.85$ mm, which corresponds via Eq. (4.20) to radius at the analysing plane of $R_A = 13$ cm,
- circular and homogeneous with $R_S = 3.7$ mm which corresponds to $R_A = 26$ cm,
- more realistic described by rotationally symmetric two-dimensional Gaussian function centered at the MoS axis with the weights proportional to

$$w(r) \propto \exp\left(-\frac{B_{\min}^{\text{eff}}(0)}{B_S} \frac{r^2}{2\sigma_S^2}\right) \quad (4.21)$$

and the Gaussian width of $\sigma_S = 1.23$ mm. In this case, we take the size of the flux tube at the analysing plane as $R_A = 40$ cm.

The consequence of the effective retarding energy dip with respect to the electrode retarding energy qU at the center of the analysing plane is a shift of the TF to negative $E - qU$ values, i.e. the transmission occurs for electrons which have lower energy than the retarding energy at the electrode. The effect of inhomogeneous fields and the non-zero flux tube size is broadening of the TF at the edges and the larger the flux tube is, the more significant this effect becomes. Thus, having a larger flux tube effectively deteriorates the spectrometer energy resolution as compared to a smaller one. The width of the Gaussian distribution for the more realistic electron distribution was chosen such that $3\sigma_S = 3.7$ mm, i.e. most of the electrons are in the area of the same size as for the homogeneous distribution with $R_S = 3.7$ mm, for comparison.

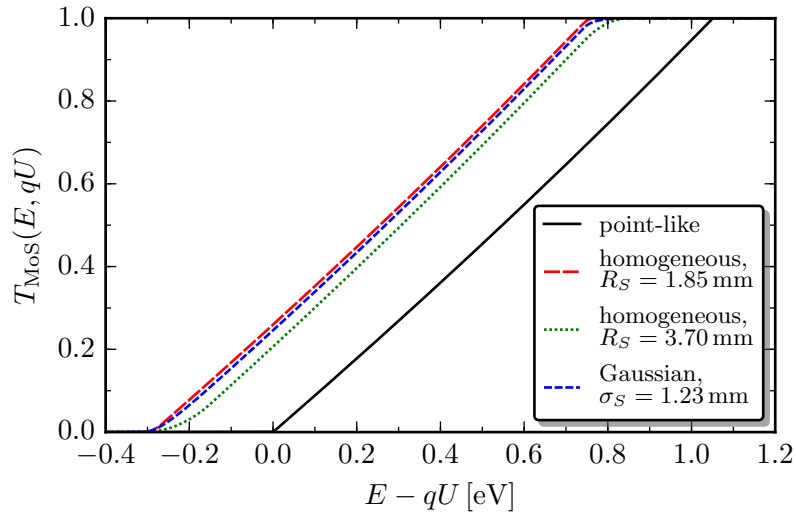


Figure 4.5: Transmission function of the monitor spectrometer for different distributions of electrons in the flux tube cross section at the electrode retarding energy of $qU = 17\,828$ eV.

Due to the larger width of the most interesting $^{83\text{m}}\text{Kr}$ conversion lines the exact shape of the TF is not critical for a reasonable description of the measured spectrum. However, it is essential if the conversion line energy is compared from measurements of sources with significantly different distribution of electrons in the flux tube cross section. Similarly, the accurate TF is necessary for analysis of measurements which were done with the same source placed at different positions with respect to the magnet. Taken from the opposite side, such a comparison represents a check for understanding of the MoS transmission properties. In such a case, the expression in Eq. (4.18) can be utilized if the real flux tube electron distribution is known. This issue will be addressed later in Chapter 5.

In the MoS measurement analysis it is customary to consider the TF shifted so that the transmission starts for $E = qU$. If absolute electron energies are needed, the values obtained from the least-squares fit can be corrected afterwards by adding to it the value of the potential dip $qU^{\text{eff}}(0)$.

4.2 The least-squares method

In order to obtain the most likely line position from the measured spectrum the least-squares method is utilized. The approach can be described as follows [Har98]. Let the set of count rates $\mathbf{M} = \{M_1, M_2, \dots, M_n\}$ vs. the set of retarding energies $q\mathbf{U} = q\{U_1, U_2, \dots, U_n\}$ be the measured electron energy spectrum. The likelihood function

$$\mathcal{L}(\mathbf{p}) = \prod_{i=1}^n p(M_i, qU_i; \mathbf{p}) \quad (4.22)$$

expresses the probability of obtaining the data sample \mathbf{M} given the parameters \mathbf{p} when each value M_i is an independent random variable distributed according to the probability

density function $p(M_i, qU_i; \mathbf{p})$. The optimal values of the parameters $\tilde{\mathbf{p}}$ are such that the likelihood function is maximized or, more conveniently, the negative log-likelihood function

$$-\ln \mathcal{L}(\mathbf{p}) = -\sum_{i=1}^n \ln p(M_i, qU_i; \mathbf{p}) \quad (4.23)$$

is minimized.

Furthermore, let $S(qU; \mathbf{p})$ be the model function of the integral spectrum in dependence of the retarding energy qU and the parameters \mathbf{p} . Let us assume that the values M_i are distributed independently of each other according to the normal distribution

$$p(M_i, qU_i; \mathbf{p}) = \frac{1}{\sqrt{2\pi\sigma_i^2}} \exp\left(-\frac{[M_i - S(qU_i; \mathbf{p})]^2}{2\sigma_i^2}\right). \quad (4.24)$$

Then the negative log-likelihood becomes

$$-\ln \mathcal{L}(\mathbf{p}) = \frac{1}{2} \sum_{i=1}^n \frac{[M_i - S(qU_i; \mathbf{p})]^2}{\sigma_i^2}, \quad (4.25)$$

where the terms independent of \mathbf{p} were dropped since constant shifts of the likelihood function are irrelevant for determination of $\tilde{\mathbf{p}}$. The sum

$$\chi^2(\mathbf{p}) = \sum_{i=1}^n \frac{[M_i - S(qU_i; \mathbf{p})]^2}{\sigma_i^2} \quad (4.26)$$

is called the ‘‘chi-square’’ function. Thus, the maximum of the likelihood function $\mathcal{L}(\mathbf{p})$ corresponds to the minimum of $\chi^2(\mathbf{p})$.

In general, besides M_i also each retarding voltage qU_i is a random variable which is distributed according to some probability density function with the variance $\sigma_{qU_i}^2$. Since the retarding voltage and the count rate are related through the function $S(qU; \mathbf{p})$, the variance σ_i^2 in the denominator inside the sum in Eq. (4.26) can be enlarged by the retarding voltage variance $\sigma_{qU_i}^2$ using the principle of propagation of uncertainty as

$$\sigma_i^2 = \sigma_{M_i}^2 + \left(\frac{\partial S}{\partial(qU)}\right)_{qU=qU_i}^2 \sigma_{qU_i}^2, \quad (4.27)$$

where we have denoted the uncertainty of the count rate as $\sigma_{M_i}^2$. Nevertheless, at the MoS the contribution from the voltage uncertainty is usually small, $(\partial S/\partial(qU))_{qU=qU_i}^2 \sigma_{qU_i}^2 \ll \sigma_{M_i}^2$.

4.2.1 Parameter uncertainties

The uncertainties of the parameters \mathbf{p} can be obtained using the so-called likelihood-ratio test [Fel71]. Let us form the null hypothesis by stating that the found value of a selected

parameter \tilde{p}_j is actually the true value of the parameter p_{j_0} . The corresponding likelihood function is denoted as $\mathcal{L}(p_{j_0}, \tilde{\mathbf{p}}')$, where $\tilde{\mathbf{p}}'$ is the vector of the remaining parameters such that $\mathcal{L}(p_{j_0}, \tilde{\mathbf{p}}')$ is maximal. The ratio of the likelihood functions $\mathcal{L}(\tilde{\mathbf{p}})$, in which generally $\tilde{p}_j \neq p_{j_0}$, and $\mathcal{L}(p_{j_0}, \tilde{\mathbf{p}}')$ is constructed as

$$\lambda_0 = 2 \ln \frac{\mathcal{L}(\tilde{\mathbf{p}})}{\mathcal{L}(p_{j_0}, \tilde{\mathbf{p}}')} = 2 [\ln \mathcal{L}(\tilde{\mathbf{p}}) - \ln \mathcal{L}(p_{j_0}, \tilde{\mathbf{p}}')]. \quad (4.28)$$

If the number of measurement points n is large enough, the ratio is statistically distributed approximately according to the chi-square distribution χ_1^2 with 1 denoting the one degree of freedom. Thus, the ratio λ_0 can be used as a measure of the statistical significance of the null hypothesis. The probability $P(\lambda \geq \lambda_0)$ of obtaining the ratio λ which is at least λ_0 or larger is given by

$$P(\lambda \geq \lambda_0) = \int_{\lambda_0}^{\infty} \chi_1^2(x) dx = 1 - \int_0^{\lambda_0} \chi_1^2(x) dx. \quad (4.29)$$

Given an initially chosen significance level α , we can reject the null hypothesis if the probability of obtaining λ or higher is smaller than α , i.e. $P(\lambda \geq \lambda_0) \leq \alpha$, and cannot reject it if otherwise.

Since we do not know the true value p_{j_0} we have to consider all possible values p_j and calculate the likelihood ratio according to Eq. (4.28), which we denote as $\lambda_{(0)}$, for each of the values p_j . By the above described principle we cannot reject those values for which $P(\lambda \geq \lambda_{(0)}) > \alpha$. In such a way, the so-called $100 \cdot (1 - \alpha) \%$ confidence interval for the parameter p_j is constructed. The interval covers the true value of the parameter with the probability of $(1 - \alpha)$. The limiting values p_j^\pm , $p_j^- < p_j^+$, are such that $P(\lambda \geq \lambda_{(0)}) = \alpha$, i.e.

$$\int_0^{\lambda_{(0)}} \chi_1^2(x) dx = 1 - \alpha. \quad (4.30)$$

This equation can be written as

$$-\ln \mathcal{L}(p_j^\pm, \tilde{\mathbf{p}}') = -\ln \mathcal{L}(\tilde{\mathbf{p}}) + \frac{Q(1 - \alpha)}{2}, \quad (4.31)$$

where $Q(1 - \alpha)$ is the inverse function of the l.h.s. of Eq. (4.30), which is a function of $\lambda_{(0)}$, and is called the quantile function of the χ_1^2 distribution. In terms of the chi-square function, Eq. (4.26), this condition translates into

$$\chi^2(p_j^\pm, \tilde{\mathbf{p}}') = \chi^2(\tilde{\mathbf{p}}) + Q(1 - \alpha). \quad (4.32)$$

The uncertainties $\sigma_A^\pm(\tilde{p}_j) = p_j^\pm - \tilde{p}_j$ shall be referred to as the positive and the negative asymptotic uncertainty. It is worth noting that the quantile function values $Q(1 - \alpha)$ corresponding to the confidence levels of the $\pm n\sigma$ intervals of the normal distribution are given simply as n^2 , e.g. for the $\pm 1\sigma$ and $\pm 2\sigma$ intervals with the confidence levels of 68.27% and 95.45% we have $Q(0.6827) = 1$ and $Q(0.9545) = 4$, respectively.

For a larger number of parameters the search for the confidence intervals by numerically solving Eq. (4.32) may be time-consuming. In such a case approximate parameter uncertainties can be obtained from the following. Asymptotically (for a large n), the optimal parameters $\tilde{\mathbf{p}}$ follow the multivariate normal distribution around their true values with the covariance matrix Σ . Thus, the limits p_j^\pm of the $100 \cdot (1 - \alpha) \%$ confidence interval for the specific parameter p_j are given as

$$p_j^\pm = \tilde{p}_j \pm \left| z \left(\frac{\alpha}{2} \right) \right| \sigma_P(\tilde{p}_j), \quad (4.33)$$

where $z(\alpha/2)$ is the quantile function of the normal distribution at $\alpha/2$ and $\sigma_P(\tilde{p}_j)$ is the square root of the variance $\sigma_P^2(\tilde{p}_j)$, i.e. the element Σ_{jj} of the covariance matrix Σ . E.g. for a 95% confidence interval we get $|z(0.05/2)| = 1.96$. It can be shown that the covariance matrix can be estimated by the inverse of the second-derivative matrix (the Hessian matrix) of the negative log-likelihood function,

$$\Sigma = H^{-1}, \quad (4.34)$$

where $H_{kl} = -\partial^2 \ln \mathcal{L} / (\partial p_k \partial p_l) |_{\mathbf{p}=\tilde{\mathbf{p}}}$. In such a case the uncertainty $\sigma_P(\tilde{p}_j)$ shall be referred to as the parabolic uncertainty.

4.2.2 Algorithm for search of χ^2 function minimum

In all but simple cases it is not possible to obtain the optimal values of the parameters \mathbf{p} analytically and a numerical search has to be performed. For this purpose the `Minuit` [Jam75] library of the software package `ROOT` [Bru97] is utilized. The minimization algorithm is based on the so-called quasi-Newton method. Starting from an initial guess \mathbf{p}_0 the parameters in the $(k + 1)$ -th iteration are given as

$$\mathbf{p}_{k+1} = \mathbf{p}_k - H^{-1} \nabla \chi^2(\mathbf{p}_k). \quad (4.35)$$

The right term is called the Newton step and follows from the requirement that the gradient of the χ^2 function, approximated in a second-order Taylor series, is zero. The iterations are stopped if the change of the χ^2 function decreases to a sufficiently small amount. In the quasi-Newton method H is not computed directly but is approximated from the gradient along the way to the minimum. `Minuit` relies on the Davidon-Fletcher-Powell updating formula [Noc99] for the approximation of H .

4.3 Observed line shape

The model function $S(qU; \mathbf{p})$ for the chi-square function in Eq. (4.26) follows from the integral shape of Eq. (2.9),

$$S(qU; \mathbf{p}) = \int_{-\infty}^{+\infty} f(E; \mathbf{p}) T(E, qU) dE + B(qU; \mathbf{p}), \quad (4.36)$$

where $T(E, qU)$ is the MoS transmission function (the index “MoS” is dropped out for simplicity), $f(E; \mathbf{p})$ is the shape of the conversion electron line and $B(qU; \mathbf{p})$ is the background term.

The background originates firstly from the partial transmission of higher energy lines (together with their loss-energy parts) and secondly from secondary electrons emitted from the retarding electrodes after being hit by cosmic muons. At the MoS the first contribution is by far the most dominant except for the highest energy conversion line N_{2,3}-32 (close doublet of N₂-32 and N₃-32). The background rate changes with the retarding energy slowly enough that the term $B(qU; \mathbf{p})$ at the interval relevant for the least-squares fit is at most a linear function of qU .

The expected shape of the conversion line is given by the Lorentzian function, cf. Eq. (3.42),

$$f_L(E; a, E_i, \Gamma_i) = a \frac{1}{(E - E_i)^2 + \Gamma_i^2/4}, \quad (4.37)$$

where a is the amplitude. This shape is symmetric around the centroid E_i . However, during the pilot studies of the SKrS [Zbo11, Zbo13] it turned out that the line shape is broadened and asymmetric at the lower energy side with respect to the centroid. The broadening and asymmetry are significant in a way that they cannot be simply neglected in precise determination of the line position. Moreover, the asymmetry cannot originate from the electron energy loss due to inelastic scattering with the substrate atoms. The reason is, as will be shown later, the energy loss distribution has its maximum at around 20 eV below the line position and is only subdominant in the region close to the elastic (no energy loss) peak.

An example of the K-32 experimental spectrum is shown in Fig. 4.6. The source substrate was platinum and the implantation energy amounted to 10 keV (the source designation is Pt-10-1). It was acquired with fine energy steps of about 0.2 eV and 20 s measurement time in each point. The spectrum was fitted utilizing Eq. (4.37) and a constant background with a single free parameter $B(qU; \mathbf{p}) = b_0$. The Lorentzian width was fixed to $\Gamma_K = 2.7$ eV. The fitted curve does not follow the measured spectrum. Deviations are seen at both sides around the inflection point and also at the lowest energies. Fitting also the width parameter Γ_K does not significantly improve the result.

The broadening could be the consequence of unaccounted Doppler effect, high voltage fluctuations [Zbo13] and possible changes of the electron binding energy in the krypton atoms caused by existence of multiple non-equivalent implantation sites within the substrate [Cit74, Lah11]. It can be reasonably well described by a Gaussian function resulting in the so-called Voigt function, which is a convolution of the Lorentzian and the Gaussian functions,

$$V(E) = \int_{-\infty}^{+\infty} G(E - y)I(y) dy, \quad G(E) = \frac{1}{\sqrt{2\pi}\sigma^2} \exp\left(-\frac{E^2}{2\sigma^2}\right). \quad (4.38)$$

To account for the asymmetry a second subdominant Voigt function being separated by a few eV from the dominant one was assumed in [Zbo11]. A doublet of lines was motivated by possible existence of the krypton atoms in two different environments, the

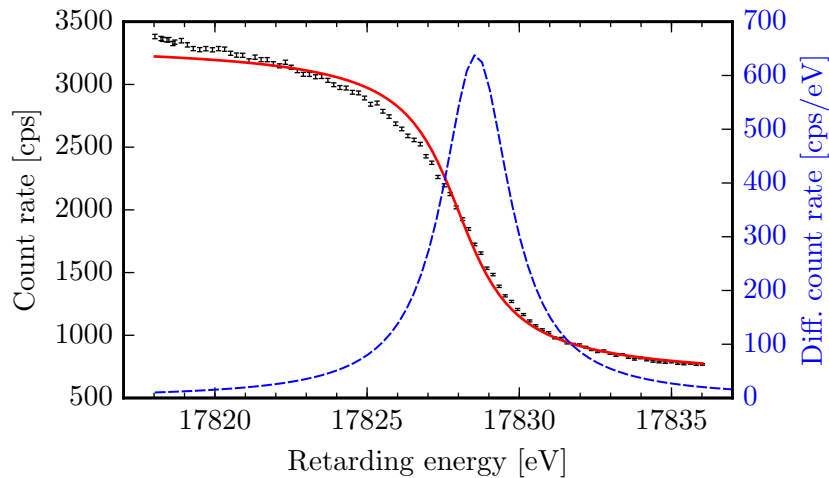


Figure 4.6: The experimental K-32 conversion electron line and its least-squares fit by the Lorentzian function. The differential line corresponding to the fit result is also shown. The measured shape is broader and asymmetric at the lower energy side.

substrate itself and a surface contamination layer. The line shape f_{VD} in the Voigt doublet (VD) approach can then be written as

$$f_{VD}(E; a, a', E_i, E'_i, \sigma, \Gamma_i) = aV(E; E_i, \sigma, \Gamma_i) + a'V(E; E'_i, \sigma, \Gamma_i), \quad (4.39)$$

where a and a' are, respectively, the amplitudes of the dominant and subdominant peaks and E'_i is the line position of the subdominant peak. The widths Γ_i and σ are assumed the same for both peaks. Such a model gives reasonable fits of the spectra in a limited range at the lower energy side of the conversion line. However, the large correlation among the fitted doublet parameters introduces large uncertainty and the limited fit interval introduces fluctuations of the dominant line position among different spectra. Moreover, as will be shown later, the asymmetry does not seem to arise due to electron emission from the contamination layer.

Since for the purposes of monitoring only the relative change of the electron energy is relevant, a second complementary approach based on comparison of two measured integral spectra was pursued. In such an approach neither an assumption of the conversion line shape has to be made nor the transmission function has to be known. There are fewer free parameters in the least-squares fit compared to the VD approach. But the method can give wrong results if the line shape is subject to gradual changes which cannot be a priori excluded in a long-term measurement. In the work [Zbo13] the approach is referred to as the “cross-correlation” method in analogy to an apparently similar signal processing technique. However, strictly speaking, the cross-correlation in signal processing is defined using an integral similar to convolution [Moo00]. This may lead to the impression that a similar integral is calculated in the case of MoS measurements. Since that is not the case, we shall rather refer this approach to as the reference method.

A new conversion line shape description for the SKrS was developed [Sle13] in an

attempt to describe the observed line asymmetry as well as to reduce the fluctuations of the line position. The model is based on the function of Doniach and Šunjić [Don70], further referred to as DS, which is derived from the concept of interaction of the metallic conduction electrons with the hole created after electron emission in the final state. The description of photoelectron lines with the DS shape was studied previously [Cit73, Hüf75, Wer78, Wer82, Lei99]. To the author's knowledge there does not exist a work in which the DS line shape was used for conversion electron lines.

4.4 Doniach-Šunjić conversion line shape

The DS line shape is based on the formula derived in [Don70] which for the purposes of the MoS measurement is written as

$$f_{DS}(E; a, E_i, \Gamma_i, \alpha) = \frac{a}{\pi [(E - E_i)^2 + \Gamma_i^2/4]^{\frac{1-\alpha}{2}}} \cos \left[\frac{\pi\alpha}{2} + (1 - \alpha) \arctan \left(\frac{E - E_i}{\Gamma_i/2} \right) \right], \quad (4.40)$$

where a , E_i , and Γ_i have the same meaning as in Eq. (4.37) and α is the asymmetry parameter, $0 \leq \alpha < 1$. For $\alpha = 0$ the shape reduces to a pure Lorentzian function, Eq. (3.42). The shape thus includes the effect of lifetime on the emitted electron energy. The amplitude is defined so that it expresses the area under the DS function for $\alpha = 0$, i.e.

$$\int_{-\infty}^{+\infty} f_{DS}(E; a, E_i, \Gamma_i, \alpha) dE = a. \quad (4.41)$$

According to [Don70] the α parameter is related to the phase shift for scattering of conduction electrons from the potential of the hole created after the electron emission.

To account for possible broadening of the conversion line the DS function f_{DS} is convoluted with the normalized Gaussian function. Thus, the DSG conversion line shape f_{DSG} is given by

$$f_{DSG}(E; a, E_i, \sigma, \Gamma_i, \alpha) = \int_{-\infty}^{+\infty} G(E - y; \sigma) f_{DS}(y; a, E_i, \Gamma_i, \alpha) dy. \quad (4.42)$$

4.4.1 Numerical methods

Utilization of the conversion line shape f_{DSG} , Eq. (4.42), in the least-squares model function, Eq. (4.36), comprises numerical calculation of a two-fold convolution, i.e. schematically

$$S(qU; \mathbf{p}) = f_{DS}(E; a, E_i, \Gamma_i, \alpha) \otimes G(E; \sigma) \otimes T(E, qU) + B(qU; \mathbf{p}). \quad (4.43)$$

The value of S has to be calculated for each point of the measured spectrum in each evaluation of the χ^2 function. The function is evaluated many times during numerical calculation of the partial derivatives for the minimization step and, moreover, there are several steps before the minimum is reached. Thus, the double convolution calculation

has to be fast and at the same time accurate so that the true minimum is reached in a reasonable time and the obtained parameter uncertainties are reliable. The numerical methods described below can be used for the VD approach as well since it also comprises a two-fold convolution.

The numerical integration method of local adaptive Gauss-Legendre quadrature with the so-called Kronrod extension proved to be efficient [Pat68, Pre07]. The Gaussian quadrature is based on interpolating functions. It relies on estimation of the integral by the sum of weighted integrand values obtained at non-equidistant points (nodes). This is in contrast to the Newton-Cotes formulas, where the integrand is evaluated at equidistant points. The Gaussian quadrature is therefore generally more accurate with the same number of integrand evaluations. The nodes are the roots of polynomials $p_i(x)$ that are orthogonal over a weighting function $W(x)$,

$$\int_a^b W(x)p_j(x)p_k(x) dx = K_j\delta_{jk}, \quad (4.44)$$

where K_j is a normalization constant and δ_{jk} is the Kronecker delta. Given $W(x)$ and an integer N a set of weights w_j and nodes x_j can be found such that

$$\int_a^b W(x)f(x) dx \approx \sum_{j=1}^N w_j f(x_j) \quad (4.45)$$

is exact if $f(x)$ is any polynomial of order up to $2N - 1$. The formula is called the N -point quadrature rule. In the case of Gauss-Legendre quadrature we have $W(x) = 1$ for $-1 < x < 1$ and the corresponding orthogonal polynomials are the Legendre polynomials. Since usually the integration boundaries $a \neq -1$ and $b \neq 1$, the integral can be recast as

$$\int_a^b f(x) dx = d_- \int_{-1}^1 f(d_-y + d_+) dy \approx d_- \sum_{j=1}^N w_j f(d_-x_j + d_+), \quad (4.46)$$

where $d_+ = (a + b)/2$ and $d_- = (b - a)/2$.

The accuracy of the quadrature result can be estimated by comparing it with a more accurate value calculated using a higher-order rule. With N fixed it is not possible to determine the accuracy of the result prior to the calculation but it is generally desired that the result is at least as accurate as specified. This can be accomplished in an adaptive quadrature where the integration interval is subdivided if the absolute difference of the less accurate and more accurate result is larger than the specified tolerance. The whole integral will then be (in case of division into two subintervals)

$$\int_a^b f(x) dx = \int_a^m f(x) dx + \int_m^b f(x) dx, \quad (4.47)$$

where $m = (a+b)/2$. The accuracy is now estimated in each of the subintervals separately and a subinterval is divided again if the tolerance is not reached. The process is repeated

recursively until the specified tolerance is reached in each subinterval. Denoting the less accurate estimate as I_{low} and the more accurate one as I_{high} , the termination criterion reads

$$|I_{\text{low}} - I_{\text{high}}| < \epsilon |I_{\text{low}}| \quad (4.48)$$

with ϵ being the specified relative tolerance. However, in some situations the above condition may never be satisfied. Therefore, it is more convenient to use the estimate of the whole integral $|I_{\text{tot}}|$ at the r.h.s. of Eq. (4.48). I_{tot} is calculated only once in the beginning using a higher-order rule than for I_{high} . The local adaptive quadrature differs from the global adaptive one in a way that in the latter the required accuracy is tested for sum of the subinterval integrals and only the subinterval with the highest value of the error estimate is subdivided.

In the usual Gaussian quadrature the nodes of a higher order rule never coincide with the ones of the lower order rule. Therefore, the previous integrand evaluations are not reused in determining the accuracy of the integral estimate leading to longer calculation times. This can be overcome in the so-called Kronrod extension which adds additional $N + 1$ points to the N -point Gauss-Legendre rule in a way that the integral in Eq. (4.45) is exact for any polynomial of degree up to $3N - 1$. The new $N + 1$ points are the roots of the polynomial $K_{N+1}(x)$ which satisfies the orthogonality condition

$$\int_{-1}^1 K_{N+1}(x) P_N(x) x^k dx = 0, \quad k = 0, 1, \dots, N, \quad (4.49)$$

where $P_N(x)$ is the Legendre polynomial of degree N . The $2N + 1$ extended rule is utilized for the more accurate estimate I_{high} which is calculated using only $N + 1$ more integrand evaluations. The extended rule can be further extended by adding additional $(2N + 1) + 1 = 2N + 2$ points in a similar way. Thus, the double-extended $(4N + 3)$ -point rule can be used for the estimate of I_{tot} utilizing all previous integrand evaluations. The nodes and weights for the 7-point rule, the 15-point extended rule and the 31-point double-extended rule, which were chosen for the integral estimation, are shown graphically in Fig. 4.7.

Despite having a fast and reliable quadrature scheme, it is still not optimal in the sense of time requirements to evaluate the inner convolution $f_{DS} \otimes G$ every time as an input for the outer convolution $f_{DSG} \otimes T$. A considerable speed-up can be achieved by the approach that the inner convolution is calculated only at some points and interpolated in between. Function approximation by expansion in the Chebyshev orthogonal polynomials [Pre07] proved to be fast and reliable. Denoting the corresponding polynomial as $T_k(x)$ the expansion of the function $f(x)$ can be written as

$$f(x) \approx \sum_{k=1}^N c_k T_k(x) - \frac{1}{2} c_0, \quad (4.50)$$

where the expansion coefficients are

$$c_j = \frac{2}{N} \sum_{k=1}^N f \left[\cos \left(\frac{\pi (k + \frac{1}{2})}{N} \right) \right] \cos \left(\frac{\pi j (k + \frac{1}{2})}{N} \right). \quad (4.51)$$

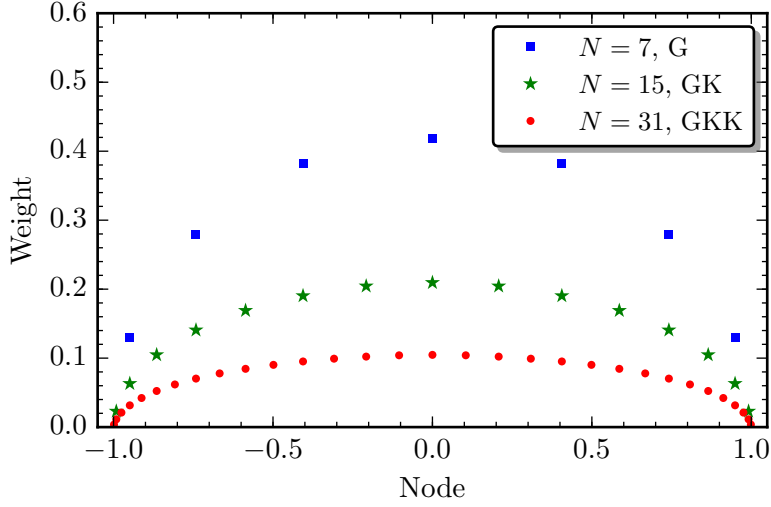


Figure 4.7: The nodes and weights of the 7-point rule of the Gauss-Legendre quadrature (G), the 15-point extended rule of the Gauss-Legendre quadrature with Kronrod extension (GK) and 31-point the double-extension rule (GKK).

The approximation is exact for x equal to all of the N roots of $T_N(x)$. The N function values $f(x_k)$ have to be computed only once and then can be reused in the calculation of all the coefficients. The polynomials in the sum in Eq. (4.50) can be evaluated from the recursion relation

$$T_{k+1}(x) = 2xT_k(x) - T_{k-1}(x) \quad (4.52)$$

with $T_0(x) = 1$ and $T_1(x) = x$.

The inner convolution should be calculated on $(-\infty, +\infty)$ whereas the outer convolution on $(qU_{\min}, +\infty)$, where qU_{\min} is the lowest retarding voltage in the spectrum, since $T(E, qU_{\min}) = 0$ for $E < qU_{\min}$. In principle, the integration over a (semi)infinite interval can be accomplished using a suitable transformation of the integration variable. However, it turned out that a higher numerical stability and faster fit can be obtained by simply using finite integration boundaries. The intervals of $(-6\sigma, 6\sigma)$ and $(qU_{\min}, E_i + 300 \text{ eV})$, respectively, were chosen.

Regarding the accuracy of the integration, the relative tolerance values of $\epsilon = 10^{-10}$ and $\epsilon = 10^{-8}$, respectively, were chosen for the inner and outer convolution. In this way, the numerical stability of the least-squares fit is ensured while not enlarging the time needed to perform the fit by an unnecessary amount. The execution time of the fit with about 90 points in the spectrum amounts to about 25 min on a given computer without the Chebyshev polynomial expansion. The Chebyshev expansion can be utilized in the whole interval $(qU_{\min}, +\infty)$. However, the coefficients of the expansion drop slowly in magnitude with increasing index j and thus many coefficients are required for an accurate approximation. It is more convenient to divide the interval into two, the first one being $(qU_{\min}, E_i + (E_i - qU_{\min}))$, and perform the expansion in each of them separately. The number of coefficients was chosen $N = 150$ and $N = 100$, respectively, for the lower and higher energy intervals. In such a way, the execution time of the same fit is only 20 s

on the same computer while the fit gives essentially the same results as the one without using the expansion.

At the MoS usually several different $^{83\text{m}}\text{Kr}$ sources were measured sequentially resulting in the need of analysis of spectra with different line shape parameters. The minimization requires an initial guess of the parameters but each spectrum may require individual values. Even for a single source the amplitude decays in time by the exponential law. Thus, it is not feasible to do the initial parameter estimation manually for each spectrum. The initial values for the most important parameters with respect to convergence of the minimization can be obtained automatically as follows. Firstly, the spectrum is interpolated using the smoothing cubic spline technique [Rei67] and the line position is estimated as the point of largest slope of the spline function (point of inflection) plus a small correction. Then the constant background term is estimated from the count rate at the largest retarding energy. Finally, the amplitude is estimated by fixing the other parameters and minimizing the χ^2 function with respect to the amplitude. The one-parameter minimization is usually performed also for the background term afterwards. Such an approach is fast and reliable in determining the initial parameters for the all-parameter minimization.

4.4.2 Comparison to the Voigt doublet approach

The result of a least-squares fit of the K-32 line obtained using the VD approach is shown in Fig. 4.8 in comparison to the DSG approach fit result. The spectrum was acquired for the source Pt-10-1 with 0.2 eV steps and 20 s measurement time in one point. In the former case the total number of fitted parameters was six: amplitudes a, a' , the line positions E_i, E'_i , Gaussian width σ and constant background b_0 . The chi-square function value divided by the number of degrees of freedom⁴ was $\chi_{\text{dof}}^2 = 1.54$ (87 dof). In order to obtain a more reasonable chi-square value the lower fit boundary has to be increased by about 5 eV leading to a narrower energy interval. Further fits with the VD approach were done in the narrower energy interval.

In the DSG case the total number of fitted parameters was five: amplitude a , line position E_i , Gaussian width σ , asymmetry parameter α and constant background b_0 . The fit result yielded $\chi_{\text{dof}}^2 = 1.03$ (88 dof). Thus, with one parameter less the DSG approach describes the line shape in a better way. The fitted Gaussian width was 0.61(4) eV which is far from zero and justifies the need for the Gaussian broadening. The 1σ -parabolic uncertainty of the DSG line position $\sigma_P(E_i)$, obtained by means of Eqs. (4.33) and (4.34), was only 20.8 meV compared to 59.4 meV for the VD in the narrower energy interval. The asymmetry α amounted to 0.100(3).

The parabolic uncertainties are reasonably accurate for the DSG but only approximate for the VD approach in the sense of confidence level of the corresponding interval. The asymptotic uncertainties $\sigma_A^\mp(E_i)$ obtained by means of Eq. (4.32) yield for the 68 %

⁴ The χ^2 function follows the chi-square distribution with $\text{dof} = n - n_p$ degrees of freedom, where n_p is the number of free parameters, if the residuals $M_i - S(qU_i; \mathbf{p})$ are normally distributed with the variance σ_i^2 . The expectation value of the distribution equals the number of dof. Thus, the chi-square function value divided by the number of dof should be around one.

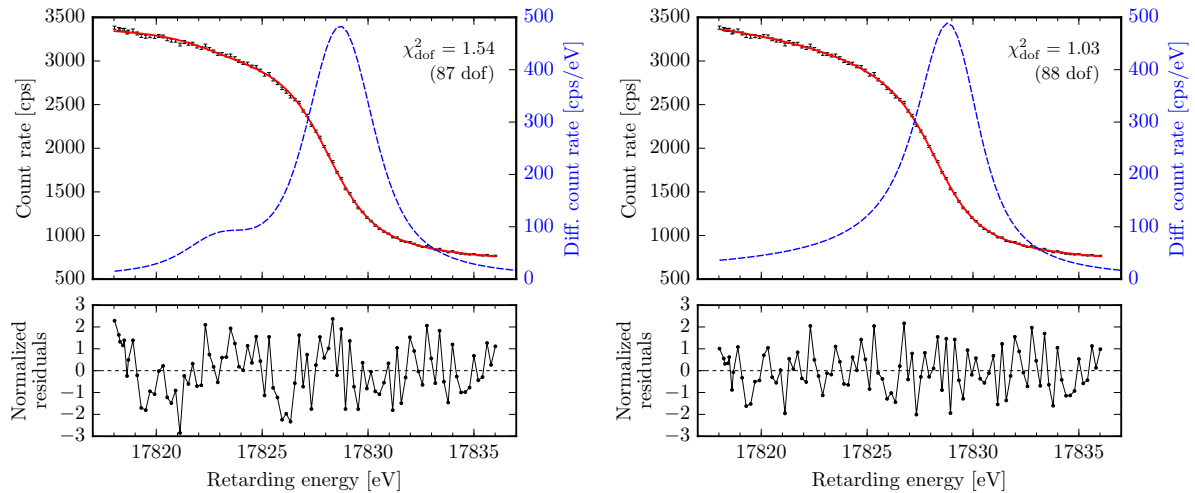


Figure 4.8: The experimental K-32 line fitted with a doublet of Voigt functions (left) and with the Doniach-Šunjić function convoluted with the Gaussian function (right). The residuals normalized to the statistical uncertainty $[M_i - S(qU_i; \mathbf{p})] / \sigma_i$ are also shown in both cases. The DSG approach is able to describe the data with one free parameter less and at the same time without any residual structure.

confidence interval the values of -20.4 meV and 20.3 meV for the DSG and -46.1 meV and 51.5 meV for the VD, respectively. Thus, in the DSG case generally the differences between the two uncertainties can be neglected.

An example of the line position results obtained from a series of K-32 measurements is shown in Fig. 4.9 for both approaches. The spectra were obtained for a period of about 30 d. The results demonstrate the instability of the VD fit results as well as the larger variance of the individual position values compared to DSG. The values with relatively small uncertainties in the VD case correspond to the situations when the chi-square function minimum was obtained for a lower subdominant peak position. In that case also the dominant peak position tends to lower values. Large variation of line position difference of the two peaks is not physically justified because the measurements were done in identical conditions with comparable statistics. Thus, it has to be a consequence of the imperfect model function. Assuming that the line position is constant in time and that the position data points are normally distributed, the weighted standard deviation from the spread of values is 38.3 meV for the VD and only 18.8 meV for the DSG approach.

4.4.3 Parameter correlations

A correlation in the context of a least-squares fit is a measure of linear dependence between two parameters. It is expressed using the correlation coefficient which is a dimensionless number in the interval $[-1, 1]$. The correlation coefficient ρ_{ij} of the parameters i and j is

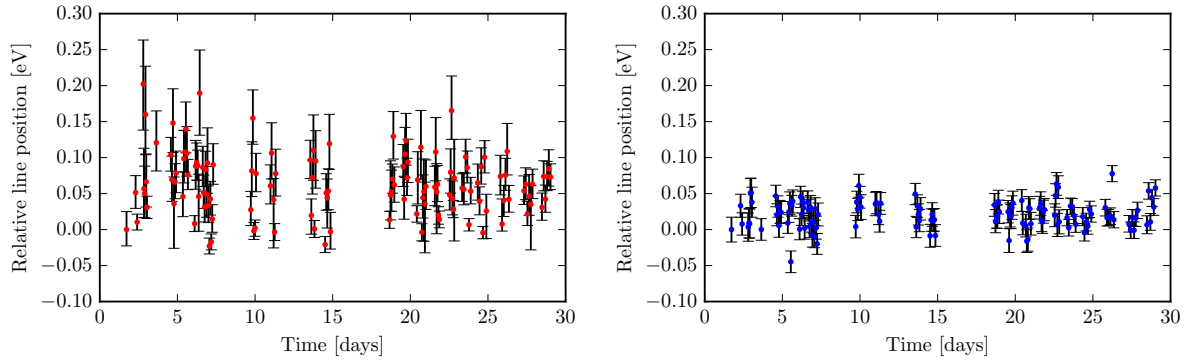


Figure 4.9: The line position of the K-32 line obtained by means of the VD approach (left) and the DSG approach (right) as measured in time at the MoS. The VD model leads to larger fluctuations of the line position and non-equal uncertainties among individual results despite similar statistics and identical measurement conditions during the time. The median of the chi-square function value was about $\chi_{\text{dof}}^2 = 1.20$ (36 dof) for the DSG compared to $\chi_{\text{dof}}^2 = 1.46$ (29 dof) for the VD.

given from the covariance matrix Σ as

$$\rho_{ij} = \frac{\Sigma_{ij}}{\sqrt{\Sigma_{ii}\Sigma_{jj}}}. \quad (4.53)$$

The matrix element Σ_{ij} is the covariance between the parameters i and j and Σ_{ii}, Σ_{jj} are the variances of the parameters i and j . If two parameters are correlated, a change of one parameter can be to some extent compensated by a change of the other parameter in the sense of the χ^2 function value. A value of $\rho_{ij} = 1$ or -1 (complete correlation) indicates a perfect linear dependence of the parameters (one parameter is a linear function of the other) and in such a case a unique minimum cannot be found because the mutual parameter compensation is complete. Thus, parameter correlations make minimization more difficult but not impossible unless $\rho_{ij} = \pm 1$.

Both the VD and DSG models comprise a few strong parameter correlations which also involve the parameter of interest, the line position E_i , but none of them equals exactly 1 or -1 (the largest one in absolute value amounts to 0.98). The quality of the minimum can be assessed by inspecting the shape of the χ^2 function around the minimum by means of function contours, i.e. a set of values of two parameters for which the function is a constant value above the minimum. For each point in the contour plot it holds that the function is minimized with respect to the remaining parameters. In the case when the model function was linear in its parameters and the case of zero (non-zero) parameter correlations the contour would be a circle (ellipse).

Examples of the χ^2 function contours for the K-32 spectrum are shown in Fig. 4.10. Even though the minimum exists for the VD approach, it is rather shallow and the shape of the contours explains the tendency of the dominant line position to fluctuate towards lower values if the subdominant peak position tends to lower values. Note that the values of $E'_i - E_i \lesssim -5.8$ eV correspond to energies outside the fitted interval, i.e. below 17823 eV.

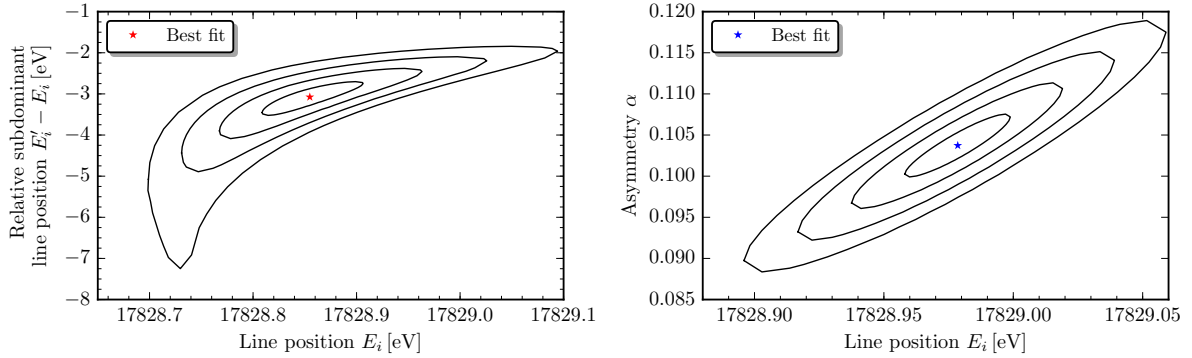


Figure 4.10: The χ^2 function contours for the parameters line position E_i and relative subdominant line position $E'_i - E_i$ for the VD approach (left) and line position E_i and asymmetry α for the DSG approach (right). The contours correspond to the values of $\chi^2 = \chi_{\min}^2 + n^2$ with $n = 1$ to 4 above the minimum value χ_{\min}^2 . The best fit parameters are also indicated. Each of the 50 points on the contour, which are connected by straight lines, corresponds to minimum of the χ^2 with respect to the remaining parameters.

In the DSG case the parameters are also correlated meaning that the line position E_i tends to lower values for lower asymmetry α but the minimum is well-defined and there is an unambiguous combination of E_i and α which minimizes the χ^2 function.

The correlations are merely a consequence of available data and model function parametrization. Moreover, an incomplete but large correlation, $|\rho_{ij}| < 1$, does not necessarily compromise the ability to uniquely determine the best-fit parameters. This can be further demonstrated by observing the line amplitude a , which in the DSG case is correlated to the line position E_i with $\rho = -0.93$ and to the asymmetry α with $\rho = -0.98$, in time since it should follow the exponential decay law. This is shown in Fig. 4.11 on the left. Although the MoS is not an optimal tool for measuring the half-life, the amplitude drops after 30 d by the expected amount of about $\exp(-30 \ln 2/86.2) \approx 0.79$ since the ratio of the measured amplitude after the time period and in the beginning is $940/1200 \approx 0.79$. In the same figure on the right the scatter plot of amplitude vs. the relative line position is shown which demonstrates lack of any significant correlation between the two parameters. The sample correlation coefficient amounts to -0.17 which is very different from -0.93 , the correlation of the relevant parameters in a single fit, as expected.

The parameter correlations can have negative effects if one of the correlated parameters is fixed in the minimization. Consider the right plot in Fig. 4.10 and let us fix the asymmetry α to e.g. 0.11. In such a case the line position that leads to a χ^2 minimum will be higher than the one indicated in the figure because the minimization takes place only along the line $\alpha = 0.11$. Thus, fixing the correlated parameter to a value which does not correspond to the common minimum will lead to a systematic shift of the other parameter with respect to the value in the common minimum. Therefore, parameters should not be fixed unless there is a good reason to do so. It is reasonable to fix the Lorentzian width Γ_i since it is determined by the lifetime of the corresponding electron vacancy which is a fixed value. But there is no reason for fixing the other parameters since a change of

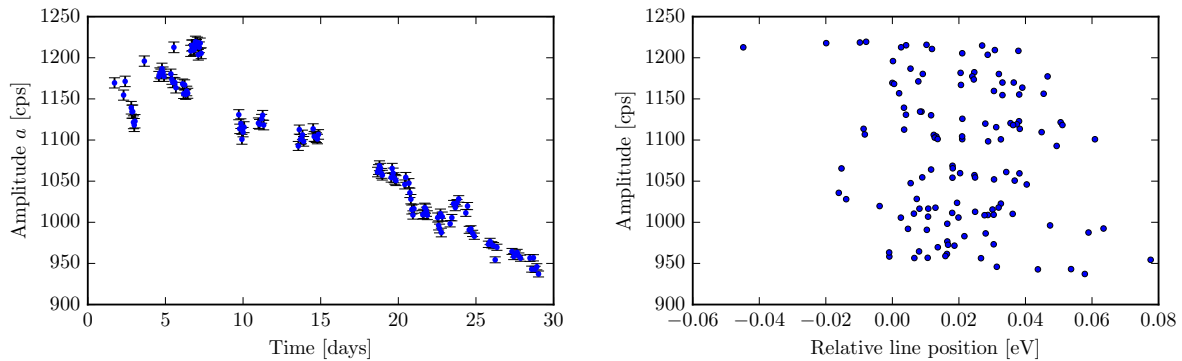


Figure 4.11: The fitted line amplitude a for the DSG approach for the same K-32 spectra as in Fig. 4.9 (left) and the scatter plot of the amplitude vs. the relative line position (right) for the same data. The correlation coefficient of -0.93 between the parameters in a single fit does not imply that the correct parameter values cannot be found.

the line shape cannot be a priori excluded in the long-term measurement. The amount of ^{83}Rb atoms is simply not negligible compared to the amount of substrate atoms (discussed in detail later in this work) and by the radioactive decay the environment of $^{83\text{m}}\text{Kr}$ could change over time.

In the work [Bau14] the correlation between the line position and the asymmetry α is used to “correct” the fitted line position based on the difference of the fitted asymmetry α and its arithmetical mean from all considered spectra. Apart from the fact that no justification why such an approach should lead to a correct result is given in [Bau14], the approach is in contradiction to the above stated since it is assumed that the asymmetry has to be constant over time and that the correct line position value cannot be found with the stated parameter correlations. It should be noted that the asymmetry parameter, which is perhaps the most “exotic” parameter in the DSG lineshape, has a precise physical meaning in the theory of Doniach and Šunjić. Thus, in this sense it is not a phenomenological parameter unlike e.g. the Gaussian width or the second Voigt peak in the VD lineshape. If it happens that an unaccounted-for systematic effect negatively influences the spectrum shape then a biased fit result can be obtained no matter how accurate the shape description is or how correlated its parameters are. This can be seen in the case of the fitted neutrino mass squared obtained from the tritium β -spectrum (Chapter 3). The parameter correlation cannot be regarded as the primary cause for the biased result. Thus, in this work no artificial correction for the correlation between the α parameter and the line position is followed.

4.4.4 Other $^{83\text{m}}\text{Kr}$ conversion lines

Although by far the largest attention was paid to the K-32 line, other conversion electron lines of both $^{83\text{m}}\text{Kr}$ nuclear transitions and of different subshells were occasionally measured at the MoS as well.

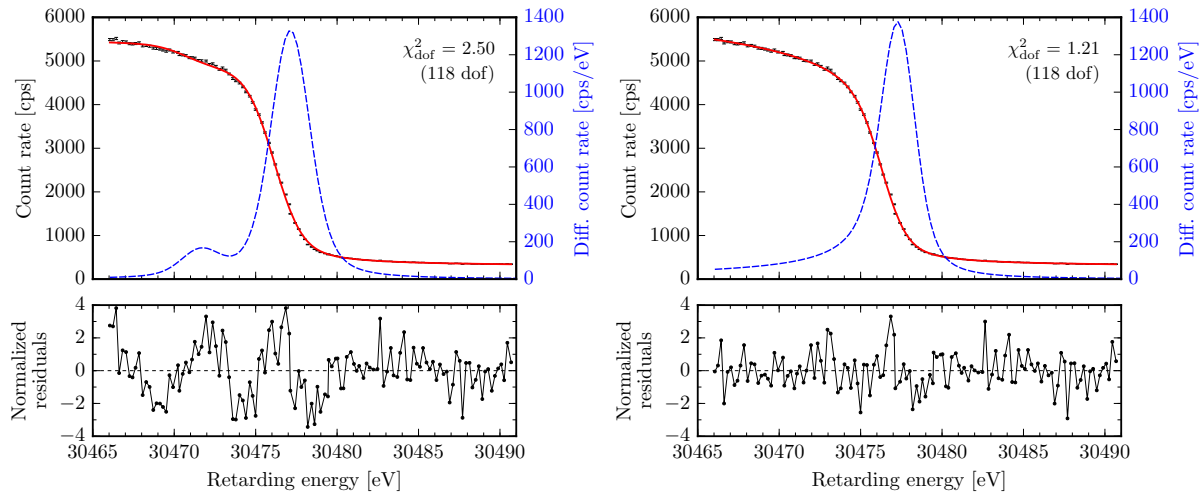


Figure 4.12: The experimental L_3 -32 line fitted with a doublet of Voigt functions (left) and with the Doniach-Šunjić function convoluted with the Gaussian function (right). The Lorentzian width Γ_{L_3} was a free parameter in the DSG fit. The obtained value was used for the fixed Lorentzian width in the VD case. The VD approach does not describe the shape in an acceptable way.

L_3 -32

Although the L_3 -32 line cannot be used directly for KATRIN high-voltage stability monitoring, together with the lines L_3 -9.4 and K-32 it serves as a valuable tool for checking the linearity of the high voltage setup. Also its small Lorentzian width, high intensity per $^{83\text{m}}\text{Kr}$ decay and small background from higher energy lines make it suitable for line shape description investigations.

A comparison of the VD and DSG fits of the L_3 -32 line measured with fine energy steps of about 0.2 eV is shown in Fig. 4.12. In the DSG case the Lorentzian width Γ_{L_3} was also fitted resulting in the total number of six fitted parameters. The reason for this is that utilizing the recommended width of $\Gamma_{L_3} = 1.19$ eV [Cam01] as a fixed value leads to a poor χ_{dof}^2 value and a clear residual structure. The fitted value amounts to $\Gamma_{L_3} = 1.059(14)$ eV with $\chi_{\text{dof}}^2 = 1.21$ (118 dof). When the obtained Lorentzian width is utilized in the VD case as fixed, the fit yields $\chi_{\text{dof}}^2 = 2.50$ (118 dof) with a clear residual structure. The DSG-fitted Gaussian width σ amounts to 0.79(2) eV which is larger than for the K-32 line presented previously. Since the two spectra were measured for the same source within a short time, the larger Gaussian width may reflect that the high voltage power supply is more unstable at the voltages of -30 kV compared to -18 kV and the subsequent noise leads to additional broadening of the line.

Other lines

Fig. 4.13 shows the DSG fit results of the reasonably strong lines L_2 -9.4, L_3 -9.4, M_1 -9.4, L_2 -32 and the close doublet $M_{2,3}$ -32 measured with fine energy steps. All fits return a

Table 4.1: List of reasonably strong lines, their energies and obtained (or fixed) DSG parameter values. The fixed Lorentzian width in the fit is indicated by absence of the parameter uncertainty. In the M_{2,3}-32 case the Gaussian width σ and the asymmetry α were common for both lines in the doublet.

Line	Energy (keV)	σ -width (eV)	Γ -width (eV)	Asymmetry α
L ₂ -9.4	7.68	0.55(5)	1.25	0.112(8)
L ₃ -9.4	7.73	0.66(10)	1.05(16)	0.104(8)
M ₁ -9.4	9.12	0.57(12)	3.50	0.107(7)
K-32	17.83	0.62(3)	2.70	0.100(3)
L ₂ -32	30.42	0.69(9)	1.25	0.103(16)
L ₃ -32	30.48	0.79(2)	1.059(13)	0.098(2)
M ₂ -32	31.93		1.33(18)	
M ₃ -32	31.94	0.83(4)	1.15(5)	0.109(12)

good χ_{dof}^2 value. The L₂-# lines were fitted using a linear background, i.e. $B(qU; \mathbf{p}) = b_0 + b_1 qU$, since they are superimposed to the loss-energy electron background of the higher energy L₃-# lines. The Lorentzian width was a free parameter in the case of L₃-9.4 and M_{2,3}-32. For the other lines the Lorentzian width was fixed to the recommended value from [Cam01] since it is difficult to obtain a reasonable value with a linear background or if the Lorentzian width is large compared to the Gaussian width.

Table 4.1 shows the approximate energies of the lines together with the fitted Gaussian width, the fitted (or fixed) Lorentzian width and the fitted asymmetry α . In the table also the results for the K-32 and L₃-32 lines as discussed above are recapitulated for comparison. The fitted Γ_{L_3} from the L₃-9.4 is in agreement with the value obtained from the fit of L₃-32 although its uncertainty is rather large. The Gaussian width is larger for all lines with the energy above 30 keV which further supports the conception that the line is broadened by possible fluctuations of the high voltage power supply. The asymmetry parameter is consistent among all the conversion lines which supports a common origin of the asymmetry.

4.4.5 ⁸³Rb in two different environments as a source of asymmetry

The Voigt doublet description of the conversion line shape was motivated by possible existence of the mother isotope ⁸³Rb and therefore the daughter ^{83m}Kr in two different environments resulting in two different binding energies. The implantation of ⁸³Rb takes place only under moderate vacuum and no cleaning of the substrate prior to the implantation is done. Therefore, a contamination layer consisting of possibly water and hydrocarbons is present at the substrate surface and due to the relatively low implantation energy some of the ⁸³Rb may end up in this layer.

Assuming a contamination layer with the thickness of 30 Å composed of carbon

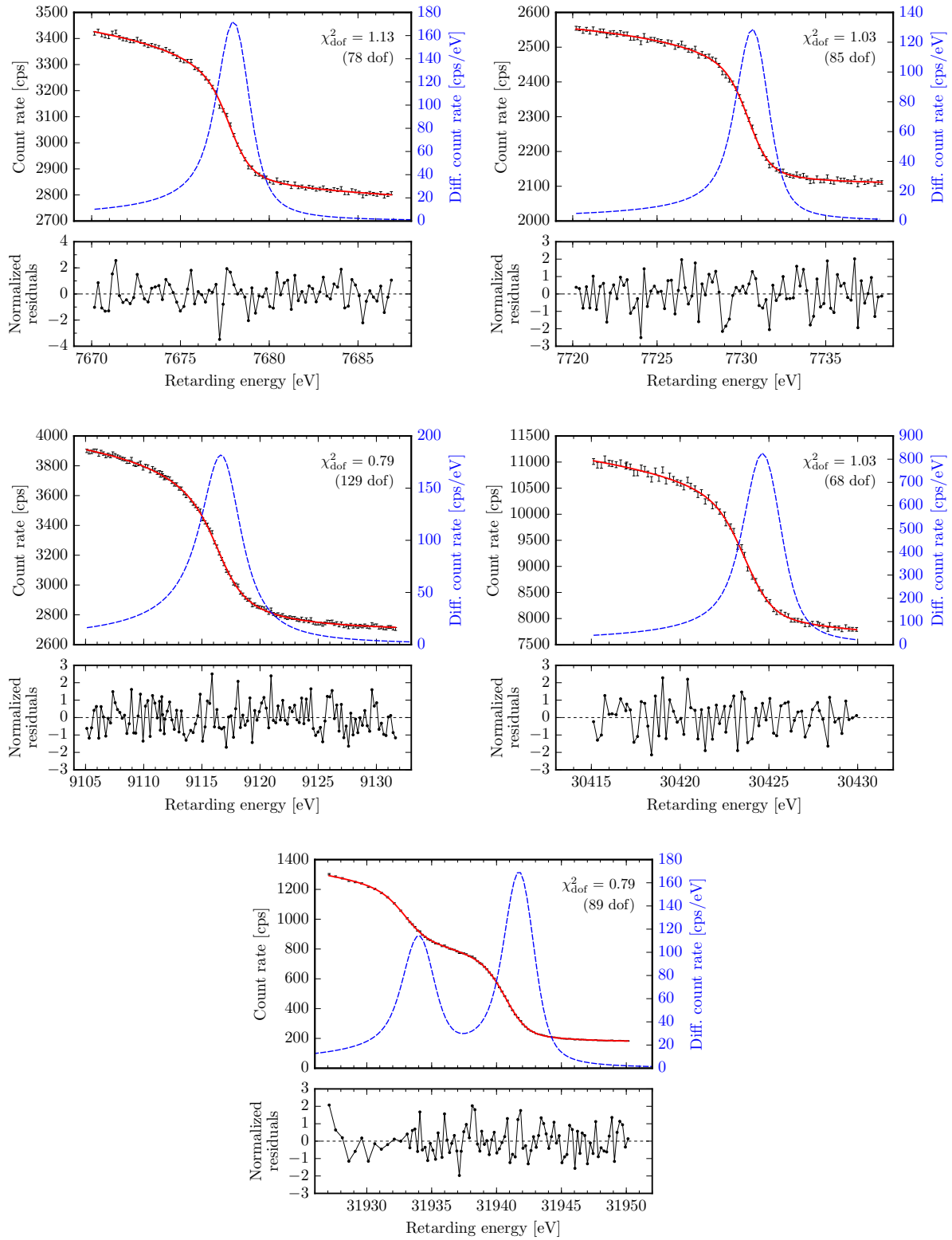


Figure 4.13: Other conversion lines of $^{83\text{m}}\text{Kr}$ fitted with the DSG approach: L₂-9.4 (top left), L₃-9.4 (top right), M₁-9.4 (middle left), L₂-32 (middle right), M_{2,3}-32 (bottom).

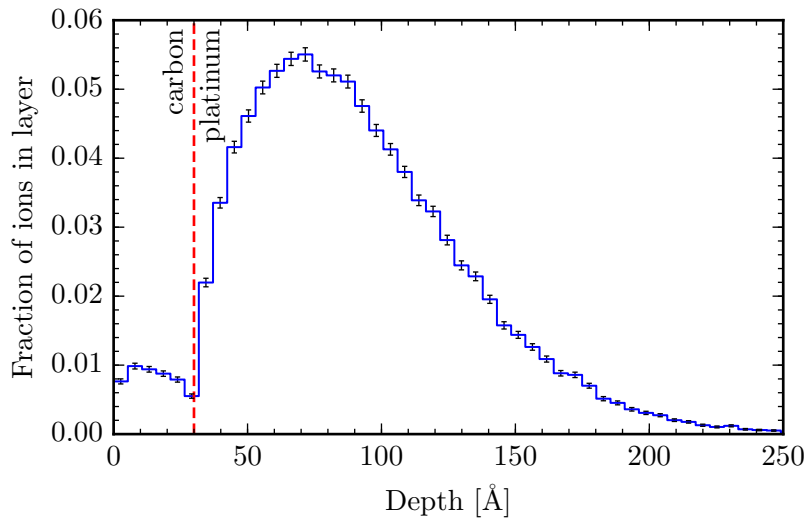


Figure 4.14: Simulated depth profile of ^{83}Rb with the implantation energy of 30 keV and the incident angle of 0° . The platinum substrate was assumed to be covered with 30 Å of contamination layer composed of carbon. The total number of simulated ions amounted to 6×10^4 . The uncertainties were estimated as a square root of the relevant binomial distribution variance.

[Špa90], a platinum substrate, and the implantation energy of 30 keV, the ^{83}Rb depth profile calculated with the SRIM code [Zie10] (stopping and range of ions in matter) for the incident angle of 0° is shown in Fig. 4.14. The fraction of ions in the contamination layer amounts to 4.4(1) % (the total number of simulated ions was 6×10^4). For the implantation energy of 15 keV the fraction of ^{83}Rb ions in the contamination layer is larger and amounts to 9.3(1) %.

The amount of ^{83}Rb present in the contamination layer was checked in the following way. The surface of the substrate was scratched with a cotton stick soaked with acetone. The contaminated part of the stick was measured at a HPGe (high purity germanium) detector. The relative intensity of the 520 keV γ -line was observed in comparison to the intensity of the line measured for the unscratched substrate. The results were 4.2(6) % and 8.8(4) % for the 30 keV and 15 keV implantation energy⁵, respectively. The values are in good agreement with the expectation from the SRIM calculation.

A similar procedure was applied to the source Pt-15-3 which was measured at the MoS both prior to wiping and after wiping in order to observe whether the conversion line becomes less asymmetric. Using the DSG approach for the line description, the asymmetry α prior to the wiping amounted to 0.114(3) and after the wiping it amounted to 0.108(3) (both numbers are a weighted average from fits of 4 spectra). Thus, the wiping had no effect on the asymmetry which disfavors the idea of two environments as the source of the asymmetry.

⁵ The sources were Pt-30-1 and Pt-15-1.

4.4.6 Loss-energy electrons

Due to $^{83\text{m}}\text{Kr}$ atoms being embedded in the solid substrate there is a substantial probability that the emitted electron loses some of its energy by inelastic scattering with the substrate atoms before leaving the substrate. Besides, an internal energy loss of the conversion electron may take place when another electron from the same atom is either excited to a higher energy atomic level (shake-up effect) or released from the atom completely (shake-off effect). This gives rise to additional structures which are present at the lower-energy side of the elastic (no-energy-loss) peak. Thus, we may ask to what extent are such energy losses responsible for the observed conversion line asymmetry.

Electron scattering

The loss-energy spectrum due to electron scattering is obtained by means of a Monte Carlo simulation [Dra87, Špa93, Dra02]. The probability density $p_{IS}(x)$ for an electron to be inelastically scattered on the substrate atoms is given by the exponential distribution as a function of the distance x as

$$p_{IS}(x) = \sigma_{IS}n \exp(-\sigma_{IS}nx) = \frac{1}{\lambda_{IS}} \exp\left(-\frac{x}{\lambda_{IS}}\right), \quad (4.54)$$

where σ_{IS} is the total inelastic cross-section, n is the substrate atoms number density and $\lambda_{IS} = 1/(\sigma_{IS}n)$ is the inelastic mean free path, i.e. the average distance the electron travels between collisions. The probability of the electron to be scattered in a single collision into the solid angle Ω with the new energy E is described by the double-differential cross section⁶ $d^2\sigma_{IS}/(d\Omega dE)$. In addition to inelastic scattering, the electron can be scattered also elastically by Rutherford scattering on substrate atoms. The electron elastic scattering is considered in the Monte Carlo simulation as well.

In the simulation the electrons are emitted with a fixed energy isotropically from a depth that is selected randomly for each electron. The chosen depth is assumed to follow the distribution of the ^{83}Rb ions in the substrate as calculated by the SRIM code [Zie10]. Generally, a pseudorandom value which follows some probability distribution $p(x)$ can be conveniently generated using the quantile function $Q(p)$ of $p(x)$. If ξ is a pseudorandom variate uniformly distributed on the interval $(0, 1)$, then

$$x = Q(\xi) \quad (4.55)$$

has the probability distribution described by $p(x)$. For the exponential distribution in Eq. (4.54) we get

$$x = -\lambda_{IS} \ln(1 - \xi). \quad (4.56)$$

Any changes of the electron path due to presence of a source magnetic field are neglected.

⁶ The differential solid angle is $d\Omega = \sin\theta d\theta d\varphi = -d(\cos\theta) d\varphi$, where θ and φ are, respectively, the polar and the azimuthal angles in spherical coordinates. However, the double-differential cross section depends only on the polar angle θ .

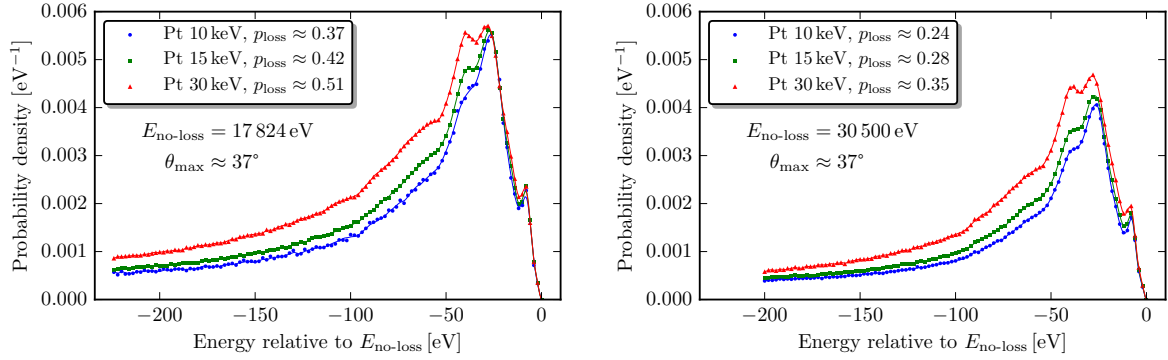


Figure 4.15: The simulated loss-energy electron spectrum of the K-32 (left) and L₃-32 (right) conversion electrons emitted from a platinum substrate with different ⁸³Rb implantation energies. The values p_{loss} denote the total probability of the energy loss neglecting electrons with the energy loss of $\gtrsim 200$ eV, which are not shown. The probability of no energy loss (the elastic peak) amounts to $p_{\text{el}} = 1 - p_{\text{loss}}$. The solid line is the interpolation by the smoothing cubic spline.

The output of the simulation is a two-dimensional histogram of number of electrons which leave the substrate within a particular interval of energies and of cosines of the angle with respect to the surface normal. The MAC-E filter collects all electrons emitted up to the acceptance angle θ_{max} which depends on the source magnetic field. Thus, the spectrum of the loss-energy electrons is made for the particular magnetic field in a way that for each energy bin the contents of the cosine angle bins are summed up to $\cos \theta_{\text{max}}$. Since this value is usually inside the bin, the counts from such a bin are simply scaled by the fraction of the bin which is covered.

The spectrum of the K-32 and L₃-32 loss-energy electrons is shown in Fig. 4.15 for $\theta_{\text{max}} \approx 37^\circ$, platinum substrate and ⁸³Rb implantation energies of 10 keV, 15 keV and 30 keV, respectively. The results show that lower implantation energy leads to a smaller amount of loss-energy electrons due to lower mean implantation depth as expected. Also electrons with higher energy are less likely to be inelastically scattered as expected due to a larger mean free path λ . The amount of loss-energy electrons becomes the most significant at about 20 eV below the elastic peak. The spectrum data are interpolated using the smoothing cubic spline technique [Rei67]. Owing to the uncertainties of the cross-sections, a systematic uncertainty estimated to 10% is assigned to the total probability of energy loss.

Having the loss-energy electron spectrum $f_{\text{loss}}(E)$ for a single elastic peak energy, the complete spectrum with the elastic peak energy described by the DSG lineshape and observed by the MoS is given schematically by

$$S(qU; \mathbf{p}) = p_{\text{el}} f_{\text{DSG}}(E; \mathbf{p}) \otimes T(E, qU) + f_{\text{loss}}(E) \otimes f_{\text{DSG}}(E; \mathbf{p}) \otimes T(E, qU) + B(qU; \mathbf{p}), \quad (4.57)$$

where p_{el} is the probability of no energy loss. The second summand involves a triple convolution since $f_{\text{DSG}} = f_{\text{DS}} \otimes G$. However, the terms $T(E, qU)$ and $f_{\text{loss}}(E)$ are fixed

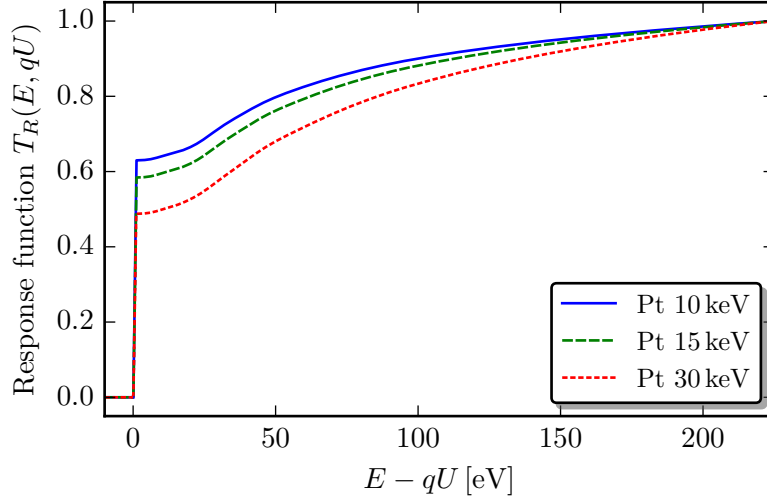


Figure 4.16: The MoS response function $T_R(E, qU)$ for the retarding energy $qU = 17\,828$ eV as a function of the electron energy E for the platinum substrate conversion electron source and various ^{83}Rb implantation energies. The electrons with the energy loss of $\gtrsim 200$ eV are neglected so that the transmission becomes equal to one at the same $E - qU$ value for all depicted functions. The functions hold under the assumption that no transmission loss due to non-adiabatic electron transport occurs in the considered energy range (see Section 2.2).

for each fit since they do not depend on any of the fitted parameters. Therefore, the convolution $f_{loss} \otimes T$ can be calculated only once prior to the minimization and interpolated afterwards. The Eq. (4.57) is rearranged as

$$\begin{aligned} S(qU; \mathbf{p}) &= f_{DSG}(E; \mathbf{p}) \otimes [p_{el} T(E, qU) + f_{loss}(E) \otimes T(E, qU)] + B(qU; \mathbf{p}) \\ &= f_{DSG}(E; \mathbf{p}) \otimes T_R(E, qU) + B(qU; \mathbf{p}), \end{aligned} \quad (4.58)$$

where we have denoted $T_R \equiv p_{el} T + f_{loss} \otimes T$ the MoS response function for a particular conversion electron source at a specified magnetic field. The response function for the K-32 line utilizing the loss-energy electron spectrum from Fig. 4.15 is shown in Fig. 4.16.

Shake-up and shake-off

After the conversion electron emission the remaining atomic electron cloud rearranges itself in order to adapt to the different electric field. Due to such a rearrangement an electron of the cloud can be left in an excited state or released from the atom completely which thus removes energy from the conversion electron. In the former case, in the shake-up effect, the conversion electron peak has the same shape as the elastic one but its centroid and amplitude are lower. The latter case, the shake-off effect, leads generally to an additional continuum of energies superimposed to the elastic shape with lower centroid due to continuous energy of the released electron. Nevertheless, owing to the weakness of the effect in the following the possible continuity of the shake-off energies is neglected.

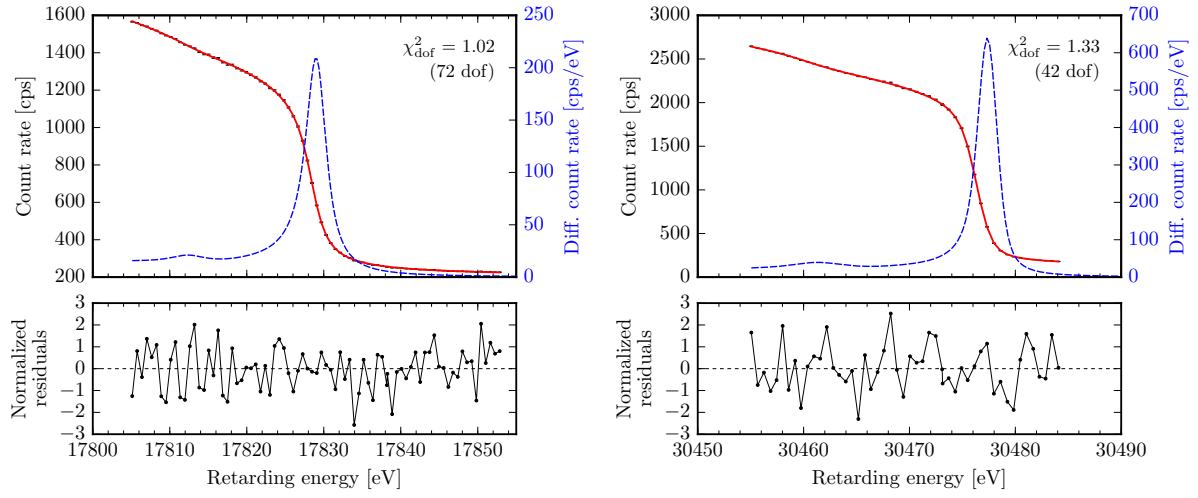


Figure 4.17: The experimental integral spectrum of the K-32 (left) and L₃-32 (right) conversion lines fitted using the DSG lineshape including the loss-energy electrons which arise due to the inelastic scattering with the substrate atoms and the shake-up/off effect.

The complete spectrum observed by the MoS including the inelastically scattered electrons as described above thus reads

$$S(qU; \mathbf{p}) = \left[f_{DSG}(E; a, E_i, \sigma, \Gamma_i, \alpha) + \sum_{j=1}^{N_{sh}} f_{DSG}(E; a_j, E_{ij}, \sigma, \Gamma_{ij}, \alpha) \right] \otimes T_R(E, qU) + B(qU; \mathbf{p}), \quad (4.59)$$

where N_{sh} is the considered number of shake-up/off conversion electron peaks and a_j, E_{ij} and Γ_{ij} are the amplitude, line position and Lorentzian width of the peak j . The Gaussian width σ and the asymmetry α are assumed the same as for the elastic peak.

Analysis results

Examples of the K-32 and L₃-32 lines least-squares fitted using Eq. (4.59) are shown in Fig. 4.17. In both fits one shake-up/off peak was considered, i.e. $N_{sh} = 1$. The obtained asymmetry α was 0.092(4) for the former and 0.084(1) for the latter. The values are far from zero which shows that the loss-energy electrons alone cannot explain the observed peak asymmetry. Performing the fits with fixed $\alpha = 0$ leads to a poor chi-square value.

The asymmetry α from a regular DSG fit, i.e. without the loss-energy electrons, in a narrower energy interval with the lower boundary at about 11 eV below the elastic peak centroid was 0.110(4) and 0.100(2), respectively. Thus, the asymmetry parameter α in such a fit absorbs a small part of the energy-loss spectrum. Also in this fit for K-32 the fitted line position was by about 50 meV higher than in the full-range fit presented above. Since such a shift is constant for a particular source at a constant magnetic field, it does not lead to differences of the observed line position among different spectra. Decreasing

the lower boundary in the regular fit by additional 2 eV increases both the α and the χ_{dof}^2 values. Thus, the present boundary for regular fits is reasonable without the need to consider the loss-energy part of the line.

The loss-energy electron term itself cannot describe the measured spectra alone without considering the shake-up/off effect. The amplitude of the shake-up/off peak relative to the elastic peak, its energy relative to the elastic peak and its Lorentzian width for the K-32 line amounted to 6.8(8) %, $-16.6(2)$ eV and 5.4(9) eV, respectively, and for the L_3 -32 line to 10.6(5) %, $-16.0(1)$ eV and 5.9(5) eV, respectively (the uncertainties are statistical only). Similar shake-up/off peaks were seen in the work [Pic92b], where two satellites below the K-32 line are reported with the relative energies of -20.3 eV and -33.3 eV, the Lorentzian width of 5.8 eV and the summed intensity of 18.5 % and one satellite below the L_3 -32 line is reported with the relative energy of -23 eV and the intensity of 19.3 % (the width for this satellite is not explicitly stated). However, the measurements in [Pic92b] were performed with a $^{83\text{m}}\text{Kr}$ source condensed on a liquid-helium cooled copper substrate. In our case, the solid-state effects in the SKrS may change the properties of the shake-up/off peaks.

4.4.7 Effect of different lower fit boundary

To further assess the DSG lineshape the following check of consistency was done. If the line shape description is accurate enough the fitted line position should be independent of the fit interval lower boundary. Such an approach closely follows the work [Kra05] where the dependence of the fitted neutrino mass squared on the lower fit boundary pointed to unaccounted-for systematics. An experimental K-32 spectrum was analysed several times with a different lower fit boundary in each case. The results for the VD and DSG methods both without and with the loss-energy part from electron scattering are shown in Fig. 4.18. The results clearly show that in the VD case the line position is fitted smaller with lower fit boundary in contrast to the DSG case. The increase of the line position observed for the DSG at the lower values of the boundary point to unaccounted-for shake-up/off peaks which were discussed above.

4.4.8 Conclusion

The observed SKrS electron spectrum is clearly not symmetric around the elastic peak. With the MAC-E filter it is not straightforward to resolve this part of the spectrum in more detail due to its integrating feature. Nevertheless, the DSG line shape seems to describe the observed spectrum in a reasonable and consistent way in contrast to the previously used doublet of Voigt functions. The lower line position uncertainty as well as lower line position fluctuations from spectrum to spectrum observed for VD represent further advantage of the DSG approach.

In the work [Wer78] it is noted that for a platinum sample the asymmetry of a photoelectron line is suppressed because the density of states around the Fermi level sharply decreases whereas a constant density of states is assumed for the DS shape. However, in our case the platinum environment is changed by presence of the ^{83}Rb atoms which could

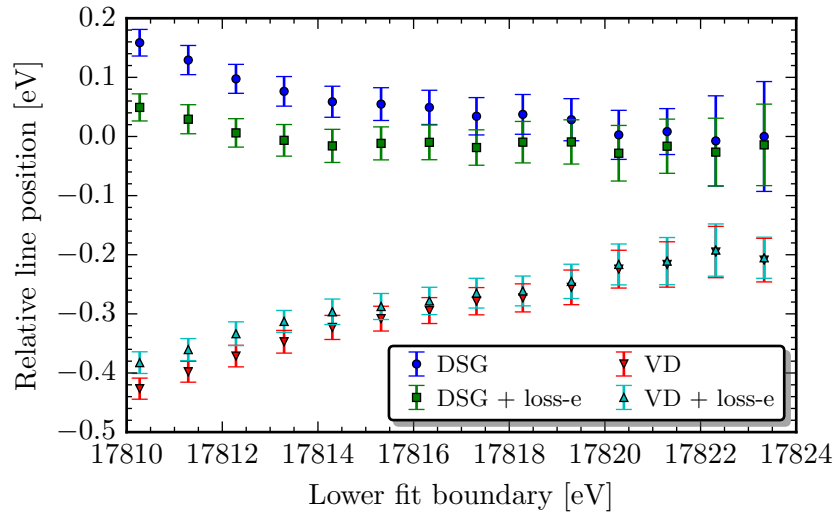


Figure 4.18: The fitted line position in dependence of the lower fit boundary for the VD and the DSG approaches. In both cases, shown are also the results which were obtained by considering the scattered loss-energy electrons in description of the measured spectrum.

possibly modify the density of states. Thus, the DS interpretation of the SKrS electron spectra cannot be excluded.

It is, nevertheless, possible that the lineshape is modified at lower energies and in the fits including the loss-energy electrons the fitted shake-up/off peak(s) compensate(s) for that. This is in accordance to the fact that the function f_{DS} in Eq. (4.40) is not integrable on $(-\infty, +\infty)$ for $\alpha > 0$ due to slow convergence towards $-\infty$. Such a property is not physically justified since the electron intensity (area under the curve) has to be finite. Despite this, the line amplitude definition according to Eq. (4.41) seems to be consistent since decay of the amplitude governed by the exponential law is observed (Fig. 4.11).

In the work [Zbo11] an attempt was carried out to investigate the structure of the rubidium electron binding energies using the x-ray photoelectron spectroscopy as a complementary measurement to the observation at the MAC-E filter. The non-radioactive isotope ^{85}Rb was implanted at 30 keV into a gold foil (gold was one of the substrates used in the long-term stability measurement). However, even for an order of magnitude larger dose the Rb peaks were not observed in the photoelectron energy spectrum. Only the material of the gold foil and contamination layer of carbon on top could be identified.

Since the DS is related to conduction electrons, one could possibly implant ^{83}Rb into an insulator where such effect would vanish. However, the insulating property of the substrate would lead to local areas of positive charge which could have a negative effect on the source properties and, especially, the emitted electron line position. Thus, this approach was not pursued.

Due to the significant benefits of the line shape in comparison to Voigt doublet (or singlet), which has to be utilized on a smaller energy interval, the DSG lineshape was used for analysis of electron spectra measured at the MoS throughout this work. For a similar reason it is also recommended to be used later for the monitoring of the KATRIN

high-voltage stability.

4.5 Reference method

The reference method (previously referred to as the cross-correlation method [Zbo11]) enables to obtain the relative shift and relative scaling factor of two integral spectra, the reference spectrum and the analysed one, by a least-squares fit. In contrast to the previously described approach no model function for the line shape and no accurate transmission function of the spectrometer are necessary. In this case, the model function in the χ^2 function is the interpolated reference spectrum. Denoting the interpolating function as f_{RM} , the model function $S(qU; \mathbf{p})$ can be written as

$$S(qU; r, \Delta, b_0) = r f_{RM}(qU - \Delta) + b_0, \quad (4.60)$$

where r is the spectrum relative scale factor, Δ is the spectrum relative shift and b_0 is the constant background term. Thus, the reference spectrum is scaled by r and shifted by Δ so that it matches the analysed spectrum in the least-squares fit. In other words, the obtained Δ is the relative shift of the analysed spectrum with respect to the reference spectrum.

With a constant background the number of free parameters is only three and thus the relative spectrum shift can be obtained with a smaller uncertainty than the line position in the DSG case. The disadvantage is that if the line shape in the analysed spectrum is different from the line shape in the reference spectrum, the method may give incorrect results since no change can be accounted for in Eq. (4.60). Moreover, the count rates in the experimentally measured reference spectrum are statistically randomized which makes interpolation more difficult. Both of these issues are addressed below.

4.5.1 Reference spectrum interpolation

The piecewise linear function is the most straightforward way to interpolate a spectrum, which is subject to random statistical fluctuations. The count rates of any two neighbouring retarding energies $x_j < x_{j+1}$, $j = 1, \dots, m - 1$ with m being number of points in the spectrum, are connected with a straight line. Thus, the interpolating function is expressed as

$$f_{RM}(qU) = k_j(qU - x_j) + q_j, \quad (4.61)$$

where $qU \in [x_j, x_{j+1})$ and k_j and q_j are the interpolation coefficients,

$$k_j = \frac{y_{j+1} - y_j}{x_{j+1} - x_j}, \quad q_j = y_j, \quad (4.62)$$

where y_j are the measured count rates in the reference spectrum. Such an interpolation was used in the work [Zbo11] where a spectrum measured with fine retarding energy steps was utilized as the reference spectrum. A part of the experimental K-32 spectrum interpolated using the piecewise linear function is shown in Fig. 4.19 on the left.

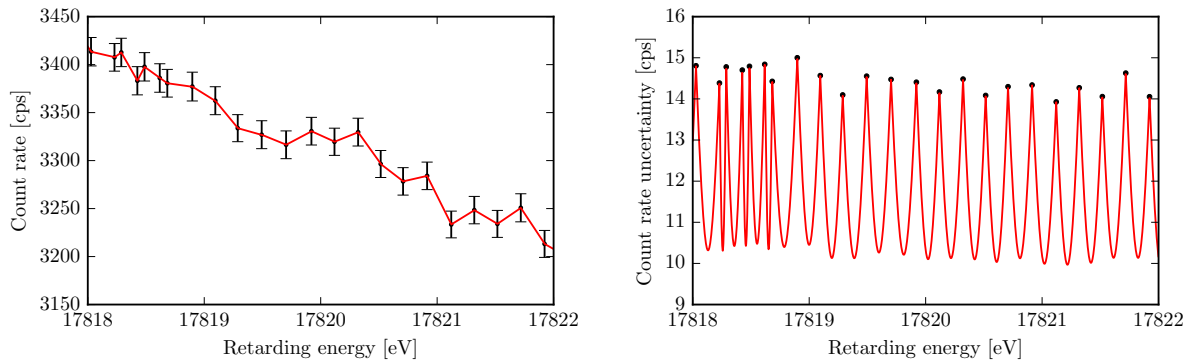


Figure 4.19: Part of the experimental K-32 line interpolated with the piecewise linear function $f_{RM}^{lin}(qU)$ (left) and the uncertainty of the interpolated spectrum (right).

It is essential to consider the uncertainties of the reference spectrum in order to obtain correct fit results and parameter uncertainties. The uncertainties and correlation of the interpolation coefficients k_j and q_j in Eq. (4.62) can be obtained by considering that the linear interpolation is actually a least-squares fit of a linear function to two points. Thus, the covariance matrix $\Sigma^{(j)}$ of k_j and q_j reads

$$\Sigma^{(j)} = \begin{pmatrix} \frac{\sigma_j^2 + \sigma_{j+1}^2}{(x_j - x_{j+1})^2} & \frac{\sigma_j^2}{x_j - x_{j+1}} \\ \frac{\sigma_j^2}{x_j - x_{j+1}} & \sigma_j^2 \end{pmatrix}. \quad (4.63)$$

By the principle of propagation of uncertainty the variance of the model function $S(qU; r, \Delta, b_0)$ is

$$\sigma^2(S(qU; r, \Delta, b_0)) = r^2 \left[(qU - x_j - \Delta)^2 \Sigma_{11}^{(j)} + \Sigma_{22}^{(j)} + 2(qU - x_j - \Delta) \Sigma_{12}^{(j)} \right]. \quad (4.64)$$

The uncertainty of the interpolated K-32 spectrum is shown in Fig. 4.19 on the right. The variance σ_i^2 in the chi-square function in Eq. (4.26) is then composed of the analysed spectrum count rate variance $\sigma_{M_i}^2$ and the reference spectrum variance $\sigma^2(S(qU; r, \Delta, b_0))$, i.e. (cf. Eq. (4.27))

$$\sigma_i^2 = \sigma_{M_i}^2 + \sigma^2(S(qU; r, \Delta, b_0)). \quad (4.65)$$

To check that the reference method with the piecewise linear interpolation gives correct results two representative artificial spectra were calculated using the DSG lineshape (the spectra were not statistically randomized). The lineshape parameters were the same except for the line position which was shifted by -100 meV for the second spectrum. The reference method fit of the second spectrum with respect to the first one yielded $\Delta = -100.81$ meV. The remaining difference of -0.81 meV, which can be attributed to the imperfection of the piecewise linear interpolation, is small and can be neglected.

As in the DSG case a further check of consistency for the reference method was done by observing the fitted relative shift in dependence of the lower fit boundary. The results for an experimental K-32 spectrum are shown in Fig. 4.20. The relative shift seems to be independent of the lower boundary as expected.

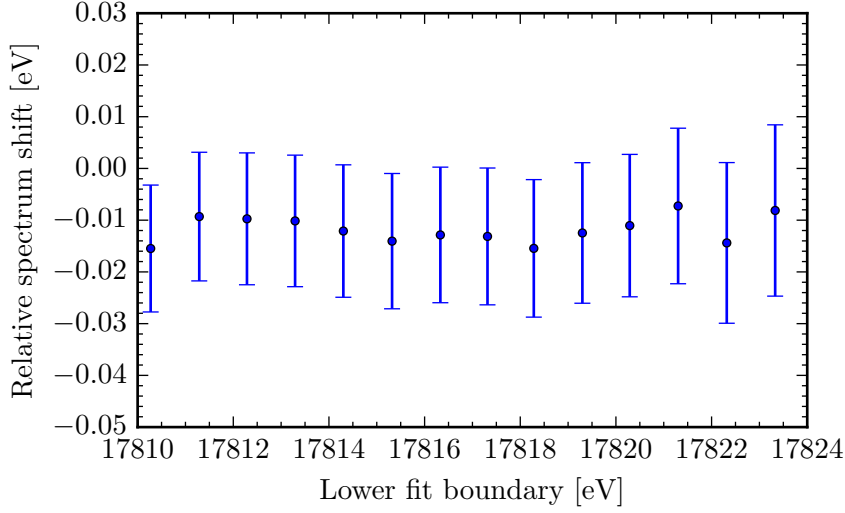


Figure 4.20: The fitted relative shift in dependence of the lower fit boundary for the reference method.

4.5.2 Effect of line shape changes

A reference method fit of a spectrum by another spectrum with a different line shape can lead to wrong value of the relative shift. The size of the error was investigated in the following way. Artificial non-randomized K-32 spectra were calculated using the DSG lineshape and with the same line position. For each spectrum the parameters Gaussian σ and asymmetry α were changed by a constant step for each parameter. The covered parameter range was 0.3 eV to 0.9 eV in the step of 0.025 eV for the σ and 0.07 to 0.13 in the step of 0.0025 for the α . These values were chosen based on the numerous spectra measured with different conversion electron sources at the MoS. In this way, 25×25 spectra were obtained.

Each spectrum was fitted by the reference method using the spectrum with $\sigma = 0.6$ eV and $\alpha = 0.1$ as the reference spectrum. The obtained relative shift Δ is shown in the form of a two-dimensional grid for the considered parameter space in Fig. 4.21. The shift varies from about -20 meV to 40 meV at the considered range of σ with $\alpha = 0.1$ and from about 130 meV to -130 meV for the considered range of α with $\sigma = 0.6$ eV. Thus, a gradual change of the line shape over time may lead to a gradual change of the observed relative shift which could thus be interpreted incorrectly as a drift of the line position. Note that for some combination of the two parameters the resulting systematic shift of Δ mutually cancels out.

4.5.3 Comparison to the DSG approach

The relative shift and relative scale factor results from the reference method analysis of the same K-32 spectra as in Fig. 4.9 are shown in Fig. 4.22. The first spectrum in the series was used as the reference. The total number of fitted parameters was three: relative

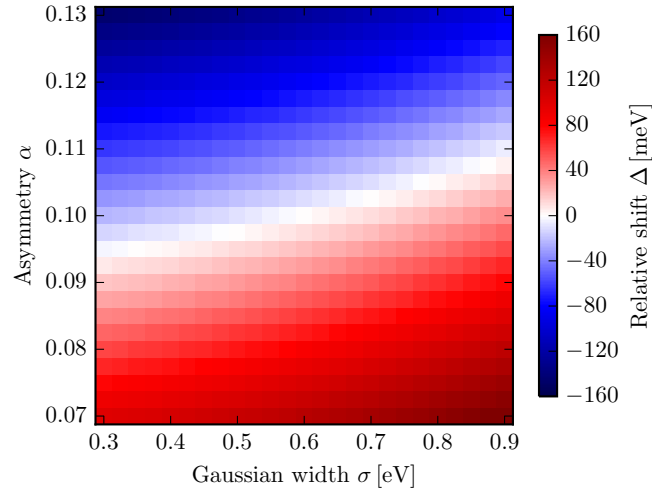


Figure 4.21: The obtained relative shift in dependence of DSG lineshape parameters of the analysed spectrum. A higher Gaussian width σ with respect to the reference spectrum leads to a positive bias in the observed relative shift (below light region). In contrast, a higher asymmetry α leads to a negative bias in the observed shift (above light region). The light region corresponds to the situation when the effects from the change of both parameters mutually cancel out.

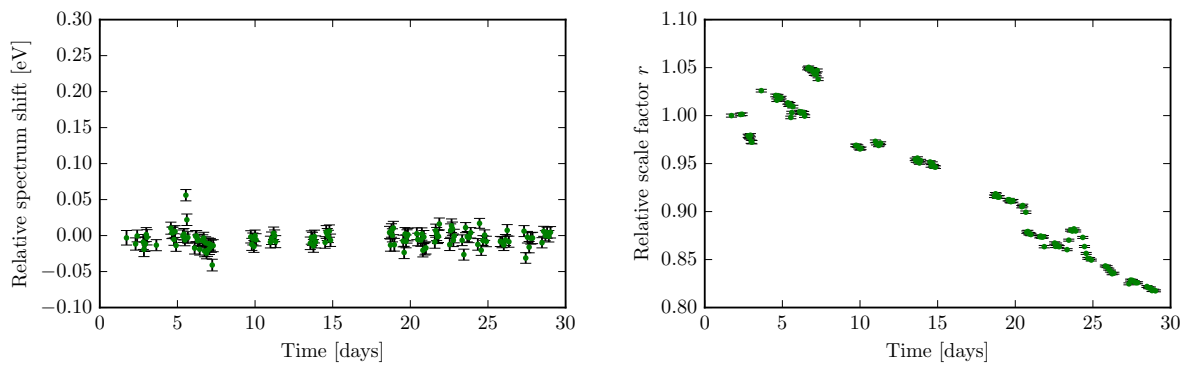


Figure 4.22: Reference method analysis results of the K-32 line utilizing the piecewise linear function for interpolation: relative shift Δ (left) and relative scale factor r (right). For the former the same vertical axis scale as in Fig. 4.9 is used for comparison. The median of the chi-square function values was about $\chi_{\text{dof}}^2 = 0.98$ (33 dof).

scale factor r , relative line position shift Δ and constant background b_0 . The fitted range was from 17 818 eV to 17 840 eV.

The results are completely analogous to the case of the DSG approach albeit a smaller uncertainties are obtained. The asymptotic uncertainties are practically equal to the parabolic ones. Assuming that the line position is constant in time and that the data points are normally distributed, the weighted standard deviation from the spread of values amounts to 11.6 meV, which is a factor of 1.5 smaller than for the DSG. The relative scale factor drops in time by the amount expected from the exponential decay of ^{83}Rb . The relative shift is mildly correlated to the relative scale factor with the correlation coefficient of $\rho \approx -0.3$ and the scale factor is moderately correlated to the constant background with $\rho \approx -0.7$.

4.5.4 Conclusion

The reference method is a convenient way to obtain a relative shift between two spectra. The smaller uncertainties of the relative shift compared to the uncertainties of the line position in the DSG approach make the method more suitable for detecting changes of the high voltage stability. However, the wrong relative shift obtained from comparison of spectra with different line shape can be assessed only by using the method together with a fit by the DSG line shape.

5 The solid $^{83\text{m}}\text{Kr}$ source

The solid $^{83\text{m}}\text{Kr}$ source (SKrS) for KATRIN is a spatially well-defined maintenance-free radioactive source of monoenergetic conversion electrons. It is intended for continuous monitoring of the high-voltage stability in KATRIN by means of the monitor spectrometer (MoS). The source is produced by ion-implanting the ^{83}Rb mother isotope into a solid substrate. In such a way, most of the $^{83\text{m}}\text{Kr}$ which is gaseous under normal conditions is captured in the substrate before it decays. The production method and the substrate influence the electron binding energy and thus its kinetic energy. In order to monitor the high-voltage stability at the ppm level the electron kinetic energy itself has to be stable at a similar level.

For the pilot studies of [Zbo11, Zbo13] altogether four sources were implanted at the ISOLDE (Isotope Separator On Line DEvice) facility in CERN using the platinum and gold substrates and the ^{83}Rb implantation energies¹ of 30 keV and 15 keV. In order to distinguish the different sources the notation

$$X-E-n$$

was used, where X is the substrate element symbol, E is the implantation energy and n denotes serial number. Thus, the sources were denoted as Pt-30-1, Pt-30-2, Au-30-1 and Pt-15-1. Such a notation is continued in the present work.

The studies utilized the MAC-E filter of the Mainz neutrino mass experiment together with the K65 high-precision high voltage divider [Bau13] and a high-precision commercial digital voltmeter. The assessment of the electron energy stability relied on stability of the two electronic devices which was checked in an independent way. The four sources were placed on the source holder all at the same time and the K-32 electron energy was gradually measured for each of them. The results showed promising line position stability especially for the Pt-15-1 source. For all sources at most a linear drift of the line position was observed.

Previously, it was customary to assign the KATRIN maximal allowed systematic uncertainty from the high voltage contribution, see Eq. (3.50), simply as the limit for the size of the allowed high voltage fluctuations. The notation that the high voltage has to be stable within ± 3.2 ppm for the whole KATRIN run was used. Considering a run with the length of two months this was translated that the line position drift has to be within ± 1.6 ppm month⁻¹. Thus, a source having the line position drift larger in absolute value would be considered as not fulfilling the KATRIN requirement. However, there is a certain confusion in these terms.

- Firstly, if the high voltage is allowed to fluctuate within ± 3.2 ppm, the range of values is 6.4 ppm. Thus, if the line position is allowed to gradually acquire the

¹ The lower implantation energy was achieved using a dedicated retardation chamber.

values throughout the whole range, the linear drift in absolute value can be as high as $3.2 \text{ ppm month}^{-1}$ in contrast to the $1.6 \text{ ppm month}^{-1}$ stated above.

- Secondly, the limit in Eq. (3.50) was derived previously [Thü07] when considering a Gaussian fluctuation with the standard deviation σ . But in such a case, about 31.7% of values would deviate by more than one standard deviation, i.e. more than $\pm 3.2 \text{ ppm}$, while the limit would still be valid. This is in contrast to the assumption that the high voltage has to fluctuate only within $\pm 3.2 \text{ ppm}$.
- Finally, the line position drift is a linear function of time and cannot be described by the Gaussian distribution. This is in contrast to using the standard deviation of the Gaussian distribution in terms of limit for the line position drift.

The limit as described by Eq. (3.50) was derived here by considering a distortion which has a general variance σ^2 and correspondingly a general standard deviation σ . The linear drift of the whole scale and linear drift of the scale slope were discussed previously, see Section 3.1.3. Thus, in this work we interpret the KATRIN maximal allowed systematic uncertainty of the high voltage with respect to the line position drift as follows. Assume that a line position drift d which originates only due to the source is measured during the tritium run. If the tritium spectrum is corrected for such a drift while the high voltage is stable, an energy scale distortion is introduced into the tritium spectrum. In such a case, there is a systematic shift introduced into the observed neutrino mass squared which is given by the line position drift according to Eqs. (3.36b) and (3.39b). According to these equations the maximal allowed drift would amount to

$$|c| < 100 \text{ meV month}^{-1} = 5.4 \text{ ppm month}^{-1} \quad (5.1)$$

for a two-month KATRIN run. However, if the SKrS is to be used for actual high-voltage monitoring, its own contribution to the systematic uncertainty budget should be smaller in order to observe distortions of the high voltage at the ppm level. In such a sense, the limit in Eq. (5.1) should not be considered as a strict one but rather as a hint what value of drift to aim for.

For this reason in this work we do not follow the approach that the line position drift should be within the previously used strict limit of $\pm 1.6 \text{ ppm month}^{-1}$, nor that the observed line position results should be within a strict $\pm 60 \text{ meV}$ band. Instead, we evaluate the sources with respect to the line position drift according to what the contribution to the neutrino mass squared shift would be if the drift was used to correct the tritium β -spectrum. For example, the drift reported for the source Au-30-1 was $43(3) \text{ meV month}^{-1}$ from the first 26 d of measurement [Zbo13]. According to Eq. (3.36b) a correction of the tritium β -spectrum for such a drift would lead to a neutrino mass squared shift of $-1.2 \times 10^{-3} \text{ eV}^2$ if the drift was only due to the source. This is about 18% in absolute value of the maximal allowed uncertainty of $7 \times 10^{-3} \text{ eV}^2$. On one hand, such a result could be considered acceptable with respect to Eq. (5.1) but on the other hand, a drift compatible with zero was reported for Pt-15-1 which is certainly more favorable.

Despite the promising results of [Zbo11, Zbo13], several questions regarding the SKrS were raised. The main ones can be briefly described as follows.

- Long-term stability.

The measurement was carried out uninterrupted for only 26 d. After that, a vacuum breakdown due to power short in the spectrometer building occurred. Since the spectrometer was not baked out after the accident, the spectrometer work function was affected which led to a change of the observed line position. However, the KATRIN run time is planned for two months. It is desirable that the electron energy stability is demonstrated for at least such a period.

- Source reproducibility.

For each source a different drift of the line position was obtained. This concerns especially the sources Pt-30-1 and Pt-30-2 which were produced using the same substrate element and implantation energy. However, it is desirable that the source performance is as reproducible as possible.

- Treatment of source after production.

The source were not treated in any special way. However, there is an option to thermally anneal the source after implantation. Such a treatment could repair the lattice damage done by the ^{83}Rb ions and possibly improve the quality of the measured spectra or the observed line position stability.

- Implantation energy.

The lowest ^{83}Rb implantation energy was 15 keV. A lower implantation energy has the advantage of higher relative amount of no-energy-loss electrons. Thus, it is desirable to investigate even lower implantation energies.

- Source substrate.

The Pt substrate seemed to be superior in contrast to the Au substrate for which a rather large drift of the line position was obtained. However, the large proton number of platinum leads to relatively high amount of energy losses of the emitted electrons. Thus, it is desirable to investigate additional substrates in an attempt to reduce the amount of loss-energy electrons.

In this chapter, these issues are addressed using measurements of further samples of the SKrS at the MoS utilizing the K35 divider [Thü09] the stability of which was checked in an independent way.

5.1 Implantation of ^{83}Rb

The SKrS samples investigated in this work were firstly implanted at the ISOLDE facility in CERN. Since the facility was shut down due to the Large Hadron Collider complex upgrade at the end of 2012, the implantations were continued at the Helmholtz-Institut für Strahlen- und Kernphysik of the Bonn University at the Bonn Isotope Separator

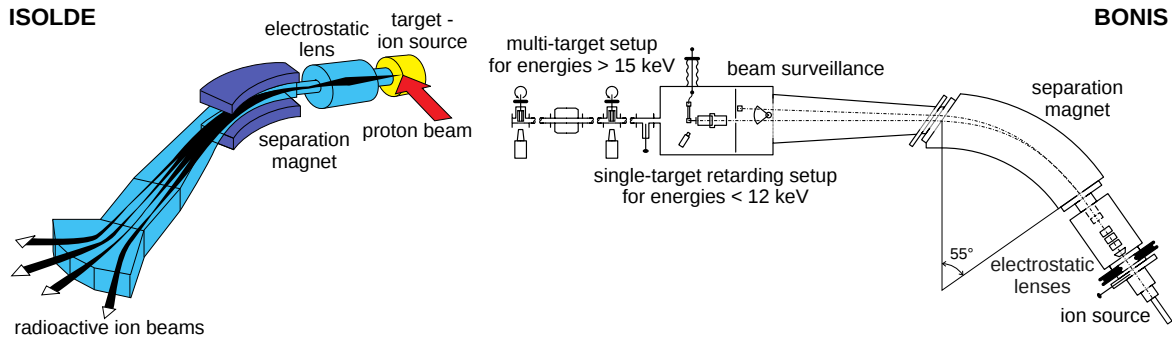


Figure 5.1: Scheme of the ISOLDE facility (left) and the BONIS facility (right). The figures are based on [For99, Are16].

(BONIS). In an ideal case, the SKrS implanted with ^{83}Rb perfectly mass-separated from other isotopes should have the same properties regardless of the implantation facility. In practice, the mass separation as well as the complete operation of the implanter is not perfect and therefore differences between sources resulting from the different implantation facilities could arise. Thus, in this chapter the sources implanted at ISOLDE and BONIS are distinguished.

5.1.1 ISOLDE facility

A scheme of the ISOLDE facility [Kug92] is shown in Fig. 5.1 on the left. At ISOLDE the radioactive isotopes are produced on-line, i.e. in reactions of protons with the energy of about 1.4 GeV with a thick target. The protons are delivered by the proton synchrotron booster. The reactions that can take place in the target include spallation, fission, and fragmentation. The target is maintained at an elevated temperature to allow diffusion of the reaction products out of the target into an ion source. In the case of ^{83}Rb , the ionization takes place on a hot surface since rubidium as an alkali metal is relatively easily ionized by surface ionization. The ions are accelerated by an applied high voltage up to several tens of keV and focused into an electromagnet. Due to the Lorentz force the magnetic field separates the ions based on their mass². The mass-separated ^{83}Rb is directed onto the SKrS substrate, a high-purity foil. The ion current is monitored by means of a Faraday cup.

The best target-ionizer combination, which yielded the highest ^{83}Rb current of up to 0.5 nA, turned out to be uranium carbide - tantalum. Such a current corresponds to ^{83}Rb activity accumulation rate of about 1 MBq h^{-1} . A slightly lower current of about 0.35 nA was reached using the combination of uranium carbide - rhenium. For the option uranium carbide - tungsten only 0.05 nA was reached resulting in slow accumulation of the activity. For all samples but one the general purpose separator (GPS) with the mass-resolving power of $m/\Delta m \approx 2400$ was used. In a single case, the high resolution separator (HRS) with $m/\Delta m \approx 7000$ to 15 000 was utilized due to malfunction of the GPS. In the

² More generally, the separation is done based on the mass-to-charge ratio.

previous work the inherent lowest possible ^{83}Rb implantation energy amounted to 30 keV. The Pt-15-1 sample was produced using a dedicated retarding chamber. For all the samples but one studied in this work the implantation energy as low as 10 keV became possible without the need for the retarding chamber.

An overview of the samples obtained at ISOLDE is given in Table 5.1. The source characteristics given in the table are discussed further in Section 5.2. The source Pt-15-2, which was implanted using the dedicated retarding chamber, was utilized primarily earlier for commissioning of the MoS [Sch11]. After four half-lives, the source became too weak and unsuitable for further studies. The purpose of the first 2011/Sep collection was to obtain a new strong source for a long-term stability measurement of the conversion line position at the MoS. Furthermore, to observe reproducibility of a single implantation a second source with the same substrate and implantation energy was made (Pt-15-3 and Pt-15-4). For the third source an iridium substrate was used (Ir-15-1) in order to assess the satellite structure observed at the $\text{N}_{2,3}$ -32 doublet which is briefly discussed in Section 5.5. Unfortunately, due to the utilized W ionizer which led to too small ^{83}Rb current and time restrictions only weaker sources were obtained. Therefore, another collection using the Ta ionizer was performed later in the month resulting in a strong source implanted at 15 keV (Pt-15-5). To further address the possible advantages of the lower implantation energy another source was obtained using the Re ionizer later in the same year (Pt-10-1). The purpose of last obtained source Pt-30-5 was to replace the Pt-10-1 after it became too weak. However, at that time the GPS developed a malfunction and the replacement source had to be obtained at 30 keV using the HRS. Unfortunately, only small amount of activity was collected.

5.1.2 BONIS facility

A scheme of the BONIS [Fre79, Are16] is shown in Fig. 5.1 on the right. The implantation at BONIS is off-line meaning that only the mass separation and implantation take place and the ^{83}Rb supply has to be obtained externally. The ^{83}Rb is conveniently produced at the NPI Řež U-120M cyclotron by reaction of 27 MeV protons with a pressurized target filled with $^{\text{nat}}\text{Kr}$ [Vén05]. A limited capability of producing ^{83}Rb is available at the Bonn isochronous cyclotron where the reaction $^{81}\text{Br}(\alpha, 2n)^{83}\text{Rb}$ is utilized for the primary energy of the α -particles of 54 MeV. The rubidium dissolved in a water solution is filled into a cylindrical tungsten furnace and the solvent is let to evaporate under an infrared lamp. The furnace is then transported to Bonn where it is filled with $^{\text{nat}}\text{Rb}$ (about 3/4 of ^{85}Rb and 1/4 of ^{87}Rb) in the form of about 0.5 mg of RbCl which acts like a carrier during the implantation process. After the furnace is closed with an endcap with 0.5 mm aperture it is put into the ion source where it is heated by impacts of electrons thermally emitted from the two surrounding coil-shaped tungsten electrodes. The temperature at the top, where the surface ionization of ^{83}Rb takes place, reaches values of up to about 3000 °C while at the bottom, where ^{83}Rb gets evaporated, it is at the level of 1000 °C. The ion source is kept on high voltage (pre-acceleration voltage) of typically 30 kV to 40 kV.

A set of electrostatic lenses extracts and focuses the ion beam into the separation

magnet which separates the isotopes of Rb by their mass. Behind the magnet the mass-separated beams enter a box which firstly contains beam diagnostic equipment. The most important beam surveillance device is the oscillating probe, a metal pin, that sweeps perpendicularly through the beams providing their actual cross-section. Since the ^{83}Rb current is too small to be observable the stable $^{\text{nat}}\text{Rb}$ is utilized for the beam surveillance. Further, in case of implantation with the energy of about 20 keV and higher deflection capacitors are present in the box to be used for aiming the beam onto a position on a multi-target collector further downstream. The setup behind the box further comprises a shutter valve for blocking instable beams, a NaI detector for in-situ online activity measurement and additionally a booster section for implantation with energies of up to 160 keV. In case a lower implantation energy is desired, the capacitors in the box are replaced by a cylindrical retarding lens, a single-target holder and a cerium-doped lutetium oxyorthosilicate (LSO) detector connected to an avalanche photodiode for in-situ activity measurement. The retarding lens is at the same electrical potential as the ion source and the target holder is at the retarding lens potential reduced by an additional power supply leading to the desired implantation energy.

Each implantation at BONIS is characterized by ^{83}Rb implantation efficiency. If A_f is the activity in the furnace prior to the implantation and A is the source activity after the implantation, the efficiency ζ is defined as

$$\zeta = \frac{A}{A_f} \cdot 100 \%. \quad (5.2)$$

The efficiency is highly affected by the geometry and temperature distribution of the furnace. While only a few percent efficiency was achieved for the first sources, values of about 25 % were reached in the later implantations.

Altogether five collections each yielding two to four samples were carried out at BONIS. An overview of the obtained samples is given in Table 5.1. It was attempted to subsequently address all the issues outlined in the beginning of this chapter. Furthermore, each subsequent collection depended also on the electron spectroscopy measurement results of the previous ones obtained at the MoS. Thus, the individual samples are discussed together with the MoS measurement results in Section 5.3.

5.2 Basic SKrS characteristics

Each SKrS is characterized by its substrate and the ^{83}Rb implantation energy and by three basic properties observable by means of γ -spectroscopy.

- Substrate.

The substrate represents the surrounding environment for the ^{83}Rb and $^{83\text{m}}\text{Kr}$ atoms and is thus the primary factor which influences the emitted electrons. The substrate is discussed in Section 5.2.1.

- Implantation energy.

Table 5.1: Overview of the solid ^{83m}Kr source samples implanted at ISOLDE (upper part) and BONIS (lower part). Listed are the basic SKrS characteristics as described in Section 5.2. For a discussion of the substrate and implantation energy see Sections 5.2.1 and 5.2.2, respectively. Furthermore, shown are the implanted ^{83}Rb activity A (Section 5.2.3), the area S of the activity distribution half maximum, the peak implanted dose Q_S^{\max} , the peak concentration Q_C^{\max} , and the peak concentration relative to the substrate concentration $Q_C^{\max}/C^{\text{subs}}$ (Section 5.2.4) and the retention R (Section 5.2.5). The uncertainties, if given, are statistical only and refer to the 68.27% (1σ) confidence level.

Produced	Source	A (MBq)	S (mm ²)	Q_S^{\max} ($10^{14} \frac{\text{ion}}{\text{cm}^2}$)	Q_C^{\max} ($10^{20} \frac{\text{ion}}{\text{cm}^3}$)	$Q_C^{\max}/C^{\text{subs}}$ (%)	R (%)
2010/Oct	Pt-15-2	2.9	6.88(3)	3.16	5.31	0.80	79.4(44)
2011/Sep	Pt-15-3	1.3	5.53(7)	1.24	2.09	0.32	91.2(42)
	Pt-15-4	1.2	5.54(5)	1.14	1.92	0.29	93.8(21)
	Ir-15-1	0.7	3.27(1)	1.13	2.05	0.29	86.3(29)
2011/Sep	Pt-15-5	2.7	5.68(6)	2.83	4.76	0.72	89.9(13)
2011/Nov	Pt-10-1	2.8	8.42(9)	2.23	5.14	0.78	91.8(10)
2012/Nov	Pt-30-5	0.4	5.60(5)	0.40	0.41	0.06	95.1(11)
2012/Oct	Pt-30-3	0.6	20.86(26)	0.21	0.22	0.03	89.5(9)
	Pt-30-4	0.2	18.39(19)	0.08	0.09	0.01	92.4(15)
2013/feb	Pt-80-1	1.5	19.66(16)	0.62	0.31	0.05	n/a
	Pt-30-6	0.7	15.05(20)	0.36	0.37	0.06	n/a
2013/Apr	Pt-30-7	4.6	16.96(27)	1.81	1.88	0.28	n/a
	ZnO-30-1	0.8	17.93(5)	0.48	0.36	0.09	n/a
	ZnO-30-2	4.2	19.94(9)	2.33	1.76	0.42	92.5(27)
2013/Oct	Pt-30-8	2.8	15.82(11)	1.50	1.56	0.24	n/a
	Pt-30-9	3.4	19.75(12)	1.62	1.68	0.25	n/a
	HOPG-30-1	3.6	15.99(16)	1.97	1.58	0.14	89.5(21)
2014/Jun	Pt-12-1	3.3	4.44(4)	5.96	11.98	1.81	78.6(17)
	HOPG-12-1	3.7	5.56(4)	6.16	9.64	0.85	96.6(24)
	HOPG-4-1	3.5	7.90(9)	3.82	12.48	1.09	97.2(25)
	HOPG-8-1	2.4	7.96(16)	1.90	3.93	0.34	> 98.9

The implantation energy determines the penetration depth of ^{83}Rb ions and thus the relative amount of no-energy-loss electrons leaving the substrate. The lower the energy, the lower the probability that an electron will be inelastically scattered. However, lowering the implantation energy for a substrate with high proton number also increases the relative amount of ^{83}Rb which resides in the contamination layer. While the lower energy decreases the amount of damage done to the lattice, at the same time it increases the ^{83}Rb peak concentration. Similarly, the $^{83\text{m}}\text{Kr}$ retention (see further) could possibly be smaller with low enough implantation energy. The implantation energy is discussed in Section 5.2.2.

- Activity of the implanted ^{83}Rb .

The count rate of $^{83\text{m}}\text{Kr}$ conversion electrons observable at the MoS is directly proportional to the activity of the mother isotope ^{83}Rb . Similarly, the implanted ^{83}Rb dose depends directly on the ^{83}Rb activity. Methods for determination of the activity are discussed in Section 5.2.3.

- Radiographical image of the activity distribution.

The lateral size of the activity spot provides information for source and detector alignment in the MoS. Moreover, the lateral activity distribution is essential to address the implanted dose. Lastly, it can be utilized for a more accurate description of the MoS transmission function. The measurement of the radiographical image is discussed in Section 5.2.4. The more accurate description of the transmission function is discussed in Section 5.6.

- $^{83\text{m}}\text{Kr}$ retention in the solid substrate.

Since $^{83\text{m}}\text{Kr}$ is a gas and has a half-life of about 1.8 h, it may escape the substrate prior to its decay. In such a situation, the emitted conversion electrons can no longer be detected by the MoS and are lost for monitoring. Thus, the retention provides information about the expected electron count rate at the MoS. The method for the retention measurement is reviewed in Section 5.2.5.

5.2.1 Source substrate

In the work [Zbo11] three platinum and one gold substrates were used for the SKrS investigation. The substrates were polycrystalline circular foils³ with the diameter of 12 mm and thickness of 25 μm having purity of at least 99.99%. The only exception was the first Pt-30-1 for which a 99.7%-purity and 40 μm -thick foil was used. The long-term electron measurements showed more favorable line position stability for the Pt-based sources compared to the Au-based one. Thus, the Au substrate was not further investigated.

The Pt (and Au) substrate was chosen for its chemical inertness, relatively good mechanical toughness, and stability under ultra-high vacuum. Due to high proton number

³ Supplier: Goodfellow Cambridge Ltd., the United Kingdom.

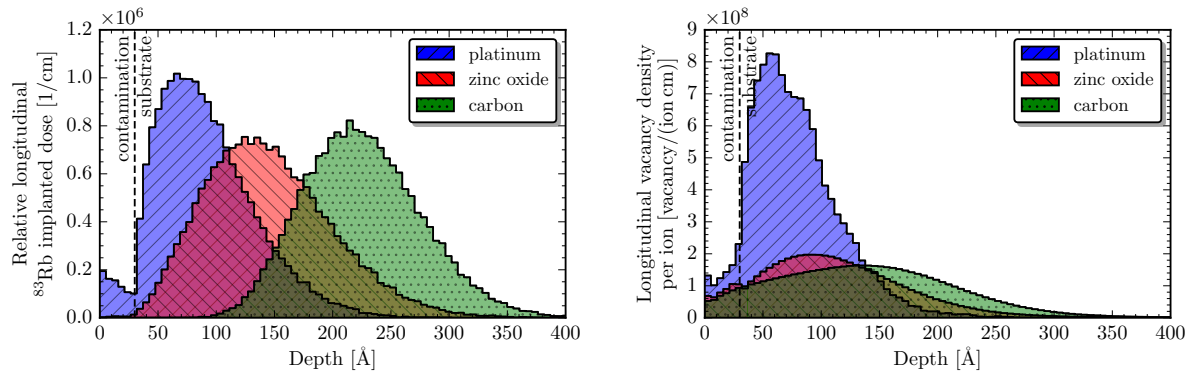


Figure 5.2: Distribution of the relative number of ^{83}Rb atoms per unit depth (left) and vacancies per ion per unit depth (right) obtained using the SRIM code [Zie10] for platinum, zinc oxide and carbon substrates. A contamination layer composed of carbon with the thickness of 30 \AA was assumed for all substrates. The ^{83}Rb energy was assumed to 30 keV . The total number of simulated ions was 6×10^4 in each case.

and density the ^{83}Rb longitudinal profile is rather shallow and sharply peaked, see Fig. 5.2 on the left. However, the same facts lead to a higher probability of electron inelastic scattering. The main disadvantage of Pt is the severe damage of the substrate lattice caused by the impacting ^{83}Rb ions which dislocate the Pt atoms from their lattice sites, see Fig. 5.2 on the right. On the other hand, some self-healing of the lattice during the implantation could take place since the ion energy prior to stopping is distributed into lattice phonons and the substrates are implanted at room temperature. Unfortunately, the self-annealing effects at room temperature are not included in the SRIM simulation.

The lattice damage can be healed by annealing the substrate at high temperature. According to [Zbo11] the recommended temperature for metals amounts to $2/3$ of the melting temperature which for Pt means about $1200\text{ }^\circ\text{C}$. However, there are suggestions that most of the lattice restoration for Pt takes place at a temperature below $400\text{ }^\circ\text{C}$ [Due69]. The formerly mentioned temperature is not reachable for the SKrS since already at about $500\text{ }^\circ\text{C}$ the ^{83}Rb starts to diffuse out of the substrate thus reducing the usable activity [Kür13] (see also further in this work). Due to the diffusion the longitudinal as well as lateral ^{83}Rb distribution can be changed after the annealing.

In this work two further substrates were investigated: zinc oxide (ZnO), a semiconductor, and highly-oriented pyrolytic graphite (HOPG), a conductor. The ZnO ⁴ was used in the form of a monocrystal with the dimensions of $5 \times 5\text{ mm}^2$ and the thickness of 1 mm . Owing to the lower proton number and density the ^{83}Rb longitudinal profile is deeper and broader, see the Fig. 5.2. The amount of lattice damage is only moderate. Moreover, annealing is possible up to about $700\text{ }^\circ\text{C}$ without any loss of activity but with almost complete restoration of the lattice [Keß08, Kür13]. Due to the monocrystalline structure the ^{83}Rb can possibly penetrate much deeper into the substrate along the crystallographic axis due to channeling when only electronic energy losses occur, i.e. when there are no

⁴Supplier: CrysTec GmbH, Germany.

collisions with the target nuclei. Thus, the substrate has to be implanted at a tilt angle to avoid the channeling effect.

The HOPG⁵ has the dimensions of $10 \times 10 \text{ mm}^2$ and the thickness of 1 mm. The substrate can be cleaved in a clear way along a plane parallel to the hexagonal graphite layers so that two substrates with 0.5 mm thickness each are obtained. The small proton number and density lead to a deep and broad ^{83}Rb longitudinal profile, see the Fig. 5.2. Thus, for HOPG lower implantation energies are more beneficial. Similarly as for ZnO only moderate lattice damage takes place. In this case, annealing is possible at about 600°C with sufficient lattice restoration and practically no ^{83}Rb loss [Kam80, Kür13]. The disadvantage is the vulnerability to mechanical manipulation. Owing to the crystallographic structure channeling has to be avoided by tilting the substrate prior to the implantation.

5.2.2 Implantation energy

The implantation energy influences the longitudinal spread of the ^{83}Rb ions and the peak concentration (with the same implanted surface dose). The relative longitudinal ^{83}Rb implanted dose for the Pt, ZnO, and HOPG substrates for different ^{83}Rb energies is shown in Fig. 5.3. In the case of platinum the ^{83}Rb ions concentrate close to the surface and some fraction of the ions is found in the contamination layer. With lower implantation energy the fraction significantly increases. In the other two cases the ions are implanted deeper and there is little or no back-scattering which would lead to presence of ^{83}Rb ions in the contamination layer. The maximal concentration is the largest for Pt regardless of the implantation energy.

The obtained profiles can be used to estimate the expected relative amount of no-energy-loss electrons. The probability density distribution for the electron inelastic scattering is given by the function $p_{IS}(x)$ in Eq. (4.54). Thus, the probability $p_{\text{no-loss}}(x)$ that the electrons from the depth x will not be inelastically scattered is given by

$$p_{\text{no-loss}}(x) = 1 - \int_0^x p_{IS}(y) dy = e^{-\frac{x}{\lambda}}, \quad (5.3)$$

where the index IS at the inelastic mean free path λ was dropped for simplicity. Since the number of electrons emitted from each depth is governed by the ^{83}Rb profile, the total probability of no energy loss is given by

$$P_{\text{no-loss}} = \int_0^{+\infty} e^{-\frac{x}{\lambda}} f_{Rb}(x) dx, \quad (5.4)$$

where $f_{Rb}(x)$ is the fraction of ^{83}Rb ions per unit depth. In general, the inelastic mean free path in the substrate λ_S is different from the mean free path in the contamination layer λ_C . In such a case, the total probability of no energy loss can be written as

$$P_{\text{no-loss}} = \int_0^a e^{-\frac{x}{\lambda_C}} f_{Rb}(x) dx + e^{-\frac{a}{\lambda_C}} \int_a^{+\infty} e^{-\frac{x-a}{\lambda_S}} f_{Rb}(x) dx, \quad (5.5)$$

⁵Supplier: SPI Supplies, the United States of America, grade SPI-1.

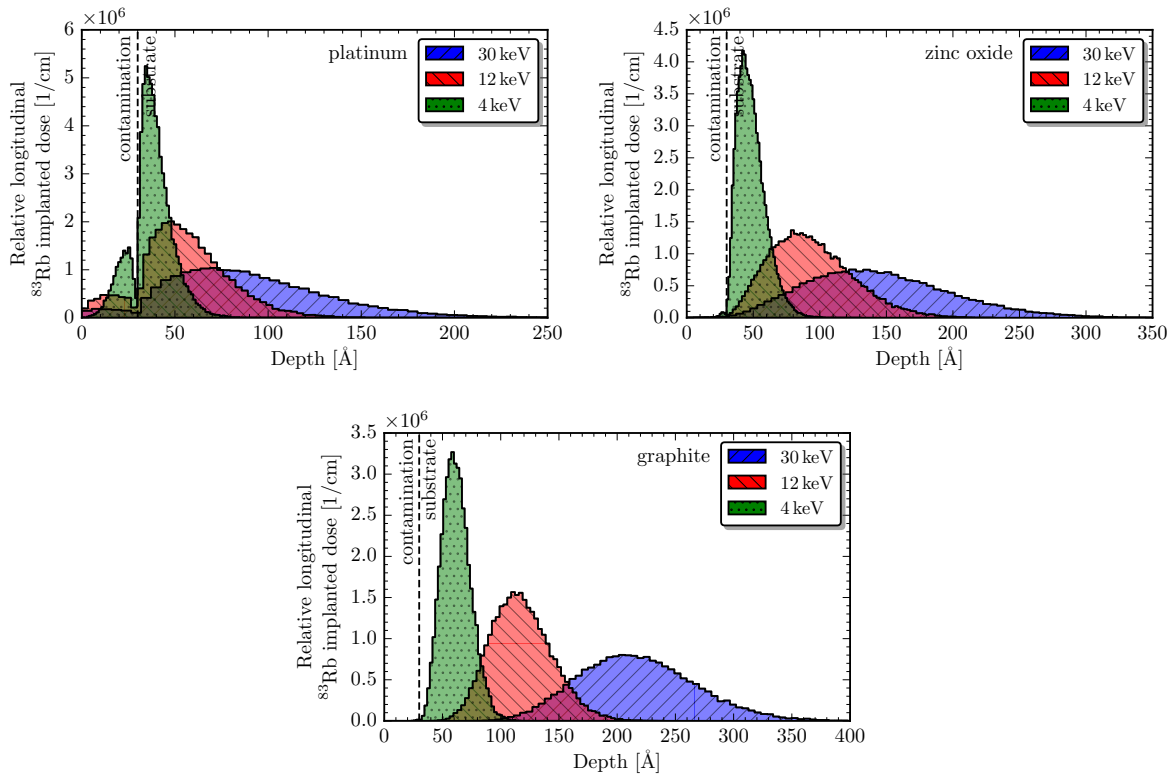


Figure 5.3: Distribution of the relative number of ^{83}Rb atoms per unit depth in platinum (top left), zinc oxide (top right), and graphite (bottom) for the ^{83}Rb implantation energies of 30 keV, 12 keV and 4 keV obtained using the SRIM code. A contamination layer composed of carbon with the thickness of 30 \AA was assumed for all substrates. The total number of simulated ions ranged from 3×10^4 to 6×10^4 .

where a is the thickness of the contamination layer.

The mean free path for the K-32 electrons with the energy of 17.83 keV in platinum amounts to about $\lambda_{Pt} = 132 \text{ \AA}$ whereas in the contamination layer we assume it amounts to $\lambda_C = 202 \text{ \AA}$ (assuming mostly carbon content) [Tan11]. We assume the same value for the highly-oriented pyrolytic graphite. The mean free path in zinc oxide amounts to about $\lambda_{ZnO} = 211 \text{ \AA}$ [Tan94]. The fractions of no-loss electrons for the three substrates and three implantation energies are listed in Table 5.2.

5.2.3 ^{83}Rb activity

High-purity germanium detector

The ^{83}Rb activity is determined by means of a coaxial high-purity germanium (HPGe) detector⁶, which is available in NPI Řež, by observing the strong 520 keV γ -line, see Fig. 3.4. The detector diameter and length amount to 5.28 cm and 4.91 cm , respectively.

⁶Supplier: ORTEC, the United States of America.

Table 5.2: Expected relative amount of no-energy-loss electrons for various ^{83}Rb implantation energies and substrates.

^{83}Rb energy (keV)	No-loss fraction		
	Pt	ZnO	HOPG
30	0.56	0.51	0.35
12	0.70	0.64	0.56
4	0.80	0.79	0.73

If $r(520)$ is the count rate observed by the detector measuring the implanted source then the activity A reads

$$A = \frac{r(520)}{f(520)\eta(520)}, \quad (5.6)$$

where $\eta(520)$ is the detector efficiency for 520 keV photons emitted isotropically from a source placed at a certain geometry with respect to the detector and $f(520) = 0.447(22)$ is the intensity per ^{83}Rb decay [McC15]. An example of the HPGe spectrum of ^{83}Rb implanted in platinum is shown in Fig. 5.4 on the left.

The efficiency was established using measurements of strong γ -lines of calibration sources with known activities at the same geometry. The dependence of the measured efficiency on energy using ^{133}Ba and ^{152}Eu calibration sources for the detector-source distance of 25.9 cm around the 520 keV energy is shown in Fig. 5.5 on the left. The uncertainty of each point includes the statistical uncertainty of the count rate in the calibration peak, the uncertainty of the corresponding intensity per decay, the uncertainty of the calibration source activity and the estimated uncertainty of reproducibility of source positioning. In the log-log plot the trend appears to be linear, i.e. the data can be fitted using

$$\ln \eta(E; \mathbf{a}) = a_0 + a_1 \ln E, \quad (5.7)$$

where E is the energy and $\mathbf{a} = (a_0, a_1)$ is a vector of parameters.

Due to common calibration sources the efficiencies are correlated which has to be taken into account in the least-squares fit using Eq. (5.7). The chi-square function generalized for the case of non-zero covariances between the data points can be written as, cf. Eq. (4.26),

$$\chi^2(\mathbf{a}) = [\eta_M - \eta(E; \mathbf{a})]^T \Sigma^{-1} [\eta_M - \eta(E; \mathbf{a})], \quad (5.8)$$

where η_M is a vector of the measured efficiencies at the energies E and Σ is the covariance matrix of the efficiencies. The matrix Σ is obtained by the principle of propagation of uncertainty as

$$\Sigma = J \Sigma_0 J^T, \quad (5.9)$$

where J is the Jacobian matrix of the transformation of n count rates (divided by the corresponding intensities) and m activities into the n efficiencies and Σ_0 is the diagonal covariance matrix of the count rates and activities.

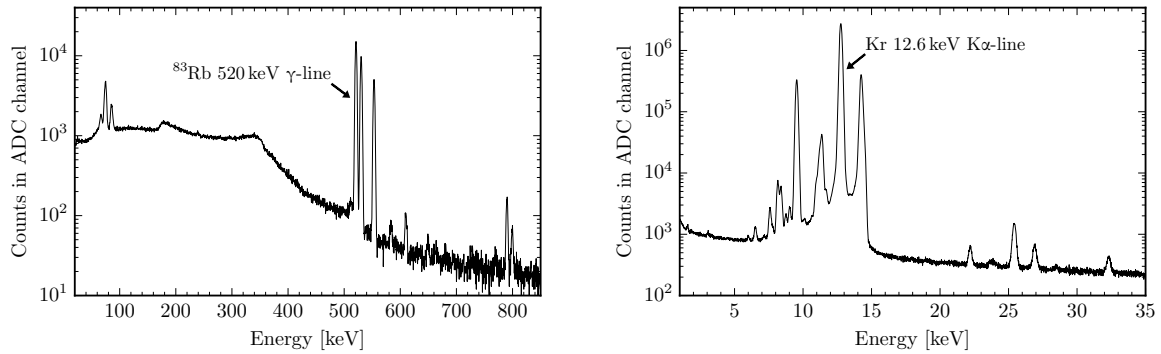


Figure 5.4: Left: Example of the γ -spectrum of ^{83}Rb implanted in platinum measured at the HPGe detector. Observed is the strong 520 keV line and additional ^{83}Rb lines together with Pt KX x-rays. Right: Example of the γ -spectrum of ^{83}Rb implanted in platinum measured at the SDD. Here mostly the Kr KX x-rays and the 9.4 keV γ -line observed in the decay of ^{83}Rb are seen together with the Pt LX x-rays. The $L\alpha$ x-rays of Pt have the energy close to 9.4 keV and therefore cannot be distinguished from the γ -line. The weak 32 keV γ -line observed in the decay of $^{83\text{m}}\text{Kr}$ is also observed.

The efficiency at 520 keV was obtained from Eq. (5.7) using the least-squares fitted parameters \mathbf{a} as

$$\eta(520) = 5.86(7) \times 10^{-4} \quad (5.10)$$

which is marked in the Fig. 5.5. The function in Eq. (5.7) is also shown in the figure. The relative uncertainty of the efficiency amounts to 1.2%. Thus, the uncertainty of the activity determined by Eq. (5.6) is dominated by the relative uncertainty of the intensity $f(520)$ of 4.9% provided that the 520 keV peak is measured with enough statistics.

Silicon drift detector

The technique of observing the 520 keV γ -ray from the decay of ^{83}Rb as described above is straightforward and reliable but it requires the presence of the HPGe detector which has to be continuously cooled by liquid nitrogen. For the ability to measure the x-ray and γ -ray spectra on site of the MoS the silicon drift detector⁷ (SDD) is utilized and the Kr-K α x-rays with the energy of 12.63 keV from the decay of both ^{83}Rb and $^{83\text{m}}\text{Kr}$ are observed. The cylindrical detector dimensions amount to $25 \text{ mm}^2 \times 0.5 \text{ mm}$. The detector is equipped with a thin beryllium window and a multilayer collimator restricting the photons to the area of 17.1 mm^2 to avoid edge effects. The detector is cooled by means of the Peltier effect.

In the transient equilibrium, which is established about 12 h after the source production, the activity A_{Kr} of $^{83\text{m}}\text{Kr}$ is given by

$$A_{Kr} = \gamma R \frac{T_{Rb}}{T_{Rb} - T_{Kr}} A, \quad (5.11)$$

⁷Supplier: Amptek, Inc., the United States of America.

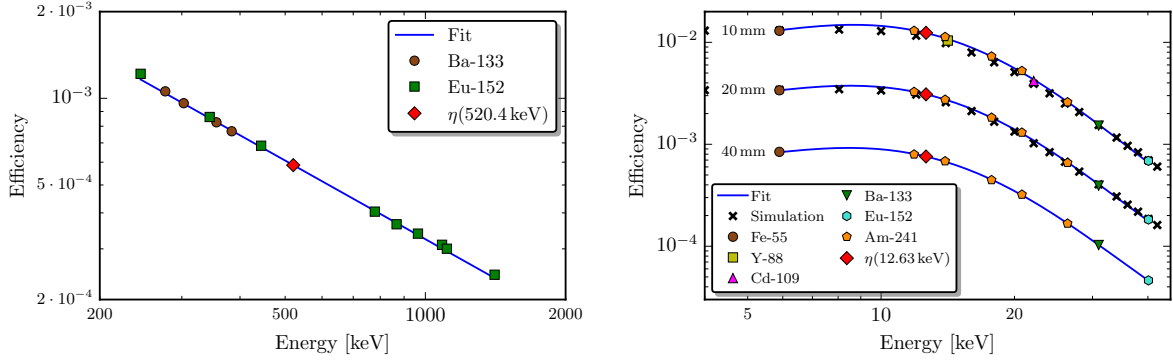


Figure 5.5: Efficiency of the HPGe detector for the source-detector distance of 25.9 cm (left) and efficiency of the SDD for the distances of 10 mm, 20 mm and 40 mm (right). The uncertainties are not shown for simplicity.

where γ is the branching ratio, R is the fraction of $^{83\text{m}}\text{Kr}$ which decay in the source, i.e. $^{83\text{m}}\text{Kr}$ retention, and T_{Rb} and T_{Kr} are the half-lives of ^{83}Rb and $^{83\text{m}}\text{Kr}$, respectively. If the count rate observed by the detector is $r(\text{Kr-K}\alpha)$ then the activity A is given as

$$A = \frac{r(\text{Kr-K}\alpha)}{\eta(12.6) \left[f_{Rb}(\text{Kr-K}\alpha) + \gamma R \frac{T_{Rb}}{T_{Rb} - T_{Kr}} f_{Kr}(\text{Kr-K}\alpha) \right]}, \quad (5.12)$$

where $\eta(12.6)$ is the corresponding detector efficiency and $f_{Rb}(\text{Kr-K}\alpha) = 0.510(16)$ and $f_{Kr}(\text{Kr-K}\alpha) = 0.149(5)$ are the intensities per decay from ^{83}Rb and $^{83\text{m}}\text{Kr}$, respectively [McC15]. An example of the SDD spectrum of ^{83}Rb implanted in platinum is shown in Fig. 5.4 on the right.

The efficiency was determined for the distances of source to the detector surface of 10 mm, 20 mm and 40 mm, respectively, by observing the intensities of x-rays and γ -rays of calibration sources with known activities. Owing to their lower energy the relative intensity of photon lines after attenuation in material between the source and the detector (source cover, air) was taken into account as a multiplicative factor of the source activity. The attenuation at the order of several percent was either measured experimentally or estimated using known mass attenuation coefficients [Hub04]. Since the detector acquisition software does not increase the measuring time in order to compensate for the dead time, the true count rate r_t in each channel was estimated manually from the measured count rate r_m by numerically solving the paralyzable dead-time equation

$$r_m = r_t \exp(-r_t T_d), \quad (5.13)$$

where $T_d = (1 + F) \cdot 23.2 \mu\text{s}$ (from detector pulse shape settings) and F equals the detector threshold divided by mean pulse amplitude (spectrum dependent). The dead time as reported by the acquisition software was not used since it was found to be inconsistent in contrast to the manual estimation described above. For details see Appendix A.

In order to check the measurement results the efficiency at 10 mm and 20 mm was also estimated by a Monte Carlo simulation. A large number of isotropically emitted photons

with the corresponding energy was randomly generated and tracked in small distance steps. The relative number of photons which caused photoelectric effect in the detector volume was taken as the efficiency. In the simulation the full detector geometry including the Be window and the multilayer collimator was taken into account. The photoelectric, coherent and incoherent scattering effects were considered by using the corresponding differential [Hub75, Hub79] and total cross sections [Ber10].

The dependence of the efficiency measured using the calibration sources ^{55}Fe , ^{88}Y , ^{109}Cd , ^{133}Ba , ^{152}Eu , and ^{241}Am , respectively, on the energy is shown in Fig. 5.5 on the right together with the simulation results. The results from various isotopes seem to be consistent and there is a fairly good agreement with the simulation. The remaining differences could be attributed to uncertainties of the geometry (simulated and/or experimental). The efficiency uncertainties have the same contributions in the HPGe case and additionally include the uncertainty of the attenuation factor. In contrast to the HPGe case the efficiency for 12.6 keV is in a region where the trend is non-linear in the log-log plot. Therefore, higher powers of $\ln E$ up to and including the fourth order were considered to fit the trend, i.e.

$$\ln \eta(E; \mathbf{a}) = \sum_{i=0}^4 a_i (\ln E)^i. \quad (5.14)$$

The efficiencies at 12.6 keV were obtained from Eq. (5.14) using the least-squares fitted parameters \mathbf{a} as

$$\eta(12.6; 10 \text{ mm}) = 1.24(1) \times 10^{-2}, \quad (5.15a)$$

$$\eta(12.6; 20 \text{ mm}) = 3.09(4) \times 10^{-3}, \quad (5.15b)$$

$$\eta(12.6; 40 \text{ mm}) = 7.59(10) \times 10^{-4}. \quad (5.15c)$$

The values are marked in the Fig. 5.5. The function in Eq. (5.14) is also shown in the figure for each geometry. The relative uncertainty of the efficiency amounts to about 1%. Thus, the determination of activity from the Eq. (5.12) is weighted mainly by the uncertainties of the decay intensities $f_{Rb}(\text{Kr-K}\alpha)$ and $f_{Kr}(\text{Kr-K}\alpha)$.

Comparison of the HPGe and SDD results

In order to verify the activity determination several ^{83}Rb sources were measured at both detectors. The sources were Pt-30-7, Pt-30-9, HOPG-8-1, and Pt-12-1 which have the $^{83\text{m}}\text{Kr}$ retention R at the level⁸ of 80% to 100%. Additionally, one measured source was made by depositing the ^{83}Rb water solution on a polyethylene (PET) foil. For such a source the 32 keV γ -ray peak is not visible in the detector spectrum and thus the $^{83\text{m}}\text{Kr}$ retention is zero⁹.

⁸ Only the retentions of the sources HOPG-8-1 and Pt-12-1 were measured explicitly due to time constraints prior to the long-term stability measurement at the MoS. For the sources Pt-30-7 and Pt-30-9 it was assumed to be 90(2)% based on numerous results for platinum-based sources implanted with ^{83}Rb

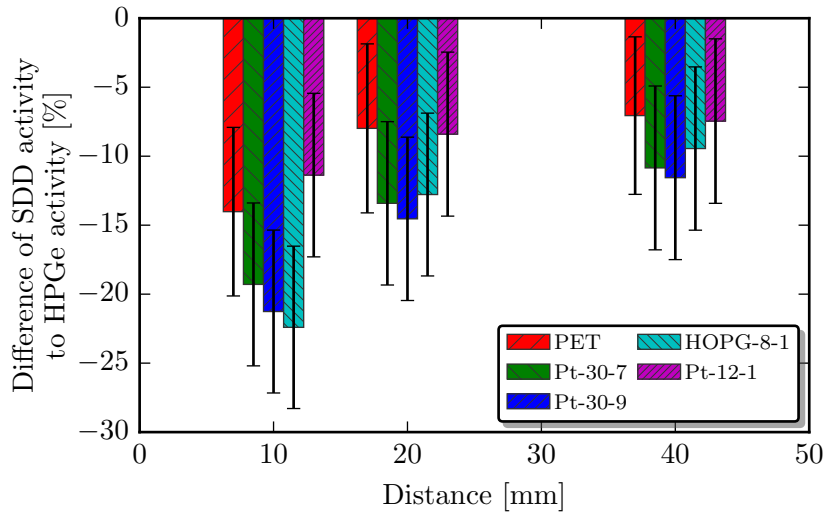


Figure 5.6: Differences of activities determined by the SDD and the HPGe for three distances source-detector at the SDD.

The relative differences between the activity determined by means of the SDD at the distances of 10 mm, 20 mm and 40 mm and the activity determined by the HPGe are shown in Fig. 5.6. The uncertainties of $f(520)$, $f_{\text{Rb}}(\text{Kr-K}\alpha)$, and $f_{\text{Kr}}(\text{Kr-K}\alpha)$ were treated as independent. All the differences tend towards negative values although the uncertainties are large and there is an agreement with zero at the level of two sigma in the case of 40 mm. For smaller distances the values seem to be even more negative. This could reflect the fact that the source activity spot is up to several mm wide and at the close geometry a loss of efficiency occurs. Moreover, centering of the source on the detector is done on the substrate but the activity spot can generally be off-centered. Such a picture is supported by the results of Pt-12-1 which has the smallest activity spot and the corresponding loss of efficiency is by far the smallest.

Owing to such results the activity of the SKrS measured by the SDD should be determined at the distance of at least 40 mm so that the efficiency loss is minimized. Due to the rather large uncertainties the ^{83}Rb decay scheme should be re-measured with higher precision. At this moment the absolute activities can be determined only at the relative uncertainty level of 10%. The activities of the SKrS samples studied in this work are given in Table 5.1.

with the energy of 30 keV. For more details see Section 5.2.5.

⁹ In a dedicated retention measurement it was possible to do a least-squares fit of a Gaussian peak in the open-chamber measurement spectrum if its centroid and width were fixed to the values obtained for the 32 keV γ -line in the closed-chamber measurement (see Section 5.2.5). From the area of the peak and its uncertainty the retention $R = 1.1(10)\%$ was obtained. Owing to the smallness of the relevant term in Eq. (5.12) and the size of the retention uncertainty such a value can be safely neglected.

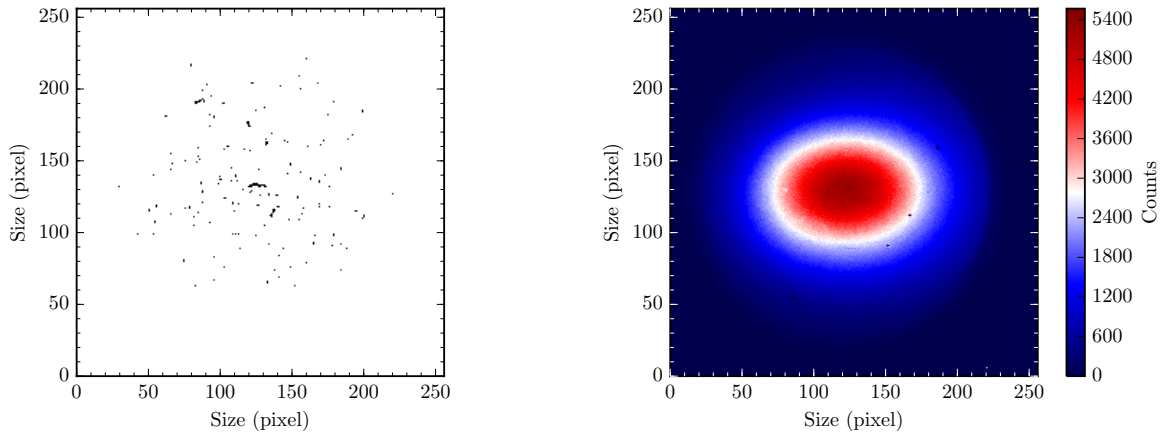


Figure 5.7: Left: Example of a single frame in the measurement of the SKrS radiographical image (Pt-30-7 placed in a holder 0.8 mm from the detector). The image includes all events recorded during the frame time of 10 ms which comprises single-pixel events, two-pixel events (charge sharing when the pixel is hit at its edge), and longer tracks (photoelectrons emerging after higher-energy photon interaction). Right: The SKrS radiographical image after the complete measurement. The color scale is chosen such that the half-maximum region is well visible.

5.2.4 Radiographical image of the activity distribution

The radiographical image is obtained by means of the Timepix detector [Llo07]. It is a silicon square-shaped chip with the dimensions of $14.08 \times 14.08 \text{ mm}^2$ and the thickness of $300 \mu\text{m}$ consisting of 256×256 pixels each with the size of $55 \times 55 \mu\text{m}^2$. Each pixel is connected to its respective spectroscopy chain, i.e. preamplifier, discriminator, and digital counter, which is integrated on the read-out chip. Additionally, each pixel enables determination of the deposited energy, i.e. collected charge, in the so-called time-over-threshold (TOT) mode when the counter acts as a Wilkinson type analog-to-digital converter using a high-frequency oscillator clock.

In the TOT mode the energy of the detected events is integrated within a single measurement frame. The whole measurement then consists of series of many such frames. The frame time has to be short enough so that the probability that a single pixel is hit twice is negligible. Additionally, due to charge sharing among neighbouring pixels leading to clusters of events the frame time has to be adjusted so that not all the events are in a cluster. Charge sharing may occur if a pixel is hit near its edge due to diffusion of the charge during collection [Jak09]. Similarly, if a higher-energy photon strikes the pixel the corresponding photoelectron may travel distance spanning several pixels before being stopped by energy loss processes. Such an effect includes also cosmic rays since the detector is not shielded in any way. The frame time is adjusted by hand for each source individually prior to the measurement. An example of events detected in a single frame is shown in Fig. 5.7 on the left.

For the radiographical image only the single-pixel events are taken into account to

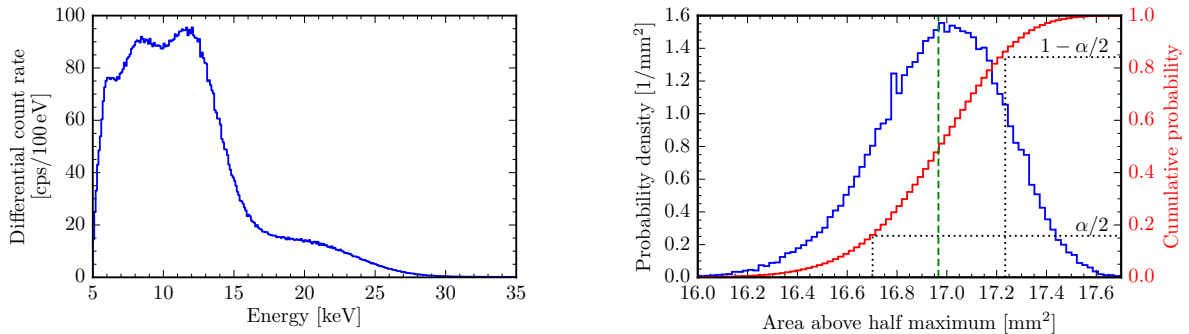


Figure 5.8: Left: Timepix energy spectrum summed for all pixels for the complete radiographic image measurement. The lines observed are mainly the strong $K\alpha$ x-rays of krypton (12.6 keV) and the 9.4 keV γ -ray together with the LX x-rays of platinum. Right: Illustration of the calculation of 68.27% (1σ) confidence interval of the area above half maximum. The left vertical axis corresponds to the bell-shaped probability density distribution while the right one corresponds to the monotonously increasing cumulative probability. The values of the area corresponding to the cumulative probabilities of $\alpha/2 \approx 0.16$ and $1 - \alpha/2 \approx 0.84$ are indicated by the dotted lines. The dashed vertical line denotes the mean. The total number of randomized images in the Monte Carlo calculation was 10^5 .

avoid additional blurring of the image (cluster size cut). Moreover, the event is taken into account only if its measured energy is in the range of 5 keV to 35 keV, which covers the energy of the characteristic x-rays of krypton taking into account the detector energy resolution at the order of a few keV (energy cut). If a pixel is selected in such a way, it is taken as a single count into the radiographical image. After sufficient number of frames the whole image, which is shown as an example in Fig. 5.7 on the right, appears. An example of the whole detector energy spectrum from the complete measurement after applying the cuts is shown in Fig. 5.8 on the left.

The single-pixel selection criterion in combination with too high frame time can lead to suppressing of the image maximum and as a consequence to an apparently larger activity spot. Such an effect is illustrated in Fig. 5.9. In this case, there even appears to be a small hollow in the center of the activity spot when the frame time was too high. An indicator for too high frame time is the ratio of events satisfying the selection criteria and all the events. The ratio was 0.83 compared to 0.95 for the improved frame time.

Area of half maximum, ^{83}Rb surface dose and peak concentration

In the previous work [Sle11] the FWHM dimensions of the activity spot along the longer and shorter axis were determined since the half-maximum shape was close to elliptical. Owing to the irregular shapes of the spot for the present sources the area S of region with counts above half of the maximum is determined instead. Due to the statistical nature of the measurement the mean value of the area and its uncertainty is estimated using a Monte Carlo calculation. The counts for the whole image are varied according

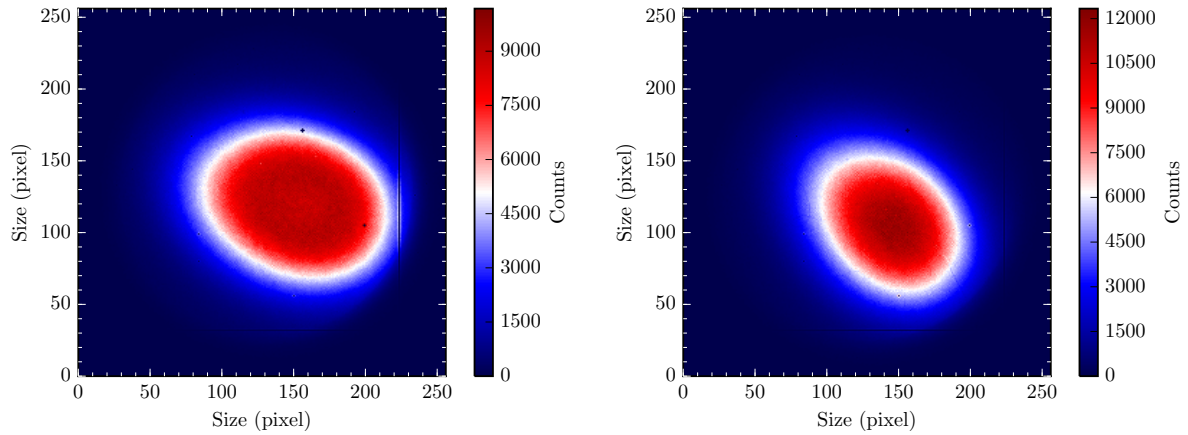


Figure 5.9: Illustration of the radiographical image obtained with too high frame time (left) and more optimal frame time (right). The source was moved in between the measurements.

to the Poisson distribution with the expected value being the measured value in each pixel. For each randomized image the area above the half maximum is calculated and a normalized histogram with 100 bins is filled with the value. In such a way the probability density distribution for the area is obtained. For each histogram bin the partial sum corresponding to the cumulative probability is calculated. Finally, the boundaries of the $100 \cdot (1 - \alpha)\%$ confidence interval are found by finding the lowest bin for which the cumulative probability is equal or larger than $\alpha/2$ and $1 - \alpha/2$, respectively. This is illustrated for the radiographical image from Fig. 5.7 in Fig. 5.8 on the right. The mean area above half maximum amounts to 17.0 mm^2 and the 68.27% (1σ) confidence interval is approximately symmetric leading to the uncertainty of about 0.3 mm^2 .

The radiographical image can be used to obtain the ^{83}Rb implanted surface dose and peak concentration which are important properties of the implanted sample. If n is the measured counts in a particular pixel and n_{tot} the total number of counts, then the relative ^{83}Rb surface dose ϱ_S is given as

$$\varrho_S [\text{cm}^{-2}] = \frac{n}{n_{\text{tot}} \Delta S}, \quad (5.16)$$

where $\Delta S = 3.025 \times 10^{-5} \text{ cm}^2$ is the area of a single pixel. Then the surface dose Q_S is given as

$$Q_S [\text{ion cm}^{-2}] = \varrho_S N, \quad (5.17)$$

where N is the number of implanted ions which is related to the activity A through

$$N = \frac{A}{\lambda} \quad (5.18)$$

with $\lambda = 9.307(11) \times 10^{-8} \text{ s}^{-1}$ being the decay constant of ^{83}Rb . For the image in the Fig. 5.7 and the implanted activity of 4.6 MBq we obtain the peak surface dose of $Q_S^{\text{max}} = 1.8 \times 10^{14} \text{ ion cm}^{-2}$. The implanted surface dose of about $10^{14} \text{ ion cm}^{-2}$ is generally accepted as the limit above which there is a uniform distribution of lattice damage

over the implanted region [Her86]. All sources investigated in the previous work [Zbo11] had the average surface dose at this order of magnitude.

Concerning the peak concentration Q_c^{max} we utilize the longitudinal ^{83}Rb profile as calculated by SRIM and proceed in a similar way. The maximal relative longitudinal ^{83}Rb implanted dose ϱ_L^{max} is given by

$$\varrho_L^{\text{max}} [\text{cm}^{-1}] = \frac{m^{\text{max}}}{m_{\text{tot}} \Delta d}, \quad (5.19)$$

where m^{max} is the maximum of the longitudinal ^{83}Rb distribution as calculated by SRIM, m_{tot} is the sum of all the distribution values, and Δd is the size of the distribution bin. The peak concentration then reads

$$Q_c^{\text{max}} [\text{ion cm}^{-3}] = \varrho_L^{\text{max}} Q_S^{\text{max}} = \varrho_S^{\text{max}} \varrho_L^{\text{max}} N. \quad (5.20)$$

For the platinum substrate and 30 keV ^{83}Rb implantation energy we have for the image in the Fig. 5.7 the peak concentration of $Q_c^{\text{max}} = 1.9 \times 10^{20} \text{ ion cm}^{-3}$. Considering the substrate in standard conditions the concentration of platinum atoms amounts to $C^{\text{subs}} = 6.6 \times 10^{22} \text{ atom cm}^{-3}$. Thus, the ^{83}Rb peak concentration is about 0.29 % of the Pt concentration, i.e. a relatively significant fraction.

Source position on the Timepix chip

Previously [Sle11] and also partly in this work the source was placed in a holder with 0.5 mm edge which itself was put onto the Timepix chip. The advantages of such a setup are that the substrate (Pt) is reliably straightened and centering and rotation on the chip is easier. The disadvantage is that the source is 0.5 mm above the chip which leads to some blurring of the radiographical image.

However, during the course of this work it was found that the blurring is a limiting factor if the image is used for calculation of the more accurate MoS transmission function, see Section 5.6. Thus, the radiographical image measurements were continued with the source being placed right on the chip with only the mylar foil in between. The substrate has to be weighted by the source holder which is placed on top of it. In such a case, care has to be taken that the mylar foil under the substrate is straightened, see Fig. 5.10. Unfortunately, the positioning can be done only in a rough way. A special care has to be taken not to damage the fine contacts of the chip to the motherboard.

The blurring effect can be understood by considering the image of a point-like isotropic source of radiation on the detector plane placed at the distance z from the source, i.e. the so-called point spread function. The differential intensity of radiation dI within the differential solid angle $d\Omega = \sin\theta d\theta d\varphi$ is independent of either the polar angle θ or the azimuthal angle φ because the source is isotropic. Let us normalize the differential intensity such that the total intensity emitted into the hemisphere of the detector plane equals I_0 , i.e.

$$\frac{dI}{d\Omega} = \frac{I_0}{2\pi}. \quad (5.21)$$

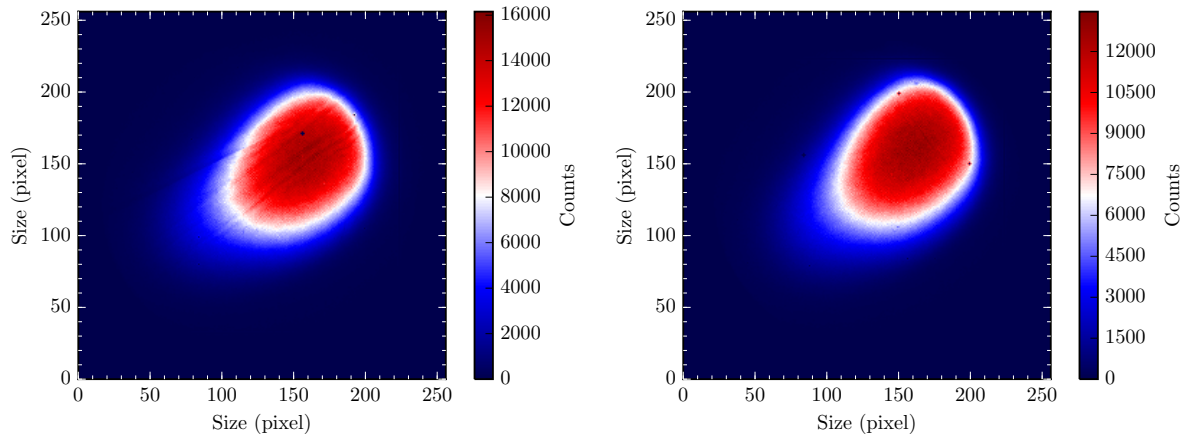


Figure 5.10: The radiographical images of Pt-30-9 measured directly on the chip with a mylar foil in between. Most likely due to the foil being bumpy under the substrate the image on the left is distorted. After stretching the foil the artifacts disappeared as shown in the image on the right.

To find the image on the plane we need to express the differential intensity dI within the differential area $dS = dx dy$ as a function of x and y , where x and y are the coordinates along the detector plane. Using the chain rule we have

$$\frac{dI}{d\Omega} = \frac{dI}{d\Omega} \frac{d\Omega}{dS}. \quad (5.22)$$

From the equations of transformation from cartesian to spherical coordinates we obtain

$$d\Omega = \frac{z}{r^3} \frac{1}{x^2 + y^2} (x dx + y dy)(x dy - y dx), \quad (5.23)$$

where r is the radius. This can be further simplified by noting that for the differential forms α and β it holds $\alpha\beta = -\beta\alpha$, where the operation between them is to be understood as the wedge product. Thus, $(dx)^2 = (dy)^2 = 0$ and $-y^2 dy dx = y^2 dx dy$ and we get

$$d\Omega = \frac{z}{r^3} dx dy. \quad (5.24)$$

The differential intensity on the detector plane thus reads using Eq. (5.22)

$$\frac{dI}{dS} = \frac{I_0}{2\pi} \frac{z}{(x^2 + y^2 + z^2)^{\frac{3}{2}}}. \quad (5.25)$$

This function is known as the bivariate Cauchy distribution. Integration of the distribution over one of the dimensions gives the familiar one-dimensional Lorentzian shape. The FWHM of the function in Eq. (5.25) is given as

$$\text{FWHM} = 2z \sqrt{4^{\frac{1}{3}} - 1} \approx 1.533z. \quad (5.26)$$

For $z = 0.5$ mm we have $\text{FWHM} \approx 0.77$ mm, i.e. about 14 pixels.

The function in Eq. (5.25) could be used to deconvolve the blurred image by a suitable algorithm (e.g. the Richardson-Lucy algorithm [Ric72, Luc74]) provided that the source-detector distance is the only source of blurring. However, for all sources there is a small but inevitable blurring caused by penetration of the dominant 12.6 keV photons through the individual pixels. The attenuation length in silicon amounts to about 0.26 mm which is almost five pixels. Besides, for the platinum-substrate sources the strong 520 keV γ -rays penetrate through the substrate in the transversal direction and excite the platinum atoms. By subsequent de-excitation platinum x-rays are emitted and since the LX x-rays have suitable energy of about 9.5 keV, they are counted by the detector. The energy resolution is not good enough to resolve these parasitic lines from the krypton lines. The attenuation length of 520 keV photons in platinum is about 3.5 mm. For the HOPG case this effect is of no concern since the x-rays of carbon are well below the detector threshold. Since all HOPG sources were measured directly on the detector and the blurring by Eq. (5.25) is not the only one for Pt sources, the deconvolution was not utilized.

In order to observe the effect of the blurring on the calculated area above half maximum and the surface dose the source Pt-30-4 was measured with enough statistics both in the source holder and directly on the chip. The area above half maximum amounts to 21.18(22) mm² and 18.39(19) mm², respectively, and for the peak surface dose we have 7.25×10^{12} ion cm⁻² and 8.18×10^{12} ion cm⁻², respectively. In both cases there is a difference of about 10% in absolute value, i.e. the measurement in the source holder tends to overestimate the area and underestimate the surface dose as expected due to the blurring.

The obtained radiographical images of the SKrS samples investigated in this work are shown in Fig. 5.11. The calculated area above half maximum S , the maximal implanted surface dose Q_S^{max} , the peak concentration Q_C^{max} and the peak concentration relative to the substrate concentration C^{subs} are listed in Table 5.1. In general, the activity spot is significantly larger for the BONIS sources than for the ISOLDE ones if the BONIS retarding setup is not utilized. Otherwise, the size considerably shrinks and becomes comparable to the ISOLDE case. All images on the second page of the figure and the one for Pt-30-4 were obtained with zero distance of the source to the detector. For the remaining ones the distance was 0.5 mm.

5.2.5 $^{83\text{m}}\text{Kr}$ retention

The $^{83\text{m}}\text{Kr}$ retention expresses the relative amount of $^{83\text{m}}\text{Kr}$ atoms which decay inside the SKrS, see Eq. (5.11). The remaining atoms escape the source prior to their decay. The higher the retention the more electrons can be observed by the MoS for a given source activity. The 32 keV γ -line de-excites the $^{83\text{m}}\text{Kr}$ state, see Fig. 3.4, and thus observation of its intensity can be used to obtain the retention. The measurement method is based on a closeable cylindrical chamber [Sle11] which captures the escaping $^{83\text{m}}\text{Kr}$ in a localized space observable by the detector. When the chamber is open the $^{83\text{m}}\text{Kr}$ atoms may freely escape and only the radiation from the $^{83\text{m}}\text{Kr}$ decaying inside the source is detected while the geometry of the setup is not changed. In the first approximation, the retention is

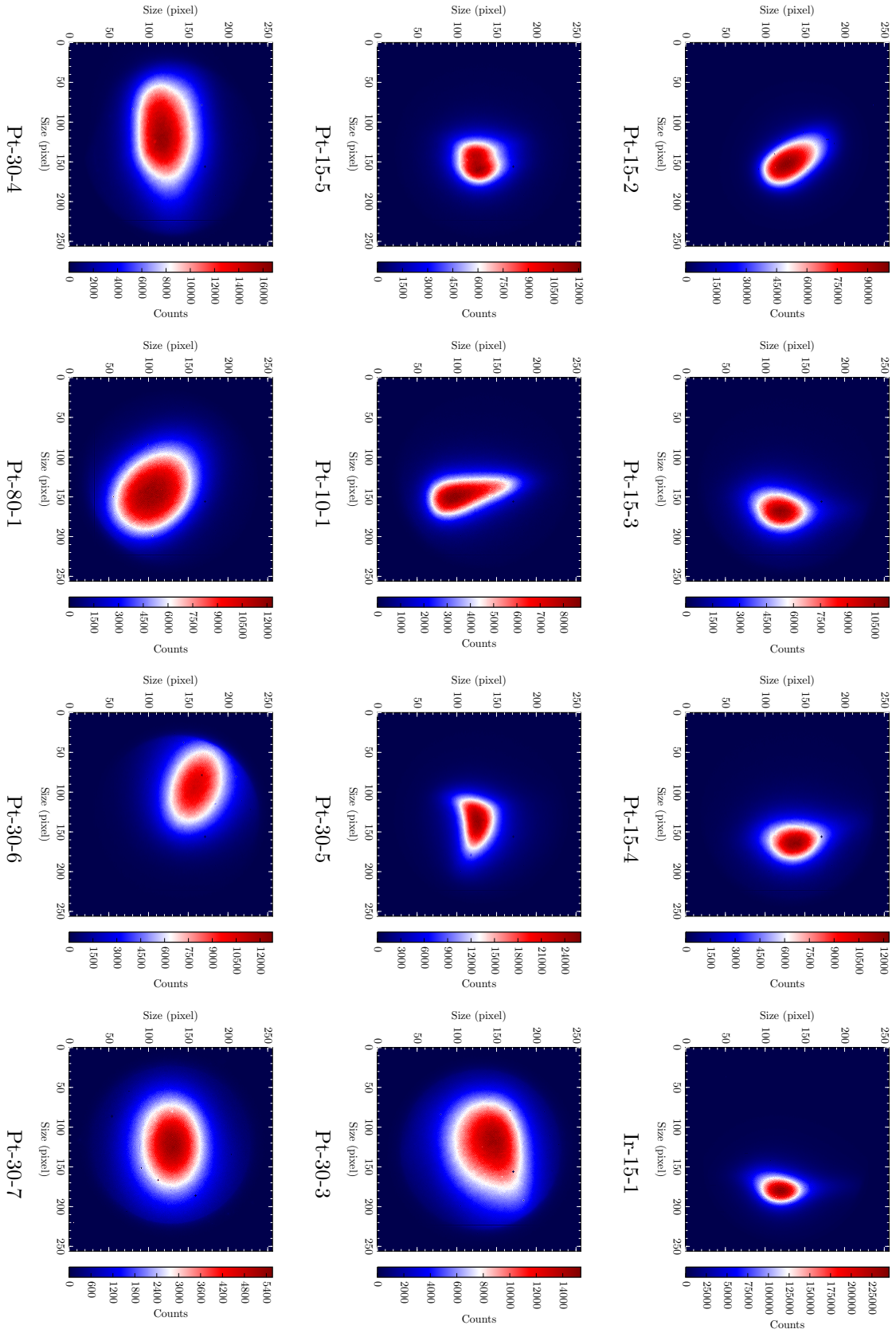


Figure 5.11: The radiographical images of the SKrS samples.

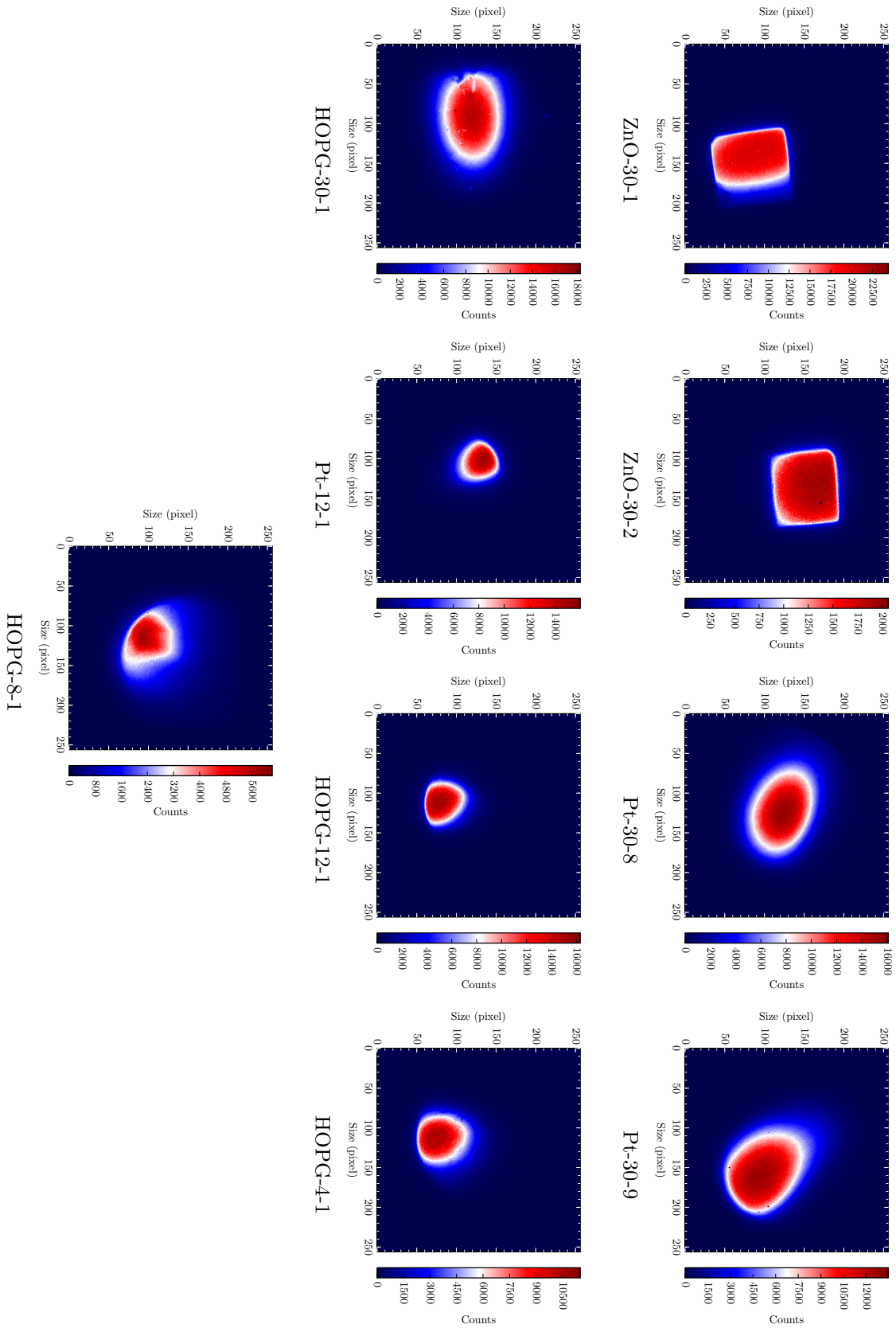


Figure 5.11: The radiographical images of the SKrS samples (continued).

given simply as the ratio of the 32 keV γ -peak count rate observed for the open and the closed chamber.

The measurement in the closed chamber has to be performed only after a transient equilibrium is established. The time dependence of the $^{83\text{m}}\text{Kr}$ activity after closing is given as

$$A_{Kr}(t) = \gamma A^{(0)} \frac{T_{Rb}}{T_{Rb} - T_{Kr}} \left(e^{-\lambda_{Rb}t} + (R - 1) e^{-\lambda_{Kr}t} \right), \quad (5.27)$$

where $A^{(0)}$ is the ^{83}Rb activity at closing time. In the transient equilibrium the second summand in the bracket is negligible compared to the first one. Requiring that the value of $(R - 1) e^{-\lambda_{Kr}t}$ is lower than $z e^{-\lambda_{Rb}t}$, where z is a small fraction, we obtain that the transient equilibrium comes at the time

$$t_{TE} = \frac{1}{\lambda_{Rb} - \lambda_{Kr}} \ln \left(\frac{z}{1 - R} \right). \quad (5.28)$$

For the fraction $z = 1\%$ and the source retention of $R = 0$ and $R = 0.9$ we obtain $t_{TE} \approx 12.2 \text{ h} = 6.7 \cdot T_{Kr}$ and $t_{TE} \approx 6.1 \text{ h} = 3.3 \cdot T_{Kr}$, respectively.

Owing to the weakness of the 32 keV γ -line (intensity per $^{83\text{m}}\text{Kr}$ decay of only about 0.05%) the measurement generally lasts several hours or more in each of the open and closed chambers. Moreover, there is an additional waiting time in the closed chamber for the transient equilibrium. The ^{83}Rb activity decays by about 0.8% each day and thus correction for the decay has to be taken into account. If firstly the closed chamber measurement takes place in the time interval $(t_{cl}, t_{cl} + \Delta t_{cl})$ and then the open chamber one in $(t_{op}, t_{op} + \Delta t_{op})$ the retention R_{dec} is obtained as

$$R_{dec} = \frac{C_{op}}{C_{cl}^{\text{corr}}}, \quad C_{cl}^{\text{corr}} = C_{cl} e^{-\lambda_{Rb}(t_{op} - t_{cl})} \frac{e^{-\lambda_{Rb}\Delta t_{op}} - 1}{e^{-\lambda_{Rb}\Delta t_{cl}} - 1}, \quad (5.29)$$

where C_{cl} and C_{op} are, respectively, the closed and open chamber peak counts and C_{cl}^{corr} is the closed chamber peak counts corrected for the ^{83}Rb decay.

In the closed chamber the gaseous $^{83\text{m}}\text{Kr}$ which was released from the source is distributed over the finite cylindrical volume of the chamber. Such $^{83\text{m}}\text{Kr}$ is closer to the detector than the source meaning that the γ -line is detected with a higher efficiency. Let the chamber height be d and the bottom of its inner volume be at the distance L from the detector surface. Assuming a homogeneous distribution of $^{83\text{m}}\text{Kr}$ in the chamber the contribution of the infinitesimal cylinder with the height dr at the distance r from the detector to the observed 32 keV γ -line intensity is given by

$$dI = \frac{1}{d} s(r) dr, \quad (5.30)$$

where $s(r)$ is the relative efficiency of the detector at r . Thus, in the closed chamber measurement the intensity

$$I_{cl} = R_{vol} s(L + d) + \frac{f(1 - R_{vol})}{d} \int_L^{L+d} s(r) dr \quad (5.31)$$

is observed, where the first summand corresponds to the source contribution and f is the fraction of the chamber volume observable by the detector. The retention R_{vol} is established from

$$R_{vol} = \frac{I_{op}}{I_{cl}^{\text{zero}}}, \quad (5.32)$$

where I_{op} is the intensity measured with the open chamber and $I_{cl}^{\text{zero}} = s(L + d)$ is the intensity which would be observed for a chamber with zero volume. From the ratio of this intensity to the actual closed chamber intensity I_{cl} from Eq. (5.31) we obtain for the retention

$$R_{vol} = \frac{I_{op}X}{I_{cl} + I_{op}(X - 1)}, \quad X = \frac{f \int_L^{L+d} s(r) dr}{s(L + d)}. \quad (5.33)$$

If the measured counts is C_{cl} and C_{op} and taking into account the ^{83}Rb decay correction, see Eq. (5.29), the volume- and decay-corrected retention R is calculated as

$$R = \frac{C_{op}X}{C_{cl}^{\text{corr}} + C_{op}(X - 1)} \quad (5.34)$$

provided that the closed chamber measurement takes place prior to the open chamber one.

In the simplest case the function $s(r)$ is given by the inverse square law

$$s(r) = \frac{1}{r^2}. \quad (5.35)$$

However, such a prescription is only approximate since the infinitesimal cylinders which were used to obtain the Eq. (5.33) are not spherically symmetric around the point of the detector surface. A more accurate approach is to use the efficiency simulation, which was described in relation to the SDD, to obtain the dependence $s(r)$ numerically in discrete points. The discrete points are then interpolated to yield $s(L + d)$ and $\int_L^{L+d} s(r) dr$. The ‘‘source’’ in the simulation is assumed to be a homogenous circle with the diameter equal to the diameter of the chamber inner volume. In such a way, the value $s(L + d)$ corresponding to the actual source is slightly inaccurate since the source activity spot has an irregular shape and smaller diameter. Nevertheless, such an inaccuracy can be considered negligible compared to the statistical uncertainties of the measured intensities unless the chamber is placed very close to the detector. In that case, the systematical uncertainties related to positioning and dimensions of the chamber could possibly dominate.

The retention measurement results for the SKrS samples investigated in this work are listed in Table 5.1. Due to occasional time constraints and the needed length of the measurement the retention for a few samples is not available. In almost all cases the retention of the implanted sources is high, i.e. around or above 90%. Only in two cases of Pt-15-2 and Pt-12-1 the retention was at around 80%. The reason for the difference is currently not clear but the difference can be safely tolerated. In the case of HOPG-8-1 only a lower limit could be established using the unified approach of Feldman and Cousins [Fel98].

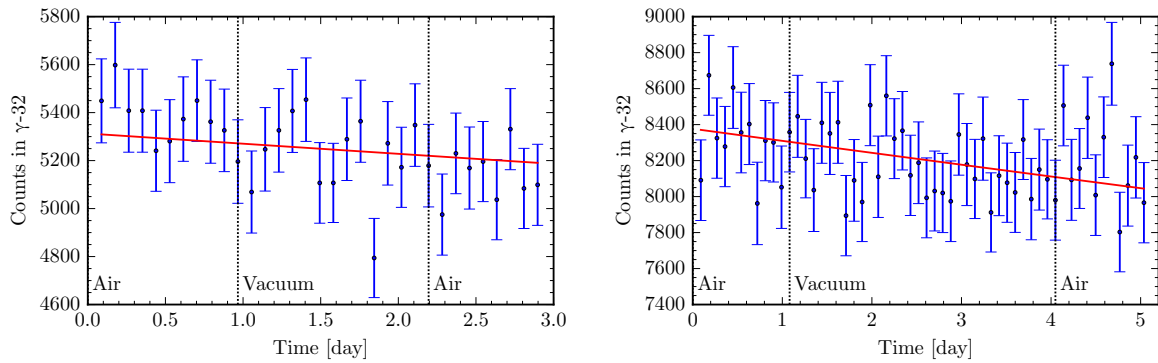


Figure 5.12: The intensity of the 32 keV γ -line observed in time for the source Pt-30-9 (left) and HOPG-8-1 (right). No difference with respect to pressure conditions is seen. The solid line is a fit of the data with the exponential decay function with fixed half-life of ^{83}Rb and free multiplicative factor. The fits yielded $\chi^2_{\text{dof}} = 0.75$ (32 dof) and $\chi^2_{\text{dof}} = 0.84$ (55 dof), respectively.

The retention measurement as described above is performed in ambient air but the sources are kept at ultra-high vacuum when measuring at the MoS. Thus, a question about the retention behaviour in vacuum arises. The relative intensity of the 32 keV γ -line was measured for the sources Pt-30-9 and HOPG-8-1 while their environment was changed from ambient air to vacuum created by a turbomolecular pump and again back to air without moving the source. The results are shown in Fig. 5.12. No difference within the uncertainties was found for the values in vacuum compared to values in ambient air.

5.3 Electron spectroscopy measurements at the monitor spectrometer

In this work mostly the high-precision high voltage divider K35 [Thü09] was utilized for the electron spectroscopy measurements at the monitor spectrometer. A calibration of the dividing ratio was done similarly as for the K65 against the PTB reference high voltage divider MT100 at the late 2011 and at the late 2013. A difference at the level of only about -1.8 ppm was obtained [Res14]. In between, low-voltage calibration measurements were performed using a commercial divider to monitor the ratio trend on site of the KIT. Although such a calibration does not fully substitute the one done at the nominal -18.6 kV, the obtained results do not indicate any drift within the uncertainties.

Taking the change of the dividing ratio as linear in time, the difference of the values obtained at the PTB corresponds to a relative drift of the dividing ratio smaller than -0.1 ppm month $^{-1}$. Thus, in the analysis of the electron spectra the dividing ratio was always considered to be a constant. When the K35 divider was not available for the MoS, the less stable divider from the Julie Research Labs (JRL) was utilized¹⁰. In such a case,

¹⁰ Model KV-50 with the certified long-term stability of the dividing ratio of about 1.3 ppm month $^{-1}$.

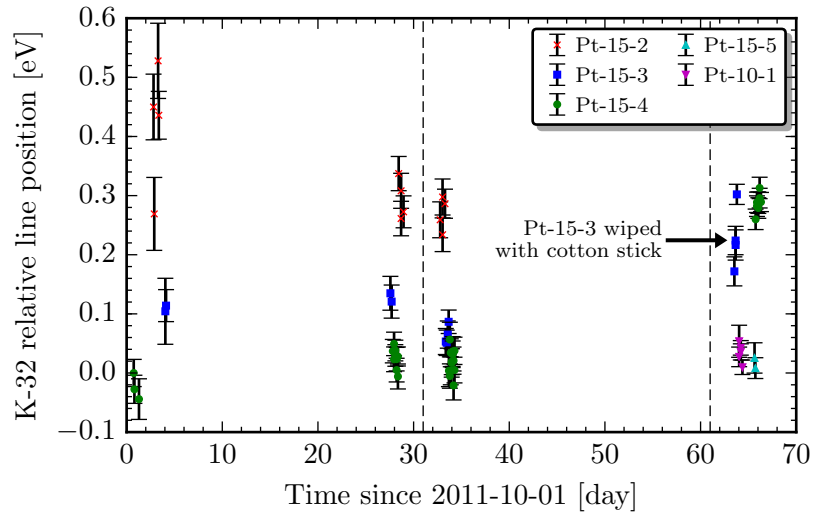


Figure 5.13: The K-32 line position obtained using the DSG lineshape for the ISOLDE Pt-based sources measured with the less stable JRL high-voltage divider. The values are relative to the first value in the graph. The two bake-outs of the source chamber are indicated with the vertical dashed lines. The data obtained using the Pt-15-3 wiped with a cotton stick soaked in acetone are also marked.

it was not possible to assess the electron line position stability in time longer than a few days and only the relative line position among different sources could be observed.

5.3.1 First investigations with the ISOLDE sources

During the first investigations of the sources only the less stable JRL high voltage divider was available. The obtained K-32 relative line position for the Pt-based sources is shown in Fig. 5.13. The source position amounted to 27 cm from the magnet center with the magnetic field B_S of about 0.5 T and the acceptance angle θ_{max} of about 17° . The line position for Pt-15-3 was measured to be slightly higher than for Pt-15-4. Also a slightly higher Gaussian width σ of about 0.6 eV was observed for Pt-15-4 compared to Pt-15-3 with the value of about 0.55 eV. Such differences between sources produced in a similar way are practically at the edge of their uncertainty and thus can be tolerated. The line position of both sources was lower than for the older Pt-15-2 while the Gaussian width was larger (around 0.4 eV for the older source). The results could indicate that by aging the line position moves towards higher energies and the Gaussian width drops.

In order not to influence the sources the source chamber was not baked out after they were mounted. To improve the vacuum and investigate a possible effect on the sources a bake-out of the source chamber was carried out later, which is indicated in the Fig. 5.13. The chamber was kept at the temperature of 120°C for about 15 h. The temperature of the sources is not measured during the bake-out but due to radiative heating from the chamber walls it is estimated to be close to the wall temperature. The K-32 was measured both before and after the heating. Unfortunately, the results are somewhat ambiguous

since there seems to be a shift towards negative values for Pt-15-3 but no shift for the sources Pt-15-4 or Pt-15-2. No effect on the line shape was observed.

In order to investigate the possible influence of two different environments on the observed electron line shape the source Pt-15-3 was wiped with cotton stick soaked with acetone. As discussed in Section 4.4.5 no effect on the line shape was observed. The line position was measured to be slightly lower than for Pt-15-4 which is the opposite as prior to wiping. The corresponding line position results are indicated in the Fig. 5.13.

The relative line position of the stronger sources Pt-15-5 and Pt-10-1 was measured to be even lower than for the weaker Pt-15-3 and Pt-15-4 but similar to each other. The Gaussian width was observed to be about 0.75 eV which is clearly larger. Both of these results could be possibly attributed to the notably higher implanted dose, see Table 5.1.

The amount of no-energy-loss electrons for the Pt-10-1 in comparison with the other sources was estimated using the amplitude-to-activity ratio. At the same activity and retention, a larger number of no-loss electrons for the lower implantation energy should lead to a higher amplitude-to-activity ratio. From the available data it seems that the amplitude-to-activity ratio is generally larger for Pt-10-1 than for Pt-15-5 by about 10%. This is in accordance to the expected amount of no-loss electrons as discussed in Section 5.2.2 where only about 9% increase of the amount of no-loss electrons was predicted.

Long-term stability of the line position

Only the sources Pt-15-5 and Pt-10-1 were measured for the line position stability after the high-precision K35 divider became available at the end of 2011. The sources were measured in a discontinuous way for around seven months in the same position of 27 cm from the magnet center (outer position). The measurement continued for about five months in a closer position of 19.2 cm with B_S of 2.5 T and θ_{\max} of 40° (inner position). The results for the two positions are distinguished since for comparison a more accurate description of the MoS transmission function is necessary (see Section 5.6). Mainly in the first half of 2012 the time at the MoS was dedicated also to various background studies and methods of its reduction to be used at the KATRIN main spectrometer. For these measurements the spectrometer setup was changed. Furthermore, there was a break of about a month after the initial measurement at the end of 2011 when the MoS operation except vacuum was brought down.

Outer source position The complete results of the K-32 line position for the outer source position are shown in Fig. 5.14. Also the results for Pt-15-3, which was measured only in the beginning, are shown for comparison. A bake-out of the source chamber at around day 20 to 120°C for 48 h was carried out to improve vacuum. The bake-out at around day 90 was done after opening the source chamber for electrical connection maintenance. It seems that neither of them made any significant difference to the line position.

On a longer time scale a general trend can be seen for both Pt-15-5 and Pt-10-1. Since the beginning of measurements the line position increased by about 0.2 eV but the trend does not seem to be monotonous since between the days 70 to 100 the line

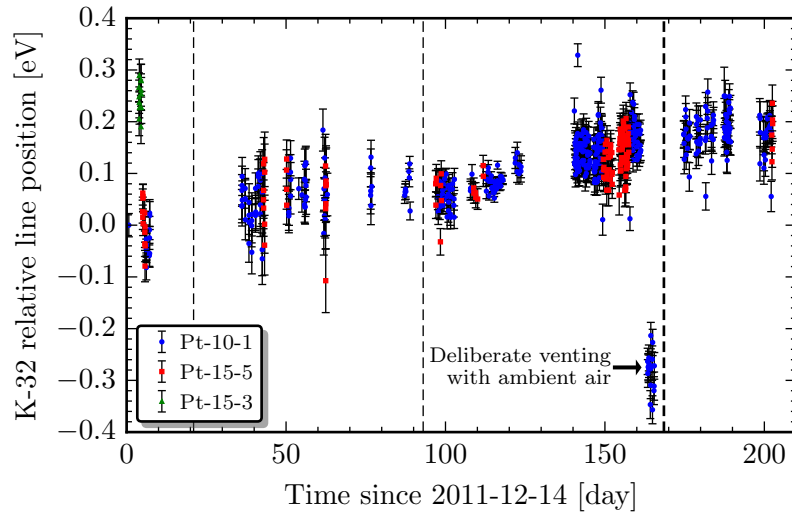


Figure 5.14: The long-term stability of the K-32 line position for the outer source position of 27 cm measured for the ISOLDE sources Pt-15-5 and Pt-10-1. The initial results for the Pt-15-3 source are also shown for comparison. The two source chamber bake-outs are indicated with thin vertical dashed lines. The thick vertical dashed line refers to the common bake-out of the whole spectrometer. The data obtained after the spectrometer was vented with ambient air and pumped out again without baking are also marked.

position was decreasing. Such a behaviour could be possibly explained by a drift of the line position towards higher values which is influenced in the opposite way by a change of the spectrometer work function.

The line position in time gradually approaches the one measured in the beginning for Pt-15-3 as the sources decay. Moreover, the sources were produced in a similar way, see Table 5.1, and so a common behaviour of the line position is likely. Most importantly, the line position continues to drift for both sources even after the spectrometer was baked out as observed in the results obtained at the inner source position which are described below. The drop of line position after the day 160, which is related to a deliberate venting of the spectrometer, is discussed below.

To address the work function, the lines L_{3-32} and $L_{3-9.4}$ were measured in the same time period together with the K-32 albeit less frequently. Unfortunately, due to the weakness of $L_{3-9.4}$, a rather large background and partial cut of the electron peak in the detector spectrum the line position results are weighted with a large uncertainty. The obtained values of the strong L_{3-32} line position are shown in Fig. 5.15 on the left. The results are analogous to the K-32 ones which disfavors that it is an effect of an unrecognized change of the high-voltage divider dividing ratio.

The spectrometer work function is highly affected by the gases adsorbed on the surface of the retarding electrode. The process of adsorption is influenced by the pressure around the surface. The pressure trend in the spectrometer vessel for the same time period is shown in Fig. 5.15 on the right. In the background studies at the MoS the pressure was artificially elevated which is clearly seen in the figure. An increased pressure may lead

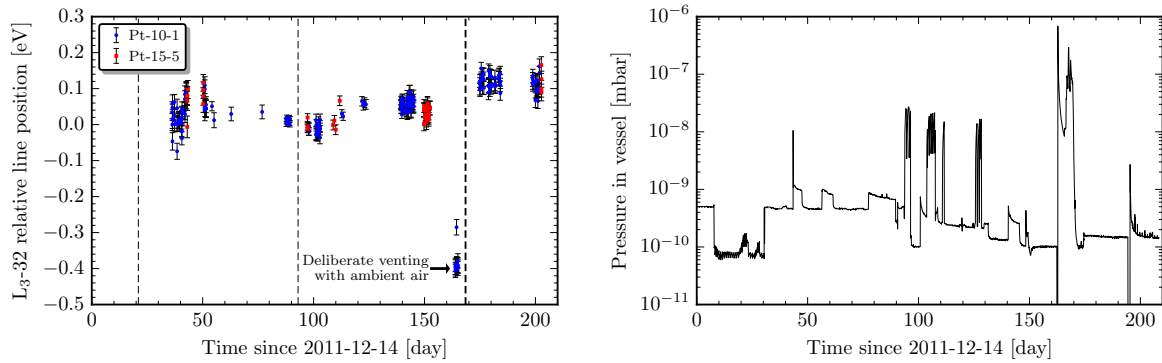


Figure 5.15: Left: The long-term stability of the L₃₋₃₂ line position for the outer source position of 27 cm measured for the ISOLDE sources Pt-15-5 and Pt-10-1. The bake-outs and venting are indicated in the same way as in the Fig. 5.14. Right: The trend of pressure inside the spectrometer vessel for the time period of the long-term stability measurements in the outer source position. The MoS was used also for background studies when an elevated pressure setting was utilized.

to a shift of the work function towards higher values and according to Section 4.1.1 to a lower line position. Such an effect was observed in [Zbo11]. A combination with the positive line position drift could lead to an apparently more or less constant observed line position in the first half of the year. After the pressure improved, the work function was not affected anymore and only the line position drift remained. Thus, such changes of the spectrometer setup are unfavorable for a long-term measurement of the line position stability.

Inner source position The complete results of the K-32 line position for the inner source position are shown in Fig. 5.16. A bake-out of the MoS was performed at around day 270 when the source chamber was at 100 °C for 6 d and the vessel was at 160 °C and 180 °C each for 3 d. At around day 235 the source chamber was opened for insertion of the Pt-15-3, which was annealed at high temperature to be discussed further, then three times at around days 315, 328 and 335 for insertion of new sources and for source re-adjustment. The bake-out of only the source chamber was performed at around day 320 at 120 °C for 14 h.

An overall increase of the line position by about 0.12 eV is observed. The pressure in the vessel was below 3×10^{-10} mbar prior to the complete bake-out and below 2×10^{-10} mbar after it, see the pressure trend in Fig. 5.17 on the left. Owing to such a low pressure and the previous spectrometer bake-out around the day 170 we may assume that the work function was constant. This assumption is supported by the line position results which merely continue in their trend after the more thorough bake-out at the day 270. The observed drift could thus be attributed to the sources themselves as mentioned already in discussing the outer source position results.

An evolution of the line shape over time is observed which further supports that some changes inside the source must have been happening with the consequence of a drifting

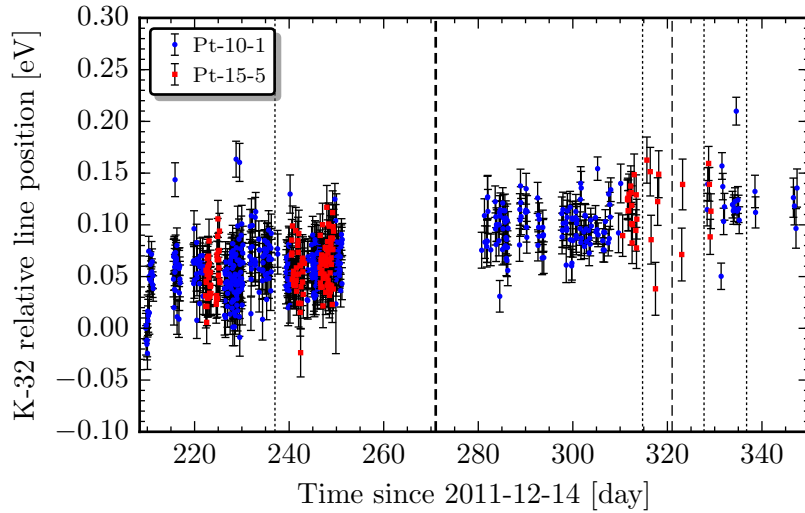


Figure 5.16: The long-term stability of the K-32 line position for the inner source position of 19.2 cm. The source chamber bake-out is indicated with thin vertical dashed line. The thick vertical dashed line refers to the common bake-out of the whole spectrometer. The dotted lines refer to opening of the source chamber and subsequent pumping out without baking.

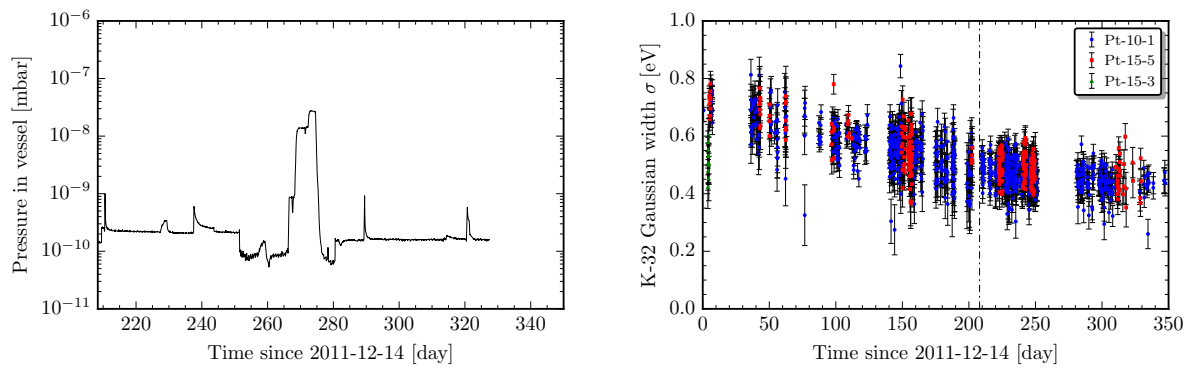


Figure 5.17: Left: The trend of pressure inside the spectrometer vessel for the time period of the long-term stability measurements in the inner source position. Unfortunately, no pressure readings are available after the day around 325 most likely due to some KATRIN database problem. Right: The Gaussian width σ of the K-32 line for Pt-15-5 and Pt-10-1 in time. The dash dotted line indicates when the source was moved closer to the magnet.

line position. The Gaussian width σ for the whole time period is shown in Fig. 5.17 on the right. For both Pt-15-5 and Pt-10-1 the widths have gradually decreased from 0.7 eV down to about 0.45 eV. Note that this value is similar to the value for Pt-15-2 which was measured also after a few half-lives. Moreover, it is only slightly less than for the weaker source Pt-15-3. This indicates that a higher implanted dose could have an effect on the line broadening and that the broadening decreases in time to a common final value.

Conclusion The only known difference between the sources Pt-15-5, Pt-10-1 and Pt-15-3, Pt-15-4 was the higher implanted dose for the formerly mentioned ones. Thus, a consistent picture seems to emerge: a higher implanted dose is correlated to a broadening of the line, which slowly decreases in time, and a lower line position, which gradually increases over time as the source decays.

Annealing of source

After their measurement at the MoS some of the ISOLDE sources were utilized for an attempt to anneal the substrate in order to observe possible effects on the line shape. A limited annealing capability was achieved by putting the sample on a tantalum boat through which a current was driven under high vacuum at the level of 10^{-5} mbar. The temperature calibration was done by putting pieces of Sn, Al, and Ag metals on the boat and observing the current at which the metal melts. The temperature for annealing of Pt of around 1200 °C recommended in [Zbo11] could not be achieved without major loss of activity. The Pt-15-2 was annealed at about 450 °C (with the uncertainty possibly at the level of 70 °C) for 35 min and about 60 % of the activity was lost. Similarly, Pt-15-3 was annealed for 15 min with about 30 % loss of activity. Moreover, in this case the current fluctuated for an unknown reason leading possibly to temperatures in the range from 400 °C to 600 °C. Only in the case of Pt-15-4 the annealing was more controllable. The temperature was 200 °C, 300 °C, 400 °C and 500 °C each for 15 min leading to a reduction of the activity by 0.5 %, 1 %, 2.5 % and 23 %. A dedicated investigation of the annealing possibilities was performed in the work [Kür13].

It seems that the area S of the radiographical image half maximum shrunk after the annealing although the shape remained practically the same. The relative difference amounts to about 17 % for Pt-15-2 and 20 % for Pt-15-3. Unfortunately, for Pt-15-4 the radiographical image was not measured after the annealing. An opposite trend can be expected due to ^{83}Rb diffusion. Thus, such an observation is not fully understood but may possibly indicate additional clustering of ^{83}Rb as a result of the annealing.

The source Pt-15-3 was re-measured at the MoS after the annealing but no difference of the line shape with respect to the previous measurements was found. Owing to the weakness of the source it was not measured for the line position stability. However, a significant difference was observed regarding the satellite structure at the $\text{N}_{2,3-32}$ doublet, see Section 5.5.

Outlying values

There are occasional outlying line position values seen in the Figs. 5.14 and 5.16. The points seem to be further from the surrounding average more than allowed statistically by their uncertainty. The most prominent one is the point at around day 140 in the first plot with the value larger by more than 0.3 eV. By using the reference method with a preceding spectrum as the reference a clear residual structure is seen at the lowest retarding energies with $\chi_{\text{dof}}^2 = 3.36$ (46 dof). Apparently, the spectrum was temporarily distorted which led to different results of the fitted parameters.

In this case, the distortion can be attributed to automatic filling of the detector dewar with liquid nitrogen. Since the detector is sensitive to vibrations, under some circumstances the filling could cause elevated background in the detector spectrum leading to the integral spectrum distortion. This is supported by the fact that the time of the spectrum distortion corresponds to the time of the filling. To counteract the vibrations a special “shower” plug was installed at the end of the nitrogen pipe. Despite this a similar correspondence was found for the first outlying value in the Fig. 5.16, although the distortion is not as severe. The other outlying points were not checked but the same problem could be suspected.

5.3.2 Stability of the MoS system

Several tests were carried out using the ISOLDE implanted sources in order to verify that the MoS system is reasonably stable.

Deliberate venting of spectrometer

In order to test that the work function can be recovered after vacuum is lost, the spectrometer was vented with ambient air (humidity 56 %, temperature 20 °C) and left in such a state for 10 h. After this time, it was pumped out again but firstly not baked out. The pressure of only about 1×10^{-8} mbar was reached. The effect on the observed line position is clearly seen for both K-32 in the Fig. 5.14 and L_3 -32 in the Fig. 5.15 (left) where a common drop of about 0.4 eV is observed. Thus, the observation of [Zbo11] that the work function gets higher with increased amount of adsorbed gases is reproduced.

After the measurements the spectrometer vessel and the source chamber were baked out to 200 °C for about 27 h and 120 °C for about 48 h, respectively, which is marked in the figures. After the bakeout the line position of both lines recovered to somewhat higher value than prior to the venting although for K-32 the result is ambiguous due to the larger uncertainty. We may obtain higher precision results by using the reference method. The obtained spectrum relative shift for Pt-10-1 for the lines K-32, L_3 -32 and L_3 -9.4 is shown in Fig. 5.18. For each line the first spectrum in the depicted time period was taken as the reference spectrum.

The average spectrum relative shift after the venting and after the baking with respect to the average relative shift prior to the venting is listed in Table 5.3. The points which differ from the average by more than four standard deviations are excluded and the

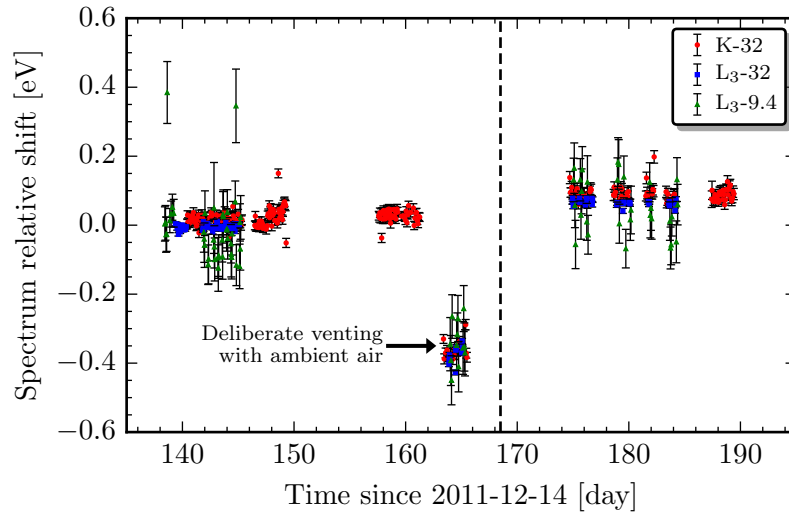


Figure 5.18: Relative spectrum shift obtained using the reference method for Pt-10-1 for the lines K-32, L₃-32 and L₃-9.4 at the time around the deliberate venting test. The bake-out and venting are indicated in the same way as in the Fig. 5.14.

average is calculated again. The results show that there is a common shift of the spectrum towards higher values after the baking compared to the values prior to the venting. The line position could not have changed by this much, so this may indicate that the retarding electrode was most likely not clean already prior to the venting. Thus, it seems appropriate that a bake-out of the spectrometer is performed prior to each measurement of the long-term stability.

Measurement by varying electrical potential at the source

For most of the measurements the sources were electrically grounded and the electron line measurements were done by varying the voltage at the retarding electrode. In the parallel mode the retarding voltage will be set by the main spectrometer and the MoS measurement will be accomplished by varying the bias voltage at the source. Using either possibility should not change the observed line position. In order to verify this the parallel

Table 5.3: The average relative spectrum shift after the venting and after the baking of the MoS relatively to the average spectrum relative shift prior to the venting. The averages are calculated using the values shown in Fig. 5.18.

Line	Average shift (eV)	
	vented	baked-out
K-32	-0.386(5)	0.066(2)
L ₃ -32	-0.363(5)	0.070(2)
L ₃ -9.4	-0.32(2)	0.071(18)

mode was experimentally simulated by keeping the retarding voltage constant at about -18.6 kV and by varying the bias at the source at around -750 V . No observable difference of the line position was found by comparing such measurements with the regular ones. Also no influence on the electron line shape was observed except for the amplitude and background which increased by about 10% for K-32.

Such an effect can be explained by considering the additional electrical field at the source which points essentially towards the spectrometer at the place of the substrate where the electrons are emitted from. The electrons experience additional acceleration towards the spectrometer and the emission is no longer isotropic. Thus, at the same acceptance angle, which is determined only by the magnetic field, more electrons are collected leading to a higher amplitude and background. This also demonstrates that the background under the electron line is due to the source itself. Obviously, the anisotropy is bias dependent, i.e. the larger the bias, the larger the anisotropy. Owing to the large energy of the electrons compared to the width of the measurement interval such a dependence has only an effect on the total amplitude and background but not on the line shape itself as verified experimentally.

Preserving vacuum

A drop of the pressure reading is observed at around day 195 in the Fig. 5.15 (right). At this time a safety test was carried out at the MoS when the power was intentionally cut off. In such a case, the TMPs can no longer pump out the system and to prevent loss of vacuum several safety valves close the inner volumes. Since there does not seem to be any significant effect on the line position, the safety system appears to be working as expected.

Elevated lab temperature

On the day 227 the air-conditioning in the MoS building was intentionally switched off. The air temperature went from the nominal $19\text{ }^\circ\text{C}$ up to $29\text{ }^\circ\text{C}$. No observable effect on the line position was seen.

5.3.3 BONIS generation 1: Pt-30-3 and Pt-30-4

The first samples obtained at the Bonn isotope separator were implanted with a small efficiency of only 4% and 2%, respectively. Thus, only low ^{83}Rb activities were obtained. For Pt-30-3 the ^{83}Rb solution was deposited on a tantalum foil which was pushed down into the furnace. Unfortunately, during the pushing some of the activity was scratched off contaminating the walls of the furnace. Such an activity was basically lost for the implantation. The furnace was loaded with 15.1 MBq and after the implantation there was 2.4 MBq left. For Pt-30-4 the solution was deposited directly inside the furnace. However, after the deposition the outer side of the furnace became contaminated possibly due to a leak in the furnace walls or due to boiling during evaporation of the solution.

The furnace held 10.2 MBq before the implantation and, interestingly, only 6 kBq after the implantation.

Comparison to the ISOLDE Pt-30-5

The line shape of the BONIS sources Pt-30-3 and Pt-30-4 were found to be comparable to the ISOLDE Pt-30-5. However, a substantially smaller amplitude-to-activity ratio for the BONIS sources was observed. At the source position of 19.2 cm from the magnet center the amplitude-to-activity ratio of only about 2.1 cps kBq^{-1} was mostly measured compared to 3.7 cps kBq^{-1} . The amplitude-to-background ratio of the BONIS sources was the same as for the ISOLDE one.

One might suspect whether the MoS detector observed electrons from the whole active area of the substrate. The area S of the activity spot half maximum is similar for both BONIS sources, see Table 5.1. Let us consider Pt-30-3 for which it amounts to about 20.9 mm^2 . With the source magnetic field of 2.5 T this corresponds to the magnetic flux of 0.52 T cm^2 . The detector was at 28.6 cm from the magnet center at the magnetic field of about 0.4 T. Since the magnetic flux is constant the flux tube area at the detector amounts to 1.31 cm^2 to be compared with the detector area of 1.5 cm^2 . Owing to the fuzzy activity spot, unfortunately some of the electrons emitted from the edges of the activity spot might not hit the detector. In case of Pt-30-5 the area is only 5.6 mm^2 corresponding to 0.35 cm^2 at the detector.

If only such an effect was present, the amplitude-to-activity ratio of the ISOLDE source would be the same relatively to the ratio for the BONIS sources regardless of the conversion line. For K-32 the amplitude-to-activity ratio of Pt-30-5 is about 1.75 times higher the BONIS sources ratio. However, for L_3 -32 the factor is only 1.60 and for L_3 -9.4 it is as high as 1.95. Therefore, it seems that the smaller the energy, the larger the difference between amplitude-to-activity ratios. Such an effect could be explained if for some reason the electrons of the BONIS sources experienced more energy losses than electrons of the ISOLDE one.

Line position stability

The obtained line position results of Pt-10-1, Pt-30-3, Pt-30-4, and Pt-30-5 are shown in Fig. 5.19. Only limited amount of data is available since at December 2012 the measurement had to be stopped in favor of work function measurement concerning candidate materials for the back plate of the KATRIN rear wall. The data of the first source are the same as in Fig. 5.16 from day 280 onwards and are shown here for comparison.

The striking observation is the significant shift of the line position for the BONIS sources after the source chamber was heated at around day 46. For the stronger Pt-30-3 the shift amounts to $83(11) \text{ meV}$. The line position shift is seen also for the L_3 -32 line but in this case it amounts to $123(9) \text{ meV}$ which is larger than for K-32. There is a line position increase observed for both BONIS sources up to around the day 55. Since then only Pt-30-3 was measured due to poor statistics obtainable with the other source. The

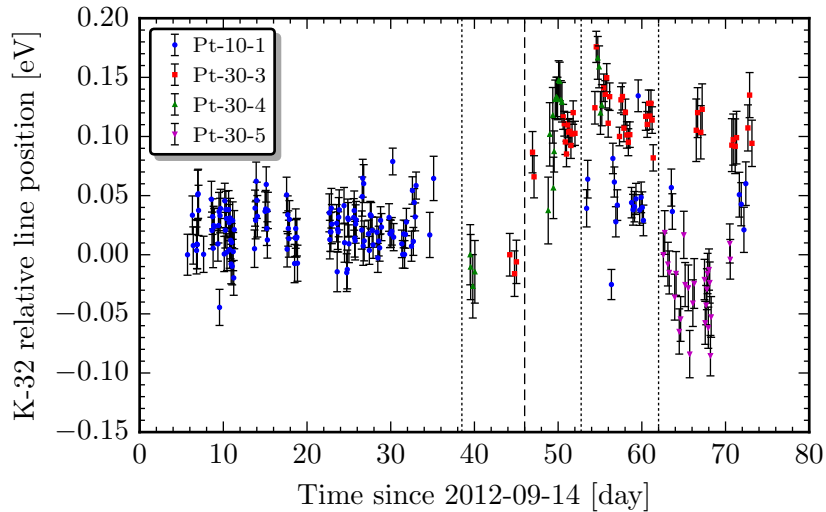


Figure 5.19: The K-32 line position in time for the older ISOLDE source Pt-10-1, newer Pt-30-5 and the two BONIS sources of the first generation Pt-30-3 and Pt-30-4. The values are relative to the first value in the graph for each source individually. The source chamber bake-out is indicated with thin vertical dashed line. The dotted lines refer to opening of the source chamber and subsequent pumping out without baking.

total time of measurement is rather short but an overall decrease of the line position can be seen.

The described observation is seen despite the sources were implanted with a rather low dose. However, it should be noted that the dose is calculated from the radioactive ^{83}Rb contribution. At the BONIS there might be beam instabilities due to high-voltage breakdowns at the furnace heating system and additionally due to partial overlap of neighbouring masses in the beam at the end of the implantation when the furnace starts to get depleted. Due to such effects a non-negligible amount of non-radioactive contamination could be implanted into the substrate. A high enough non-radioactive dose could possibly lead to the observed effects since the ^{83}Rb environment would be highly affected. Unfortunately, it is not possible to estimate the contamination for these two sources since the current integrator was not operational at that moment. Similarly, the Timepix detector cannot reveal information about the non-radioactive contamination.

5.3.4 BONIS generation 2: Pt-30-6, Pt-80-1

For this generation of BONIS samples it was attempted to reduce the risk of implanting contamination. Two furnaces were loaded with about 40 MBq of ^{83}Rb each. From each furnace one source was produced with the efficiency of 3.8% and 1.8%, respectively. Using the repaired current integrator it was observed that at the end of the implantation the current was staying constant or even rising while from the online activity monitor the additionally implanted activity was decreasing. At this point the implantation was stopped and the amount of activity which remained in the furnace after the implantation

amounted to 12 MBq and 10 MBq, respectively. In this way, both implantations were terminated well before depleting the furnace.

Unfortunately, the first source Pt-80-1 was accidentally implanted with the ^{83}Rb energy of 80 keV leading to a large amount of loss-energy electrons and thus the source was not used for a long-term stability measurement. Moreover, for this source several ^{83}Rb beam breakdowns occurred which could possibly lead to more implanted contamination. The ion source had to be repaired in order to continue with the implantation. Prior to implanting the second source Pt-30-6 the ^{83}Rb solution was found to be not completely evaporated. During deposition of the RbCl powder using a spatula a thin film of liquid was removed from the furnace on the spatula. It is possible that in this way some activity was also removed. The efficiency stated above is calculated under the assumption that no activity was removed.

Comparison to the ISOLDE Pt-30-5 and BONIS Pt-30-3

The line shape appears to be the same as for the older sources. The amplitude-to-activity ratio of Pt-30-6 was found to be at about 3cps kBq^{-1} , which is notably higher than for Pt-30-3 but slightly lower than for Pt-30-5. The ratio for Pt-80-1 was found to be 1.7cps kBq^{-1} , i.e. only slightly lower than for Pt-30-3, despite the activity area S was practically the same. Therefore, either there was a very large amount of contamination implanted for the first generation leading to larger densities the electrons have to encounter or the sources were produced using a higher implantation energy than stated.

Line position stability

The first measurements of Pt-30-6 showed rapidly decreasing line position where a difference of about 4 eV was reached within a single day. Since no other source showed such a behaviour, the source grounding wire was inspected and found to be broken. This caused that the decaying source charged itself positively by giving away negative electrons which led to a lower line position. Excluding the data taken with the broken wire several K-32 and L₃-32 measurements were taken for an outer source position of 28.3 cm from the magnet center prior to and after heating of the source chamber. The source chamber was heated at 100 °C for about 10 h and additionally at 120 °C for about 6 h. The line position results showed a similar shift for Pt-30-6 as previously for the first generation sources of about 90(30) meV. For L₃-32 the shift amounted to 133(8) meV. There is no apparent shift for Pt-30-5 but since only a single value with large uncertainty is available, no further conclusion can be drawn.

For the long-term line position stability only the sources Pt-30-5 and Pt-30-6 were measured. The complete results are shown in Fig. 5.20. The source position was 19.2 cm from the magnet center. No immediate drift is seen for Pt-30-6 as was observed for Pt-30-3 and therefore the attempt to reduce the implanted contamination might seem to have a positive effect. The complete measurement was interrupted only by two short background measurements not related to the SKrS and on-site calibration of the K35 divider. At around day 46 a restart of the MoS slow control system was needed. However, after the

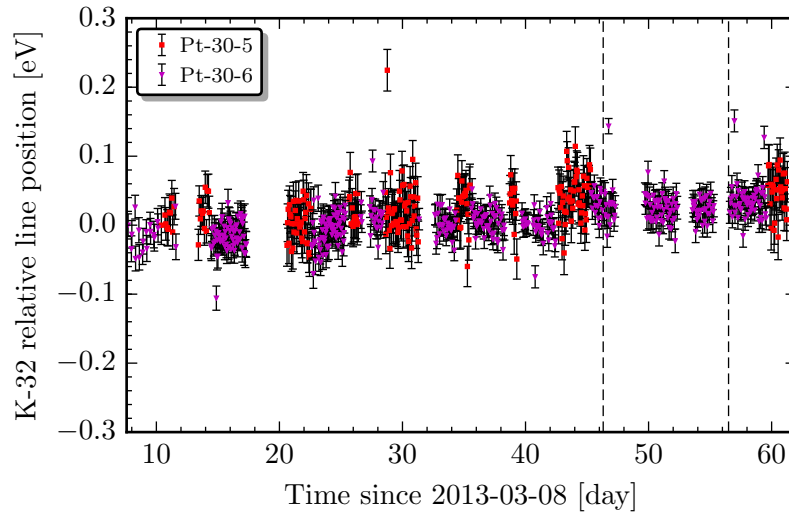


Figure 5.20: The long-term stability of the K-32 line position for the ISOLDE source Pt-30-5 and BONIS source Pt-30-6 of the second generation. The values are relative to the first value in the graph for each source individually. The left (right) vertical dashed lines refer to closing (opening) of the valve between the intermediate vacuum and the fore-vacuum.

restart the valve between the intermediate and the fore-vacuum remained closed and thus the spectrometer was pumped out only into the space of the intermediate vacuum. The situation was not recognized for about 10d which led to a gradual increase of pressure inside the spectrometer which is shown in Fig. 5.21. After the valve was opened again, residual gas analysis showed dominance of nitrogen and water while prior to the incident the pressure was dominated by hydrogen. This indicates presence of air and possibly influence on the spectrometer work function concerning the lastly taken measurements.

The drift of the K-32 line position amounted to $30(4) \text{ meV month}^{-1}$ for Pt-30-5 and $31.0(18) \text{ meV month}^{-1}$ for Pt-30-6, respectively. The outlying points, which are again correlated to the filling of the detector dewar, were excluded from the drift calculation. Relatively to the tritium endpoint energy of $18\,575 \text{ eV}$ this corresponds to $1.6(2) \text{ ppm month}^{-1}$ and $1.7(1) \text{ ppm month}^{-1}$, respectively. According to the approach described in the beginning of this chapter the contribution of the larger of the drifts to the neutrino mass squared shift Δm_β^2 would be about $-6.7 \times 10^{-4} \text{ eV}^2$. This is in absolute value only about 10% of the maximal allowed KATRIN systematic uncertainty from a single contribution of $7 \times 10^{-3} \text{ eV}^2$. Thus, such a result could be considered acceptable for the purpose of KATRIN. The L_{3-32} line was also measured in the same time period less frequently. The drift of its position amounts to $18(5) \text{ meV month}^{-1}$ for Pt-30-5 and $31(3) \text{ meV month}^{-1}$ for Pt-30-6, respectively. The second value matches the one for K-32 line for the same source. For the first value there is an agreement at the level of two sigma.

Following the results of the first investigations described in the previous section, such an agreement between the two sources and the two lines is most likely not attributed to the sources themselves since the sources were implanted with a relatively low dose, see Table 5.1. Also no change of the Gaussian width was observed during the course of the

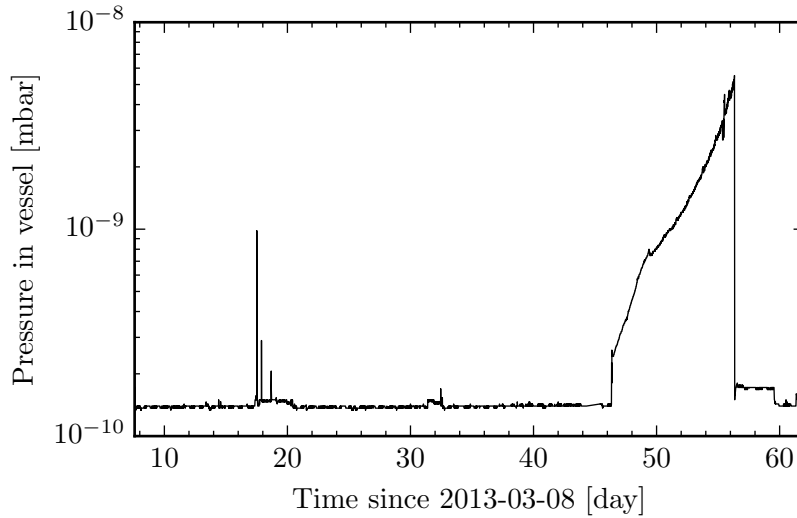


Figure 5.21: The pressure inside the spectrometer for the time of the long-term stability measurements of Pt-30-5 and Pt-30-6. The gradual increase observed after the day 46 is due to unrecognized closed valve.

measurement. The similarity of the different line position drifts points to a drift of the spectrometer work function which could be the result of not baking out the spectrometer after work function measurement of the rear wall back plate.

Due to rather small source activities the time of measurement of a single K-32 spectrum had to be rather large in order that the uncertainty of the line position from the fit is reasonably small. The median of the time between measurements was 66 min for both sources leading to the median of line position uncertainties of 29 meV and 16 meV, respectively. For KATRIN a stronger source for the high-voltage stability monitoring is desired.

5.3.5 BONIS generation 3: Pt-30-7, ZnO-30-1, and ZnO-30-2

The purpose of the third generation of BONIS sources was to investigate the effect of controlled annealing of the sources on the observed line position stability. Also the zinc oxide (ZnO) substrate was investigated.

The Pt-30-7 was implanted with the efficiency of about 13% while the activity which remained in the furnace was 12.4 MBq. The source was subsequently cleaned with propanol and annealed in vacuum at 360 °C and 400 °C each for 15 min. The activity after such a procedure was practically the same as before. The radiographical image as shown in the Fig. 5.11 was obtained after the annealing. Due to time constraints no image is available prior to the annealing. The implanted surface dose and the peak concentration as listed in Table 5.1 might not be fully representative due to the annealing.

Due to a comparable size of the beam to the size of the ZnO substrate, a metal foil was placed behind to collect the remaining activity. In the case of ZnO-30-1 the total implantation efficiency (substrate and the metal foil) amounted to about 7% and the

activity remaining in the furnace was 10 MBq. Unfortunately, the source was implanted with 0° tilt angle with respect to the beam so channeling effects might have occurred. For this reason, the peak concentration as listed in Table 5.1 might not be fully representative. The implantation into the ZnO substrate was repeated. For ZnO-30-2 the efficiency amounted to as high as 31 % and only 1.4 MBq was left in the furnace. The tilt angle for the second ZnO source was 10° .

Both ZnO sources were immersed in propanol over a night to loosen an aluminum scotch tape which was used to fix the substrate to the target holder during the implantation. A drop of activity by about 0.2 MBq and 0.6 MBq, respectively, was observed after removing the tape. The ZnO-30-1 was subsequently annealed in vacuum at 800°C for 15 min resulting in an additional 0.2 MBq loss of activity. The ZnO-30-2 was annealed firstly at 600°C and then at 700°C each for 15 min. Unfortunately, only the first step was done in vacuum while the second step was done at ambient air and pressure for which diffusion of air compounds into the substrate could possibly take place. A similar 0.2 MBq loss of activity was observed. The activities stated in the Table 5.1 are given for the state after the annealing. To measure the retention of ZnO-30-2 the source had to be stucked to the blank flange of the retention chamber since it was too small to be fixed there by the chamber middle part. A further loss of activity of about 0.35 MBq was observed after removing the source from the flange using propanol.

Comparison to Pt-30-6

The line shape of the ZnO sources appears to be less asymmetrical but broader compared to Pt-30-6. The line position is about 2 eV lower than for Pt-30-6. Examples of the fit of a K-32 spectrum of ZnO-30-1 and ZnO-30-2 are shown in Fig. 5.22. The DSG lineshape seems to describe the observed spectrum in a reasonable way. However, problematic description was found for the L_3 -32 line of ZnO-30-2 whereas the description is acceptable in the case of ZnO-30-1. Examples of the L_3 -32 spectrum fit of both ZnO sources are shown in Fig. 5.23. The residuals have a similar pattern in other spectra of the same line.

The line shape of the strong Pt-30-7 showed a K-32 Gaussian width of about 0.6 eV which is larger than for the older Pt-30-6 but not as large as for the ISOLDE Pt-15-5 and Pt-10-1 after their production. Moreover, the line position was by about 0.2 eV lower than for Pt-30-6. Interestingly, a similar problem with the description of the L_3 -32 as for ZnO-30-2 was found for Pt-30-7. Examples of the fits of Pt-30-7 K-32 and L_3 -32 spectra are shown in Fig. 5.24. No such residuals were observed for any of the older sources even in the situation when the line was measured with comparable statistics. The effect is not observed for the K-32 line in a significant way (the chi-square function value tends to about 1.5). This could be explained if the Gaussian distribution does not optimally describe the additional broadening for the two strong sources. The consequent effect seen in the fits would be more apparent for the L_3 -32 line, which has the Lorentzian width of 1.06 eV comparable to the Gaussian width, than for the K-32 line, which is broader with the Lorentzian width of 2.7 eV.

At the source position of 24.4 cm with the magnetic field of 0.9 T the amplitude-to-activity ratio amounted to 1.3 cps kBq^{-1} for Pt-30-6 whereas it was only 1.1 cps kBq^{-1}

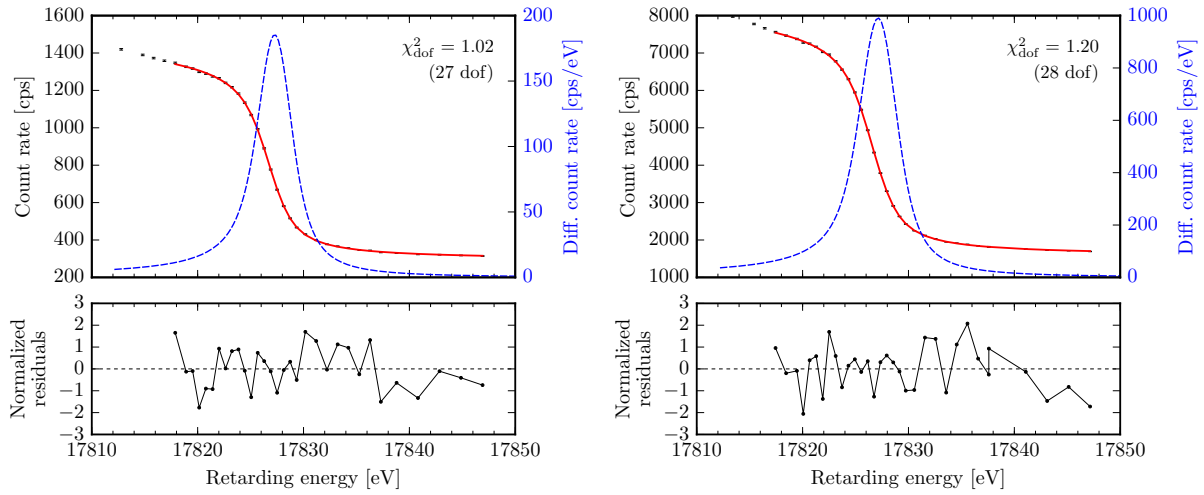


Figure 5.22: The K-32 spectrum for ZnO-30-1 (left) and ZnO-30-2 (right). The Gaussian width σ was 0.90(4) eV and 1.06(3) eV, respectively, and the asymmetry α amounted to 0.055(6) and 0.059(5), respectively.

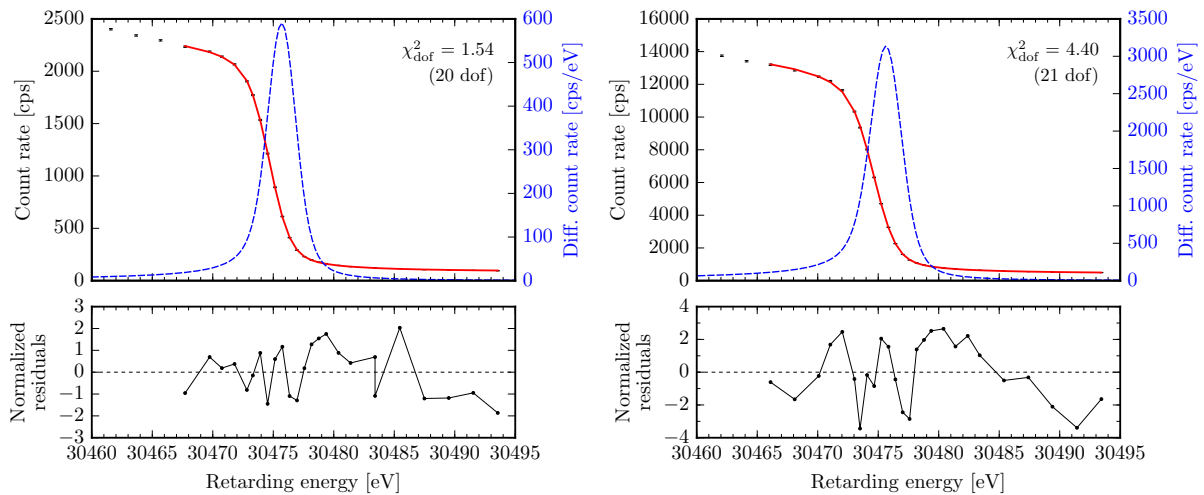


Figure 5.23: The L_3 -32 spectrum for ZnO-30-1 (left) and ZnO-30-2 (right). The fits were obtained using the Lorentzian width fixed to 1.06 eV.

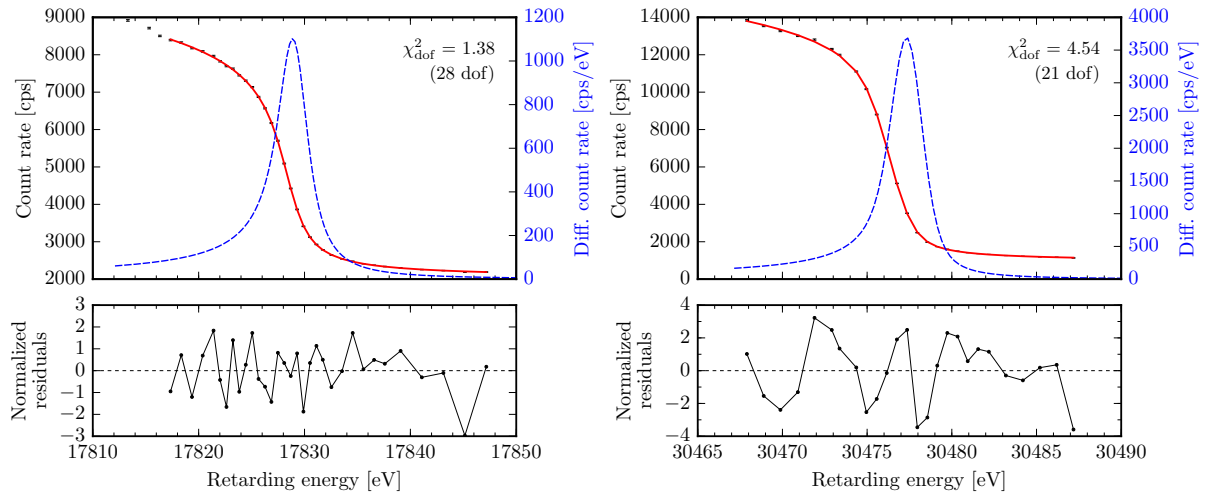


Figure 5.24: The spectrum of K-32 (left) and L_3 -32 (right) for Pt-30-7.

for Pt-30-7. The lower value for Pt-30-7 could reflect diffusion of ^{83}Rb deeper into the substrate during annealing. The values for the ZnO-30-1 and ZnO-30-2 sources were 1.3 cps kBq^{-1} and 1.5 cps kBq^{-1} , respectively. The lower value for ZnO-30-1 could reflect the possible channeling effects but since the difference is small, it is likely that the ^{83}Rb ions did not channel too deep into the substrate. According to Table 5.2 the fraction of no-loss electrons should be by about 10% lower for ZnO. The measured results may indicate that the inelastic mean free path of the electrons is larger than previously assumed.

Line position stability

After the initial measurements both the spectrometer and the source chamber were baked out in order to improve vacuum and to recondition the retarding electrode. The spectrometer was at 170°C for 13 h and additionally at 200°C for 24 h and the source chamber was at 120°C for 42 h. A line position shift after the bake-out was found for all sources. The shifts are listed in Table 5.4. The different results among sources point to changes inside the sources besides possible change of the spectrometer work function. The Pt-30-6 was already heated once inside the chamber but in this case the heating was for a longer time period. The annealed Pt-30-7 showed the same shift for both lines which may indicate a change of the work function by 55 meV or less.

To assess the ZnO sources we have to take into account the long-term behaviour of the line position. The complete results of the stability measurement which comprises four months worth of data are shown in Fig. 5.25. The measurement was interrupted only by two short background measurements not related to the SKrS. Additionally, the source chamber was heated up to 140°C for about 24 h at around day 75 in order to observe any effect on the line shape while the source is kept at an elevated temperature (no effect was observed within the parameter uncertainties).

The drift values considering all data obtained after the spectrometer bake-out at

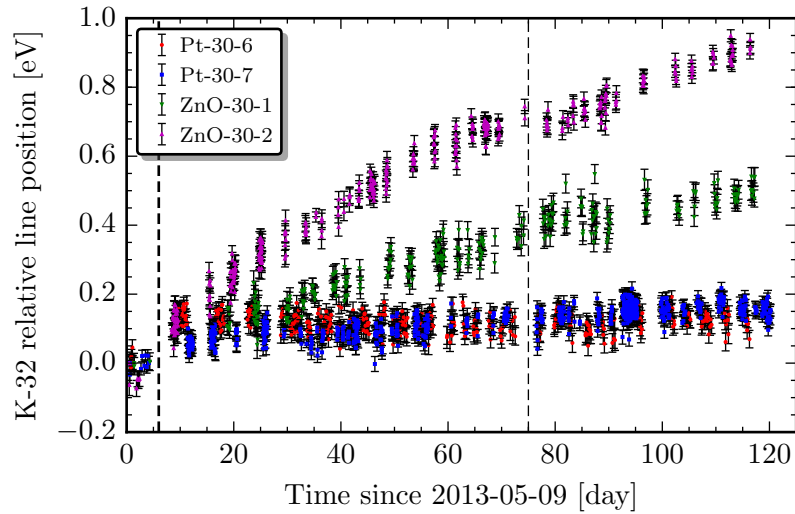


Figure 5.25: The long-term stability of the line position of the third generation BONIS sources Pt-30-7, ZnO-30-1, and ZnO-30-2 and the older source Pt-30-6. The values are relative to the first value in the graph for each source individually. The thick dashed vertical line refers to the bake-out of both the spectrometer vessel and the source chamber while the thin one refers to heating up of the source chamber only.

around day 6 are given in Table 5.4. The large drifts of the ZnO sources indicate that a comparison of measurements which are only a few days apart might be influenced by the drift. Using the drift values to extrapolate the line position from the time of measurement prior to the bake-out to the time of measurement after the bake-out we obtain that the line position shift for ZnO-30-2 amounts to about 120 meV for K-32 and 90 meV for L₃-32, respectively, and for ZnO-30-1 to about 60 meV and 30 meV, respectively. The latter values are somewhat similar to the ones for Pt-30-7.

The Gaussian width for ZnO-30-2 dropped to about 0.75 eV whereas it remained practically constant for ZnO-30-1. A drop to 0.4 eV is seen also for Pt-30-7. Moreover, the imperfect description of the L₃-32 line for Pt-30-7 seemed to have improved over time. Detailed K-32 and L₃-32 spectra of Pt-30-7 with the steps of 0.2 eV were measured

Table 5.4: Average line position shift after the spectrometer and source chamber bake-out and line position drift from the third generation long-term stability measurement. The values of the shift for ZnO-30-1 were obtained only after about two weeks after the bake-out.

Source	Average shift (meV)		Drift (meV month ⁻¹)	
	K-32	L ₃ -32	K-32	L ₃ -32
Pt-30-6	134(9)	79(8)	-5.3(15)	-3.8(13)
Pt-30-7	54(7)	55(5)	30.2(9)	12.7(9)
ZnO-30-1	120(11)	90(9)	118.6(23)	104.4(23)
ZnO-30-2	168(10)	134(8)	210.1(25)	175.4(22)

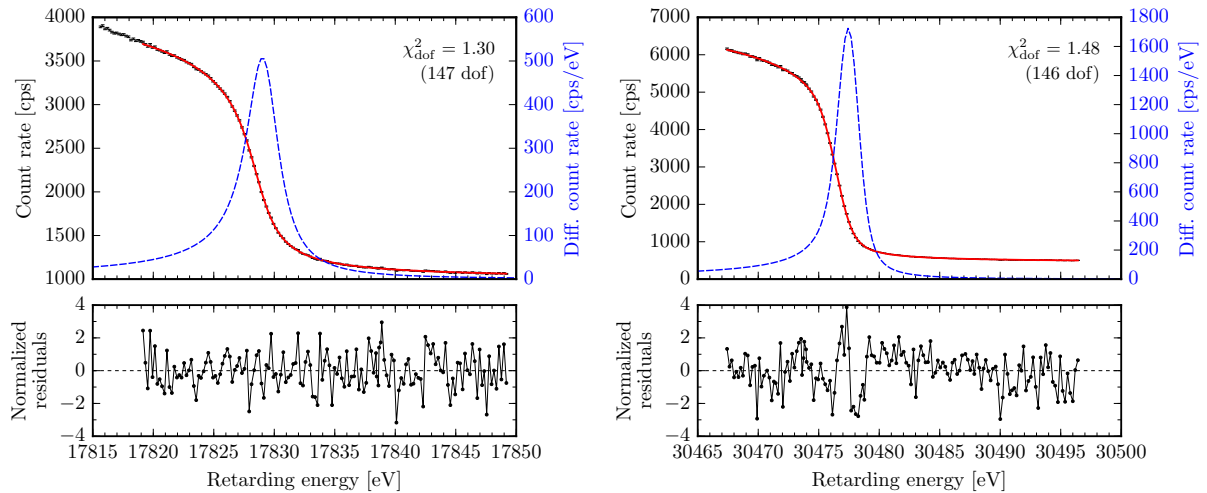


Figure 5.26: The detailed spectrum of K-32 (left) and L₃-32 (right) for Pt-30-7. The spectra were measured at around day 106, i.e. after the source aged.

at around day 106. The fit results are shown in Fig. 5.26. The obtained chi-square value is acceptable in both cases although still some residual structure is observed for L₃-32. Nevertheless, the situation is significantly better than in the beginning of the measurements, cf. Fig. 5.24 on the right. Thus, it seems that the line shape improved over the time the source aged.

Owing to the large line position drift the ZnO sources are not suitable for the monitoring of the KATRIN high-voltage stability since the values of $6.4 \text{ ppm month}^{-1}$ and $11.3 \text{ ppm month}^{-1}$ would lead according to Eq. (3.39b) to the neutrino mass squared shift of $-9.4 \times 10^{-3} \text{ eV}^2$ and $-2.9 \times 10^{-2} \text{ eV}^2$, respectively. The reason for such a large drift for this substrate is currently not known and the ZnO substrate was not investigated further. The drift of Pt-30-7 would be acceptable with the neutrino mass squared shift of only $-6.1 \times 10^{-4} \text{ eV}^2$. Interestingly, the drift of Pt-30-6 seems to be slightly negative whereas it was positive during the second generation measurements. This clearly demonstrates the need for a good enough condition of the retarding electrode prior to start of the measurement.

5.3.6 BONIS generation 4: Pt-30-8, Pt-30-9, and HOPG-30-1

In order to avoid problems with the line shape description as was observed for the Pt-30-7, the fourth generation of samples was produced with moderate activity and without annealing. The sources Pt-30-8 and Pt-30-9 were produced in a similar way in order to check the reproducibility of the BONIS sources. Also the highly-oriented pyrolytic graphite (HOPG) was investigated.

The Pt sources and partly the HOPG source were implanted using a single furnace. As before, the implantation was stopped well before depleting the furnace by measuring the stable Rb current. Unfortunately, the remaining activity was not measured. The

total efficiency from the first furnace amounted to about 27% with the initial furnace activity of 30 MBq. The HOPG-30-1 was implanted at an incident angle of 10° to avoid channeling effects. No further treatment of the sources was performed.

Comparison of line shape

No problems with the line shape description were observed for Pt-30-8 and Pt-30-9. The line shape of HOPG-30-1 seemed to be also asymmetrical but slightly narrower with the Gaussian width of about 0.3 eV. The line position is by about 1 eV lower as compared to the Pt-substrate sources. The amplitude-to-activity ratio for the two fourth-generation Pt-substrate sources was similar of about 1.9 cps kBq^{-1} at the source position of 20.9 cm from the magnet center compared to about 1.8 cps kBq^{-1} for the older source. For HOPG-30-1 the ratio was only about 1.7 cps kBq^{-1} . A lower number of no-loss electrons for the HOPG substrate at the implantation energy of 30 keV is expected, see Table 5.2. However, the inelastic mean free path, which was assumed for the estimations in the Table 5.2, is most probably not accurate.

However, residual structure was found in the fits of both the K-32 and L_{3-32} line of HOPG-30-1. The fit results of detailed spectra of these lines are shown in Figs. 5.27 and 5.28, respectively, on the left. The residual structure is different from the one seen for Pt-30-7 and ZnO-30-2 (Figs. 5.22 to 5.24). It turned out that for a good description the background has to be considered as a linear function of the retarding energy instead of a constant one. When the linear background coefficient is also fitted, the obtained fit result is acceptable, see the Figs. 5.27 and 5.28, respectively, on the right. The retarding energies shown in the figures are only approximate since only the less stable JRL divider with an approximately known dividing ratio was available for the initial measurements. Interestingly, the amplitude-to-background ratio of HOPG-30-1 is 7 compared to about 2 in the Pt case. The amplitude-to-background ratio has an effect on the line position uncertainty (see also further).

Line position stability

The spectrometer was heated up to 200°C for 16 h prior to the first measurements of the sources. Due to calibration of the K35 high-voltage divider at the PTB the line position stability measurement was possible only about three months after the source production. Using the less stable JRL divider line position results were obtained before and after heating of the source chamber. Unfortunately, no definite conclusion can be drawn regarding the line position due to issues with the high voltage which were caused by unclean high-voltage insulators.

The complete data obtained using the K35 divider are shown in Fig. 5.29. Since the Pt-30-7 was still sufficiently strong, it was measured as well. The line position drifts are given in Table 5.5. The drift value for the older Pt-30-7 dropped by a factor of about two but still seemed to be higher than for any of the fourth-generation sources. Moreover, the drift values are reproducible among Pt-30-8 and Pt-30-9. The contribution to the neutrino mass squared shift using Eq. (3.39b) from the largest drift of $0.33 \text{ ppm month}^{-1}$

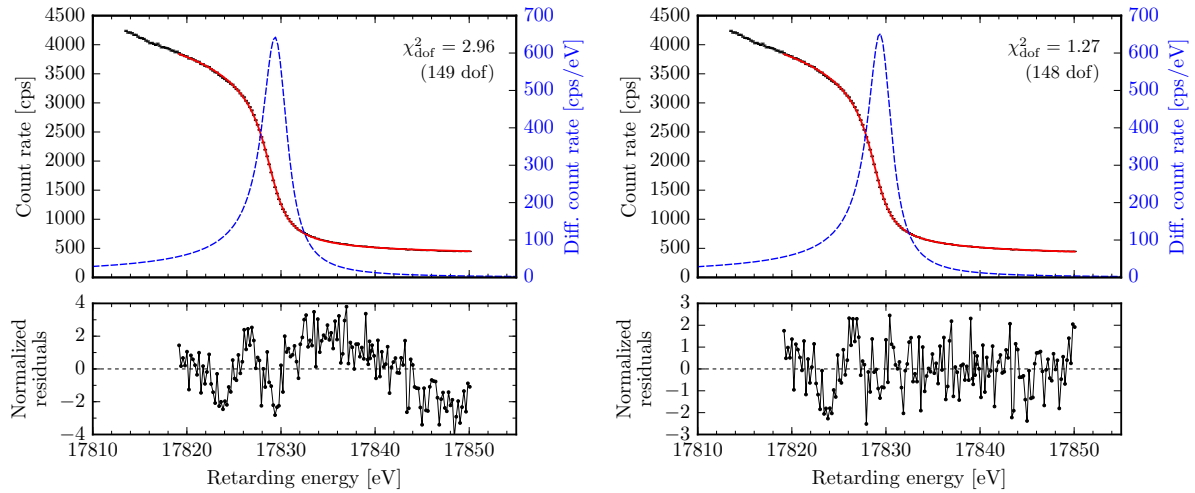


Figure 5.27: The detailed spectrum of K-32 for HOPG-30-1 fitted utilizing a constant background term (left) and a linear background term (right).

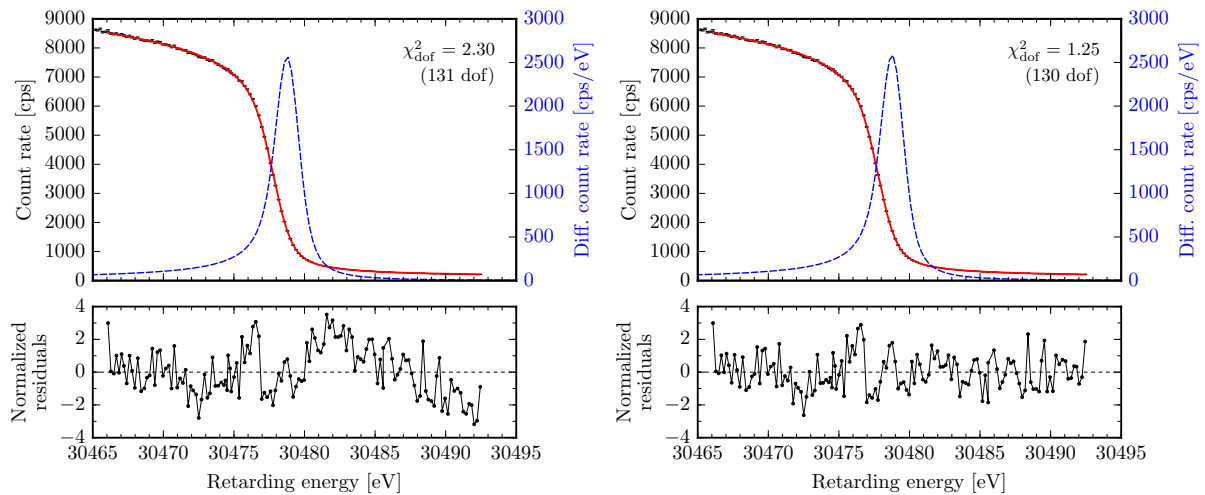


Figure 5.28: The detailed spectrum of L₃-32 for HOPG-30-1 fitted utilizing a constant background term (left) and a linear background term (right).

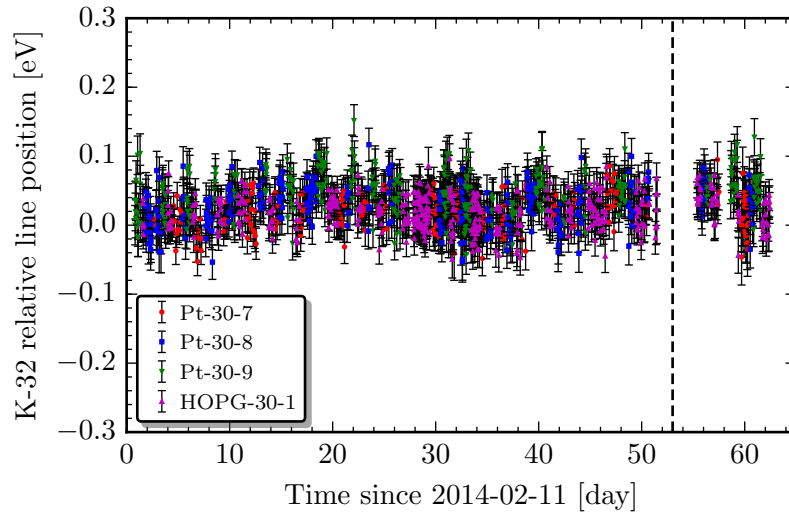


Figure 5.29: The long-term K-32 line position stability for the fourth generation sources Pt-30-8, Pt-30-9, and HOPG-30-1 and the older source Pt-30-7. The values are relative to the first value in the graph for each source individually. The thick dashed vertical line denotes bake-out of the spectrometer vessel.

for Pt-30-9 would be only $-2.5 \times 10^{-5} \text{ eV}^2$ which is completely negligible compared in absolute value to the maximal allowed systematic uncertainty of $7 \times 10^{-3} \text{ eV}^2$. Note that such drift values are at a similar level as the drift of the dividing ratio which thus might be responsible for part of the observed values.

After about 50 d the spectrometer vessel was baked out to 200°C for 30 h in order to investigate possible change of the work function. The source chamber was kept at the room temperature. No shift of the line position was observed, i.e. the condition of the retarding electrode was good during the course of the measurement. The measurement had to be stopped to allow further rear wall work function measurements as well as testing of the electron gun for the main spectrometer. The data from the days of around 30 to 45 and 60 were obtained by varying the potential at the source while the MoS retarding electrode was at the constant voltage of -18.6 kV .

Table 5.5: The line position drift observed from the long-term stability measurement of the fourth generation BONIS sources measured together with the older Pt-30-7 from the previous generation.

Source	Drift (meV month^{-1})	
	K-32	L ₃ -32
Pt-30-7	16.6(34)	19.8(37)
Pt-30-8	3.7(32)	12.3(28)
Pt-30-9	6.1(31)	11.6(22)
HOPG-30-1	2.5(21)	8.8(22)

5.3.7 BONIS generation 5: Pt-12-1, HOPG-12-1, HOPG-4-1, HOPG-8-1

The last investigated samples were obtained using a lower ^{83}Rb implantation energy utilizing the retarding lens setup. The first three sources and partly the fourth source were implanted using a single furnace. The utilized furnace was pre-heated at about 3000°C for several minutes in order to clean its surface. The furnace was loaded with 45 MBq of activity leading to the efficiency of about 28% (2.1 MBq was implanted from the first furnace into HOPG-8-1). During implantation of Pt-12-1 several high-voltage sparks occurred which led to a momentary beam breakdown when possibly heavier elements present in the furnace might be implanted. For HOPG-8-1 there were problems to get a stable beam at all in the course of the implantation. In order to continue, the ion source would have to be refurbished. Since the ion source was heavily contaminated by ^{83}Rb , it was decided to postpone the refurbishing by two half-lives to avoid irradiation of personnel. All the HOPG sources were implanted at the tilt angle of 10° to avoid channeling effects. No further treatment of the sources was carried out.

Comparison of line shape

Similarly as for the older HOPG-30-1 the spectra of the newer HOPG-substrate sources could be described in a reasonable way using the DSG lineshape with the linear background only. However, the χ^2_{dof} values of the L_{3-32} fits tend to values above 2 for the HOPG-substrate sources and above 2.5 for Pt-12-1. Moreover, for the K-32 they tend to about 1.5 in the case of Pt-12-1. Owing to strong focusing due to the retarding lense setup the sources were implanted with a much higher dose despite the moderate activity and so the tendency for a problematic line shape description could be related to that. The source HOPG-8-1 was not measured in favor of the source HOPG-30-1 from the previous generation.

The line position of Pt-12-1 was measured to be lower by about 0.6 eV compared to the previous generation Pt sources. Also the line position of HOPG-12-1 and HOPG-4-1 was lower compared to HOPG-30-1 and by a different amount for each source. A striking observation was the large Gaussian width of 0.8 eV for Pt-12-1. Similarly, the width was at about 0.45 eV for HOPG-12-1 and 0.5 eV for HOPG-4-1 which are both larger than for the older HOPG-30-1. Similar effects were observed for the strong ISOLDE sources Pt-15-5 and Pt-10-1. The amplitude-to-activity ratio in the same source position as for the previous generation of 20.9 cm from the magnet center was found to be 2.5 cps kBq^{-1} compared to the previous 1.9 cps kBq^{-1} for the implantation energy of 30 keV and Pt substrate. From the expected amount of no-loss electrons from the Table 5.2 and taking into account the different retention of Pt-12-1 such a result is about as expected. The ratios 3.7 cps kBq^{-1} and 4.6 cps kBq^{-1} , respectively, were obtained for HOPG-12-1 and HOPG-4-1 which are both larger than expected based on the Table 5.2 in comparison to the previous 1.7 cps kBq^{-1} . The amplitude-to-background ratio was only by a few percent larger for Pt-12-1 compared to the previous generation but it was larger by a factor of 1.7 and 2.3, respectively, for HOPG-12-1 and HOPG-4-1.

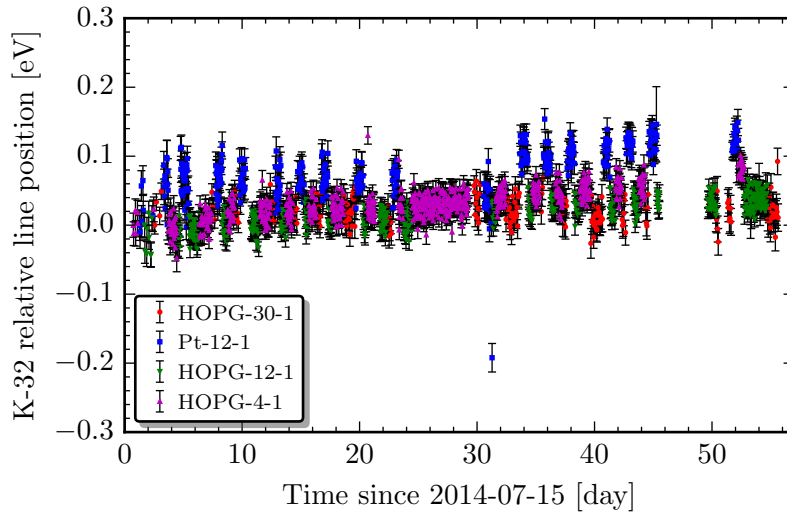


Figure 5.30: The long-term K-32 line position stability for the fifth generation sources Pt-12-1, HOPG-12-1, and HOPG-4-1 and the older source HOPG-30-1. The values are relative to the first value in the graph for each source individually.

Line position stability

The complete line position results are shown in Fig. 5.30. The spectrometer vessel was baked out prior to the measurements at 200 °C for 40 h while the source chamber was baked out at 120 °C for 24 h. A positive drift was observed for the fifth-generation sources while essentially no drift was observed for the older HOPG-30-1. The drift values are listed in Table 5.6 (the line L_{3-32} was not continuously measured). The largest drift value of $2.5 \text{ ppm month}^{-1}$ would lead using Eq. (3.39b) to the neutrino mass squared shift of $-1.4 \times 10^{-3} \text{ eV}^2$. This is in absolute value about 20 % of the maximal allowed systematic uncertainty of $7 \times 10^{-3} \text{ eV}^2$. Owing to the much better line position stability results for the previous generation such a drift cannot be considered acceptable.

There is a small shift observed when comparing the HOPG-30-1 results obtained at the end of the fourth-generation sources measurements and at the beginning of the fifth-

Table 5.6: The line position drift observed from the long-term stability measurement of the fifth generation BONIS sources measured together with the older HOPG-30-1 from the previous generation.

Source	Drift (meV month^{-1})
	K-32
HOPG-30-1	-3.4(28)
Pt-12-1	45.8(21)
HOPG-12-1	28.1(11)
HOPG-4-1	42.3(13)

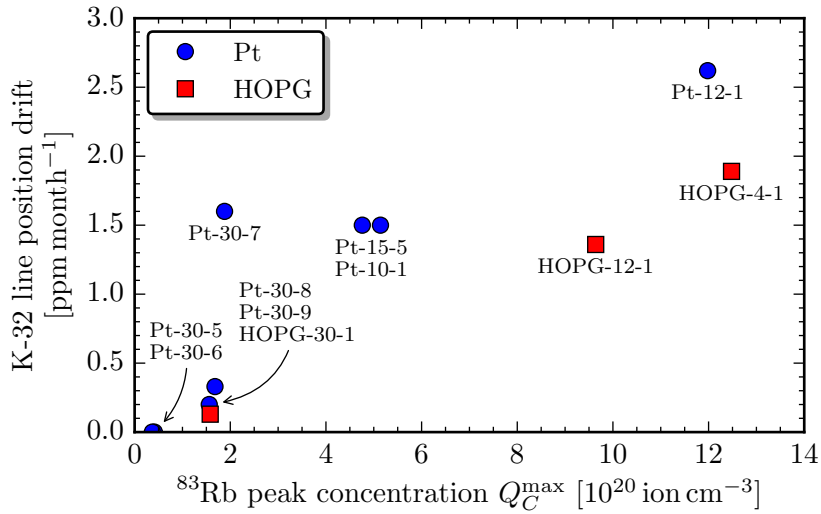


Figure 5.31: The K-32 line position drift shown against the ^{83}Rb peak concentration.

generation sources measurements. For K-32 the shifts amounts to about 20 meV while for L_3 -32 it is compatible with zero within the uncertainty. The time gap between the measurements amounts to about 90 d.

5.4 Correlation between peak concentration and line position drift

The last generation of BONIS sources had the largest surface peak implanted dose and peak concentration of ^{83}Rb from all samples investigated in this work. The reason was the unusually small activity spot comparable in size to the one for the ISOLDE sources together with a slightly larger activity. There does not seem to be a direct correspondence between the implanted surface dose and the drift. The HOPG-4-1 had the surface dose by a factor of two smaller than HOPG-12-1 but showed a factor of 1.5 larger drift of the K-32 line position. Moreover, the ZnO-substrate sources, which were annealed and their lattice should have been mostly restored, showed the largest drift ever observed for the SKrS. Some drift was also observed for the annealed Pt-30-7.

It seems that there might be a correlation of the drift to the ^{83}Rb peak concentration. The K-32 line position drift is shown against the peak concentration in the Fig. 5.31 for the fourth- and fifth-generation BONIS sources, which were produced and treated all in the same way and measured with a baked-out spectrometer thus ensuring good retarding electrode surface conditions. The only difference is that the fourth generation was measured for the stability only after three months after the production. These results clearly show that a source with a stable enough energy of the emitted electrons can be achieved by keeping the ^{83}Rb concentration low enough. Such a statement holds under the assumption that no significant amount of non-radioactive contamination is implanted.

To include the other sources which were measured for the long-term stability some

additional assumptions have to be taken first.

- ISOLDE Pt-15-5 and Pt-10-1: As described previously the K-32 line position increased by about 0.2 eV in seven months. Therefore, the drift could be taken as $1.5 \text{ ppm month}^{-1}$. On the other hand, the influence of the other experiments performed at the MoS and imperfection of the retarding electrode surface condition prohibits a clearer interpretation of the results. Also the seven-month period is rather long to establish a single drift value because the drift most likely saturates over the time. We take the mentioned value as a drift for these sources having in mind its large uncertainty. We also need to keep in mind the blurred radiographical image, measured due to the non-zero distance of the source to the detector, used to calculate the peak concentration. The actual concentration might be by some 10 % larger.
- ISOLDE Pt-30-5 and BONIS Pt-30-6: As described previously both the K-32 and L_3 -32 lines of both sources showed about the same drift value. The most likely reason is a drifting spectrometer work function. Taking the observed drift of about $1.7 \text{ ppm month}^{-1}$ as a common one the actual drift from the source amounts to zero. Note that the ISOLDE source was measured for the line position stability only after about four months after production. In this case, the note about the blurring as mentioned in the previous point also applies.
- BONIS Pt-30-7, ZnO-30-1, and ZnO-30-2: The annealing of the sources could have caused changes in the substrate which makes the sources difficult to compare with the remaining ones. The problematic line shape description for the strongest Pt-30-7 and ZnO-30-2 represents further complication. Since no other ZnO-substrate source was obtained in a better way (no channeling, no annealing at ambient air) it is not possible to evaluate the substrate further. Also the observed drift was an order of magnitude larger than for the other substrate sources. Since this is not understood we do not compare the results to the other sources. For the Pt-30-7 we take the observed drift after production assuming that the calculated peak concentration did not change after the annealing.

Only three HOPG-substrate sources were measured, but the three different drift values lie on a straight line in the Fig. 5.31. To evaluate such a high correlation further a source with the ^{83}Rb peak concentration in the range of $2 \times 10^{20} \text{ ion cm}^{-3}$ to $10 \times 10^{20} \text{ ion cm}^{-3}$ could be produced and measured for the line position stability. In the Pt-substrate case the situation is somewhat more complex but apart from the annealed Pt-30-7 result and taking into account the uncertainty of the ISOLDE points the values also seem to lie on a straight line in the Fig. 5.31. As in the HOPG case a Pt-substrate source could be produced with the peak concentration in the mentioned range to address the correlation further.

Such a correlation between the peak concentration and the line position drift can actually be seen also in the results of the previous work [Zbo11, Zbo13]. Due to using the retardation chamber which led to broadening of the ion beam and the lower activity the

implanted surface dose was lower for Pt-15-1 by a factor of about six compared to Pt-30-2 (the concentration was lower by only a factor of four due to the lower implantation energy and consequently higher relative peak longitudinal dose). The line position drift of the source Pt-15-1 was compatible with zero within its uncertainty while the drift for Pt-30-2 was at the level of a ppm month⁻¹.

The actual mechanism that could be responsible for such a correlation is currently not known. We could speculate that in the case of concentration at the level of a percent the ^{83}Rb atoms form clusters and influence the $^{83\text{m}}\text{Kr}$ environment. As the ^{83}Rb decays the environment of $^{83\text{m}}\text{Kr}$ originally influenced by the ^{83}Rb slowly changes leading to a gradual drift of the line position. In the case of lower concentration the influence from single or a few ^{83}Rb atoms at one place is much weaker and thus the decay of ^{83}Rb leads to only minor changes of the $^{83\text{m}}\text{Kr}$ surroundings. Apparently, annealing of the source after implantation does not improve its quality with respect to the line position stability and it actually seems to make the stability worse. Nevertheless, it could be worth annealing one of the future HOPG substrates to observe the effects.

Information about the $^{83\text{m}}\text{Kr}$ surrounding environment and possibly its evolution in time could be addressed using the perturbed angular correlation (PAC) technique [Are13, Are16]. The cascades of interest observed in the decay of ^{83}Rb are the 553 keV-9.4 keV γ - γ and 17.83 keV-9.4 keV e- γ ones with the common intermediate $7/2^+$ state with the half-life of about 150 ns. Such a time is long enough for the nuclear spin precession to take place as a result of interaction of the nuclear quadrupole moment and electrical field gradient due to lattice or its defects. Consequently, the angular correlation among the selected radiation will be perturbed and measurement of its time dependence can provide information about the field gradient. Moreover, in the first case, the half-life of the relevant krypton excited state is only 6 ps and thus the method provides information about the field gradient in the surroundings of the original ^{83}Rb atom. In the second case, the $^{83\text{m}}\text{Kr}$ state has a half-life of about 1.8 h during which the atom can possibly diffuse around the lattice and thus the PAC could give information about the behaviour of $^{83\text{m}}\text{Kr}$ after the decay of ^{83}Rb takes place.

5.5 Valence electrons of the SKrS

Since the work [Zbo11] it has been known that an additional structure exists close to the $\text{N}_{2,3}$ -32 doublet, which is the highest energy conversion line observed in the $^{83\text{m}}\text{Kr}$ spectrum (see also Fig. 3.5). An example of the electron spectrum of Pt-10-1 is shown in Fig. 5.32 on the left. The separation of the N_2 -32 and N_3 -32 lines is only 0.7 eV which is not resolvable by the spectrometer which has a resolution of about 1.6 eV at such an energy. However, there is clearly a “doublet of lines” visible with the separation of about 5 eV. Although the conversion line is not utilized for the high-voltage stability monitoring in KATRIN, the line was measured for every source after its production and occasionally later. The structure is observable for all the SKrS samples investigated in this work although with generally different separation and ratio of the amplitudes. The spectrum can be reasonably well be described by a doublet of DSG functions. Owing to the large

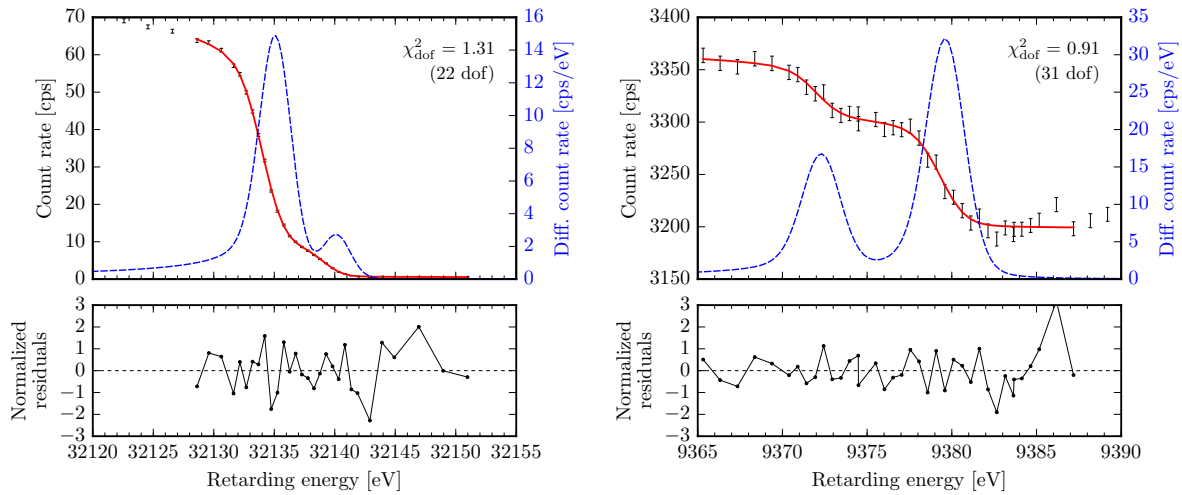


Figure 5.32: An example of the $N_{2,3}$ -32 spectrum of Pt-10-1 (left) and N_1 -9.4 spectrum of ZnO-30-2 (right). In the former case, the conversion line doublet is not resolvable by the spectrometer and the higher energy subdominant peak is an additional structure. In the latter case, only a single line is expected.

correlation between the parameters of the two peaks we perform the fit using a fixed Lorentzian width $\Gamma_{N_{2,3}} = 0.1 \text{ eV}$ [Cam01] and a common asymmetry α for both peaks. The amplitude ratio of the higher-energy peak to the lower-energy one amounts to about 0.16.

A similar structure was observed in this work for the N_1 -9.4 line for the strongest sources Pt-30-7 and ZnO-30-2. It was not measured for the other sources since the line is weak and has a large background making its observation difficult and time-consuming. An example of the measured spectrum for ZnO-30-2 is shown in Fig. 5.32 on the right. The separation of about 7 eV and the amplitude ratio of about 2.0 are different than for the $N_{2,3}$ -32 line. As in the first case, the structure can be reasonably well described using a doublet of DSG functions with the fixed Lorentzian width $\Gamma_{N_1} = 0.4 \text{ eV}$ [Cam01] where additionally the Gaussian width σ is common for both peaks. The lines N_1 -32 and $N_{2,3}$ -9.4 are even weaker than N_1 -9.4 and were not measured.

The measurements of the $N_{2,3}$ -32 line of the other sources indicate the following.

- The amplitude ratio for Pt-substrate sources with the implantation energy of 10 keV to 15 keV tends to 0.15 to 0.18 while for the higher implantation energy it tends to 0.19 to 0.22. For the ZnO-substrate sources it was measured only after the annealing and the results indicate about 0.12 for ZnO-30-1 and 0.08 for ZnO-30-2. For HOPG it tends to only about 0.04 and seemingly regardless of energy, although the results for HOPG-30-1 were obtained using the JRL divider and are affected by the high-voltage insulation problems. There does not seem to be any obvious correlation between the radioactive implanted dose (or peak concentration) and the amplitude ratio. For the Ir-15-1 substrate the ratio was about 0.13.

- The annealing of Pt-substrate sources seems to decrease the amplitude ratio. For Pt-15-3 it dropped to about 0.09 and for Pt-30-7 it was 0.18, i.e. lower than for the other Pt-30 sources.
- The amplitude ratio seems to decrease in time. For Pt-15-5 and Pt-10-1 it decreased by about 0.02 in a year and for the ZnO sources it decreased by about 0.03 in about seven months. The time dependence for any other source is not available.
- The peak centroid separation was 5 eV within ± 0.3 eV for all Pt sources regardless of implantation energy or dose. Similarly, the separation was 4 eV for the two ZnO sources, 3 eV for the HOPG sources and as high as about 6.3 eV for Ir-15-1. Perhaps a decrease at the level of 0.1 eV in two months could be suspected for the Pt sources.
- The Gaussian widths of both peaks tend to 1.0 eV to 1.4 eV (the spread is large due to the large uncertainties and correlation).

5.5.1 Possible explanation

Lattice vacancy

According to [Erh12] a vacancy in the platinum lattice could be interpreted as a single positive charge giving the electrical potential of 3.7 V at the distance of the Pt lattice constant of $a = 3.9 \text{ \AA}$. Such a value is at the same order as the observed splitting. The electron binding energy of some of the $^{83\text{m}}\text{Kr}$ would be shrunk leading to a doublet structure. However, such a potential would affect all the $^{83\text{m}}\text{Kr}$ electrons and not only the outer-shell ones and the splitting would be the same for the $\text{N}_1\text{-9.4}$ line which was not observed. The amplitude ratio seems to be mostly independent of the implanted dose which is contrast to what could be expected based on number of lattice vacancies. Finally, the doublet structure did not disappear after the annealing which should have almost fully restarted the lattice.

Internal conversion on neighboring atoms

In the work [Zbo11] it was speculated that the doublet structure could be the result of internal conversion on electrons of the substrate atoms. The relevant electrons were considered to be from the outermost shell $\text{O}_{4,5}$ with the binding energy of 2.1(5) eV for Pt and 2.5(13) eV for Au. Thus, the separation of such electrons from the $^{83\text{m}}\text{Kr}$ line in Au substrate should decrease by 0.4(14) eV compared to the Pt substrate. However, due to the large uncertainty such a value is compatible with zero.

A lower uncertainty is obtained when considering the iridium substrate with the electron binding energy at the $\text{O}_{4,5}$ shell of 3.8(4) eV. The separation should now decrease by 1.7(6) eV compared to the Pt substrate which should be clearly observable using the MoS. The Ir-15-1 was made to test such a hypothesis. However, as discussed above the splitting actually increased by about 1 eV and such a hypothesis seems to be disfavored at first glance.

Internal conversion on valence electrons

The above described approach does not take into account that the substrate is a solid and has a band structure described by a continuous density of states at energies close to the Fermi level. The density of states of Pt and Ir was measured experimentally using x-ray photoelectron spectroscopy [Smi74]. However, in our case the density of states can be modified by the implanted ^{83}Rb . The possibility of observing the local density of states using the internal conversion of valence electrons was recognized previously and also experimentally measured [Pet92, Pet93]. In the same works the experimental spectra are compared to a prediction from the so-called linear-muffin-tin-orbital (LMTO) Green's-function method [Gun83]. An excellent agreement was found if an extra broadening probably due to residual lattice damage and shifting of the bound state component (from the implanted atom) was assumed.

It seems that the conversion on valence electrons could be an explanation for the observed structure in the case of ^{83}Rb implanted into a solid substrate at least for the higher-energy $\text{N}_{2,3}$ -32 line. The line N_1 -9.4 is lower in energy with respect to the Fermi level due to the higher binding energy of the N_1 electrons. Thus, it is not clear whether the structure observed there could also be related to the valence electrons. On the other hand, the binding energy can be affected since the $^{83\text{m}}\text{Kr}$ is present in the solid environment. For a strong source it could be desirable to measure the region around the N_1 -9.4 line further higher in energy to search for possible additional peaks.

A better understanding of the observed patterns and possibly also of the environment of the $^{83\text{m}}\text{Kr}$ could be obtained by calculating the density of states theoretically using the LMTO approach. It should be noted that high-luminosity high-resolution electron spectroscopy in combination with internal conversion of implanted atoms on valence electrons is a potentially powerful method to yield information about the electronic structure around dilute impurities in solids when e.g. the usual x-ray photoelectron spectroscopy cannot be applied [For99].

5.6 More accurate transmission function of the monitor spectrometer

As described in Section 4.1.2 the MoS transmission function is generally calculated according to Eq. (4.18). Owing to the width of the conversion lines compared to the width of the TF the weighting function in the formula can be assumed to be $w(r) = 1$. The assumption corresponds to a circular homogeneous source, together with the fixed radius of the electron flux tube in the analysing plane $R_A = 26$ cm. Such an approach is straightforward but does not allow comparison of line position results measured with source at different magnetic fields or accurate mutual comparison of the line position of sources with significantly different size of the activity spot since the actual transmission function changes. A change of the source magnetic field should not change the line position provided that the measurements are carried out in time during which the change of the line position due to its long-term drift is negligible. Thus, observation of the line position in

different source magnetic fields provides information about the accuracy of transmission function description.

In order to improve the transmission function description the source radiographical image is utilized. The axis of the cylindrical coordinate system is assumed to intersect the source image in the coordinates of the activity spot mean. Each ring of the electron flux tube in the analysing plane with the inner and outer radii r and $r + dr$, respectively, is mapped by the conservation of magnetic flux, see Eqs. (4.19) and (4.20), to a smaller ring at the source with the radii r_S and $r_S + dr_S$, respectively. The relative number of counts n in the radiographical image in such a ring then gives the weight multiplied by the radius as

$$n = r_S w(r_S) = \sqrt{\frac{B_A}{B_S}} r w \left(\sqrt{\frac{B_A}{B_S}} r \right), \quad (5.36)$$

where B_S and B_A are, respectively, the magnetic fields at the source and at the analysing plane. The individual pixels are taken into account if the coordinates of a pixel are within the ring.

A dedicated measurement of the line position was carried out using the ZnO-30-1 source in two different source positions of 27.0 cm and 19.2 cm from the magnet center corresponding to the magnetic fields of 0.5 T and 2.5 T, respectively. The source was chosen due to small dimensions of the substrate, lower number of parasitic x-rays from fluorescence in the substrate compared to Pt, and relatively better line position stability compared to ZnO-30-2. However, the measurement could be repeated using a HOPG-substrate source with no parasitic x-rays originating in the substrate. The weights multiplied by the radius are shown in Fig. 5.33 on the left as a function of the radius r in the analysing plane using a constant step dr of 1 cm for both the outer and the inner source positions. The weights are shown in Fig. 5.33 on the right. The Gaussian function, Eq. (4.21), with $\sigma_S \approx 1.7$ mm is shown for comparison both with the outer and inner position results in both figures. The value of σ_S was obtained by a least-squares fit of the Gaussian function multiplied by the radius to the data in the left figure.

The measurement results obtained using the radiographical image in Fig. 5.11 show a relatively small shift of the line position between the outer and inner source position of 34(24) meV for K-32 and 75(19) meV for L_3 -32, respectively. Using a blurred radiographical image, which was measured with the source placed 1 mm above the detector, the shift amounts to 60(24) meV and 118(19) meV, respectively, which is larger than for the sharp image. The reason is that due to the blurring the weights for the outer rings are overestimated. Such a result illustrates that the blurred image is unsuitable for an accurate description of the transmission function.

The remaining difference from zero could be explained partly by the inevitable residual blurring due to a few-pixel penetration of the dominant 12.6 keV x-rays. Possibly, an imprecise distance of the source to the magnet center could be a further reason. Although the relative change of the position is measured with 0.1 mm precision, the absolute distance is necessary since the magnetic field is non-linear with distance.

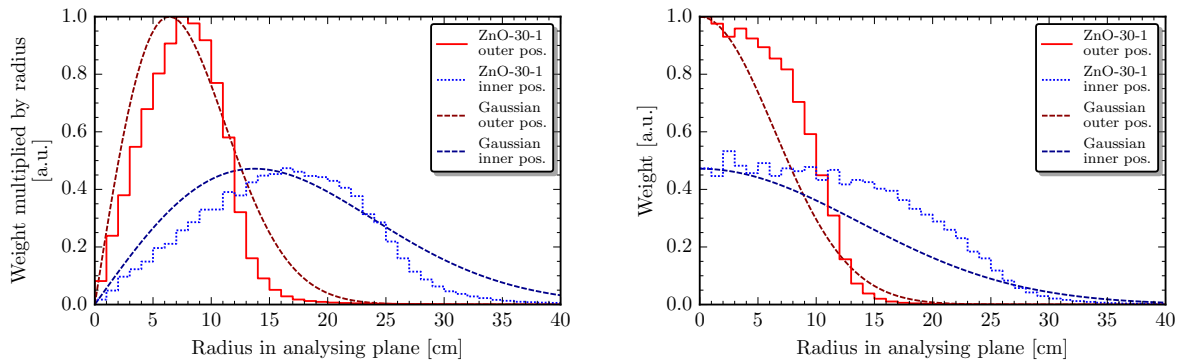


Figure 5.33: The weights multiplied by the radius (left) and the weights (right) for the ZnO-30-1 source and two different source positions for the more accurate MoS transmission function. The Gaussian function follows Eq. (4.21) with $\sigma_S \approx 1.7$ mm and is shown for comparison with the results of both source positions.

5.7 Conclusion

The primary purpose of the solid krypton source and the monitor spectrometer is to provide high-voltage stability monitoring at the ppm level for KATRIN by means of the K-32 conversion electrons of $^{83\text{m}}\text{Kr}$. The necessary sub-ppm stability of the electron energy was clearly demonstrated for the period of about two months for two Pt-substrate and one HOPG-substrate sources implanted at BONIS with 30 keV ^{83}Rb implantation energy and sufficient activity of about 3 MBq to 3.5 MBq (fourth BONIS source generation). Necessary conditions for the demonstration were to have a baked-out spectrometer to ensure good retarding electrode surface condition and thus stable spectrometer work function and stable measurement setup without influence of other experiments not related to the SKrS. The similar results obtained for the two Pt sources also demonstrate that the SKrS can be obtained in a reproducible way. Thus, in this way the development of the SKrS for KATRIN with respect to the primary goal of stable conversion electron energy can be considered to be finished.

Addressing further the points outlined in the beginning of this chapter, a lower implantation energy is preferred with respect to the larger amount of no-energy-loss electrons leading to shorter measurement times. However, for the fifth generation of BONIS sources, which were implanted using the retarding setup, a significant line position drift was observed. This demonstrated that a lower implantation energy does not necessarily lead to an improvement since the larger amount of no-loss electrons is not an advantage if the electron energy is not stable as needed. The side-effect of the retarding setup was that a significantly smaller activity spot was obtained leading to a high ^{83}Rb implanted dose and peak concentration. A correlation between the peak concentration and the line position drift was found. The next generation(s) of BONIS sources should be produced with a larger spot size if possible and the electron energy stability assessed. The actual mechanism for the electron energy drift is not fully understood and should be a subject

of further investigations either by means of further SKrS samples measured at the MoS and/or the perturbed angular correlation measurements.

The annealing of the sample after the implantation, which is generally customary in order to repair the damage done to the lattice, does neither make any difference with respect to the line shape asymmetry nor seems to improve the electron line position stability. As discussed, this indicates that the line position drift is possibly related to the ^{83}Rb concentration and not to the implanted dose and consequently not to the amount of lattice damage. To further address this issue annealing of a HOPG-substrate source could be performed and the electron energy stability assessed. However, time should be taken in order to evaluate the source retention and radiographical image both prior and after the annealing.

Regarding the suitable substrate, the zinc oxide is clearly not an option due to the significantly large line position drift. At 30 keV there is practically no difference in the amount of no-energy-loss electrons between platinum and highly-oriented pyrolytic graphite but the amplitude-to-background ratio, which influences the uncertainty of the fitted line position, is a factor of about three larger for HOPG. The disadvantage of HOPG is that a linear background has to be used for the DSG shape for a reasonable description of the line shape whereas a constant one is sufficient in the Pt case. However, for the reference method such a complication does not apply.

In the case of lower implantation energy, the amount of no-loss electrons is clearly higher for HOPG (for 12 keV implantation energy by a factor of 1.5), so is the amplitude-to-background ratio. However, it should be noted that the line position uncertainty does not drop significantly anymore if the amplitude-to-background ratio is above three, for details see Fig. 7.6. With the HOPG it is possible to lower the implantation energy significantly while keeping essentially no ^{83}Rb implanted into the contamination layer which is not the case for Pt due to backscattering of the ions. Obviously, the lower implantation energy increases the peak concentration and since the line position drift seems to be correlated to it, it is not desired. The lowest energy explored in this work was 4 keV for HOPG and 10 keV for Pt. It is not recommended to lower the energy further.

In summary, the HOPG substrate might be the preferred choice although there have been only three HOPG-substrate sources produced so far. Since more experience has been obtained with the Pt-substrate sources (14 used in this work, 17 produced altogether), demonstrating good enough line position stability for a Pt-substrate source implanted at BONIS with the energy of lower than 30 keV would complete the development for this substrate. Furthermore, while the DSG lineshape seems to describe the observed spectrum of a HOPG-substrate source using linear background in a reasonable way, the line shape description could be assessed in greater detail.

As already mentioned the retarding electrode surface condition was critical for a reasonable assessment of the line position stability. The reconditioning was achievable by baking out the spectrometer to 200 °C for at least 16 h or preferably more. It was only since the third BONIS source generation that the bake-out was performed prior to each long-term stability measurement because the criticality was not recognized sooner. It is strongly recommended that the bake-out is performed also prior to any future measure-

ment. At this point it should be pointed out that the stability of the main spectrometer work function is currently completely unknown but it cannot be addressed by the MoS in the parallel operation. Owing to the observations presented in this work it is strongly recommended that a long-term line position stability measurement using the gaseous $^{83\text{m}}\text{Kr}$ source is performed at the KATRIN main beamline in order to address this issue.

Although reproducibility of the line position stability was achieved for the fourth generation BONIS sources, due to the possibility of beam instabilities and risk of implanting non-radioactive contamination the source should be measured for the line position stability for at least a week or two prior to the parallel operation and monitoring. In this way, the line shape and some performance of the source with respect to the line position stability can be verified and unexpected drift excluded before using the source for the monitoring.

6 The gaseous $^{83\text{m}}\text{Kr}$ source

The gaseous $^{83\text{m}}\text{Kr}$ source (GKrS) for KATRIN is a radioactive source of monoenergetic conversion electrons which is released from a spatially well-defined maintenance-free emanator in the form of a gas. The gaseous $^{83\text{m}}\text{Kr}$ is intended for systematic studies of the KATRIN tritium source (WGTS) as well as of the KATRIN main spectrometer. The emanator is produced by depositing water solution with the generator ^{83}Rb into zeolite, a molecular sieve, and letting the water to evaporate by heating the zeolite. Since the zeolite acts as a cation-exchanger, the ^{83}Rb is tightly bound in it which minimizes the risk of contaminating the experimental apparatus with a longer-lived radioactive isotope.

The use of zeolite as a trap for ^{83}Rb was reported in [Vén05] where both good retention of ^{83}Rb and high release of $^{83\text{m}}\text{Kr}$ were observed. The published results had more or less qualitative character and, moreover, concerned only freshly prepared sources (up to 3 d old). A dedicated experiment for studying the ^{83}Rb retention was performed in [Han11] where an upper limit for the contamination rate of only $2.4 \mu\text{Bq h}^{-1}$ from a 1.8 MBq source could be established.

In this chapter, a quantitative description of the $^{83\text{m}}\text{Kr}$ release is given [Vén14]. Several types of zeolites and sources of different age were studied in different gas environments using semiconductor γ -ray spectroscopy. Moreover, the amount and composition of gas released from zeolite in ultra-high vacuum (UHV) conditions was studied using the residual gas analysis technique.

6.1 The $^{83}\text{Rb}/^{83\text{m}}\text{Kr}$ zeolite source

The zeolites are highly porous, crystalline materials composed of aluminosilicates. The crystal structure is formed by tetrahedras of AlO_4 and SiO_4 creating pores with precisely defined diameter. Due to the presence of the aluminum atoms the zeolites exhibit negative charge which is balanced by positive cations. For example, the sodium form of zeolite A (sodalite crystal structure) has a pore opening of about 4 \AA (4A molecular sieve). The pore size is reduced to 3 \AA in case the sodium ion is exchanged with the larger potassium ion (3A molecular sieve). If two sodium ions are replaced by a single calcium ion the opening of 5 \AA is obtained (5A molecular sieve). For the zeolite X (faujasite crystal structure) and sodium form the pore opening is about 8 \AA (13X molecular sieve). Macroscopically, the zeolite is in the form of beads with the size of 1 mm to 2 mm in diameter.

The sieving capability of the zeolite is due to physical adsorption of only those molecules which are smaller than the pore diameter. Due to highly polar surface within the pores the zeolite has very high capability for adsorbing water and other polar molecules. The physisorption can be reversed by heating the zeolite to a few hundred $^\circ\text{C}$. The cation-

exchanger property of zeolite makes it an ideal trap for ^{83}Rb ions. Previously [Vén05], only the 5A zeolite was used. In this work, additionally the types 3A, 4A and 13X were also investigated with respect to the $^{83\text{m}}\text{Kr}$ retention [Vén14].

6.1.1 Source production

The ^{83}Rb isotope is produced at the U-120M cyclotron in NPI Řež in the reaction of protons and natural krypton, i.e. $^{\text{nat}}\text{Kr}(p, xn)^{83}\text{Rb}$. According to the work [Vén05] using the 27 MeV protons at a current of 6 μA and the krypton gas target at the pressure of 7 bar (volume 22 cm^3) leads to about 150 MBq of ^{83}Rb after 12 h of irradiation time. Due to proton energy loss in the cyclotron output window, the gas target input window, and the gas itself the proton energy in the reaction is in the range of 19.5 MeV to 24.1 MeV. Such values are optimal for maximizing the ^{83}Rb yield and minimizing the yield of ^{84}Rb . The irradiated target is left for one week to allow the short-lived isotopes to decay. Then the target is washed out with distilled water with the elution efficiency of about 90 %.

For the possibility to produce higher amounts of ^{83}Rb activity a new gas target with additional cooling of the input windows by helium gas was manufactured. Such a target allows higher proton current (15 μA) and higher krypton pressure (13 bar) which thus increases the ^{83}Rb yield by a factor of 3.6. Moreover, since the inner walls are nickel-plated the elution efficiency is as high as 97 %.

In order to produce the GKrS emanator the zeolite beads¹ are firstly dried at 320 °C for 3 h under a flow of pure nitrogen. After cooling down the ^{83}Rb water solution is added to the beads. According to [Vén05] a 1 cm^3 of ^{83}Rb water solution was entirely absorbed in 2 g of zeolite (3 cm^3) in 10 min. Finally, the zeolite is dried again in similar conditions to remove the solvent and sealed in a dry ampoule.

6.2 Retention of $^{83\text{m}}\text{Kr}$ in the zeolite source

The technique for studying the $^{83\text{m}}\text{Kr}$ release is based on measuring the intensity of the 32 keV γ -line observed in the $^{83\text{m}}\text{Kr}$ decay using semiconductor γ -ray spectroscopy. Since the line de-excites the isomeric state, the observed intensity gives direct information about the amount of the $^{83\text{m}}\text{Kr}$ atoms present in the source. Therefore, rather than release the retention of $^{83\text{m}}\text{Kr}$ is measured. Such a technique was already described in Section 5.2.5 in connection with the solid $^{83\text{m}}\text{Kr}$ source where conversely a low $^{83\text{m}}\text{Kr}$ release is demanded. Clearly, the retention and the emanation add up to one.

6.2.1 Absolute retention of source kept in air

In order to measure the absolute $^{83\text{m}}\text{Kr}$ retention the zeolite source is moved into a dedicated closeable chamber. When the chamber is open, the released $^{83\text{m}}\text{Kr}$ is allowed to escape the chamber and thus the space observable by the detector. In such a situation,

¹Supplier: Merck KGaA, Germany.

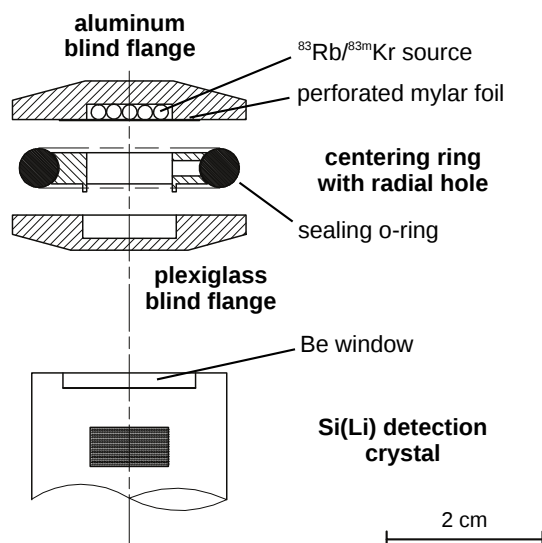


Figure 6.1: The sketch of the closeable chamber for measurement of the GKrS absolute retention. The clamping ring is not shown.

only the intensity of the γ -line originating in the source is measured. By closing the chamber all the $^{83\text{m}}\text{Kr}$ is trapped and additionally the intensity of the photons originating in the released $^{83\text{m}}\text{Kr}$ is also observed. The ratio of the two intensities gives in the first approximation the absolute $^{83\text{m}}\text{Kr}$ retention of the source. Such a measurement usually takes up to several hours or more and represents the measurement of the source held in air.

The closeable chamber is similar in functionality to the one used for the SKrS retention measurement, see the sketch in Fig. 6.1. Always 15 zeolite beads are positioned in a single layer in the well of the upper aluminum flange. The beads are fixed with a perforated mylar foil with the thickness of $8.2\ \mu\text{m}$. The perforation allows the released $^{83\text{m}}\text{Kr}$ atoms to move freely around the inner volume of the chamber and to escape the chamber through the hole in the center ring.

The tightness of the arrangement of the blind flange, center ring, mylar foil, and o-ring was tested by using it to seal a vacuum setup connected to a turbomolecular pump. The check if the $^{83\text{m}}\text{Kr}$ can leave in the open-chamber measurement a source was produced by dropping the ^{83}Rb water solution on a polyethylene foil. Such a source has practically zero $^{83\text{m}}\text{Kr}$ retention since the 32 keV γ -line is not visible in the detector spectrum. In the open-chamber measurement the γ -line was also not visible thus confirming the openness of the chamber.

Similarly as in the SKrS case, after closing the chamber the measurement is done only after a transient equilibrium is established. During the waiting time the intensity of the γ -line increases as described by Eq. (5.27) if the retention is not 100% which is another check for the tightness of the chamber. Corrections are applied for the effects of ^{83}Rb decay and for the difference of detection geometry for the open and closed chamber. Additionally, the attenuation of the γ -rays in the zeolite beads is calculated by means

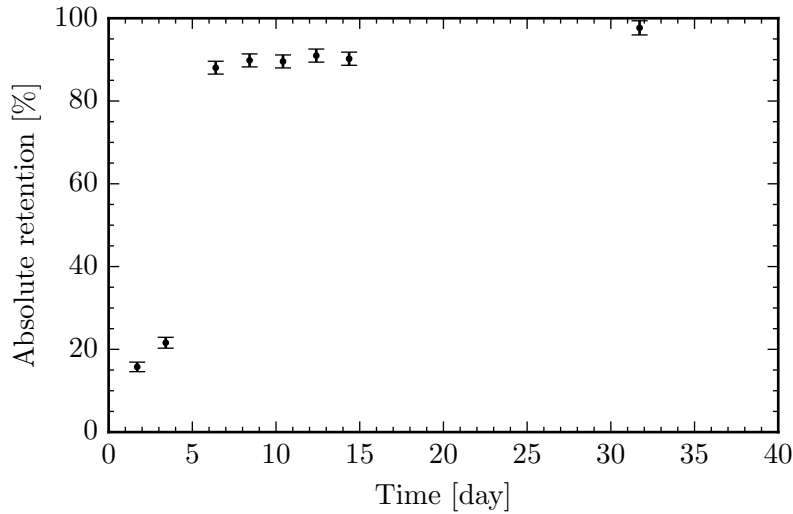


Figure 6.2: The absolute $^{83\text{m}}\text{Kr}$ retention in time for the type-5A zeolite source kept at ambient air and room temperature.

of the Monte Carlo simulation which was briefly described in Section 5.2.3. Since the composition and thus the attenuation coefficient are not known precisely, this correction is subject to a somewhat larger uncertainty. Nevertheless, all corrections together change the obtained value by only a few percent.

Several type-5A zeolite sources were produced with the activities in the range of 1 MBq to 30 MBq and fairly reproducible retention results were obtained. The typical evolution of the absolute retention of a type-5A zeolite $^{83\text{m}}\text{Kr}$ source, which is kept in ambient air at room temperature, in time is shown in Fig. 6.2. The retention of a freshly prepared source is at the level of 20%. Within a few days, the retention raises to about 90% and reaches up to almost 100% after one month. The low retention can be re-established by heating the zeolite source in an oven for 3 h at 320 °C.

The situation was found to be significantly different for the other zeolite types. The retention measured after the source production amounted to 80%, 70% and 50%, respectively, for the types 3A, 4A, and 13X, and remained constant regardless of the presence of air around the source. The activities were in the range of 3 MBq to 5 MBq.

6.2.2 Relative retention in dependence of source gas environment

In order to measure influence of vacuum or specified gases the relative retention is obtained by sequentially measuring the intensity of the γ -line in time. In such a case, the single line intensity value is obtained in two hours. The observed intensity is corrected for the ^{83}Rb decay. The source is placed on a plexiglass or beryllium window, which are used due to their high transparency for the 32 keV photons, of a dedicated vacuum chamber. A few spectra in the beginning of the measurement are taken with the chamber left open to the air. In such a way, the retention is stabilized at the high value of about 90% (for the 5A

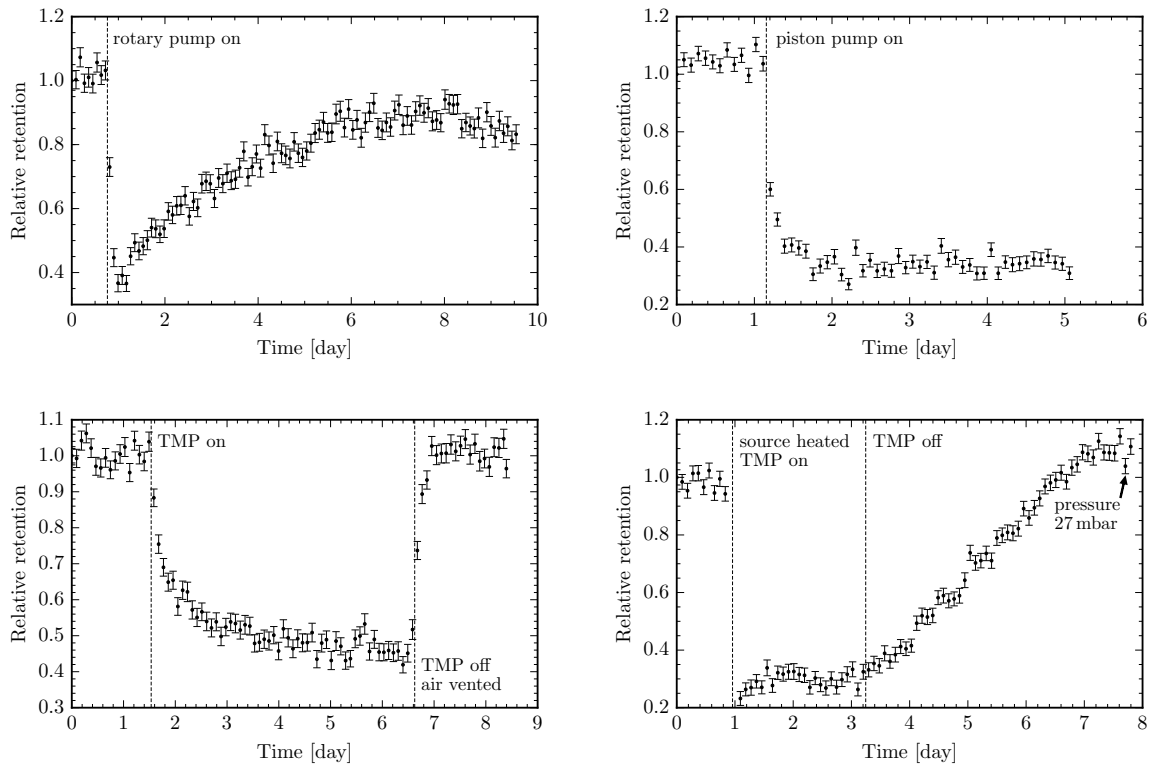


Figure 6.3: The relative $^{83\text{m}}\text{Kr}$ retention in time for the type-5A zeolite source under different vacuum conditions: oil rotary pump vacuum (upper left), oil-free piston pump vacuum (upper right), turbomolecular pump vacuum (lower left), and TMP vacuum with a pre-heated source (lower right). In the TMP vacuum cases the pumping was stopped after a few days. In the first case, the chamber was vented with ambient air while in the second case the chamber was left evacuated. Due to outgassing and possible leak the pressure went up to about 27 mbar at the end of the measurement.

zeolite). The observed γ -line intensity corresponds to the $^{83\text{m}}\text{Kr}$ decaying in the source only since the released $^{83\text{m}}\text{Kr}$ diffuses away from the space observable by the detector. Without interruption the source environment can be changed by evacuating the chamber and additionally by venting it with a given gas. With interruption but without change of the geometry the source can be heated in an oven and returned into the chamber.

The evolution of the relative retention in time for zeolite 5A source in different vacuum conditions is shown in Fig. 6.3. A high-vacuum chamber (volume 1.4 dm^3) with the plexiglass window was utilized. The initial pumpdown leads to a drop of the retention by a factor of about 2.5 within a few hours. In the case of oil rotary pump vacuum, where the reached pressure is about 3×10^{-2} mbar, the retention gradually increases after the pumpdown. This is in contrast to the oil-free piston pump vacuum with the pressure of 1×10^{-1} mbar where the retention stays constant. This can be possibly explained by presence of the rotary pump oil vapors which are absorbed by the zeolite leading to a gradual decrease of the $^{83\text{m}}\text{Kr}$ emanation.

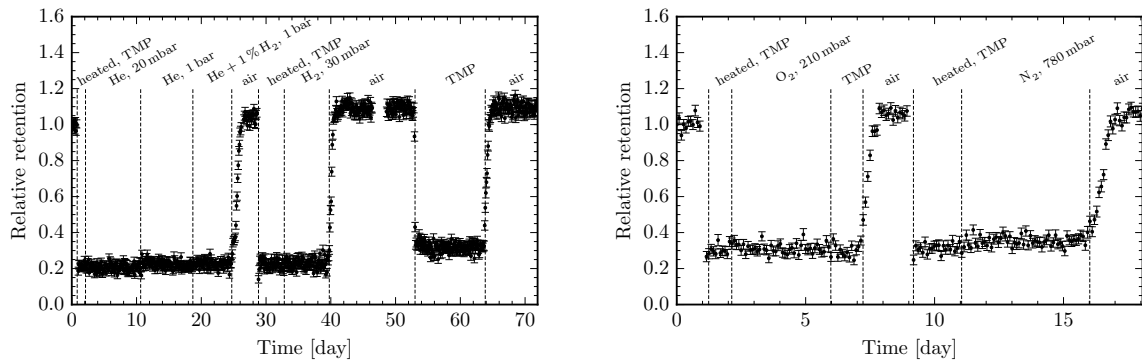


Figure 6.4: The relative $^{83\text{m}}\text{Kr}$ retention in time for the type-5A zeolite source under different gaseous or vacuum conditions.

The turbomolecular pump (TMP) vacuum with the pressure of about 5×10^{-6} mbar leads to a similar decrease of the retention. The observed slower rate in this case can be attributed to the longer time when the source was held at ambient air. Stopping the pumping and venting the chamber with ambient air leads to a sharp increase of the retention while the increase is slower if the chamber is not vented. The results also demonstrate that a low and stable retention can be achieved in the vacuum by using a source which was previously heated (outside the vacuum chamber). Interestingly, the other zeolite types do not show such a behaviour with respect to the retention. In these cases, no reduction of the retention under vacuum was observed.

The relative retention in time for zeolite 5A source in different gaseous conditions is shown in Fig. 6.4. In this case, an UHV chamber (volume 41 dm^3) with a 0.25 mm thick Be window was utilized in order to maintain the composition of the gaseous environment as stable as possible. Prior to exposing it to a gas the source was firstly heated, inserted into the chamber and kept under TMP vacuum for some time in order to establish the γ -line intensity. Then the source was gradually exposed to He (pressure 20 mbar), He (1 bar), He+1% H_2 (1 bar), H_2 (30 mbar), O_2 (210 mbar), and N_2 (780 mbar) each for several days. The retention remained practically constant in all cases. Therefore, the degradation of $^{83\text{m}}\text{Kr}$ emanation in ambient air is most likely caused by water vapours although the influence of the other components present in untreated air cannot be excluded. Note that slightly higher retention was obtained if the source was placed in the vacuum without heating.

The results obtained for the cases when H_2 was used are encouraging for KATRIN since hydrogen is an isotopologue of tritium and the zeolite source will be held in a tritium gas environment in order to allow the $^{83\text{m}}\text{Kr}$ to distribute with the tritium. The measurements show that about 80% of all $^{83\text{m}}\text{Kr}$ created by the decay of ^{83}Rb will be released. Nevertheless, the actual $^{83\text{m}}\text{Kr}$ retention in the tritium gas environment should be checked experimentally at the Tritium Laboratory Karlsruhe.

6.3 Emanation of absorbed air from zeolite in ultra-high vacuum

The zeolite has great absorption and desorption capabilities and has to be heated both prior and after deposition of the ^{83}Rb water solution. After the heating the zeolite is in contact with air and until it is put into the vacuum the adsorption of air components takes place. Conversely, the desorption of air compounds in the vacuum proceeds which deteriorates the vacuum of the experimental setup.

The effect was studied using a vacuum system equipped with a gate valve separating UHV and transition vacuum chambers. The system is pumped out by a piston pump ($17\text{ m}^3\text{ h}^{-1}$) and a turbomolecular pump (50 l s^{-1}) in a cascade. Additionally, the UHV chamber (volume 3.6 dm^3 , internal surface area 16 dm^2) is equipped with a sputter-ion pump (25 l s^{-1}) used to achieve pressures below 10^{-8} mbar and a bake-out system used to reach temperatures of $250\text{ }^\circ\text{C}$. A mass spectrometer for the residual gas analysis (RGA) equipped with a secondary electron multiplier as an ion detector is connected to the UHV chamber. A sample of 50 zeolite beads is placed on a holder which is introduced from outside through the pre-pumped transition chamber into the UHV chamber which reduces deterioration of the UHV. The introduced holder can be also heated up to $230\text{ }^\circ\text{C}$.

In the top left plot of Fig. 6.5 the rest-gas spectrum is shown for the case when only the holder was inserted into the chamber. The pressure stabilized at about 1.3×10^{-8} mbar after 0.5 h. The usual components of the rest gases of the vacuum system are observed, namely H_2 , O, OH, H_2O and N_2 . Then, the zeolite beads underwent the same procedure as when producing the zeolite source except no ^{83}Rb was present in the de-ionized water. After pre-heating the beads at $320\text{ }^\circ\text{C}$ for 3 h they were moved into the UHV chamber on the holder. The pressure stabilized at 1.7×10^{-6} mbar after about 2 h. The corresponding RGA spectrum is shown in the top right plot of Fig. 6.5. The composition is similar as in the previous case but the amount of gases is about a factor of 100 larger while the amount of water compounds is larger by a factor of 300. In this case, also the O_2 contribution is well visible. A low pressure of 1.3×10^{-8} mbar could be achieved only after about a week of pumping. Lastly, the zeolite beads which were not pre-heated outside were inserted into the chamber and heated there at $230\text{ }^\circ\text{C}$ for 3 h. After cooling down, the achieved pressure was 1.5×10^{-8} mbar. The obtained RGA spectrum is shown in the bottom plot of Fig. 6.5. The spectrum is similar to the one measured in the case of only the empty holder.

6.4 Conclusion

The emanator based on ^{83}Rb deposited in type-5A zeolite seems to be a reliable source of gaseous $^{83\text{m}}\text{Kr}$ for the KATRIN experiment. As discussed previously, about 80 % of the $^{83\text{m}}\text{Kr}$ produced by decay is released from the source under vacuum. In the transient equilibrium, which is established a few hours after the source production, the activity of $^{83\text{m}}\text{Kr}$ which decays inside the source is given by Eq. (5.11). Therefore, the released $^{83\text{m}}\text{Kr}$

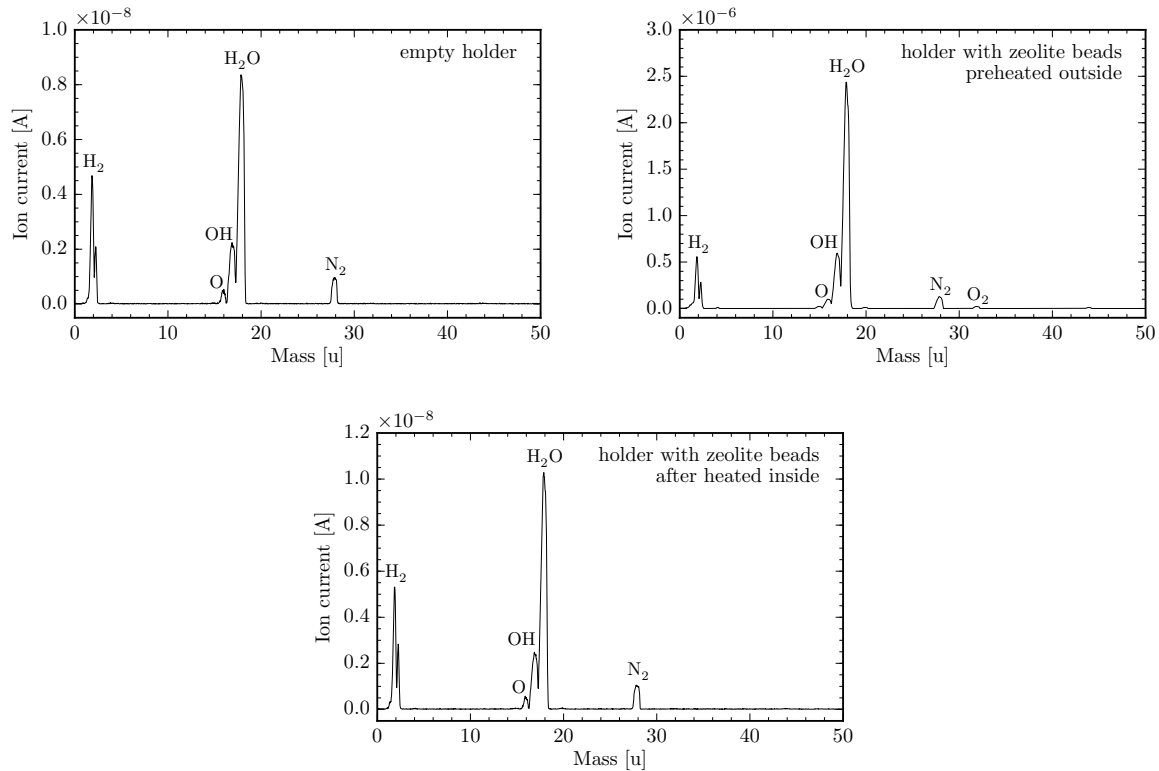


Figure 6.5: The rest-gas mass spectrum of the UHV chamber measured with the source holder only (top left), pre-heated zeolite beads (top right), and zeolite beads heated inside in chamber (bottom). The individual elements and compounds are identified according to their mass.

activity is about 0.6 times the ^{83}Rb activity. If the source is previously heated, the release is high and stable since the initial pumpdown. Moreover, if the heating is done in the vacuum conditions, the amount of air compounds and especially water released into the vacuum setup is significantly reduced. Thus, at KATRIN the apparatus for housing the zeolite source should have heating elements installed in order to heat the source prior to connecting it to the WGTS tritium loop.

It was also demonstrated that the favorably high emanation persists while the source is exposed to various dry gases. The tritium pressure at the point where the zeolite source will be attached to the WGTS tritium loop is at the order of only 10^{-4} mbar. Owing to such a low value and the results obtained while being exposed to hydrogen at much larger pressure no problems with the $^{83\text{m}}\text{Kr}$ release are expected after the source is attached. Nevertheless, an experimental confirmation of this expectation is foreseen.

The improvement of the krypton gas target allowed for a factor of 3.6 higher yield of ^{83}Rb . Thus, the amount of 1 GBq of ^{83}Rb activity, which will be potentially needed for KATRIN, is obtainable from a 22 h-irradiation at the U-120M cyclotron. Besides, nickel plating of the target walls increased the elution efficiency by about 7% thus further improving the activity yield.

7 Monitoring of the KATRIN high-voltage stability

Having a reliable source of monoenergetic conversion electrons, the solid $^{83\text{m}}\text{Kr}$ source, the strategy of the actual high-voltage stability monitoring using the monitor spectrometer should be considered. In this chapter, a technique for optimization of the measurement of the conversion electron integral spectrum is described. Furthermore, several options for the monitoring measurement are discussed. The statistical uncertainty of the electron line position and the necessary time to achieve the uncertainty are evaluated utilizing both calculated and experimental observations. Also the question of measuring an additional conversion line and SKrS sample is addressed. Finally, the recommended approach for the monitoring is given.

7.1 Optimization of the retarding energy and time distribution

For the measurement of the integral spectrum at a MAC-E filter it is possible to select both the retarding energy points for which the electron count rate is measured and the time spent measuring at each point. The simplest approach in the case of conversion electrons is to measure the no-energy-loss part of the electron line with uniform energy steps and uniform time distribution. However, the distributions can be optimized so that the parts of the line which are most sensitive to the line position are preferably measured and the less sensitive parts are measured correspondingly less. Such an approach leads to a decrease of the line position statistical uncertainty without increasing the overall measurement time of the spectrum.

For much of the MoS measurements carried out in this work a uniform time distribution and a “semi-optimized” energy distribution was utilized. For such a distribution the energy points were chosen by hand such that they are the most dense around the point of inflection of the integral conversion line and least dense at the edges. Such an approach already leads to some improvement over the uniform distribution in terms of the obtained line position uncertainty at the level of 15 % to 20 %.

Further improvement can be obtained using numerical methods. Finding the optimal set of retarding energy points or times per energy such that the line position uncertainty is minimal basically represents a minimization problem where the energies or the times (or both) are considered to be the variables. However, such a task represents minimization in a few tens of dimensions which is not feasible to solve using traditional techniques (such as the quasi-Newton method described in Section 4.2.2). Special techniques have to be

employed to ensure convergence.

In the work [Kaš08] the approach was based on minimization of the uncertainty (applied to the neutrino mass in the tritium β -spectrum) by varying the time at one point only while keeping the total measurement time constant. After applying this to all measurement points a set of one-dimensional time distributions was obtained. The first optimized time distribution was calculated as the average of the one-dimensional ones. Starting with this distribution the process was repeated to obtain the second optimized time distribution. In this way, the sequence iteratively converged to the final optimized time distribution. An improvement at the level of about 20 % for the neutrino mass statistical uncertainty was achieved over the uniform time distribution. It is not stated how many iterations were required to reach the result but generally one may expect a relatively large number. Moreover, the process clearly involves many evaluations of the uncertainty which may be time-consuming on its own.

In the work [Kle14] the minimization was performed in all dimensions simultaneously by using the so-called Markov Chain Monte Carlo (MCMC) method which is usually used for sampling from probability distributions. A new time distribution (or part of it) is drawn from a proposal probability distribution and the parameter uncertainty is evaluated. If the uncertainty is smaller than the previous one, the proposal distribution is accepted, otherwise it is accepted with some probability proportional to the ratio of the two uncertainties. In this way, the parameter space is explored mostly in the region where the uncertainty is minimal but also higher uncertainty values are reached which enables to go over local minima. A stationary distribution is reached after a few thousand iterations each of which requires evaluation of the uncertainty. Clearly, the performance of the minimization depends on the proposal distribution and some adaptation mechanism is necessary in order to keep the rate of accepting the proposals at a reasonable level. Compared to the previous approach and depending on the assumed conditions about 5 % to 10 % further improvement was gained.

In this section, we present an alternative approach which is based on the idea of relative importance of data to the parameters in a least-squares fit [Aud86]. The method does not require neither any evaluation of the parameter uncertainty nor an iterative process in contrast to the above mentioned approaches. As a consequence the optimized distribution is obtained practically instantly. It can be utilized for both the time and the retarding energy distributions. In the works [Kaš08, Kle14] optimization of only the time distribution was considered although an energy distribution with twice the density of points around the tritium endpoint was used in both. The optimization of the energy distribution can be potentially more beneficial for the MoS since due to relatively short measurement times of one spectrum the time distribution optimization can lead to impractically small values. The largest disadvantage of the approach is that the first derivatives of the model function in its parameters are needed. In some cases, it might be difficult or even impossible to calculate the derivatives if the function is badly behaved or discontinuous. Thus, in such situations the approach is not usable.

Due to time constraints and only recent development of MCMC method computer code for KATRIN the relative importance method was not compared to the two approaches

discussed above. Nevertheless, an improvement for the line position uncertainty at the level of 30 % to 40 % was achieved as discussed below. Such an improvement is at the same order as the one achieved for the neutrino mass. Thus, it seems perhaps reasonable to expect similar numbers if the MCMC method is applied for the line position of the conversion electrons.

7.1.1 Relative importance of data

In the work [Aud86] the so-called ‘‘influence’’ $F_{i\lambda}$ of a particular data point M_i on a least-squares fit parameter p_λ is defined as how much of the information carried by the data point flows into the parameter. The influences $F_{i\lambda}$ are the elements of the ‘‘flow-of-information’’ matrix F . It is shown that it can be calculated as

$$F = (WKA^{-1}) \otimes K, \quad (7.1)$$

where the matrix elements $W_{ij} = \frac{\delta_{ij}}{\sigma_i^2}$ (δ_{ij} is the Kronecker delta) and $K_{i\lambda} = \frac{\partial S_i}{\partial p_\lambda}$, $A = K^T W K$ is the defining matrix of the normal equations of the minimization problem and the symbol \otimes denotes that the corresponding matrix elements are multiplied. The symbol S_i denotes the model function evaluated at the relevant retarding energy point qU_i , i.e. $S_i = S(qU_i)$. The sum of all influences amounts to $\sum_i F_{i\lambda} = 1$ which is expected since by definition the parameter is determined by all data points. Moreover, the ‘‘significance’’ \mathcal{S}_i is defined as the sum of influences for all parameters,

$$\mathcal{S}_i = \sum_\lambda F_{i\lambda}, \quad (7.2)$$

and represents the amount of information which flows from the particular data point into all the parameters. The sum of all significances equals the number of parameters and it holds $0 < \mathcal{S}_i \leq 1$. Note that no such relation holds for the influence $F_{i\lambda}$.

To evaluate which parts of the K-32 conversion line are the most sensitive for estimation of the line position (influence) and all the parameters (significance) we calculate the influence and the significance in many points along the no-energy-loss part. Let us consider a representative shape S_i of the line calculated using the DSG function having the amplitude $a = 1000$ cps, line position $E_i = 17829$ eV, Gaussian width $\sigma = 0.6$ eV, constant background $b_0 = 200$ cps, and asymmetry $\alpha = 0.1$. To calculate the uncertainty σ_i we assume the time per point of $t_0 = 50$ s and Poisson statistics which leads to the formula

$$\sigma_i = \sqrt{\frac{S_i}{t_0}}. \quad (7.3)$$

The no-loss part is considered in the interval (17818 eV, 17850 eV).

The influence for the line position and the significance for the DSG lineshape are shown in Fig. 7.1 in the upper plots. In the calculation it was assumed that the five mentioned DSG parameters are the ones which are varied in a least-squares fit. Clearly the region around the point of inflection has the largest influence for the line position. Note, however,

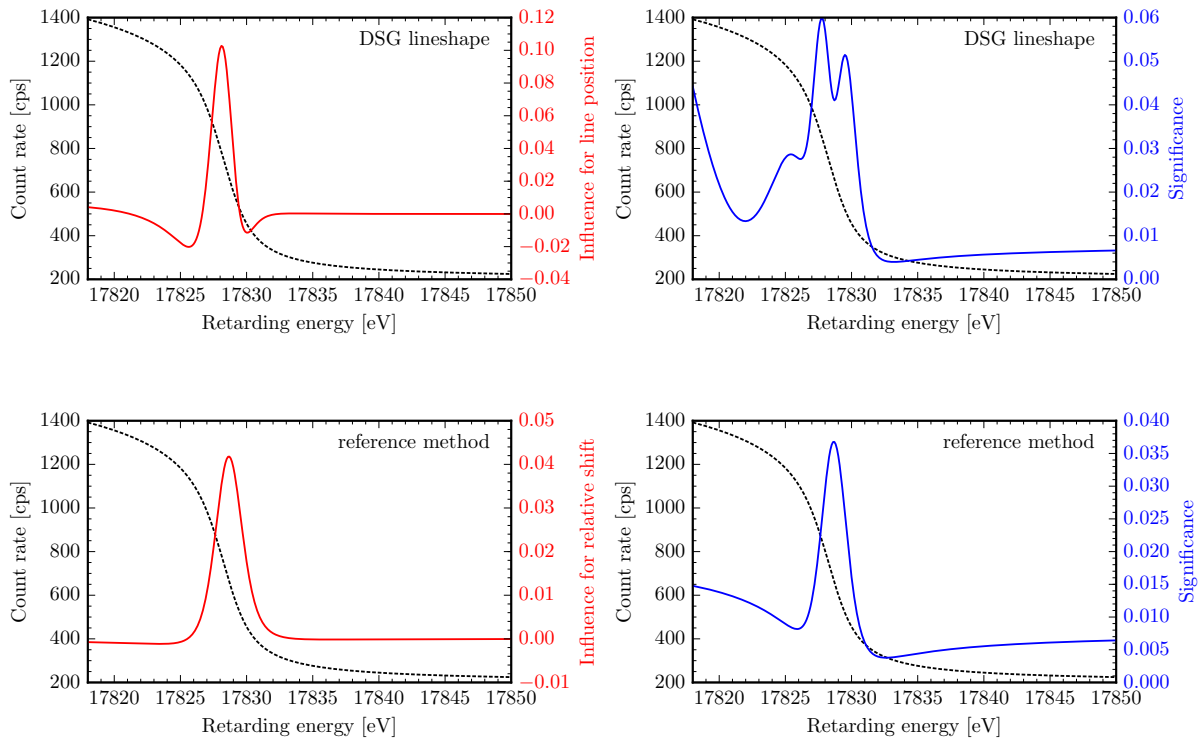


Figure 7.1: The influence and the significance for the DSG method (top left and right) and for the reference method (bottom left and right) shown together with a representative shape of the K-32 line (dashed line).

that the influence is negative for a significant part of the spectrum. The significance is large also at the inflection point though in a more complicated way and also at the lowest energies. This explains why the semi-optimized retarding energy distribution with points concentrated around the point of inflection led to some improvement of the line position uncertainty.

The results for the reference method are shown in Fig. 7.1 in the lower plots. In the calculation it was assumed that the three parameters relative scale factor r , relative shift Δ , and constant background b_0 are varied in a least-squares fit. The influence and the significance show similarities to those in the DSG case but are not exactly the same. Also in this case the influence is negative for some part of the spectrum.

Due to the non-positiveness of the influence we therefore utilize only the significance for deriving the retarding energy and time distributions.

Application to time distribution

Assuming a uniform retarding energy distribution we apply the significance in a way that the time t_{qU_i} in the retarding energy point qU_i is proportional to the interpolated

significance $\mathcal{S}(qU_i)$, i.e.

$$t_{qU_i} \propto \mathcal{S}(qU_i). \quad (7.4)$$

The proportionality constant is chosen such that the total measurement time equals the total time prior to the optimization. If the measurement time per point was t_0 and the number of points is N , the total time is Nt_0 . Therefore, we get for the time distribution

$$t_{qU_i} = \frac{Nt_0}{\sum_{i=1}^N \mathcal{S}(qU_i)} \mathcal{S}(qU_i). \quad (7.5)$$

As an example let us consider the number of points of $N = 43$ and the time per point in the uniform time distribution of $t_0 = 50$ s. From the DSG fit of the representative line shape the obtained line position uncertainty amounts to 30.1 meV for the uniform distribution and only 20.9 meV for the optimized distribution. Thus, by only re-arranging the measurement time within the spectrum the statistical uncertainty was lowered by about 31 %. In the case of the reference method we utilize an energy- and time-uniform reference spectrum of the same shape with two more points at the edges outside the original interval. We obtain the relative shift uncertainty of 17.4 meV for the uniform time distribution and 15.2 meV for the optimized one. Here the improvement is only 13 %.

Application to retarding energy distribution

Assuming a uniform time distribution we apply the significance such that the density of retarding energy points $\rho(qU)$ is proportional to the interpolated significance $\mathcal{S}(qU)$, i.e.

$$\rho(qU) \propto \mathcal{S}(qU). \quad (7.6)$$

The proportionality constant is chosen such that the integral of the density over the specified energy interval (qU_{\min}, qU_{\max}) equals the total number of points N ,

$$\rho(qU) = \frac{N}{\int_{qU_{\min}}^{qU_{\max}} \mathcal{S}(E) dE} \mathcal{S}(qU). \quad (7.7)$$

To obtain the energy points we integrate the density,

$$n(qU) = \int_{qU_{\min}}^{qU} \rho(E) dE + C, \quad (7.8)$$

where C is an integration constant, and find those values of qU for which $n(qU)$ is a natural number. This can be done conveniently by interpolating the monotonous function $n(qU)$, inverting the interpolating function and evaluating the inversed interpolation function at $n = 1, 2, \dots, N$.

Due to the presence of the integration constant C the energy points are not determined uniquely by the Eq. (7.8). If we choose simply $C = 0$ then the last point will be exactly at the upper boundary of the energy interval since in that case $n(qU_{\max}) = N$. Similarly,

choosing $C = 1$ leads to the first point being at the lower boundary of the interval since $n(qU_{\min}) = 1$. We therefore choose $C = 0.5$ so that the interval boundaries are half-way to the first nearest point inside the interval.

As an example we compare the fit of a energy-optimized spectrum to the uniform spectrum with $N = 43$ and $t_0 = 50$ s as before. The DSG lineshape fit yields the line position uncertainty of 20.4 meV which is similar to the value obtained from the fit of the time-optimized spectrum. The improvement over the uniform distribution case is 32 %. In case of the reference method the relative shift uncertainty is 9.9 meV which is significantly better than in the time-optimized case and represents an improvement of about 43 % with respect to the uniform distribution case.

Combined retarding energy and time optimization

If the retarding energy distribution is derived using the Eq. (7.8) the corresponding time distribution can then be optimized using Eq. (7.5). In the DSG lineshape case such a procedure leads to the line position uncertainty of 18.7 meV and thus the improvement over the uniform distribution is 38 %. Such a value is not significantly larger compared to the case of using only the energy- or the time-optimized distribution. In the reference method case the relative shift uncertainty is 9.1 meV which yields the total improvement of 48 %. Also in this case the value is not significantly larger compared to the case of only the energy-optimized distribution and it is only larger comparing to the case of the time-optimized distribution.

7.1.2 Discussion of the optimization results

The choice of the number of points $N = 43$ and the non-optimized time per point $t_0 = 50$ s leads to the total spectrum measurement time of about 36 min neglecting waiting time in between the individual points. At such a situation the combined retarding energy and time optimization leads to times per point as small as 7 s in the DSG case and 13 s in the reference method case. If a smaller spectrum measurement time is desired then these extrema scale to smaller values accordingly. Such small measurement times per point might not be feasible and useful from the practical point of view. On the other hand, the energy optimization leads to the smallest energy step of about 0.2 eV which is achievable without problem. Since there is a smaller benefit of using the optimized time distribution and only small further improvement of using both distributions optimized, the optimized retarding energy distribution should be preferred.

The optimized retarding energy distributions for the DSG and the reference method are shown in Fig. 7.2. It should be pointed out that the distributions as shown in the Fig. 7.2 are related to the assumed representative line shape. In case a different line shape is considered or different parameters are varied in a least-squares fit (e.g. the linear background term is considered) the distribution as well as the improvement of the uncertainty might change. Nevertheless, no significant difference is expected.

Since one might consider to analyse a spectrum with both the DSG and the reference methods, it is worth evaluating the parameter uncertainty when the other method dis-

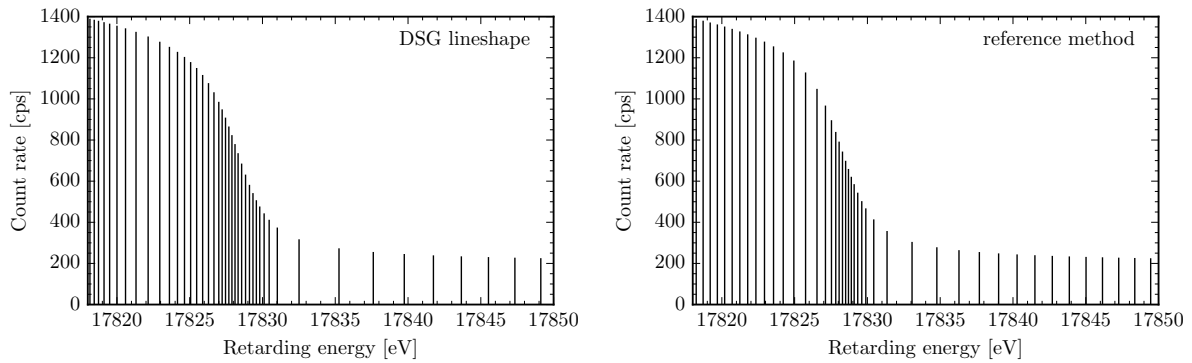


Figure 7.2: The optimized retarding energy distribution for the DSG lineshape (left) and the reference method (right) for the number of points in the spectrum of $N = 43$.

tribution is utilized. In case the DSG is used for a spectrum optimized for the reference method the uncertainty is 23.4 meV to be compared to 20.4 meV. In the reversed case the reference method fit yields the uncertainty of 10.9 meV to be compared to 9.9 meV. Thus, as expected there is a notable improvement over the uniform distribution but it is not as large as if the optimization is carried out for the respective method.

7.2 The method of high-voltage stability monitoring

7.2.1 Introduction

The energy scale distortions observable by the MoS by measuring the conversion line include the following.

- A long-term drift of the line position which is best observable by means of the DSG method due to its capability of describing changes of the electron line shape in time, which were in some cases observed during the line position stability measurements at the standalone MoS.
- A sudden shift of the line position which is best observable by means of the reference method due to the smaller uncertainty of the relevant fitted parameter, the spectrum relative shift.
- Additionally, a periodical distortion (ripple) could be observed by measuring the Gaussian line width using the DSG method. Denoting the undistorted Gaussian line width as σ and the ripple root mean square as σ_{rip} , the observed line width σ_{obs} reads in the first approximation

$$\sigma_{obs} \approx \sqrt{\sigma^2 + \sigma_{rip}^2}. \quad (7.9)$$

Suppose that no ripple is observed, i.e. $\sigma_{obs} = \sigma$, and the statistical uncertainty of both σ and σ_{obs} from the least-squares fit of the conversion line is $\Delta\sigma$. Then, using

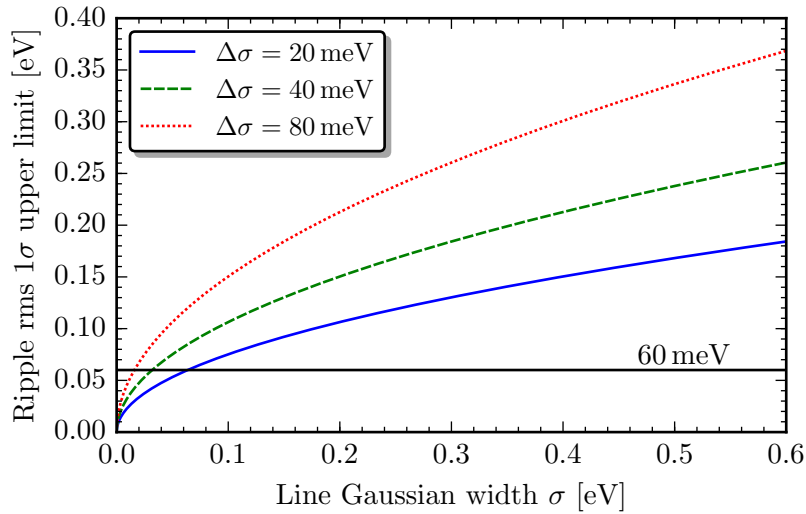


Figure 7.3: The 1σ upper limit of the ripple root mean square in dependence of the undistorted Gaussian line width σ . The dependency is shown for three values of the Gaussian line width uncertainty $\Delta\sigma$. The KATRIN limit for the maximal allowed ripple RMS is indicated.

the principle of propagation of uncertainty, we obtain the uncertainty of σ_{rip}^2 and further the 1σ upper limit for σ_{rip} as

$$\sigma_{rip} \lesssim 1.68 \sqrt{\sigma \Delta\sigma} \quad (68\% \text{ C.L.}). \quad (7.10)$$

The limit as a function of the line width σ for the uncertainties $\Delta\sigma = 20 \text{ meV}$, 40 meV and 80 meV is shown in Fig. 7.3. Thus, the ripple is observable only if its root mean square σ_{rip} is comparable in size to the line Gaussian width σ . However, since the maximal root mean square of the ripple must not exceed 60 meV and the usual line width σ is at the order of 0.3 eV to 0.5 eV , the MoS is not well suited for observation of such small AC fluctuations and other measures have to be taken (post-regulation with a ripple probe and triode shunt).

7.2.2 Possible alternatives for the concept of monitoring

Some alternatives how to proceed with the actual measurement can be considered:

1. Measure the elastic part of the conversion line repeatedly during the monitoring. The sequence of such spectra A_i can be written schematically as

$$A_1, A_2, \dots, A_n. \quad (7.11)$$

Analyse the spectra with both the DSG lineshape and the reference method by using a detailed spectrum measured in the beginning as the reference. The DSG method will provide maximum information about the electron line, which as an important check of the MoS operation, and the possible long-term drift. The reference method

will provide higher sensitivity for detection of possible sudden shifts. The information about the long-term drift from the reference method will be limited. In order to allow a reasonably small uncertainty of the line position the spectrum measurement time will be moderate.

2. Measure the full conversion line with higher statistics or more retarding energy points longer once in a while (“precise spectra” P_i) and in between measure lower statistics or fewer points spectra faster (“subsequent spectra” $S_{i,j}$). The sequence can be written as

$$P_1, S_{1,1}, S_{1,2}, \dots, S_{1,k}, P_2, S_{2,1}, S_{2,2}, \dots, S_{2,k}, \dots, P_n, S_{n,1}, S_{n,2}, \dots, S_{n,k}. \quad (7.12)$$

Use the DSG lineshape to determine the line position for the precise spectra P_i and the reference method to determine the relative shift of the subsequent spectra $S_{i,j}$ with respect to the precise spectrum P_i . In this way, the lower uncertainties provided by the reference method can be combined with the long-term drift and electron line information from the DSG method. Such a concept enables lower measurement times of the subsequent spectra in comparison with the spectra A_i from the option 1.

3. Measure the conversion line only at a few points or even at a single point to obtain the dependence of electron count rate on time (e.g. the inflection point where a change of voltage leads to the largest change of the count rate). A detailed base spectrum measured in the beginning of the monitoring can be interpolated¹ in order to obtain the calculated voltage as a function of the measured count rate. Comparison of the calculated voltage to the one measured by the voltmeter gives information about the voltage stability.

The option 1 above represents a straightforward and transparent way of monitoring. Also it is the way spectra have been measured and analysed at the MoS during the line position stability measurements. The disadvantage is that the moderate time needed to obtain the line position or the relative shift leads to a relatively slower response of the MoS system. The option 2 is more complicated in terms of feasibility and analysis and there is no experience with such a method for measurement of the conversion lines. The advantage is that the response time of the MoS system can be relatively smaller due to faster measurement of most of the spectra. In the option 3 the interpretation of possible differences of the calculated and measured voltage is ambiguous without having measured further points of the conversion line. Thus, the conversion line spectrum as a base spectrum would have to be measured from time to time in any case. Besides, as the sources decay the count rate drops even if the line position and the high voltage is stable and a correction for the decay has to be taken into account. In the previous two

¹ The interpolation should be done for the DSG lineshape of the base spectrum so that the correspondence between count rate and voltage is unique. This is generally not the case if only the linear interpolation of the statistically randomized spectrum itself is used.

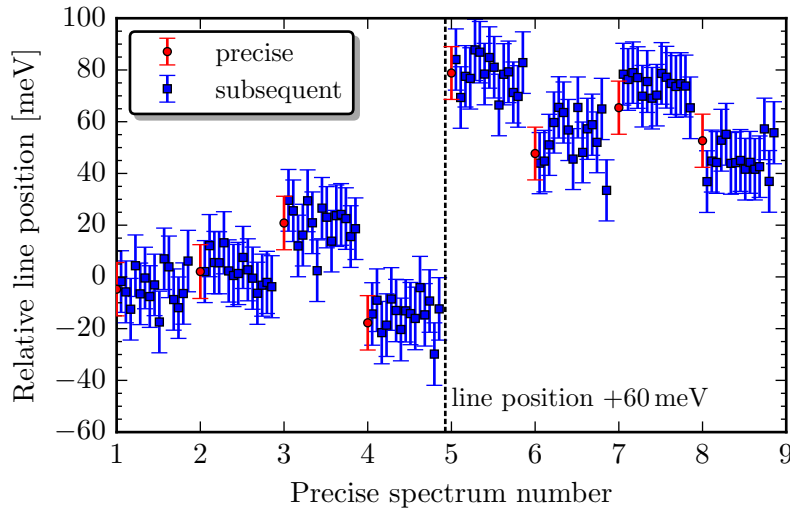


Figure 7.4: Illustration of the precise spectrum line position x_i and the subsequent spectrum line position $x_{i,j}$ as obtained from artificial spectra analysed using the option 2. The calculated line position $x_{i,j}$ is strongly correlated to the fitted line position x_i .

approaches the decay is accounted for by fitting the amplitude or the relative scale factor. For these reasons the option 3 is not further considered.

It turns out that the combination of the DSG and the reference methods in the option 2 is at the same time the most limiting factor since it introduces an unwanted effect which shall now be described. Let us denote the line position obtained from the precise spectrum P_i as x_i and the relative shift of the subsequent spectrum $S_{i,j}$ as $\Delta_{i,j}$. Then the absolute line position corresponding to the spectrum $S_{i,j}$ is

$$x_{i,j} = x_i + \Delta_{i,j}. \quad (7.13)$$

Since P_i is used as the reference spectrum to obtain $\Delta_{i,j}$, the values of x_i and $x_{i,j}$ are correlated.

The problem is illustrated in Fig. 7.4 on artificial statistically randomized precise spectra with a representative lineshape and time per point of 200 s and subsequent spectra with the same line shape and the time per point of 50 s. In the figure the fitted DSG line positions x_i and the line positions $x_{i,j}$ calculated using Eq. (7.13) are shown. The last four sets of spectra are calculated using the line position increased by 60 meV to simulate a sudden shift distortion. The values $x_{i,j}$ are statistically randomized but their mean is not at zero but close to the line position x_i , i.e. the values x_i and $x_{i,j}$ are highly correlated (the correlation coefficient amounts to 0.97). Such an effect is unacceptable for clear detection of a sudden shift. For this reason the option 2 is not recommended for the monitoring and the option 1 should be preferred.

7.2.3 Line position uncertainty and measurement time

The maximal allowed value of the sudden shift is given by Eq. (3.24b). Given the KATRIN limit on the maximal allowed systematic uncertainty $7 \times 10^{-3} \text{ eV}^2$ and assuming no other energy scale distortion takes place the maximal shift amounts in absolute value to about 120 meV, i.e. 6.4 ppm. However, the KATRIN limit applies to all distortions of the high voltage simultaneously so the actual detectable shift should be smaller in order to allow for the other types of distortions.

The obtainable K-32 line position uncertainty at the MoS depends on several factors. As discussed in Section 7.1 the DSG line position uncertainty amounts to about 20 meV for the optimized retarding energy distribution with 43 measurement points, 50 s time in each point, amplitude of 1 kcps and amplitude-to-background ratio of 5 (using a representative lineshape). The spectrum measurement time is about 36 min with no pauses in between the points. At the end of the two-month measurement the activity and thus the amplitude drop to 0.6 of the values in the beginning which leads to an increase of the line position uncertainty by about 30 %.

The amplitude of 1 kcps corresponds to a particular ^{83}Rb activity and the axial position of the source. Based on the results of the fourth and fifth generation BONIS sources the amplitude-to-activity ratio at the source position of 20.9 cm from the magnet center is at the order of 1.7 cps kBq^{-1} for a HOPG-30-type source up to 4.6 cps kBq^{-1} for a HOPG-4-type source. For the Pt substrate the span is from 1.9 cps kBq^{-1} (Pt-30-#) up to 2.5 cps kBq^{-1} (Pt-12-#). Thus, the amplitude might correspond to activities in the range of 200 kBq to 600 kBq.

Amplitude-to-activity ratio

The amplitude-to-activity ratio depends on the source position. By moving the source towards the spectrometer, the magnetic field and thus the acceptance angle increase leading to larger amplitude-to-activity ratio. Ideally, the ratio would be proportional to the solid acceptance angle. Relative to 4π the solid acceptance angle $\Omega_{\text{rel}}(z)$ is calculated in dependence of the source position z as

$$\Omega_{\text{rel}}(z) = \frac{1}{2} (1 - \cos \theta_{\text{max}}(z)) = \frac{1}{2} \left(1 - \sqrt{1 - \frac{B_S(z)}{B_{\text{max}}}} \right), \quad (7.14)$$

where we have used Eq. (2.6) and where the source magnetic field $B_S(z)$ depends on the source position as depicted previously in Fig. 4.4 on the right. A comparison of the experimental observation with the expectation from Eq. (7.14) is shown in Fig. 7.5. The observed increase in the amplitude-to-activity ratio with increasing magnetic field is smaller due to larger amount of loss-energy electrons emitted from the source at higher angles and possibly partly also due to too large size of the source image at the detector.

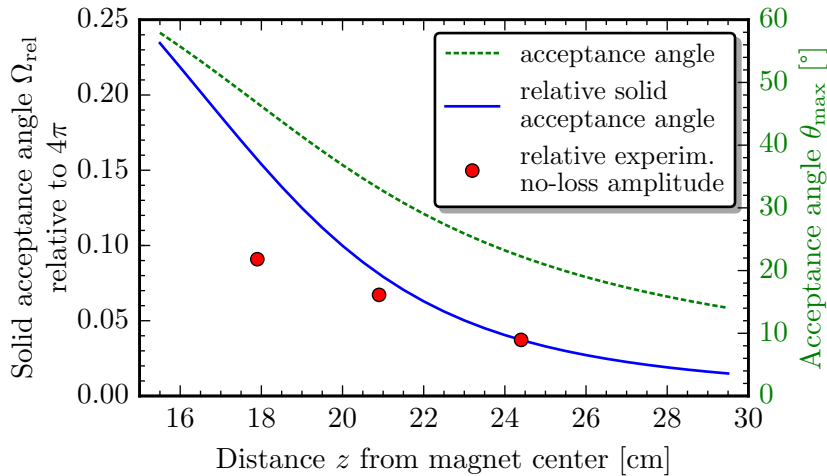


Figure 7.5: Comparison of the relative solid acceptance angle $\Omega_{\text{rel}}(z)$ and the experimental no-loss amplitude (Pt-30-9) in dependence of the source distance z from the magnet center. The experimental points are relative to the value at 24.4 cm which is scaled such that it matches the solid angle value. The acceptance angle θ_{max} is also shown for comparison.

Amplitude-to-background ratio

A smaller amplitude-to-background ratio leads to a higher line position uncertainty. A significantly different value was observed for the Pt-substrate sources compared to the HOPG-substrate ones. For the former the value of 2 was measured while for the latter it spans the values of 7 (HOPG-30-1) to 16 (HOPG-4-1). The dependence of the K-32 line position uncertainty on the amplitude-to-background ratio is shown in Fig. 7.6. The values were obtained by fitting artificial spectra calculated using the DSG function for the representative line shape, constant amplitude and varying background. If only the different amplitude-to-background ratio is considered the uncertainty is larger by about 13 % for the Pt-substrate sources compared to HOPG-30-1 and 20 % compared to HOPG-4-1 (assuming that only constant background is fitted for both).

Dead time correction

By using a stronger source (activity at the level of 3 MBq) and inner enough source position amplitudes of up to 10 kcps and accordingly smaller measurement times could be achieved. However, there is an additional effect that prevents a small enough uncertainty of the line position due to the method for calculating the count rate uncertainty. The relative number of electron pulses lost due to the detector dead time is estimated using a pulser which feeds the detector at a constant known rate. The true electron counts uncertainty is calculated using Eq. (4.17) which takes into account both the statistical uncertainty of the electron peak as well as of the pulser peak in the detector spectrum. However, since such an approach is applied pointwise, i.e. for each spectrum point individually, with increasing rate the uncertainty coming from the pulser peak starts to dominate and actually starts

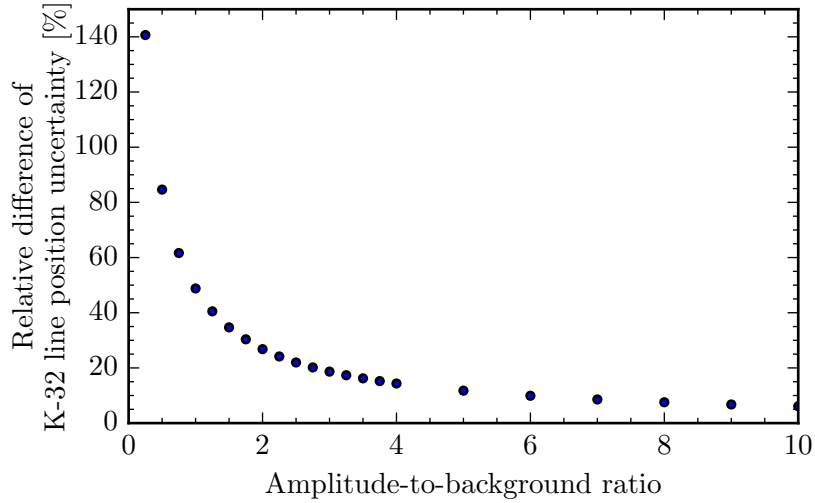


Figure 7.6: Dependence of the fitted K-32 line position uncertainty on the amplitude-to-background ratio. The values are differences relative to the value at the ratio of ∞ , i.e. with zero background. Similar results apply to the uncertainty of the relative spectrum shift obtained using the reference method.

to increase the estimated true relative count rate uncertainty. This is illustrated using an experimental K-32 spectrum in Fig. 7.7 on the left. The expectation from the Poisson distribution of $\sqrt{1/N_e}$ is also shown for comparison.

Such a problem can be overcome by using detector spectra acquired for all points of the integral spectrum simultaneously [Zbo11]. The correction factor $k = ft/N_p$, which is used to estimate the true electron counts N according to Eq. (4.14), is the ratio of the true pulser counts and the observed pulser counts. From the non-paralyzable model of radiation detection it follows that the factor k depends on the total measured detector rate n_{tot} as

$$k(n_{\text{tot}}) = \frac{1}{1 - \tau n_{\text{tot}}}, \quad (7.15)$$

where τ is the detector dead time. For each point of the integral spectrum the coefficient k is calculated and plotted against the total rate, see Fig. 7.7 on the right. The observed trend is fitted using Eq. (7.15) with the free parameter² τ . The true electron counts N is calculated as

$$N = k(n_{\text{tot}})N_e. \quad (7.16)$$

The uncertainty $\sigma(N)$ is estimated using the principle of propagation of uncertainty as

$$\sigma^2(N) \approx N_e^2 \sigma^2(k) + k^2 N_e, \quad (7.17)$$

where $\sigma^2(k) \approx n_{\text{tot}}^2 k^4 \sigma^2(\tau)$. Such an approach significantly decreases the relative uncertainty for the higher count rates, see also Fig. 7.7 on the left. Although the approach was not routinely utilized for the analysis of the integral spectra in this work, it is highly

² In the work [Zbo11] another free parameter is used in the numerator of r.h.s. of Eq. (7.15).

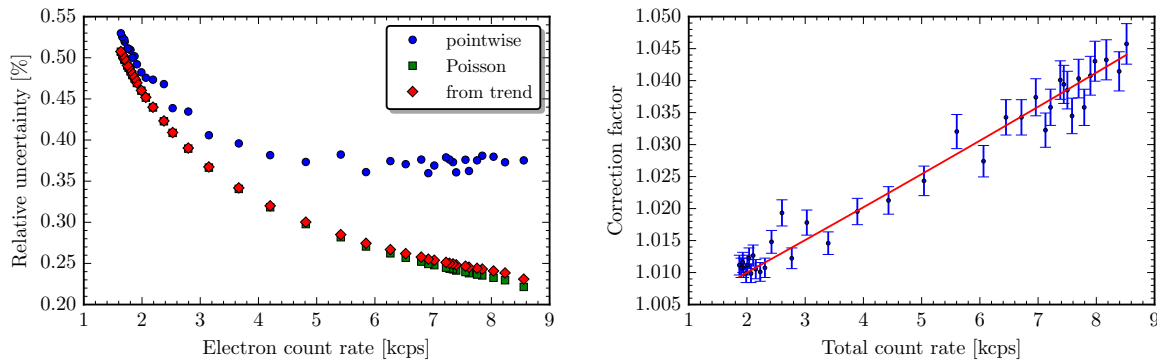


Figure 7.7: Left: The relative uncertainty of the true electron counts $\sigma(N)/N$ of an experimental K-32 spectrum in dependence of the true electron count rate for pointwise calculation from Eq. (4.17), for expectation from Poisson statistics, and for calculation using the trend of the correction factor k from Eq. (7.17). Right: The experimental correction factor k in dependence of the total count rate fitted by Eq. (7.15). The chi-square value divided by the number of degrees of freedom amounted to $\chi_{\text{dof}}^2 = 1.08$ (37 dof).

recommended for analysis of the spectra used for KATRIN high-voltage stability monitoring.

Conclusion

Based on the above considerations it is possible to achieve the DSG line position uncertainty of about 15 meV for a 3 MBq Pt-30-# source in the inner source position of 17.9 cm using the spectrum measurement time of 15 min. The time includes the assumed waiting time between each point of the spectrum of 4 s which is required for the DAQ system to communicate and for the change of the retarding energy to stabilize. Such an uncertainty allows a clear detection (at the level of 4σ) of a sudden line position shift at the level of 60 meV, i.e. 3 ppm, from just a single spectrum. The sudden shift corresponds to the neutrino mass squared shift of only $-1.8 \times 10^{-3} \text{ eV}^2$, i.e. 25 % of the KATRIN limit in absolute value, and thus detection of shift of such a size is sufficient. In case the reference method is used, the uncertainty of the relative shift can be only 10 meV or even less if a precise reference spectrum is used.

The time of measurement needed to obtain the uncertainty represents only the fraction of about 0.02 % of the two-month KATRIN run. Thus, such a time can be considered short enough for the MoS system to raise an alarm about a line position shift. At this rate there would be about 5000 spectra and thus line position results available for the whole run. The duty cycle of the MoS, defined as the ratio of the time the system is taking data to the total measurement time, equals to about 80 %. Increasing the measurement time to 30 min leads to the DSG line position uncertainty of 10 meV and the duty cycle of about 90 % which might be more favorable. A clear detection of 40 meV shift is possible corresponding to the neutrino mass squared shift of only $-8 \times 10^{-4} \text{ eV}^2$. It is precisely such ppm-level detection capability and stability of the high-voltage dividers and the MoS

system that is required for KATRIN. Short measurement times are weighted with a larger uncertainty and lower duty cycle and make the detection of a few-ppm shift difficult.

The uncertainty $\sigma(c)$ of the line position drift c can be calculated using the analytical formula

$$\sigma^2(c) = \frac{\sum_i w_i}{\sum_i w_i \sum_i w_i t_i^2 - (\sum_i w_i t_i)^2}, \quad (7.18)$$

where $w_i = \frac{1}{\sigma_i^2}$, t_i is the time of the line position measurement and σ_i is the uncertainty of the line position. The uncertainty from the two-month measurement with 15 min spectra can be estimated to be at the order of $0.5 \text{ meV month}^{-1}$ taking into account the increase of the line position uncertainty over time due to the radioactive decay of the source. Such a low uncertainty is by far sufficiently small.

7.2.4 Measurement of additional conversion line and electron source

The primary purpose of the MoS is to continuously measure the K-32 conversion electrons which have energy close to the tritium β -spectrum endpoint energy using a solid $^{83\text{m}}\text{Kr}$ source. However, as discussed and shown before measurement of the L₃-32 line and another electron source can possibly lead to distinction of different types of distortions which is not possible using a single line and source only. Specifically,

- a common change of the positions of the two lines points to a change of an additive factor such as the MoS work function,
- a line position change proportional to the line position points to a change of a multiplicative factor such as the high-voltage divider dividing ratio,
- a change which is different for two sources points to a change due to the source itself.

Thus, it seems reasonable that such an approach is followed during the high-voltage stability monitoring.

However, currently there are certain limitations for such an approach.

- The MoS retarding voltage in the parallel mode is determined by the main spectrometer retarding voltage and is thus fixed to values at around -18.6 kV during the tritium β -spectrum measurement. To measure the L₃-32 line in such a configuration the source bias voltage of almost -12 kV would be required. Such a voltage is not feasible due to its high value and due to the need to utilize another high-precision voltage divider in order to precisely measure the voltage.
- The change of the measured source requires change of the source holder position. Besides the fact that the MoS measurement has to be interrupted the change is currently possible only using a manual mechanical manipulator. It is not feasible to perform regular changes in such a way during the continuous two-month KATRIN

tritium run. An electrically controlled positioning unit similar to the one used to change the axial position is currently not installed.

Clearly, prior to and after the parallel operation the above two limitations do not apply at all. Thus, to obtain at least limited information for disentangling the various distortions it is recommended to measure the other conversion line and the electron source both prior to and after the tritium run.

Let us estimate the uncertainty of the K-32 line position drift measured with the second source only prior to and after the parallel operation. We assume a 15 min measurement leading to the line position uncertainty of 15 meV at the beginning as before. Additionally, we assume that the L_3 -32 line of both sources is measured each for 10 min and the K-32 of the primary source is measured for 15 min. This leads to having the K-32 line position of the second source at every³ 50 min. About 200 line position values are available after a week of measurement prior to the parallel operation and another 200 after it. According to Eq. (7.18) the line position drift uncertainty can be estimated to about 1 meV month^{-1} which is sufficiently small. Clearly, a linear behavior of the line position is assumed for the time of the parallel operation.

7.3 Conclusion

The method of the KATRIN high-voltage monitoring should be transparent and “easy-to-use”. Therefore, based on the above considerations the following approach is recommended.

- At least two SKrS samples with an activity of about 3 MBq should be utilized in an inner source position to maximize the count rate.
- Prior to the parallel operation of the MoS the K-32 and L_3 -32 spectra of the sources should be measured without detailed optimization of the measurement distribution in order to characterize the conversion line shape of the fresh sources.
- Then the K-32 and L_3 -32 lines should be gradually and repeatedly measured for a period of at least a week using the optimized retarding energy distribution in order to establish early line position stability for a smaller time period.
- During the parallel operation the measurement of only the K-32 line of one of the sources should be continued. The spectra should be analysed both with the DSG lineshape and the reference method using the improved dead time correction. For a Pt-30-# source the DSG line position uncertainty of 15 meV is achievable in 15 min. A longer measurement time can increase the duty cycle of the MoS.

³ A more practical situation is to measure the same line and the same source a couple of times and only then switch to a different line or source. We do not consider such a situation here for simplicity.

- After the parallel operation again the two conversion lines of both sources should be measured for at least a week. In this way, the line position stability over the complete time period can be evaluated using more than one source.
- A bake-out of the MoS vessel at the beginning of each measurement should be performed in order to avoid possible drift of the spectrometer work function. Such an approach should be followed especially since the source chamber has to be baked out in any case and since the MoS heating system is reliable and fully automatic.

The above proposed approach should be experimentally tested in the parallel operation of the main and the monitor spectrometer prior to application for tritium data in order to verify the estimated uncertainties and the overall applicability of the method.

8 Conclusion

The absolute mass scale of neutrinos is of great interest in modern particle physics, astrophysics, and cosmology. The aim of the KATRIN experiment is to address the absolute mass scale of neutrinos with an unprecedented sensitivity using high-resolution and high-luminosity electron spectroscopy. KATRIN will measure the tritium β -spectrum in the region close to its endpoint which is sensitive to the neutrino mass in a model-independent way. As was discussed in Chapter 2, after three years of data taking the discovery potential for the effective electron antineutrino mass will be 0.35 eV (5σ). In case no signal is found, the upper limit will be 0.2 eV (90 % C.L.). Thus, KATRIN will probe the quasi-degenerate region of the neutrino mass hierarchy.

One of the major systematic effects in KATRIN is the instability of the experimental energy scale. An unrecognized variation of the observed electron energy could lead to a shift of the observed neutrino mass squared towards smaller or even negative values. As was described in detail in Chapter 3, in order to reach the design sensitivity the maximal allowed standard deviation of the energy scale distortions can be at most only 60 meV (3 ppm). It is by no means obvious that the energy scale will be stable at such a level for the whole KATRIN run of two months.

Besides high-precision and high-stability electronic devices developed within the KATRIN collaboration the energy scale will be calibrated and monitored in an independent way using internal conversion electrons emitted from a nuclear standard based on the metastable isotope $^{83\text{m}}\text{Kr}$. The $^{83\text{m}}\text{Kr}$ will be applied in three different forms. The gaseous $^{83\text{m}}\text{Kr}$ will be introduced into the KATRIN tritium source for space charge measurement and energy calibration. The condensed $^{83\text{m}}\text{Kr}$ will be utilized further downstream of the main beamline for energy calibration. Lastly, the $^{83\text{m}}\text{Kr}$ embedded in a solid through implantation of its mother isotope ^{83}Rb will be used at the monitor spectrometer parallel to the main beamline for continuous monitoring of the high-voltage system. The properties and applications of $^{83\text{m}}\text{Kr}$ in KATRIN for the energy scale calibration and monitoring were described in detail in Chapter 3.

A good description of the conversion electron line shape is necessary for the $^{83\text{m}}\text{Kr}$ to be applicable in KATRIN. The monitor spectrometer, the expected conversion line shape and the actually observed line shape of the solid $^{83\text{m}}\text{Kr}$ source were discussed in Chapter 4. It was shown that the observed line shape is asymmetric in contrast to the expected symmetrical Lorentzian shape. A new description based on the asymmetric function of Doniach and Šunjić convoluted with the Gaussian function was developed. Such a function, based on the idea of interaction of the substrate conduction electrons with the hole created after conversion electron emission, was shown to describe the observed line shape in a reasonable and consistent way in contrast to the previously used doublet of Voigt functions. Besides, the reference method was introduced and shown to be a

convenient method for obtaining a relative shift between two spectra. The disadvantage of the method resides in the possibility of obtaining a wrong shift if two spectra with different line shape are compared. Thus, its applicability as for the long-term drift of the electron energy is limited.

The solid $^{83\text{m}}\text{Kr}$ source, its basic characteristics and development were discussed in Chapter 5. The primary purpose of the source is to provide high-voltage stability monitoring at the ppm level by means of the K-32 conversion electrons. The necessary electron energy stability was demonstrated for the period of about two months for sources implanted at the BONIS facility at the energy of the ^{83}Rb ions of 30 keV.

The further questions which arose during the pilot studies of the solid $^{83\text{m}}\text{Kr}$ source in the work [Zbo11] were addressed. A lower implantation energy was also attempted but in that case the electron energy was not stable as desired. This was most likely due to the notably higher implanted ^{83}Rb peak concentration. As a consequence, such high concentration has to be avoided for future sources. The thermal annealing used to repair the damage done to the substrate lattice after implantation did not improve the source quality. Besides platinum, the zinc oxide and the highly-oriented pyrolytic graphite substrates were also investigated. Only the HOPG substrate was found to be suitable since the electron energy was not stable when the ZnO was used. Based on the measurement results it was concluded that the HOPG might be a better choice than Pt but more HOPG sources should be produced and measured at the monitor spectrometer to confirm the conclusion. The stability of the spectrometer work function, achievable by means of a thorough bake-out, was found to be a critical factor for the line position stability measurements. Such a factor is likely to be critical also at the KATRIN main spectrometer. It was thus strongly recommended that a long-term stability measurement using the gaseous $^{83\text{m}}\text{Kr}$ is performed at the main spectrometer to address this issue.

The gaseous $^{83\text{m}}\text{Kr}$ source, based on the mother generator ^{83}Rb trapped in zeolite, was discussed in Chapter 6 with respect to the release of $^{83\text{m}}\text{Kr}$ under various surrounding vacuum and gas conditions. Several zeolite types were studied and it was concluded that the zeolite type 5A seems to be the most suitable one. It was demonstrated that a pre-heated source releases about 80 % of all the $^{83\text{m}}\text{Kr}$ produced by the decay of ^{83}Rb leading to the available activity of $^{83\text{m}}\text{Kr}$ of about 0.6 relatively to the activity of ^{83}Rb . Besides, heating under vacuum ensures removal of air compounds and especially water which are otherwise released from the zeolite into the vacuum apparatus. As a result, the apparatus for housing the zeolite source at the KATRIN tritium source should have heating elements installed in order to heat the source prior to its connection to the tritium loop. No influence on the $^{83\text{m}}\text{Kr}$ release was found even when the source was exposed to various dry gases under different pressures. Thus, it can be expected that the release will be similarly high in case of tritium atmosphere although an experimental confirmation of such an expectation is desired.

Based on the experience and measurement results from the monitor spectrometer options for the actual high-voltage stability monitoring using the solid $^{83\text{m}}\text{Kr}$ source were discussed in Chapter 7. Besides, a fast technique for optimization of the retarding energy and time distribution of the conversion electron integral spectrum was presented. The

achievable statistical uncertainty of the measured electron energy was evaluated. It was concluded that the line position uncertainty of 15 meV should be possible to achieve in 15 min using a 3 MBq source with platinum substrate implanted at 30 keV at the BONIS facility. Such an uncertainty would allow a clear detection of a 60 meV shift from a single spectrum. If lower implantation energy sources are produced and good enough stability of the line position is achieved, the uncertainty or time needed for the measurement could be improved. In case the reference method is used, the sensitivity for the detection of a sudden shift can be even higher. Based on further considerations concerning measurement of an additional solid $^{83\text{m}}\text{Kr}$ source and conversion line an approach for the monitoring was proposed.

8.1 Outlook

The following items should be addressed in future work.

- As discussed in Section 5.2.3, due to the relatively large uncertainties the source ^{83}Rb activity (and consequently the implanted dose and peak concentration) cannot be determined better than to about 10%. The ^{83}Rb decay scheme could be re-measured using silicon and germanium detectors to improve the precision of the activity determination.
- A correlation between the line position drift and the ^{83}Rb peak concentration for the solid $^{83\text{m}}\text{Kr}$ source was found as discussed in Section 5.4. The ^{83}Rb activity spot is much smaller when using the retarding setup at BONIS due to additional focusing. Further samples produced at lower implantation energies should be produced with a large activity spot, if possible, and shed further light on the actual mechanism responsible for the line position drift. Similarly, the problem could be addressed using the perturbed angular correlation measurements.
- Although annealing of the SKrS substrate after implantation did not improve the source quality as described in Section 5.3, a further test could be accomplished with the HOPG substrate. It is recommended that two sources are produced with the same ^{83}Rb implantation energy and similar activity and one of them is utilized for the annealing. Time should be taken in order to evaluate the source retention and radiographical image both prior to and after the annealing. The two sources could then be compared with respect to the conversion line position stability from a long-term measurement at the monitor spectrometer.
- The monitor spectrometer transmission function improved using the source radiographical image, discussed in Section 5.6, could be further tested using a HOPG-substrate source. No parasitic x-rays which could cause blurring in the radiographical image are emitted leading to even a more accurate calculation of the transmission function.

-
- The effect of internal conversion on valence electrons seems to be a reasonable explanation for the satellite structure observed at the $N_{2,3-32}$ line of the solid ^{83m}Kr source as addressed in Section 5.5. Nevertheless, the density of states around the ^{83m}Kr impurity could be calculated theoretically in order to improve the understanding of the observed patterns and possibly also of the ^{83m}Kr environment.
 - It is not expected that the tritium atmosphere will influence the release of ^{83m}Kr from the zeolite ^{83}Rb source since other dry gases and especially hydrogen do not seem to influence it either as discussed in Section 6.2. Nevertheless, an actual measurement confirming the expectation should be carried out prior to using the source in the tritium loop of KATRIN.
 - The parallel operation of the monitor and the main spectrometer and the monitoring scheme should be experimentally tested. Moreover, the long-term stability of the line position should be accomplished prior to measuring tritium data.

A Dead time of the silicon drift detector

The silicon drift detector (SDD)¹ was used in this work for γ -spectroscopy measurements of the solid $^{83\text{m}}\text{Kr}$ sources in order to evaluate the activity of the sources. For the activity evaluation the experimental intensity of the emitted x-ray or γ -ray lines is necessary. To correctly assess the intensity the detector dead time has to be taken into account. However, inconsistencies of the dead time as reported by the detector system were found. In this chapter, the experimental observations are reported and the SDD dead time is assessed.

A.1 Analogue and digital electronics

In analogue spectroscopy electronics the pulse coming from the detector preamplifier is firstly fed into the amplifier where it is shaped and only then it is sent further into the analogue-to-digital (ADC) converter. There the conversion is performed for the pulse amplitude which carries the information about the detected radiation energy. Based on the digitized result the number of counts in the corresponding channel in the spectrum is incremented by one.

It is the time when the ADC performs the conversion during which other pulses cannot be processed and must be rejected. This is what is in analogue systems referred to as the dead time [Gil08]. In this case, the so-called detector live time (LT) is simply the time when the ADC input gate is open. To assess the dead time, usually a live time clock is present that feeds impulses at a constant rate through the input gate and the number of pulses that pass the gate are recorded afterwards. The decrease of the passed pulses with respect to the ones expected from the clock rate (which can also be measured internally), which expresses the real elapsed time (RT), is a measure of the dead time. Specifically, the dead time τ is given as

$$\tau = \frac{\text{RT} - \text{LT}}{\text{RT}}. \quad (\text{A.1})$$

On the other side, in digital electronics the analogue-to-digital conversion is done before the shaping in the amplifier takes place. That is, the pulse from the preamplifier is digitized at a high rate, e.g. 80 MHz, meaning that at each clock tick the actual pulse value is converted into a pre-defined number approximating the true value. After shaping the pulse becomes triangular (or in general trapezoidal) and again its amplitude corresponds

¹ Supplier: Amptek, Inc., the United States of America. Detector type: X-123 complete x-ray spectrometer, digital processor DP5. Acquisition software: DPPMCA version 1.0.0.16.

to the detected energy. At this moment, the analysis of the amplitude is done almost instantaneously as the required information is already digitized.

It follows that, in this case, the dead time in the sense of analogue systems is not present. Instead, what is referred in digital electronics to as the dead time is the duration for which two shaped pulses overlap. This is because the pulse that came later in time is rejected [AMP]. This is not the same effect as “pile-up” when the shaped pulses are so close that they appear as a single pulse with correspondingly higher amplitude. The overlap occurs also in the case of analogue systems but is usually subdominant to the dead time due to the ADC. As a consequence the digital electronics can accept much higher input rates.

A.1.1 SDD electronics

In the SDD detector the pulse shaping is done in parallel in two different channels for different purposes [AMP].

- The slow channel has a long shaping time constant and is optimized to obtain accurate pulse heights. These are then fed into the spectrum.
- The fast channel has a short shaping time constant and is optimized to detect pulses that overlap in the slow channel and for pile-up rejection if enabled.

In order to identify pulses, both channels use thresholds. If an event has its amplitude below the threshold, it is rejected. It is recommended that the thresholds are set just above the noise and since the fast channel usually has a higher noise, the threshold there will be higher. The slow channel threshold is equivalent to what is generally known as low-level discriminator. In the case of the slow channel, also pulses with amplitudes higher than value corresponding to the uppermost channel in the spectrum are rejected. There is no upper limit for the fast channel.

As there is no dead time present in the sense of analogue systems, there is no corresponding live time. What the SDD detector reports is known as accumulation time which represents the duration when acquisition was running, i.e. when the digital electronics was active. The acquisition clock is turned off only during certain events, including some data transfers etc. The count rate is calculated using the accumulation time. The real time also reported by the detector is the true elapsed time from the beginning of measurement and is generally slightly larger than the accumulation time.

Dead time in the SDD

To assess the digital electronics dead time the fast channel is utilized. Let us firstly consider the case of low input count rates (below ~ 10 kcps). In this case, the fast channel count rate F represents the true input count rate that is coming into the detector. The slow channel count rate is $S < F$ and the dead time τ is simply expressed as

$$\tau = \frac{F - S}{F}. \quad (\text{A.2})$$

If the input count rate is high, correction has to be applied to F because pulse overlap starts to occur in the fast channel also. The recommended correction is

$$F'_t = \frac{F}{1 - Ft_F}, \quad (\text{A.3})$$

where t_F is twice the fast channel peaking time. The correction is 1% at 12 kcps for peaking time of 400 ns. For the dead time calculation in Eq. (A.2) the true fast channel count rate F'_t is then used instead of the measured rate F . The true count rate $s_t(i)$ in the channel i is then calculated from the measured count rate $s(i)$ as

$$s_t(i) = \frac{s(i)}{1 - \tau}. \quad (\text{A.4})$$

The uncertainty $\sigma(s_t(i))$ of the true count rate is calculated using the principle of propagation of uncertainty as

$$\sigma(s_t(i)) = \frac{\sqrt{s(i)}}{1 - \tau}. \quad (\text{A.5})$$

where the numerator follows from Poisson statistics of the measured count rate.

The dead time τ calculated utilizing the fast channel information can be compared to the estimation obtained from the paralyzable dead time model. The true slow channel rate S_t is obtained numerically from²

$$S = S_t \exp(-S_t T_d), \quad (\text{A.6})$$

where

$$T_d = 2(1 + f)(T_p + T_{fl}) \quad (\text{A.7})$$

with T_p being the peaking time, T_{fl} the flat top width and f accounts for the time required to confirm that a peak occurred. In our case, $T_d = (1 + f) \cdot 23.2 \mu\text{s}$, where according to [Red08] f equals threshold divided by mean pulse amplitude. The threshold channel i_{th} is the minimal channel such that $s(i_{\text{th}} + 1) > 0$ and the mean pulse amplitude is given by the spectrum weighted mean channel i_{mean} as

$$i_{\text{mean}} = \frac{\sum_{i=1}^n i s(i)}{\sum_{i=1}^n s(i)}. \quad (\text{A.8})$$

Then $f = i_{\text{th}}/i_{\text{mean}}$. The dead time τ is

$$\tau = \frac{S_t - S}{S_t}. \quad (\text{A.9})$$

² Since the function $S_t \exp(-S_t T_d)$ is not monotonous there are always two solutions of the equation. Nevertheless, the detector load was small enough that the actual true load could always safely correspond to the smaller of the two solutions.

Table A.1: Important SDD settings for the measurement of the detector dead time.

Setting	Value
Slow channel threshold	0.585
Pile-up rejection	enabled
Peaking time	11.2 μ s
Reset lockout	204 μ s
Flat top width	0.4 μ s
Fast channel peaking time	0.4 μ s
Baseline restoration down corr.	3
Baseline restoration up corr.	0
Number of MCA channels	4096

A.2 Measurement of the SDD dead time

The experimental goal was to compare the count rate of the 26 keV γ -line emitted from the radioactive decay of ^{241}Am measured under three different settings of the detector fast channel threshold (FT), two different amplifier gain settings and different detector radiation load. The count rate should depend neither on the gain nor on the load if the dead time correction works in a consistent way because the physical γ -line intensity is always the same (the half-life of ^{241}Am is 432.6 yr).

A.2.1 Measurement setup

Three sets of measurements differing by the setting of the FT were conducted. The settings were: 5.18 (set automatically by the control software), 10 and 15 (both set manually). In each set altogether four measurements were performed, two of them with the total amplifier gain of 30.284 (for which the lowest FT setting was found) and the other two with the gain of 20.999. The higher gain leads to coverage of the energy interval of 6 keV to 40 keV while the lower one enables to measure the strong 59 keV γ -line emitted from ^{241}Am . In each pair of measurements with the same gain one was conducted with the ^{241}Am source³ alone at a distance to the detector surface of 10 mm and the other one with an additional ^{83}Rb source⁴ placed on top of the americium source serving as an additional load for the detector. The ^{241}Am source was moved neither during the measurements nor in between them.

The measurement time (accumulation time) was set to 15 min except for the two measurements with the lowest FT and higher gain where it was set to 1 h. The other important detector settings are listed in Table A.1. The 26 keV line in each spectrum was least-squares fitted with the Gaussian function superimposed to a linear background⁵.

³ ^{241}Am deposited between two polyethylene foils further covered with aluminum foil and sealed in a metal ring, activity of about 2 MBq.

⁴ ^{83}Rb deposited on polyethylene foil, activity of about 1.4 MBq.

⁵ In all measurements an additional Gaussian function was used at the lower energy side of the peak

The line count rate was obtained by dividing the area of the Gaussian function above the background by the accumulation time.

A.2.2 Measurement results and discussion

Tables A.2 to A.4 list the obtained results for the three FT settings. The γ -line count rate is presented in three ways:

- “uncorrected”: count rate obtained from the spectrum with uncorrected counts,
- “software”: the counts were corrected for the software reported dead time in Eq. (A.2),
- “manual”: the counts were corrected for the estimated dead time in Eq. (A.9).

The number in bracket denotes the statistical uncertainty of the rate applied to the least significant figures of the rate value which was obtained from the fit. The weighted standard deviation σ_w for a single measurement originates from the spread of the values and is calculated as

$$\sigma_w = \sqrt{\frac{\sum_{j=1}^m \frac{(x_j - \bar{x})^2}{\sigma_j^2}}{\frac{m-1}{m} \sum_{j=1}^m \frac{1}{\sigma_j^2}}}, \quad (\text{A.10})$$

where x_j and σ_j are, respectively, the value and its standard uncertainty, \bar{x} is the weighted mean of the values and m is the number of values.

The main points can be summarized as follows.

- As expected the detector exhibits some dead time because the uncorrected count rate decreases with increased radiation load for all gain and FT settings.
- The software count rate is inconsistent among gains and loads. The differences between the numbers (expressed by means of the weighted standard deviation) are much larger than what can be expected based on the statistical uncertainties.
- The manual count rate does not depend on the load but it is inconsistent for the lowest FT setting as it depends on the gain. For the other two FT settings it appears to be consistent. Also note that the values are by some 5% higher than for the first FT setting.

to account for its asymmetry. In measurements with both radioactive sources a third Gaussian function was used at the higher energy side to describe a small asymmetry arising probably due to sum of some lower energy peaks. In all cases, the function describing the 26 keV peak was by far the most dominant.

Table A.2: Dead time measurement results for the fast threshold setting of 5.18.

Gain	Load	S (cps)	Dead time (%)		γ -line count rate (cps)		
			softw.	man.	uncorr.	softw.	man.
higher	Am	4599.8	45.4	11.9	80.1(2)	146.2(4)	90.4(3)
	Am+Rb	7252.4	49.0	19.8	73.2(3)	143.5(4)	90.4(4)
lower	Am	4567.9	50.6	11.9	77.4(5)	156.8(9)	87.5(5)
	Am+Rb	7098.4	54.4	19.3	71.8(5)	157.0(11)	88.4(6)
Weighted standard deviation						5.6	1.4

Table A.3: Dead time measurement results for FT of 10.

Gain	Load	S (cps)	Dead time (%)		γ -line count rate (cps)		
			softw.	man.	uncorr.	softw.	man.
higher	Am	4832.9	30.3	12.6	82.9(5)	119.0(7)	94.5(6)
	Am+Rb	7590.4	37.2	20.8	76.1(6)	121.1(10)	95.1(8)
lower	Am	4983.0	28.4	13.0	83.2(5)	116.3(7)	95.3(6)
	Am+Rb	7712.2	36.4	21.2	76.7(5)	120.2(8)	96.5(7)
Weighted standard deviation						2.1	0.8

Table A.4: Dead time measurement results for FT of 15.

Gain	Load	S (cps)	Dead time (%)		γ -line count rate (cps)		
			softw.	man.	uncorr.	softw.	man.
higher	Am	4899.4	24.0	12.8	82.9(5)	109.0(7)	94.5(6)
	Am+Rb	7534.9	32.7	20.7	76.5(6)	113.5(9)	95.5(8)
lower	Am	5066.0	20.5	13.3	83.1(5)	104.4(6)	95.3(6)
	Am+Rb	7808.9	30.9	21.5	75.6(7)	109.6(10)	96.0(9)
Weighted standard deviation						3.9	0.6

A.3 Conclusion

Based on experimental observation of the intensity of the 26 keV γ -line of ^{241}Am , which is constant in time and between individual measurements, under different load of the detector we have to conclude that the dead time reported by the software is not correct. This is in contrast to the results presented in [Red08] where an x-ray tube with Mn target was used as a source of x-rays. Similarly, the agreement between experimental and simulated efficiencies, as described in Section 5.2.3, could not be achieved by using the software dead time. The software values would lead to too high and inconsistent efficiency values obtain from each calibration source. We were able to obtain consistent results after manually calculating the dead time in case of measurements with a fast channel threshold which was higher than the one set automatically by the software.

References

- [Akh09] E. K. Akhmedov and A. Y. Smirnov, *Paradoxes of neutrino oscillations*, Phys. Atom. Nucl. 72, 1363–1381 (2009), DOI: [10.1134/S1063778809080122](https://doi.org/10.1134/S1063778809080122).
- [AMP] *DP5 user manual and operating instructions*, Amptek, Inc., URL: http://www.advancedlab.org/mediawiki/images/c/cc/DP5_User_Manual_A1.pdf (visited on 11/06/2015).
- [Are13] M. Arenz and R. Vianden, *^{83m}Kr , a potentially powerful PAC probe*, Hyperfine interact. 222, 73–76 (2013), DOI: [10.1007/s10751-012-0723-3](https://doi.org/10.1007/s10751-012-0723-3).
- [Are16] M. Arenz, Doctoral thesis, University of Bonn, 2016, in prep.
- [Ase11] V. N. Aseev et al., *Upper limit on the electron antineutrino mass from the Troitsk experiment*, Phys. Rev. D 84, 112003 (2011), DOI: [10.1103/PhysRevD.84.112003](https://doi.org/10.1103/PhysRevD.84.112003).
- [Aud86] G. Audi, W. G. Davies, and G. E. Lee-Whiting, *A method of determining the relative importance of particular data on selected parameters in the least-squares analysis of experimental data*, Nucl. Instr. Meth. Phys. Res. A 249, 443–450 (1986), DOI: [10.1016/0168-9002\(86\)90700-X](https://doi.org/10.1016/0168-9002(86)90700-X).
- [Bah01] J. N. Bahcall, M. H. Pinsonneault, and S. Basu, *Solar models: current epoch and time dependences, neutrinos, and helioseismological properties*, Astrophys. J. 555, 990–1012 (2001), DOI: [10.1086/321493](https://doi.org/10.1086/321493).
- [Bah63] J. N. Bahcall et al., *Solar neutrino flux*, Astrophys. J. 137, 344–346 (1963), DOI: [10.1086/147513](https://doi.org/10.1086/147513).
- [Bau13] S. Bauer et al., *Next generation KATRIN high precision voltage divider for voltages up to 65kV*, J. Instrum. 8, P10026 (2013), DOI: [10.1088/1748-0221/8/10/P10026](https://doi.org/10.1088/1748-0221/8/10/P10026).
- [Bau14] S. Bauer, *Energy calibration and stability monitoring of the KATRIN experiment*, Doctoral thesis, University of Münster, 2014.
- [Bel08] A. I. Belesev et al., *Investigation of space-charge effects in gaseous tritium as a source of distortions of the beta spectrum observed in the Troitsk neutrino-mass experiment*, Phys. Atomic Nuclei 71, 427–436 (2008), DOI: [10.1134/S1063778808030046](https://doi.org/10.1134/S1063778808030046).
- [Ber10] M. J. Berger et al., *XCOM: Photon cross sections database*, The National Institute of Standards and Technology (NIST), 2010, URL: <http://www.nist.gov/pml/data/xcom/> (visited on 09/11/2015).

- [Bhu13] P. S. Bhupal Dev et al., *Constraining neutrino mass from neutrinoless double beta decay*, Phys. Rev. D 88, 091301 (2013), DOI: [10.1103/PhysRevD.88.091301](https://doi.org/10.1103/PhysRevD.88.091301).
- [BOR08] C. Arpesella et al. (The Borexino Collaboration), *First real time detection of ^7Be solar neutrinos by Borexino*, Phys. Lett. B 658, 101–108 (2008), DOI: [10.1016/j.physletb.2007.09.054](https://doi.org/10.1016/j.physletb.2007.09.054).
- [Bru97] R. Brun and F. Rademakers, *ROOT - An object oriented data analysis framework*, Nucl. Instr. Meth. Phys. Res. A 389, 81–86 (1997), DOI: [10.1016/S0168-9002\(97\)00048-X](https://doi.org/10.1016/S0168-9002(97)00048-X).
- [Cam01] J. L. Campbell and T. Papp, *Widths of the atomic $K-N7$ levels*, At. Data Nucl. Data Tables 77, 1–56 (2001), DOI: [10.1006/adnd.2000.0848](https://doi.org/10.1006/adnd.2000.0848).
- [Cit73] P. H. Citrin, *High-resolution x-ray photoemission from sodium metal and its hydroxide*, Phys. Rev. B 8, 5545–5556 (1973), DOI: [10.1103/PhysRevB.8.5545](https://doi.org/10.1103/PhysRevB.8.5545).
- [Cit74] P. H. Citrin and D. R. Hamann, *Measurement and calculation of polarization and potential-energy effects on core-electron binding energies in solids: x-ray photoemission of rare gases implanted in noble metals*, Phys. Rev. B 10, 4948–4963 (1974), DOI: [10.1103/PhysRevB.10.4948](https://doi.org/10.1103/PhysRevB.10.4948).
- [Cle98] B. T. Cleveland, *Measurement of the solar electron neutrino flux with the Homestake chlorine detector*, Astrophys. J. 496, 505–526 (1998), DOI: [10.1086/305343](https://doi.org/10.1086/305343).
- [Dav68] R. Davis Jr., D. S. Harmer, and K. C. Hoffmann, *Search for neutrinos from the Sun*, Phys. Rev. Lett. 20, 1205–1209 (1968), DOI: [10.1103/PhysRevLett.20.1205](https://doi.org/10.1103/PhysRevLett.20.1205).
- [DB12] F. P. An et al. (The Daya Bay Collaboration), *Observation of electron antineutrino disappearance at Daya Bay*, Phys. Rev. Lett. 108, 171803 (2012), DOI: [10.1103/PhysRevLett.108.171803](https://doi.org/10.1103/PhysRevLett.108.171803).
- [DCH13] Y. Abe et al. (The Double Chooz Collaboration), *First measurement of θ_{13} from delayed neutron capture on hydrogen in the Double Chooz experiment*, Phys. Lett. B 723, 66–70 (2013), DOI: [10.1016/j.physletb.2013.04.050](https://doi.org/10.1016/j.physletb.2013.04.050).
- [Don70] S. Doniach and M. Šunjić, *Many-electron singularity in x-ray photoemission and x-ray line spectra from metals*, J. Phys. C 3, 285–291 (1970), DOI: [10.1088/0022-3719/3/2/010](https://doi.org/10.1088/0022-3719/3/2/010).
- [Dra02] O. Dragoun et al., *Scattering of 7.3 keV conversion electrons from a ^{57}Co source covered gradually by gold absorbers of various thicknesses*, Nucl. Instr. Meth. Phys. Res. B 194, 112–122 (2002), DOI: [10.1016/S0168-583X\(02\)00688-2](https://doi.org/10.1016/S0168-583X(02)00688-2).

- [Dra04] O. Dragoun, A. Špalek, and F. J. Wuilleumier, *Increased accuracy of the binding energy of K- and L-subshell electrons in krypton from re-analysis of experimental data: importance for determination of the neutrino mass*, Czech. J. Phys. 54, 833–839 (2004), DOI: [10.1023/B:CJOP.0000038591.13369.e1](https://doi.org/10.1023/B:CJOP.0000038591.13369.e1).
- [Dra87] O. Dragoun et al., *Some nuclear and atomic properties of ^{201}Hg determined by conversion electron spectroscopy*, Z. Phys. 326, 279–285 (1987), DOI: [10.1007/BF01297582](https://doi.org/10.1007/BF01297582).
- [Due69] G. Duesing and W. Schilling, *Stage III recovery in electron-irradiated platinum*, Radiat. Eff. 1, 65–67 (1969), DOI: [10.1080/00337576908234461](https://doi.org/10.1080/00337576908234461).
- [Ell04] S. R. Elliott and J. Engel, *Double-beta decay*, J. Phys. 30, R183–R215 (2004), DOI: [10.1088/0954-3889/30/9/R01](https://doi.org/10.1088/0954-3889/30/9/R01).
- [Eng64] F. Englert and R. Brout, *Broken symmetry and the mass of gauge vector mesons*, Phys. Rev. Lett. 13, 321–323 (1964), DOI: [10.1103/PhysRevLett.13.321](https://doi.org/10.1103/PhysRevLett.13.321).
- [Erh12] M. Erhard, *Untersuchung der Langzeitstabilität des nuklearen Standards für die Energieskala des KATRIN-Experiments* (in German), Diploma thesis, Karlsruhe Institute of Technology, 2012.
- [Erh14] M. Erhard et al., *High-voltage monitoring with a solenoid retarding spectrometer at the KATRIN experiment*, J. Instrum. 9, P06022 (2014), DOI: [10.1088/1748-0221/9/06/P06022](https://doi.org/10.1088/1748-0221/9/06/P06022).
- [EXO14] J. B. Albert et al. (The EXO-200 Collaboration), *Search for Majorana neutrinos with the first two years of EXO-200 data*, Nature 510, 229–234 (2014), DOI: [10.1038/nature13432](https://doi.org/10.1038/nature13432).
- [Fel71] W. Feller, *An introduction to probability theory and its applications*, 2nd ed., John Wiley and Sons Ltd., 1971.
- [Fel98] G. J. Feldman and R. D. Cousins, *Unified approach to the classical statistical analysis of small signals*, Phys. Rev. D 57, 3873–3889 (1998), DOI: [10.1103/PhysRevD.57.3873](https://doi.org/10.1103/PhysRevD.57.3873).
- [For99] D. Forkel-Wirth, *Exploring solid state physics properties with radioactive isotopes*, Rep. Prog. Phys. 62, 527–597 (1999), DOI: [10.1088/0034-4885/62/4/002](https://doi.org/10.1088/0034-4885/62/4/002).
- [Fre79] K. Freitag, *A facility for ion implantation in samples colder than 0.5 K*, Radiat. Eff. 44, 185–190 (1979), DOI: [10.1080/00337577908245993](https://doi.org/10.1080/00337577908245993).
- [GAL92] P. Anselmann et al. (The GALLEX Collaboration), *Solar neutrinos observed by GALLEX at Gran Sasso*, Phys. Lett. B 285, 376–389 (1992), DOI: [10.1016/0370-2693\(92\)91521-A](https://doi.org/10.1016/0370-2693(92)91521-A).
- [GER13] M. Agostini et al. (The GERDA Collaboration), *Results on neutrinoless double β decay of ^{76}Ge from phase I of the GERDA experiment*, Phys. Rev. Lett. 111, 122503 (2013), DOI: [10.1103/PhysRevLett.111.122503](https://doi.org/10.1103/PhysRevLett.111.122503).

- [Gil08] G. R. Gilmore, *Practical gamma-ray spectrometry*, 2nd ed., John Wiley and Sons Ltd., 2008.
- [Giu07] C. Giunti and C. W. Kim, *Fundamentals of neutrino physics and astrophysics*, Oxford University Press, 2007.
- [Gla61] S. L. Glashow, *Partial-symmetries of weak interactions*, Nucl. Phys. 22, 579–588 (1961), DOI: [10.1016/0029-5582\(61\)90469-2](https://doi.org/10.1016/0029-5582(61)90469-2).
- [Gri69] V. Gribov and B. Pontecorvo, *Neutrino astronomy and lepton charge*, Phys. Lett. 28, 493–496 (1969), DOI: [10.1016/0370-2693\(69\)90525-5](https://doi.org/10.1016/0370-2693(69)90525-5).
- [Grö10] R. Gröble, *Konzeptionierung und Systematik der Hochspannungsversorgung für das KATRIN Experiment* (in German), Diploma thesis, Karlsruhe Institute of Technology, 2010.
- [Gro15] S. Groh et al., *Kassiopeia: A modern, extensible C++ particle tracking package*, 2015, in prep.
- [Gun83] O. Gunnarsson, O. Jepsen, and O. K. Andersen, *Self-consistent impurity calculations in the atomic-spheres approximation*, Phys. Rev. B 27, 7144–7168 (1983), DOI: [10.1103/PhysRevB.27.7144](https://doi.org/10.1103/PhysRevB.27.7144).
- [Gur64] G. S. Guralnik, C. R. Hagen, and T. W. B. Kibble, *Global conservation laws and massless particles*, Phys. Rev. Lett. 13, 585–587 (1964), DOI: [10.1103/PhysRevLett.13.585](https://doi.org/10.1103/PhysRevLett.13.585).
- [Han11] V. Hannen et al., *Limits on the release of Rb isotopes from a zeolite based ^{83m}Kr calibration source for the XENON project*, J. Instrum. 6, P10013 (2011), DOI: [10.1088/1748-0221/6/10/P10013](https://doi.org/10.1088/1748-0221/6/10/P10013).
- [Har98] J. W. Harris and H. Stöcker, *Handbook of mathematics and computational science*, Springer-Verlag, 1998.
- [Hau13] N. Haußmann, *Development of analysis tools and automatisisation of run control for KATRIN*, Diploma thesis, Karlsruhe Institute of Technology, 2013.
- [Her86] P. Herzog, in: *Low-temperature nuclear orientation*, ed. by N. J. Stone and H. Postma, Elsevier Science Ltd., 1986.
- [Hig64a] P. W. Higgs, *Broken symmetries and the masses of gauge bosons*, Phys. Rev. Lett. 13, 508–509 (1964), DOI: [10.1103/PhysRevLett.13.508](https://doi.org/10.1103/PhysRevLett.13.508).
- [Hig64b] P. W. Higgs, *Broken symmetries, massless particles and gauge fields*, Phys. Lett. 12, 132–133 (1964), DOI: [10.1016/0031-9163\(64\)91136-9](https://doi.org/10.1016/0031-9163(64)91136-9).
- [Hoř02] J. Hořejší, *Fundamentals of electroweak theory*, Karolinum Press, 2002.
- [Hub04] J. H. Hubbell and S. M. Seltzer, *Table of x-ray mass attenuation coefficients and mass energy-absorption coefficients for 1 keV to 20 MeV for elements $Z = 1$ to 92 and 48 additional substances of dosimetric interest*, The National Institute of Standards and Technology (NIST), 2004, URL: <http://www.nist.gov/pml/data/xraycoef/> (visited on 09/11/2015).

- [Hub75] J. H. Hubbell et al., *Atomic form factors, incoherent scattering functions, and photon scattering cross sections*, J. Phys. Chem. Ref. Data 4, 471–538 (1975), DOI: [10.1063/1.555523](https://doi.org/10.1063/1.555523).
- [Hub79] J. H. Hubbell and L. Øverbø, *Relativistic atomic form factors and photon coherent scattering cross sections*, J. Phys. Chem. Ref. Data 8, 69–105 (1979), DOI: [10.1063/1.555593](https://doi.org/10.1063/1.555593).
- [Hüf75] S. Hüfner and G. K. Wertheim, *Core-line asymmetries in the x-ray photoemission spectra of metals*, Phys. Rev. B 11, 678–683 (1975), DOI: [10.1103/PhysRevB.11.678](https://doi.org/10.1103/PhysRevB.11.678).
- [IMB91] D. Casper et al. (The IMB Collaboration), *Measurement of atmospheric neutrino composition with the IMB-3 detector*, Phys. Rev. Lett. 66, 2561–2564 (1991), DOI: [10.1103/PhysRevLett.66.2561](https://doi.org/10.1103/PhysRevLett.66.2561).
- [Jak09] J. Jakubek, *Energy-sensitive X-ray radiography and charge sharing effect in pixelated detector*, Nucl. Instr. Meth. Phys. Res. A 607, 192–195 (2009), DOI: [10.1016/j.nima.2009.03.148](https://doi.org/10.1016/j.nima.2009.03.148).
- [Jam75] F. James and M. Roos, *Minuit - a system for function minimization and analysis of the parameter errors and correlations*, Comput. Phys. Commun. 10, 343–367 (1975), DOI: [10.1016/0010-4655\(75\)90039-9](https://doi.org/10.1016/0010-4655(75)90039-9).
- [K2K05] E. Aliu et al. (The K2K Collaboration), *Evidence for muon neutrino oscillation in an accelerator-based experiment*, Phys. Rev. Lett. 94, 081802 (2005), DOI: [10.1103/PhysRevLett.94.081802](https://doi.org/10.1103/PhysRevLett.94.081802).
- [Kam80] N. Kambe, G. Dresselhaus, and M. S. Dresselhaus, *Electron diffraction from superlattices in graphite-rubidium intercalation compounds*, Phys. Rev. B 21, 3491–3501 (1980), DOI: [10.1103/PhysRevB.21.3491](https://doi.org/10.1103/PhysRevB.21.3491).
- [KAM88] K. S. Hirata et al. (The Kamiokande Collaboration), *Experimental study of the atmospheric neutrino flux*, Phys. Lett. B 205, 416–420 (1988), DOI: [10.1016/0370-2693\(88\)91690-5](https://doi.org/10.1016/0370-2693(88)91690-5).
- [KAM89] K. S. Hirata et al. (The Kamiokande Collaboration), *Observation of ^8B solar neutrinos in the Kamiokande-II detector*, Phys. Rev. Lett. 63, 16–19 (1989), DOI: [10.1103/PhysRevLett.63.16](https://doi.org/10.1103/PhysRevLett.63.16).
- [Kaš04] J. Kašpar et al., *Effect of energy scale imperfections on results of neutrino mass measurements from β -decay*, Nucl. Instr. Meth. Phys. Res. A 527, 423–431 (2004), DOI: [10.1016/j.nima.2004.03.201](https://doi.org/10.1016/j.nima.2004.03.201).
- [Kaš08] J. Kašpar, *Am/Co photoelectron source for energy scale monitoring of the KATRIN neutrino experiment*, Doctoral thesis, Czech Technical University in Prague, 2008.
- [KAT04] J. Angrik et al. (The KATRIN Collaboration), *KATRIN design report*, 2005, URL: <http://www.katrin.kit.edu/>.
- [Keß08] P. Keßler, *Implantationsschäden in polaren und unpolaren ZnO Einkristallen* (in German), Diploma thesis, University of Bonn, 2008.

- [Kin04] S. F. King, *Neutrino mass models*, Rep. Prog. Phys. 67, 107–157 (2004), DOI: [10.1088/0034-4885/67/2/R01](https://doi.org/10.1088/0034-4885/67/2/R01).
- [KL03] K. Eguchi et al. (The KamLAND Collaboration), *First results from KamLAND: evidence for reactor antineutrino disappearance*, Phys. Rev. Lett. 90, 021802 (2003), DOI: [10.1103/PhysRevLett.90.021802](https://doi.org/10.1103/PhysRevLett.90.021802).
- [KL11] A. Gando et al. (The KamLAND Collaboration), *Constraints on θ_{13} from a three-flavor oscillation analysis of reactor antineutrinos at KamLAND*, Phys. Rev. D 83, 052002 (2011), DOI: [10.1103/PhysRevD.83.052002](https://doi.org/10.1103/PhysRevD.83.052002).
- [Kla04] H. V. Klapdor-Kleingrothaus et al., *Search for neutrinoless double beta decay with enriched ^{76}Ge in Gran Sasso 1990-2003*, Phys. Lett. B 586, 198–212 (2004), DOI: [10.1016/j.physletb.2004.02.025](https://doi.org/10.1016/j.physletb.2004.02.025).
- [Kla06] H. V. Klapdor-Kleingrothaus and I. V. Krivosheina, *The evidence for the observation of $0\nu\beta\beta$ decay: the identification of $0\nu\beta\beta$ events from the full spectra*, Mod. Phys. Lett. A 21, 1547–1566 (2006), DOI: [10.1142/S0217732306020937](https://doi.org/10.1142/S0217732306020937).
- [Kle14] M. Kleesiek, *A data-analysis and sensitivity-optimization framework for the KATRIN experiment*, Doctoral thesis, Karlsruhe Institute of Technology, 2014.
- [KLZ13] A. Gando et al. (The KamLAND-ZEN Collaboration), *Limit on neutrinoless $\beta\beta$ decay of ^{136}Xe from the first phase of KamLAND-Zen and comparison with the positive claim in ^{76}Ge* , Phys. Rev. Lett. 110, 062502 (2013), DOI: [10.1103/PhysRevLett.110.062502](https://doi.org/10.1103/PhysRevLett.110.062502).
- [Kom09] E. Komastu et al., *Five-year Wilkinson Microwave Anisotropy Probe observations: cosmological interpretation*, Astrophys. J. Suppl. 180, 330–376 (2009), DOI: [10.1088/0067-0049/180/2/330](https://doi.org/10.1088/0067-0049/180/2/330).
- [Kra05] C. Kraus et al., *Final results from phase II of the Mainz neutrino mass search in tritium β decay*, Eur. Phys. J. C 40, 447–468 (2005), DOI: [10.1140/epjc/s2005-02139-7](https://doi.org/10.1140/epjc/s2005-02139-7).
- [Kra12] M. Kraus, *Kalibration und Entwicklung von Komponenten für das KATRIN-Präzisions-Hochspannungs-System* (in German), Diploma thesis, Karlsruhe Institute of Technology, 2012.
- [Kug92] E. Kugler et al., *The new CERN-ISOLDE on-line mass-separator facility at the PS-Booster*, Nucl. Instr. Meth. Phys. Res. B 70, 41–49 (1992), DOI: [10.1016/0168-583X\(92\)95907-9](https://doi.org/10.1016/0168-583X(92)95907-9).
- [Kür13] S. Kürten, *Untersuchung über die Rückhaltung von ^{83}Rb beim thermischen Ausheilen von Platin, Zinkoxid und Graphit* (in German), Bachelor thesis, University of Bonn, 2013.
- [Lah11] A. R. Lahrood et al., *X-ray photoelectron spectroscopy on implanted argon as a tool to follow local structural changes in this films*, Thin Solid Films 520, 1625–1630 (2011), DOI: [10.1016/j.tsf.2011.07.040](https://doi.org/10.1016/j.tsf.2011.07.040).

- [Lei99] J. A. Leiro and M. H. Heinonen, *Ka_{1,2} x-ray emission and Doniach-Šunjić-type line shapes*, Phys. Rev. B 59, 3265–3269 (1999), DOI: [10.1103/PhysRevB.59.3265](https://doi.org/10.1103/PhysRevB.59.3265).
- [LEP06] The ALEPH, DELPHI, L3, OPAL and SLD Collaborations, the LEP Electroweak Working Group, the SLD Electroweak and Heavy Flavour Groups, *Precision electroweak measurements on the Z resonance*, Phys. Rep. 427, 257–454 (2006), DOI: [10.1016/j.physrep.2005.12.006](https://doi.org/10.1016/j.physrep.2005.12.006).
- [Les06] J. Lesgourgues and S. Pastor, *Massive neutrinos and cosmology*, Phys. Rep. 429, 307–379 (2006), DOI: [10.1016/j.physrep.2006.04.001](https://doi.org/10.1016/j.physrep.2006.04.001).
- [Llo07] X. Llopart et al., *Timepix, a 65k programmable pixel readout chip for arrival time, energy and/or photon counting measurements*, Nucl. Instr. Meth. Phys. Res. A 581, 485–494 (2007), DOI: [10.1016/j.nima.2007.08.079](https://doi.org/10.1016/j.nima.2007.08.079).
- [Lob02] V. M. Lobashev, *Study of the tritium beta-spectrum in experiment “Troitsk ν -mass”*, Prog. Part. Nucl. Phys. 48, 123–131 (2002), DOI: [10.1016/S0146-6410\(02\)00118-7](https://doi.org/10.1016/S0146-6410(02)00118-7).
- [Lob85] V. M. Lobashev and P. E. Spivak, *A method for measuring the electron antineutrino rest mass*, Nucl. Instr. Meth. Phys. Res. A 240, 305–310 (1985), DOI: [10.1016/0168-9002\(85\)90640-0](https://doi.org/10.1016/0168-9002(85)90640-0).
- [Luc74] L. Lucy, *An iterative technique for the rectification of observed distributions*, Astron. J. 79, 745–754 (1974), DOI: [10.1086/111605](https://doi.org/10.1086/111605).
- [Mak62] Z. Maki, M. Nakagawa, and S. Sakata, *Remarks on the unified model of elementary particles*, Prog. Theor. Phys. 28, 870–880 (1962), DOI: [10.1143/PTP.28.870](https://doi.org/10.1143/PTP.28.870).
- [Man84] F. Mandl and G. P. Shaw, *Quantum field theory*, John Wiley and Sons Ltd., 1984.
- [Mar67] M. A. Mariscotti, *A method for automatic identification of peaks in the presence of background and its application to spectrum analysis*, Nucl. Instr. Meth. Phys. Res. 50, 309–320 (1967), DOI: [10.1016/0029-554X\(67\)90058-4](https://doi.org/10.1016/0029-554X(67)90058-4).
- [McC15] E. A. McCutchan, *Nuclear data sheets for A = 83*, Nucl. Data Sheets 125, 201–394 (2015), DOI: [10.1016/j.nds.2015.02.002](https://doi.org/10.1016/j.nds.2015.02.002).
- [Mik85] S. P. Mikheev and A. Y. Smirnov, *Resonant amplification of neutrino oscillations in matter and spectroscopy of solar neutrinos*, Sov. J. Nucl. Phys. 42, 913–917 (1985), DOI: [10.1007/BF02508049](https://doi.org/10.1007/BF02508049).
- [Mik86] S. P. Mikheev and A. Y. Smirnov, *Resonant amplification of neutrino oscillations in matter and solar neutrino spectroscopy*, Nuovo Cim. C 9, 17–26 (1986), DOI: [10.1007/BF02508049](https://doi.org/10.1007/BF02508049).
- [MIN06] D. G. Michael et al. (The MINOS Collaboration), *Observation of muon neutrino disappearance with the MINOS detectors in the NuMi neutrino beam*, Phys. Rev. Lett. 97, 191801 (2006), DOI: [10.1103/PhysRevLett.97.191801](https://doi.org/10.1103/PhysRevLett.97.191801).

- [Moo00] T. D. Moon and W. C. Stirling, *Mathematical methods and algorithms for signal processing*, Prentice Hall, 2000.
- [Mor00] M. Morháč et al., *Identification of peaks in multidimensional coincidence γ -ray spectra*, Nucl. Instr. Meth. Phys. Res. A 443, 108–125 (2000), DOI: [10.1016/S0168-9002\(99\)01005-0](https://doi.org/10.1016/S0168-9002(99)01005-0).
- [Mye15] E. G. Myers et al., *Atomic masses of tritium and helium-3*, Phys. Rev. Lett. 114, 013003 (2015), DOI: [10.1103/PhysRevLett.114.013003](https://doi.org/10.1103/PhysRevLett.114.013003).
- [Nag06] S. Nagy et al., *On the Q -value of the tritium β -decay*, Europhys. Lett. 74, 404–410 (2006), DOI: [10.1209/epl/i2005-10559-2](https://doi.org/10.1209/epl/i2005-10559-2).
- [NEM14] R. Arnold et al. (The NEMO-3 Collaboration), *Search for neutrinoless double-beta decay of ^{100}Mo with the NEMO-3 detector*, Phys. Rev. D 89, 111101 (2014), DOI: [10.1103/PhysRevD.89.111101](https://doi.org/10.1103/PhysRevD.89.111101).
- [Noc99] J. Nocedal and S. J. Wright, *Numerical optimization*, Springer-Verlag, 1999.
- [OPE14] N. Agafonova et al. (The OPERA Collaboration), *Evidence for $\nu_\mu \rightarrow \nu_\tau$ appearance in the CNGS neutrino beam with the OPERA experiment*, Phys. Rev. D 89, 051102 (2014), DOI: [10.1103/PhysRevD.89.051102](https://doi.org/10.1103/PhysRevD.89.051102).
- [Ost08] B. Ostrick, *Eine kondensierte ^{83m}Kr -Kalibrationsquelle für das KATRIN - Experiment* (in German), Doctoral thesis, University of Münster, 2008.
- [Ott08] E. W. Otten and C. Weinheimer, *Neutrino mass limit from tritium β decay*, Rep. Prog. Phys. 71, 086201 (2008), DOI: [10.1088/0034-4885/71/8/086201](https://doi.org/10.1088/0034-4885/71/8/086201).
- [Pat68] T. N. L. Patterson, *The optimum addition of points to quadrature formulae*, Math. Comp. 22, 847–856 (1968), DOI: [10.2307/2004583](https://doi.org/10.2307/2004583).
- [PDG14] K. A. Olive et al. (Particle Data Group), *Review of particle physics*, Chin. Phys. C 38, 090001 (2014), DOI: [10.1088/1674-1137/38/9/090001](https://doi.org/10.1088/1674-1137/38/9/090001).
- [Pet92] J. W. Petersen et al., *High resolution conversion electron spectroscopy of impurities in semiconductors*, Nucl. Instr. Meth. Phys. Res. B 63, 179–185 (1992), DOI: [10.1016/0168-583X\(92\)95191-S](https://doi.org/10.1016/0168-583X(92)95191-S).
- [Pet93] J. W. Petersen, A. Svane, and E. Holzschuh, *Densities of states of substitutional tin and germanium impurities in GaAs, GaP, and InP: Experiment and theory*, Phys. Rev. B 47, 1811–1822 (1993), DOI: [10.1103/PhysRevB.47.1811](https://doi.org/10.1103/PhysRevB.47.1811).
- [Pic92a] A. Picard et al., *A solenoid retarding spectrometer with high resolution and transmission for keV electrons*, Nucl. Instr. Meth. Phys. Res. B 63, 345–358 (1992), DOI: [10.1016/0168-583X\(92\)95119-C](https://doi.org/10.1016/0168-583X(92)95119-C).
- [Pic92b] A. Picard et al., *Precision measurement of the conversion electron spectrum of ^{83m}Kr with a solenoid retarding spectrometer*, Nucl. Instr. Meth. Phys. Res. A 342, 71–78 (1992), DOI: [10.1007/BF01294491](https://doi.org/10.1007/BF01294491).
- [PLA14] P. A. R. Ade et al. (The Planck Collaboration), *Planck 2013 results. XVI. Cosmological parameters*, Astron. Astrophys. 571, A16 (2014), DOI: [10.1051/0004-6361/201321591](https://doi.org/10.1051/0004-6361/201321591).

- [Pon57] B. Pontecorvo, *Mesonium and anti-mesonium*, Sov. Phys. JETP 6, 429 (1957).
- [Pon58] B. Pontecorvo, *Inverse beta processes and nonconservation of lepton charge*, Sov. Phys. JETP 7, 172–173 (1958).
- [Pon68] B. Pontecorvo, *Neutrino experiments and the problem of conservation of leptonic charge*, Sov. Phys. JETP 26, 984–988 (1968).
- [Pre07] W. H. Press et al., *Numerical recipes*, 3rd ed., Cambridge University Press, 2007.
- [Red08] R. H. Redus, A. C. Huber, and D. J. Sperry, Dead time correction in the DP5 digital pulse processor, in: *Nuclear Science Symposium Conference Record, 2008. NSS '08. IEEE*, 2008, DOI: [10.1109/NSSMIC.2008.4775075](https://doi.org/10.1109/NSSMIC.2008.4775075).
- [Rei67] C. H. Reinsch, *Smoothing by spline functions*, Numer. Math. 10, 177–183 (1967), DOI: [10.1007/BF02162161](https://doi.org/10.1007/BF02162161).
- [REN12] J. K. Ahn et al. (The RENO Collaboration), *Observation of reactor electron antineutrinos disappearance in the RENO experiment*, Phys. Rev. Lett. 108, 191802 (2012), DOI: [10.1103/PhysRevLett.108.191802](https://doi.org/10.1103/PhysRevLett.108.191802).
- [Res14] O. Rest, *Inbetriebnahme der Präzisionshochspannung am Hauptspektrometer des KATRIN-Experiments* (in German), Diploma thesis, University of Münster, 2014.
- [Ric72] W. Richardson, *Bayesian-based iterative method of image restoration*, J. Opt. Soc. Am. 62, 55–59 (1972), DOI: [10.1364/JOSA.62.000055](https://doi.org/10.1364/JOSA.62.000055).
- [Rob83] R. G. H. Robertson et al., *Limit on ν_e^- mass from observation of the β decay of molecular tritium*, Phys. Rev. Lett. 67, 957–960 (1983), DOI: [10.1103/PhysRevLett.67.957](https://doi.org/10.1103/PhysRevLett.67.957).
- [Rob88] R. G. H. Robertson and D. A. Knapp, *Direct measurements of neutrino mass*, Ann. Rev. Nucl. Part. Sci. 38, 185–215 (1988), DOI: [10.1146/annurev.ns.38.120188.001153](https://doi.org/10.1146/annurev.ns.38.120188.001153).
- [SAG94] J. N. Abdurashitov et al. (The SAGE Collaboration), *Results from SAGE (The Russian-American gallium solar neutrino experiment)*, Phys. Lett. B 328, 234–248 (1994), DOI: [10.1016/0370-2693\(94\)90454-5](https://doi.org/10.1016/0370-2693(94)90454-5).
- [Sal68] A. Salam, *Weak and electromagnetic interactions*, Conf. Proc. C 680159, 367–377 (1968).
- [Sch11] M. Schupp, *Inbetriebnahme des Monitorspektrometers und erste Messungen* (in German), Diploma thesis, Karlsruhe Institute of Technology, 2011.
- [Sch82] J. Schechter and J. W. F. Valle, *Neutrinoless double- β decay in $SU(2)\times U(1)$ theories*, Phys. Rev. D 25, 2951–2954 (1982), DOI: [10.1103/PhysRevD.25.2951](https://doi.org/10.1103/PhysRevD.25.2951).
- [Sil96] Z. K. Silagazde, *A new algorithm for automatic photopeak searches*, Nucl. Instr. Meth. Phys. Res. A 376, 451–454 (1996), DOI: [10.1016/0168-9002\(96\)00230-6](https://doi.org/10.1016/0168-9002(96)00230-6).

- [SK04] Y. Ashie et al. (The Super-Kamiokande Collaboration), *Evidence for an oscillatory signature in atmospheric neutrino oscillations*, Phys. Rev. Lett. 93, 101801 (2004), DOI: [10.1103/PhysRevLett.93.101801](https://doi.org/10.1103/PhysRevLett.93.101801).
- [SK06] J. Hosaka et al. (The Super-Kamiokande Collaboration), *Solar neutrino measurements in Super-Kamiokande I*, Phys. Rev. D 73, 112001 (2006), DOI: [10.1103/PhysRevD.73.112001](https://doi.org/10.1103/PhysRevD.73.112001).
- [SK98] Y. Fukuda et al. (The Super-Kamiokande Collaboration), *Evidence for oscillation of atmospheric neutrinos*, Phys. Rev. Lett. 81, 1562–1567 (1998), DOI: [10.1103/PhysRevLett.81.1562](https://doi.org/10.1103/PhysRevLett.81.1562).
- [Sle11] M. Slezák, *The source of monoenergetic electrons for the monitoring of spectrometer in the KATRIN neutrino experiment*, Diploma thesis, Charles University in Prague, 2011.
- [Sle12] M. Slezák et al., *Precise energy of the 9.4 keV gamma transition observed in the ^{83}Rb decay*, Eur. Phys. J. A 48, 12 (2012), DOI: [10.1140/epja/i2012-12012-y](https://doi.org/10.1140/epja/i2012-12012-y).
- [Sle13] M. Slezák et al., *Electron line shape of the KATRIN monitor spectrometer*, J. Instrum. 8, T12002 (2013), DOI: [10.1088/1748-0221/8/12/T12002](https://doi.org/10.1088/1748-0221/8/12/T12002).
- [Smi74] N. V. Smith et al., *Photoemission spectra and band structures of d-band metals. IV. X-ray photoemission spectra and densities of states in Rh, Pd, Ag, Ir, Pt, and Au*, Phys. Rev. B 10, 3197–3206 (1974), DOI: [10.1103/PhysRevB.10.3197](https://doi.org/10.1103/PhysRevB.10.3197).
- [SNO01] Q. R. Ahmad et al. (The SNO Collaboration), *Measurement of the rate of $\nu_e + d \rightarrow p + p + e^-$ interactions produced by ^8B solar neutrinos at the Sudbury Neutrino Observatory*, Phys. Rev. Lett. 87, 071301 (2001), DOI: [10.1103/PhysRevLett.87.071301](https://doi.org/10.1103/PhysRevLett.87.071301).
- [Špa90] A. Špalek, *Effect of scattering processes on the spectra of electrons emitted from the surface of solids: Monte Carlo calculations*, Surf. Interface Anal. 15, 739–744 (1990), DOI: [10.1002/sia.740151206](https://doi.org/10.1002/sia.740151206).
- [Špa93] A. Špalek and O. Dragoun, *The effect of electron backscattering on the shape of the ^{63}Ni beta-ray spectrum*, J. Phys. G 19, 2071–2077 (1993), DOI: [10.1088/0954-3899/19/12/012](https://doi.org/10.1088/0954-3899/19/12/012).
- [Sto95] W. Stoeffl and D. J. Decman, *Anomalous structure in the beta decay of gaseous molecular tritium*, Phys. Rev. Lett. 75, 3237–3240 (1995), DOI: [10.1103/PhysRevLett.75.3237](https://doi.org/10.1103/PhysRevLett.75.3237).
- [Str14] S. Streubel et al., *Toward a more accurate Q value measurement of tritium: status of THe-Trap*, Appl. Phys. B 114, 137–145 (2014), DOI: [10.1007/s00340-013-5669-x](https://doi.org/10.1007/s00340-013-5669-x).
- [T2K12] K. Abe et al. (The T2K Collaboration), *First muon-neutrino disappearance study with an off-axis beam*, Phys. Rev. D 85, 031103 (2012), DOI: [10.1103/PhysRevD.85.031103](https://doi.org/10.1103/PhysRevD.85.031103).

- [Tan11] S. Tanuma, C. J. Powell, and D. R. Penn, *Calculations of electron inelastic mean free paths. IX. Data for 41 elemental solids over the 50 eV to 30 keV range*, Surf. Interface Anal. 43, 689–713 (2011), DOI: [10.1002/sia.3522](https://doi.org/10.1002/sia.3522).
- [Tan94] S. Tanuma, C. J. Powell, and D. R. Penn, *Calculations of electron inelastic mean free paths. V. Data for 14 organic compounds over the 50-2000 eV range*, Surf. Interface Anal. 21, 165–176 (1994), DOI: [10.1002/sia.740210302](https://doi.org/10.1002/sia.740210302).
- [Thü07] T. Thümmler, *Präzisionsüberwachung und Kalibration der Hochspannung für das KATRIN-Experiment* (in German), Doctoral thesis, University of Münster, 2007.
- [Thü09] T. Thümmler, R. Marx, and C. Weinheimer, *Precision high voltage divider for the KATRIN experiment*, New J. Phys. 11, 103007 (2009), DOI: [10.1088/1367-2630/11/10/103007](https://doi.org/10.1088/1367-2630/11/10/103007).
- [Vén05] D. Véнос et al., *^{83m}Kr radioactive sources based on ^{83}Rb trapped in cation-exchange paper or in zeolite*, Appl. Radiat. Isot. 63, 323–327 (2005), DOI: [10.1016/j.apradiso.2005.04.011](https://doi.org/10.1016/j.apradiso.2005.04.011).
- [Vén06] D. Véнос et al., *Precise energy of the weak 32-keV gamma transition observed in the ^{83m}Kr decay*, Nucl. Instr. Meth. Phys. Res. A 560, 352–359 (2006), DOI: [10.1016/j.nima.2005.12.213](https://doi.org/10.1016/j.nima.2005.12.213).
- [Vén14] D. Véнос et al., *Gaseous source of ^{83m}Kr conversion electrons for the neutrino experiment KATRIN*, J. Instrum. 9, P12010 (2014), DOI: [10.1088/1748-0221/9/12/P12010](https://doi.org/10.1088/1748-0221/9/12/P12010).
- [Wei67] S. Weinberg, *A model of leptons*, Phys. Rev. Lett. 19, 1264–1266 (1967), DOI: [10.1103/PhysRevLett.19.1264](https://doi.org/10.1103/PhysRevLett.19.1264).
- [Wei93] C. Weinheimer et al., *Improved limit on the electron-antineutrino rest mass from tritium β -decay*, Phys. Lett. B 300, 210–216 (1993), DOI: [10.1016/0370-2693\(93\)90355-L](https://doi.org/10.1016/0370-2693(93)90355-L).
- [Wer78] G. K. Wertheim and P. H. Citrin, *Fermi surface excitations in x-ray photoemission line shapes from metals*, Top. Appl. Phys. 26, 197–236 (1978), DOI: [10.1007/3540086854_5](https://doi.org/10.1007/3540086854_5).
- [Wer82] G. K. Wertheim, *Shape of core-electron photoemission spectra from metals*, Phys. Rev. B 25, 1987–1989 (1982), DOI: [10.1103/PhysRevB.25.1987](https://doi.org/10.1103/PhysRevB.25.1987).
- [Wol78] L. Wolfenstein, *Neutrino oscillations in matter*, Phys. Rev. D 17, 2369–2374 (1978), DOI: [10.1103/PhysRevD.17.2369](https://doi.org/10.1103/PhysRevD.17.2369).
- [Zbo11] M. Zbořil, *Solid electron sources for the energy scale monitoring in the KATRIN experiment*, Doctoral thesis, University of Münster, 2011.
- [Zbo13] M. Zbořil et al., *Ultra-stable implanted Rb/Kr electron sources for the energy scale monitoring in the KATRIN experiment*, J. Instrum. 8, P03009 (2013), DOI: [10.1088/1748-0221/8/03/P03009](https://doi.org/10.1088/1748-0221/8/03/P03009).

- [Zie10] J. F. Ziegler, M. D. Ziegler, and J. P. Biersack, *SRIM - The stopping and range of ions in matter (2010)*, Nucl. Instr. Meth. Phys. Res. B 268, 1818–1823 (2010), DOI: [10.1016/j.nimb.2010.02.091](https://doi.org/10.1016/j.nimb.2010.02.091).

List of Figures

1.1	Neutrino oscillation probability	12
1.2	Experimental observation of neutrino oscillations	14
1.3	Neutrino masses and hierarchies	16
1.4	Kurie plot of the single β -decay	20
2.1	Principle of the MAC-E filter	23
2.2	Transmission function of an ideal MAC-E filter	24
2.3	Overview of the KATRIN experiment	26
3.1	Time-dependent energy scale fluctuation	35
3.2	Effects of energy scale distortions	39
3.3	Comparison of numerical and approximate analytical shifts of the neutrino mass squared	40
3.4	The decay scheme of ^{83}Rb and $^{83\text{m}}\text{Kr}$	42
3.5	The conversion electron spectrum of $^{83\text{m}}\text{Kr}$	43
3.6	The K-32 conversion electron line	44
3.7	Energy diagrams for considerations of the source and spectrometer work function	45
3.8	Principal scheme of a voltage divider	48
4.1	Cross-section of the monitor spectrometer and its electric and magnetic field configuration	52
4.2	CAD drawing of the monitor spectrometer	54
4.3	Example of the monitor spectrometer detector spectrum	58
4.4	Monitor spectrometer electric and magnetic fields at the analysing plane and at the source	59
4.5	Transmission function of the monitor spectrometer for different distributions of electrons in the flux tube	61
4.6	Experimental K-32 spectrum least-squares fitted by the Lorentzian function	66
4.7	Nodes and weights of the Gauss-Legendre quadrature	70
4.8	Experimental K-32 line fitted with a doublet of Voigt functions and with the Doniach-Šunjić function convoluted with the Gaussian function	72
4.9	Line position of the K-32 line in time	73
4.10	Contours of the χ^2 function	74
4.11	K-32 line amplitude in time and against line position	75
4.12	Experimental L_3 -32 line fitted with a doublet of Voigt functions and with the Doniach-Šunjić function convoluted with the Gaussian function	76

4.13	Other conversion line of ^{83m}Kr fitted with the DSG approach	78
4.14	Simulated depth profile of ^{83}Rb	79
4.15	Simulated loss-energy electron spectrum of the K-32 and L_3 -32 conversion electrons	81
4.16	Response function of the monitor spectrometer	82
4.17	Experimental integral spectrum of K-32 and L_3 -32 fitted using the DSG lineshape including the loss-energy electrons	83
4.18	Fitted line position in dependence of the lower fit boundary	85
4.19	Linear piecewise interpolation and uncertainty of the reference spectrum	87
4.20	Fitted spectrum relative shift in dependence of the lower fit boundary	88
4.21	Spectrum relative shift in dependence of the different lineshape parameters of the analysed spectrum with respect to the reference spectrum	89
4.22	Reference method analysis results of the K-32 line in dependence of time	89
5.1	Scheme of the ISOLDE and BONIS facilities	94
5.2	Distribution of the relative number of ^{83}Rb atoms per units depth and vacancies per ion per unit depth	99
5.3	Distribution of the relative number of ^{83}Rb atoms per units depth in plat- inum, zinc oxide, and graphite	101
5.4	Examples of the ^{83}Rb γ -spectrum measured at the HPGe and SDD detectors	103
5.5	Efficiency of the HPGe and SDD detectors	104
5.6	Differences of activities determined by the SDD and the HPGe detectors	106
5.7	Single frame and complete measurement of the source radiographical image	107
5.8	Timepix energy spectrum and illustration of calculation of the area above half maximum uncertainty	108
5.9	Illustration of the effect of too high frame time on the radiographical image	109
5.10	Illustration of the effect of bumpy mylar foil on the radiographical image	111
5.11	Radiographical images of the solid ^{83m}Kr source samples	113
5.12	Intensity of the 32 keV γ -line of two SKrS samples in dependence of time and different surrounding conditions	117
5.13	K-32 line position for the ISOLDE Pt-based sources measured with the JRL high-voltage divider	118
5.14	Long-term stability of the K-32 line position for the outer source position measured for the ISOLDE sources Pt-15-5 and Pt-10-1	120
5.15	Long-term stability of the L_3 -32 line position and pressure trend for the outer source position	121
5.16	Long-term stability of the K-32 line position for the inner source position	122
5.17	Pressure trend and Gaussian width of the K-32 line for the inner source position	122
5.18	Relative spectrum shift at the time around the deliberate venting test	125
5.19	K-32 line position in time for ISOLDE and first-generation BONIS sources	128
5.20	Long-term stability of the K-32 line position for the sources Pt-30-5 and Pt-30-6	130

5.21	Pressure trend inside the spectrometer for the time of the long-term stability measurements of Pt-30-5 and Pt-30-6	131
5.22	K-32 spectrum for ZnO-30-1 and ZnO-30-2	133
5.23	L ₃ -32 spectrum for ZnO-30-1 and ZnO-30-2	133
5.24	K-32 and L ₃ -32 spectra for Pt-30-7	134
5.25	Long-term stability of the line position of the sources Pt-30-6, Pt-30-7, ZnO-30-1, and ZnO-30-2	135
5.26	Detailed spectra of K-32 and L ₃ -32 for Pt-30-7 after the source aged	136
5.27	Detailed spectrum of K-32 for HOPG-30-1 fitted utilizing constant and linear background terms	138
5.28	Detailed spectrum of L ₃ -32 for HOPG-30-1 fitted utilizing constant and linear background terms	138
5.29	Long-term K-32 line position stability for the fourth generation sources Pt-30-8, Pt-30-9, and HOPG-30-1 and the older source Pt-30-7	139
5.30	Long-term K-32 line position stability for the fifth generation sources Pt-12-1, HOPG-12-1, and HOPG-4-1 and the older source HOPG-30-1	141
5.31	Correlation between the K-32 line position drift and the ⁸³ Rb peak concentration	142
5.32	Example of N _{2,3} -32 spectrum of Pt-10-1 and N ₁ -9.4 spectrum of ZnO-30-2 .	145
5.33	Weights for calculation of the more accurate transmission function of the monitor spectrometer	149
6.1	Sketch of the closeable chamber for measurement of the gaseous ^{83m} Kr source absolute retention	155
6.2	Absolute ^{83m} Kr retention in time for the type-5A zeolite source kept at ambient air and room temperature	156
6.3	Relative ^{83m} Kr retention in time for the type-5A zeolite source under different vacuum conditions	157
6.4	Relative ^{83m} Kr retention in time for the type-5A zeolite source under different gaseous or vacuum conditions	158
6.5	Rest-gas mass spectrum of the UHV chamber and influence of the zeolite beads	160
7.1	Influence and significance for the DSG method and for the reference method	164
7.2	Optimized retarding energy distribution for the DSG lineshape and the reference method	167
7.3	1σ upper limit of the ripple root mean square in dependence of the undistorted gaussian line width	168
7.4	Illustration of the correlation between precise and subsequent spectrum line position obtained from artificial spectra analysed using the option 2	170
7.5	Comparison of the solid acceptance angle and the experimental no-loss amplitude in dependence of the source distance from the magnet center . .	172
7.6	Dependence of the fitted K-32 line position uncertainty on the amplitude-to-background ratio	173

- 7.7 Comparison of the relative uncertainty of true electron counts of an experimental K-32 spectrum calculated by different means and the trend of the correction factor in dependence of the total count rate 174

List of Tables

4.1	List of reasonably strong lines, their energies and obtained (or fixed) DSG parameter value	77
5.1	Overview of the solid $^{83\text{m}}\text{Kr}$ source samples implanted at ISOLDE and BONIS	97
5.2	Expected relative amount of no-energy-loss electrons	102
5.3	Average relative shift after the venting and after the baking of the monitor spectrometer	125
5.4	Line position shift after bake-out and line position drift from the third generation long-term stability measurement	135
5.5	Line position drift observed from the long-term stability measurement of the fourth generation BONIS sources	139
5.6	Line position drift observed from the long-term stability measurement of the fifth generation BONIS sources	141
A.1	Important SDD settings for the measurement of the detector dead time . .	186
A.2	Dead time measurement results for the fast threshold setting of 5.18	188
A.3	Dead time measurement results for the fast threshold setting of 10	188
A.4	Dead time measurement results for the fast threshold setting of 15	188

List of publications

Journal articles

1. M. Slezák, D. Vénos, O. Lebeda, and T. Trojek, *Precise energy of the 9.4 keV gamma transition observed in the ^{83}Rb decay*, Eur. Phys. J. A 48, 12 (2012), DOI: [10.1140/epja/i2012-12012-y](https://doi.org/10.1140/epja/i2012-12012-y).
2. M. Slezák, S. Bauer, O. Dragoun, M. Erhard, K. Schlösser, A. Špalek, D. Vénos, and M. Zbořil, *Electron line shape of the KATRIN monitor spectrometer*, J. Instrum. 8, T12002 (2013), DOI: [10.1088/1748-0221/8/12/T12002](https://doi.org/10.1088/1748-0221/8/12/T12002).
3. M. Zbořil, S. Bauer, M. Beck, J. Bonn, O. Dragoun, J. Jakůbek, K. Johnston, A. Kovalík, E. W. Otten, K. Schlösser, M. Slezák, A. Špalek, T. Thümmler, D. Vénos, J. Žemlička, and C. Weinheimer, *Ultra-stable implanted Rb/Kr electron sources for the energy scale monitoring in the KATRIN experiment*, J. Instrum. 8, P03009 (2013), DOI: [10.1088/1748-0221/8/03/P03009](https://doi.org/10.1088/1748-0221/8/03/P03009).
4. M. Erhard, S. Bauer, A. Beglarian, T. Bergmann, J. Bonn, G. Drexlin, J. Goullon, S. Groh, F. Glück, M. Kleesiek, N. Haußmann, T. Höhn, K. Johnston, M. Kraus, J. Reich, O. Rest, K. Schlösser, M. Schupp, M. Slezák, T. Thümmler, D. Vénos, C. Weinheimer, S. Wüstling, and M. Zbořil, *High-voltage monitoring with a solenoid retarding spectrometer at the KATRIN experiment*, J. Instrum. 9, P06022 (2014), DOI: [10.1088/1748-0221/9/06/P06022](https://doi.org/10.1088/1748-0221/9/06/P06022).
5. D. Vénos, M. Slezák, O. Dragoun, A. Inoyatov, O. Lebeda, Z. Pulec, J. Sentkerestiová, and A. Špalek, *Gaseous source of ^{83m}Kr conversion electrons for the neutrino experiment KATRIN*, J. Instrum. 9, P12010 (2014), DOI: [10.1088/1748-0221/9/12/P12010](https://doi.org/10.1088/1748-0221/9/12/P12010).

Conference proceedings contributions

1. M. Slezák, *Electron line shape and transmission function of the KATRIN monitor spectrometer*, AIP Conference Proceedings 1572, 89–92 (2013), DOI: <http://dx.doi.org/10.1063/1.4856556>.